Barker, P.F., Camerlenghi, A., Acton, G.D., et al., 1999
Proceedings of the Ocean Drilling Program, Initial Reports Volume 178

4. SITE 1095[1]

Shipboard Scientific Party[2]

BACKGROUND AND SCIENTIFIC OBJECTIVES

Site 1095 (Fig. **F1**) is the more distal of two sites on a hemipelagic sediment drift on the continental rise off the northwestern Pacific margin of the Antarctic Peninsula. Site 1095 lies in a water depth of 3840 m on the northwestern termination of the drift and was selected to obtain the deeper part of the stratigraphic section, where the overlying sediments are thinner than at the drift crest (Site 1096).

The site was chosen on the upper part of the northwest flank of the drift, bordering the deep-sea channel system that separates sediment Drifts 7 and 6 on the continental rise (Figs. **F1A, F2**). The sedimentary cover, more than 1200 m thick, rests on a dissected oceanic basement dated at ~42.7 Ma by magnetic anomalies (Barker, 1982; see also **"Site 1096"** chapter, and Barker and Camerlenghi, **Chap. 2,** this volume). A short 3.5-kHz sub-bottom profile crossing the slope (Fig. **F3**) shows layering parallel to the seafloor for 25 ms (~20 m). Multichannel seismic (MCS) profiles across the site (I95-137 and I95-135A [Fig. **F1B;** also see **"Appendix,"** p. 24, and Fig. **AF1,** p. 59, both in the "Leg 178 Summary" chapter]) indicate that the upper part of the section (~100 ms) rests unconformably on a highly reflective unit, whose base was correlated with the base of Unit M2 (onset of "Drift Maintenance" stage) of Rebesco et al. (1997). The total thickness of Units M1 and M2 here is 300 ms, compared with the 740 ms at the proximal drift site (Site 1096; about 75 km closer to the margin). The deeper Units M3 and M4 ("Drift Growth" stage of Rebesco et al., 1997) are therefore more accessible to drilling than at Site 1096.

Drilling at Site 1095 was intended to examine the earlier stages of drift development and glacial evolution (see Barker and Camerlenghi, **Chap. 2,** this volume) and to answer specific questions related to the state of glaciation of the adjacent continent.

F1. Bathymetric map and morphologic elements of Drifts 6 and 7, **p. 43.**

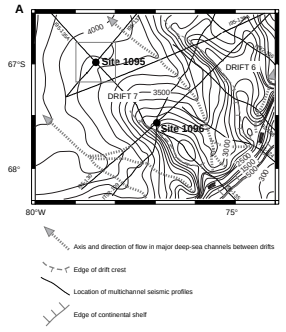

F2. Part of MCS reflection profile I95-137 across Site 1095, **p. 45.**

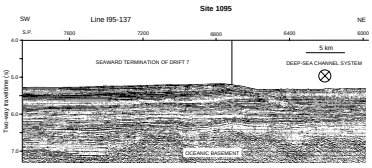

F3. 3.5-kHz sub-bottom profile across Site 1095, **p. 46.**

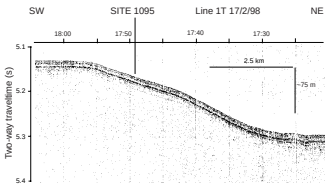

[1]**Examples of how to reference the whole or part of this volume.**
[2]**Shipboard Scientific Party addresses.**

1. Is the present depositional system, documented from work on piston cores (Camerlenghi et al., 1997b; Pudsey and Camerlenghi, 1998), a plausible analogue for the older depositional environment reflected within the cored section?
2. Was deposition cyclic within the lower part of the drift section? If so, what are the cycle frequencies? And what does this cyclicity represent?
3. Can the onset of the present stage of continental glaciation (involving regular ice-sheet excursions to the shelf edge) be recognized in the drift sediments? Is there a relationship between drift development and continental glacial history?
4. Can the terrigenous fraction be used to examine the erosional (uplift?) history of the Antarctic Peninsula?

The answers to many of these questions will come only after detailed and extensive work onshore, but it will be possible here to assess the potential of the recovered cores and point toward some of the work required.

OPERATIONS

Transit to Site 1095

At 0806 hr on 12 February 1998 the *JOIDES Resolution* departed Punta Arenas, Chile, heading northeastward for 95 nmi through the eastern Straits of Magellan, and then generally southward toward the first site of Leg 178 (Fig. **F1,** p. 28, in the "Leg 178 Summary" chapter). *Polar Duke,* chartered as an ice-support ship for Leg 178, sailed a few hours later. Slow progress across Drake Passage in a 2-day full gale delayed the approach to Site 1095 until 17 February (all times are local times, Universal Time Coordinated [UTC] minus 3 hr, unless otherwise stated).

Hole 1095A

As the *JOIDES Resolution* approached Site 1095, a short 3.5-kHz precision depth recorder profile (Fig. **F3**) was acquired to refine the site selection. The positioning beacon was launched at 1615 hr on 17 February, and drilling operations began for the leg. Before spudding, a drill-pipe swab (pig) was pumped down to clear any rust that might have accumulated inside the drill pipe.

Hole 1095A was spudded with the advanced hydraulic piston corer (APC) at 0530 hr on 17 February, with the seafloor depth estimated from recovery as 3841.6 m (3852.6 meters below rig floor). APC coring had advanced to 87.3 meters below seafloor (mbsf) with core recovery of 99.1% (Table **T1**) when operations had to be stopped because an iceberg (one of only two on the 24-mi radar screen) closed within 1.6 nmi. The iceberg had a computed closest point of approach to the drill site of less than 0.5 nmi. Pipe was pulled above the seafloor and the vessel offset in dynamic position mode 1000 feet north of the location while the iceberg passed directly over the drilling site. As the ice cleared the site, the vessel was repositioned 20 m west of Hole 1095A.

T1. Site 1095 coring summary, **p. 119.**

Hole 1095B

After three hours spent waiting on ice, Hole 1095B was spudded at 2145 hr on 18 February. The bit was washed down to 83.0 mbsf, where APC coring resumed. Coring advanced from 83.0 to 205.0 mbsf and ceased when overpulls of 100 kilopounds could not dislodge the core barrel (Core 13H) from the formation. The stuck core barrel was drilled over to release it from the sediment. Coring continued in Hole 1095B with the extended core barrel (XCB) advancing to 483.3 mbsf (Core 43X) with 89.0% recovery. Below this, core recovery was only 18.1%. This factor, together with increasing vessel heave, influenced the decision to terminate drilling at 570 mbsf. Pump pressure was abnormally high below 483.3 mbsf, and on recovery, three of the four bit nozzles were found to be clogged.

In preparation for logging Hole 1095B, a wiper trip was conducted up to 89 mbsf with no drag. While running pipe back to bottom, the region from 541 to 570 mbsf was washed and reamed. The bit contacted 2 m of hard fill on the bottom, which was cleaned from the hole by circulating a 30-bbl high-viscosity mud pill. The drill string was pulled back to 95 mbsf with no drag experienced.

The Schlumberger logging equipment was rigged by 1615 hr on 22 February, and three downhole logging runs were completed in Hole 1095B: a triple combination (TC; lithodensity, porosity, resistivity, and natural gamma ray) log, a geological high-sensitivity magnetic tool (GHMT) log, and a well seismic tool (WST) experiment (see **"Downhole Measurements,"** p. 27). For the TC log, the vessel heave exceeded the maximum stroke of the wireline heave compensator, which was therefore turned off. At the start of the repeat TC run, the hostile environment lithodensity sonde (HLDS) caliper arm became detached, probably when the tool moved downward during a large heave. Because of concern about tool safety, heave, and the large diameter of much of the hole (16–19 in), the Formation MicroScanner–sonic tool string was not run. Seas were lower for the GHMT run, and the wireline heave compensator could be activated. The heave was still large enough to require slow (1000 m/hr) tool speeds through the pipe.

On 20 February, during the drilling of Hole 1095B and at a time when ice conditions permitted, the *Polar Duke* was able to divert to a position close to 67°20.41′S, 77°38.38′W, some 56 km from the drillship, in order to recover a current meter mooring in a water depth of 3580 m. Roberto Laterza, from Osservatorio Geofisico Sperimentale (which had deployed the mooring from *OGS-Explora* in 1997), supervised recovery and extracted the recorded data. The current meters had successfully recorded 11.5 months of data, which help to define the modern oceanographic environment of the sediment drifts being drilled at Sites 1095 and 1096.

Holes 1095C and 1095D

Hole 1095C was spudded with the APC at 0215 hr on 24 February, 20 m west of Hole 1095B. After one mudline core, the driller repositioned the bit 5 m lower and spudded Hole 1095D at 0400 hr. APC coring advanced to the depth objective of 84.6 mbsf (Core 9H) with 93.3% recovery. The drill string was recovered, the positioning beacon released and retrieved, and the vessel departed for Site 1096 at 1930 hr on 24 February. For a summary of drilling at Site 1095, see Table **T1,** p. 54, in the "Leg 178 Summary" chapter.

LITHOSTRATIGRAPHY

Three lithostratigraphic units are identified at Site 1095 (Figs. F4, F5; Table T2). The uppermost, Unit I, is mainly composed of clays and silty clays, which are locally biogenic rich, contain scattered ice-rafted debris, and alternate in color between gray and brown. The underlying Unit II is the thickest and is characterized by thick and repetitive sequences of green laminated silt and mud. Ice-rafted debris is scattered throughout Unit II and appears concentrated within bioturbated intervals. Unit III, the lowest identified at Site 1095, is mainly composed of dark greenish gray laminated claystone.

Unit I

Intervals: Cores 178-1095A-1H through 6H; Core 178-1095C-1H; Core 178-1095D-1H through Section 6H-2
Age: Holocene to late Pliocene (0.00–1.77 Ma)
Depth: 0.0–49.3 mbsf

Unit I is mainly composed of fine-grained brown and dark gray diatom-bearing silty clay, silty clay, and clay, with minor siliceous ooze (Figs. F4, F5). The sediments are indistinctly laminated and extensively bioturbated. Two subunits are identified. Subunit IA consists of alternating diatom-bearing silty clay and clay, probably extending from the present back to marine oxygen isotope Stage 11 at ~7.5 mbsf, by comparison with the results of Pudsey and Camerlenghi (1998). Subunit IB consists of alternating silty clay with sand grains, and clay with silt laminae, down to the top of a coarse-grained unit at 49.3 mbsf (in Hole 1095A).

Description

The biogenic-rich facies of Subunit IA, diatom silty clay and diatom-bearing silty clay, dark grayish brown to brown and olive brown (10YR 4/2, 4/3, 5/3, 6/4; 2.5Y 4/2), are intensely bioturbated and are in five layers, 30–70 cm thick (reduced to 10 cm at the core top; Fig. F6), with gradational burrowed tops and bases. In addition to well-preserved diatoms, these sediments contain foraminifers (most common in the second layer from top) plus rare radiolarians and nannofossils. This facies has low magnetic susceptibility and high values of chromaticity parameters a* and b* (see "Lithostratigraphy," p. 3, in the "Explanatory Notes" chapter; Figs. F6, F7).

The terrigenous facies of Subunit IA consists of clay with ≤1% diatoms and is olive gray and grayish brown (5Y 5/2 and 2.5Y 5/2). It occurs in layers 0.9–1.7 m thick between the biogenic-rich facies. Sedimentary structures include faint, diffuse lamination visible as color contrasts (browner/grayer layers, indistinguishable on the Munsell scale) and minor bioturbation. Scattered sand grains and granules are present from 2 mbsf downward. This facies has high and variable magnetic susceptibility and low values of a* and b* (Figs. F6, F7).

The massive facies of Subunit IB is silty clay with scattered sand grains and granules. This occurs in layers 0.5–2.1 m thick and is mainly grayish brown, gray, and olive gray (2.5Y 5/2, 5Y 4/2, 5Y 5/1). It appears to be almost structureless, although burrow mottling is seen where there are faint color contrasts. The biogenic content is low, but there are a few thin foraminifer-bearing (e.g., interval 178-1095A-5H-1, 86–105

F4. Simplified lithostratigraphy of Site 1095, p. 47.

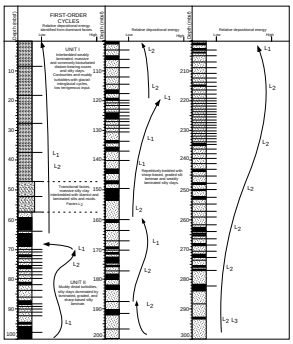

F5. Comparison of downhole sedimentological data from smear slides for Site 1095, p. 49.

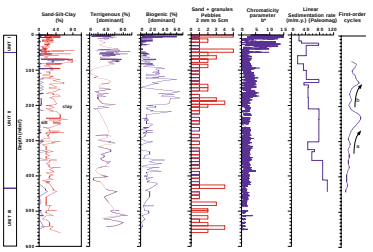

T2. Lithostratigraphic units identified at Site 1095, p. 121.

F6. Alternation of diatomaceous facies and terrigenous facies in Subunit IA, p. 50.

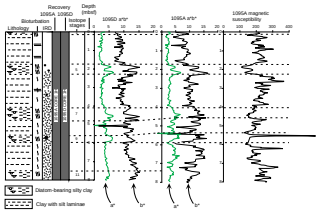

F7. Alternation of silty clay with sand grains, and clay with silt laminae, p. 51.

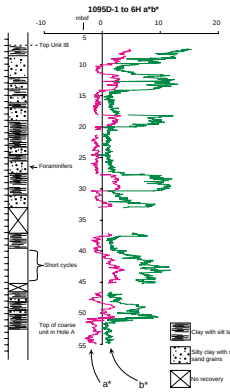

cm; Section 178-1095D-2H-7; and intervals 178-1095D-2H-6, 43–62 cm; 4H, 3–88 and 4–44 cm) and diatom-bearing (e.g., Sections 178-1095D-2H-2 and 3) layers (Figs. F6, F7, F8).

The laminated facies of Subunit IB consists of clay with silt laminae. The clay is dark gray to gray or dark grayish brown (N4/0, N5/0, 5Y 5/1, 5Y 4/2, 2.5Y 4/2). Silt laminae are olive gray (5Y 4/2), 1–10 mm thick, rarely up to 30 mm. The silts have very sharp bases, locally scoured or microburrowed, and are weakly graded with sharp tops (Fig. F9). Silts form 5%–10% of the section, and units of the clay plus silt lithology are 1.3–4.0 m thick. In general, no vertical trends are seen in thickness or number of silt laminae; only two thinning-upward sequences occur (intervals 178-1095A-4H-2, 75–98 cm, and 5H-3, 68–78 cm). Fine to very fine sand occurs locally as graded beds up to 6 cm thick (e.g., Sections 178-1095A-2H-2, 42 and 130 cm; and 5H-2, 95 cm). There are isolated thin (1–3 cm) layers of poorly sorted sand.

In most of Subunit IB, these two facies alternate on a scale of meters (Fig. F7). In the lower part, particularly in Core 178-1095D-5H, thinner cyclic alternations of silty clay with scattered sand grains pass downward to clay containing a few thin silt laminae.

F8. Burrow-mottled silty clay with dispersed sand grains and foraminifers, p. 52.

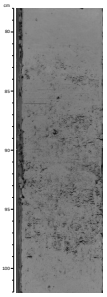

F9. Clay with silt laminae 1–8 mm thick, p. 53.

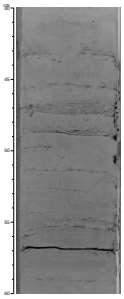

Interpretation

Unit I records deposition from suspension in a low-energy environment, as indicated by the fine grain size, lack of sorting, and absence of sedimentary structures indicating current winnowing. Slow sedimentation of the biogenic-rich facies in Subunit IA and the massive silty clay in Subunit IB allowed complete reworking by benthic burrowing organisms. In the terrigenous facies of Subunit IA, the diffuse nature of the lamination, and the absence of silt laminae or graded-laminated facies, suggests an origin as hemipelagites, which have been influenced by a regime of weak bottom currents (Pudsey and Camerlenghi, 1998). Dispersed sand grains and granules were transported to the area by ice rafting.

Sharp-based, parallel-laminated silt laminae in Unit I are interpreted as distal turbidites (Bouma $T_{D–E}$ divisions; see "Lithostratigraphy," p. 3, in the "Explanatory Notes" chapter). Their limited occurrence in Unit I, compared with Unit II (see below), is consistent with low input of sediment by turbidity currents and a reduction in deposition rates (Fig. F5). Short depositional coarsening-upward cycles toward the base of Subunit IB record, from the bottom up, distal turbidity current activity (clays with thin silt laminae), which is followed by increasing input of ice-rafted debris accompanied by bioturbation.

The downward disappearance of diatoms from Subunit IA is not yet understood but may reflect long-term (longer than a glacial–interglacial cycle) changes in sea ice cover, or in seawater chemistry and hence dissolution. The presence of rare foraminiferal layers attests to open water conditions, free of ice cover for short periods (few hundred to few thousand years?) during the time span of Subunit IB (Fig. F7).

Unit II

Intervals: Core 178-1095A-7H to base of Hole 1095A; Cores 178-1095B-1H through 37X; Section 178-1095D-6H-3 to base of Hole 1095D

Age: late Pliocene to late Miocene (1.77–8.93 Ma)

Depth: 49.3–435.5 mbsf

Unit II is characterized by sharp-based, graded, variably laminated fine sands and silts and laminated silty clays, interbedded with massive deposits (Fig. F4). Three distinct laminated lithofacies (L_1, L_2, and L_3; see "Lithostratigraphy," p. 3, in the "Explanatory Notes" chapter) are identified by the presence or absence of fine sand and silt laminae. The massive facies (M) is characterized by the absence of primary sedimentary structures, except for diffuse grading (Fig. F10). As will be shown below, Facies L_1, L_2, and L_3 are genetically related and part of a facies continuum deposited by muddy turbidity currents (Fig. F11). They are described separately because they tend to occur in different parts of Unit II. Facies M results from hemipelagic sedimentation and intense bioturbation. Diamict deposits (Facies D; see "Lithostratigraphy," p. 3, in the "Explanatory Notes" chapter) are also recognized but constitute a minor component of Unit II. Sediments of Unit II show an alternation of facies, which develop a cyclic depositional pattern. These cycles occur at several scales from a few meters to many tens of meters and are identified by different facies associations.

The contact between Unit I and the underlying Unit II at Site 1095 is not sharp but occurs over a 10-m-thick interval (e.g., in Cores 178-1095A-6H and 7H). This transitional zone is marked by an upward increase in ice-rafted debris and sand content (see Figs. F4, F5; Table T3) and a reduction in the frequency of laminated silts and fine sands. In Core 178-1095A-7H, several beds of diamict, as much as 85 cm thick, have clasts supported by a silty clay matrix.

Description

Facies L_1: Cross-Laminated Sand, Silt, and Silty Clay

Facies L_1 accounts for ~10% of the total thickness of Unit II (Fig. F4). This facies consists of repetitive sequences of laminated (<1 cm) to thin-bedded (1–3 cm) fine sand and silt that grades upward into laminated and massive diatom-bearing silty clay (Fig. F10A, F10C). Facies L_1 shows a consistent internal structure for each depositional sequence, with four distinct fining-upward divisions (Fig. F11). The lowermost division 1 consists of cross-laminated fine sand/silt with a sharp upper contact with parallel-laminated silt and mud in division 2. Division 2 passes upward into a laminated/graded silty mud component that comprises division 3. Finally, massive silty clay comprises division 4. In some cases, muds contain sufficient diatoms to be classified as oozes. The top division of the sequence shows varying degrees of bioturbation from intense, where primary structure has been destroyed, to absent. *Planolites, Zoophycos, Chondrites,* and *Phycosiphon* ichnofacies types can be identified and belong to the *Nereites* (bathyal) ichnofacies assemblage of Pemberton et al. (1992). Ice-rafted debris is concentrated in bioturbated bed tops (division 4). Basal bed contacts are conformable or erosional.

Facies L_2: Parallel-Laminated Silt and Silty Clay

Facies L_2 is the most abundant in Unit II, accounting for ~70% of the total stratigraphic thickness. It consists of repetitive sequences of the three upper divisions of Facies L_1 (divisions 2, 3, and 4). Silt beds in division 2 are parallel laminated and have an erosional or sharp lower contact (Figs. F10B, F11). Silt grades upward into overlying laminated

F10. Representative photographs of lithofacies in Unit II, p. 54.

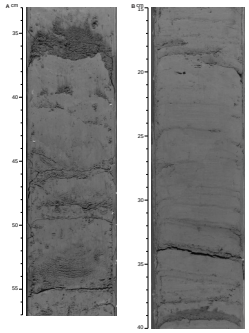

F11. Schematic representation of internal structure of Facies L_1–L_3 at Site 1095, p. 57.

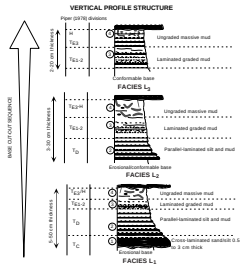

T3. Ice-rafted sand/granules and pebble contents at Site 1095, p. 122.

or massive diatom-bearing silty clay (divisions 3 and 4). *Nereites*-type bioturbation is limited to the upper few centimeters of bed tops. This facies is progressively indurated downcore and becomes claystone toward the bottom of Unit II.

Facies L_3: Laminated Silty Clays

This facies accounts for ~10% of the total stratigraphic thickness of Unit II. It consists of repetitive depositional sequences of the thinly laminated (<1 cm) and massive silty clay (divisions 3 and 4, respectively) that are present in the upper parts of Facies L_1 and L_2 (Fig. **F11**). Color banding is common, and upward transitions from dark to light hues within the depositional sequences suggest upward grading in grain size. In most cases, this facies is bioturbated and shows ichnofacies characteristic of the bathyal *Nereites* ichnofacies assemblage (see above). The degree of bioturbation varies from minimal to moderate. A mottled "bioturbate" texture occurs where bioturbation is moderate, which is characteristic of the few-centimeters-thick, overlying "hemipelagic" interval of the sequence. Ice-rafted debris is concentrated in such hemipelagic intervals, and diatoms are present.

Facies M: Massive, Bioturbated, Sandy Silty Clay

Facies M is diatom-bearing homogenous silty clay, largely lacking any distinct internal structure as a result of intensive bioturbation (Fig. **F10D, F10E**). This facies accounts for ~10% of the deposits of Unit II. In contrast to the rather thin hemipelagic intervals of the laminated facies, the massive facies is present in beds up to 1 m thick and is generally grayish green (5G 5/2), in comparison with the predominantly dark greenish gray (5G 4/1) of other Unit II facies.

Subtle gradations in texture are present within Facies M, and beds may show a gradual upward coarsening from silty clay to sandy, clayey silt beds, or upward fining from clayey silt into silty clay. Ice-rafted debris is more common in Facies M than in any other facies at Site 1095. Ice-rafted terrigenous sand particles, also dispersed in the fine-grained matrix of these facies, may account for as much as 10% of the total composition. Bed tops are typically abrupt and sharply defined; lower contacts are locally blurred by burrowing (typically *Planolites*).

Facies D: Diamict

Diamict is defined as a poorly sorted admixture of clasts (>2 mm in diameter) and matrix (see **"Lithostratigraphy,"** p. 3, in the "Explanatory Notes" chapter). At Site 1095, diamict is present between 51 and 63.8 mbsf. Gray (5Y 5/1) diamict beds are massive and have a fine-grained silty clay matrix that supports sand- to pebble-sized clasts. They are interbedded with laminated silts and clays (Facies L_1 and L_2). In Hole 1095A, approximately seven diamict beds range in thickness from 1 to 3 cm (with one 85 cm thick); bed contacts are sharp, but with no evidence of erosion at the base of beds. In Hole 1095D, one diamict bed 34 cm thick is present at 57.1 mbsf. Diamicts and associated laminated sediments are not bioturbated.

Interpretation

Sediments resembling laminated sand, silt, and mud sequences of Facies L_1, L_2, and L_3 within Unit II are well described in the literature as "parallel silt-laminated muds" (Stow and Piper, 1984), "mud turbidites" (Stow and Townsend, 1990), and "thin-bedded turbidites." These facies

are characteristic of deep-sea depositional environments dominated by muddy sediment gravity flows (e.g., Pickering et al., 1988; Alonso and Maldonado, 1990). Consequently, Facies L_1, L_2, and L_3 are all interpreted as turbidites (see "Lithostratigraphy," p. 3, in the "Explanatory Notes" chapter).

Facies M probably results from slow hemipelagic settling of fine-grained particles derived from various sources such as low-density turbid flows, sediment plumes following the pycnocline and transported by geostrophic flows, and biogenic components formed by primary productivity. Bioturbation in this facies is very intense, and normally all original bedding is obliterated or obscured. This indicates low deposition rates and sufficient time to allow infauna to completely mix seafloor sediments. The low carbonate and organic matter content (see "Organic Geochemistry," p. 20, and "Inorganic Geochemistry," p. 21) of these sediments indicates well-oxygenated bottom-water conditions and deposition below the carbonate compensation depth. Ice-rafted debris is a more conspicuous component of Facies M than L_1 to L_3. This may be attributed either to a reduction in the rate of supply of fine-grained sediment relative to the influx of ice-rafted debris or to an increase in the flux of ice-rafted debris (see below).

The beds of diamict that are present between Unit I and Unit II are massive and nonbioturbated and appear conformable with interbedded laminated sediments deposited by turbidites. One possible interpretation of these is that they record episodes of enhanced deposition of debris from floating ice relative to background deposition of mud, such as recorded in Unit II by Facies M (see above). There are important differences, however, between these two facies. For example, Facies M is intensely bioturbated, which is strong evidence of reduced mud deposition and an extended time in which to accumulate ice-rafted debris. Diamicts, however, are nonbioturbated and occur conformably with nonbioturbated laminated silty clays, which indicates a short recurrence interval between successive turbidites and insufficient time to accumulate debris. The alternative suggestion is to invoke a vastly increased flux of ice-rafted debris sufficient to deposit beds up to 85 cm thick. The number and thickness of diamict beds are variable between Holes 1095A and 1095D, offset only 40 m from Hole 1095A, which indicates very local extent. This would appear to rule out a simple ice-rafting origin as this process could be expected to leave a blanket of ice-rafted debris across a large area. The occurrence of diamict as sharply defined beds also argues against a simple ice-rafted debris origin; very abrupt changes in ice-rafted debris are unlikely unless such beds are the equivalent of Heinrich events recorded from the North Atlantic Ocean (e.g., Heinrich, 1988). The depositional context of the diamict facies (conformable with turbidites deposited on a slope) suggests an origin as debrites (debris flows) produced by the local resedimentation and mixing of ice-rafted debris and silty clay.

Unit III

Interval: Cores 178-1095B-38X through 52X
Age: late Miocene (8.93–10.1 Ma)
Depth: 435.5–570.2 mbsf

A zone of poor core recovery in the lower part of Core 178-1095B-37X (432.0–435.5 mbsf) marks an abrupt change in physical properties from

indurated silts and muds of Unit II to lithified siltstones and mudstones of Unit III (see "Physical Properties," p. 24). The same facies, however, are present throughout Units II and III, and the distinction between these lithostratigraphic units does not imply a drastic change in the lithology, except in the proportion of the different facies. Unit III can be differentiated from Unit II, however, by the absence of cyclic alternation of facies observed in Unit II, in addition to the sharp change in physical properties. It is likely that the overall depositional setting was maintained, but the environmental factors influencing sedimentation were somewhat different. Core recovery in Unit III is poor below 481 mbsf (Core 178-1095B-43X). Sufficient core was recovered, however, to allow facies description, and it is considered unlikely that poor core recovery is related to a significant change in facies.

Unit III is composed of finely laminated claystone and siltstone, lacking bioturbation (Fig. F12). The laminated facies with siltstone layers show cross and planar lamination typical of turbidite Facies L_2 and L_3 described above for Unit II (Fig. F12A, F12C). Bioturbation is limited to small-scale *Nereites*-type burrows at bed tops (Fig. F12B). Ice-rafted debris is scattered throughout (Fig. F12D, F12E; see below). Unit III shows an overall upward fining from dominantly Facies L_2 at the base to Facies L_3 at the top (Fig. F4).

F12. Lithofacies types in Unit III, p. 58.

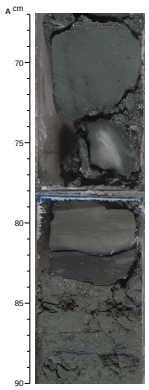

Smear-Slide Analysis

Smear-slide data provide insight into long-term trends in depositional conditions at Site 1095. This data set has not yet been fully evaluated and related to lithofacies, but several trends are evident in Figure F5. Downhole variation in the biogenic component, in general, is inversely related to sedimentation rate (Fig. F5). In intervals of more rapid sedimentation (such as between ~380 and 220 mbsf), the biogenic component is reduced as a result either of lowered production or dilution by enhanced influx of terrigenous sediment. This same stratigraphic interval is marked by a prominent "first-order" depositional cycle in Unit II, possibly recording progradation along the margin of the Antarctic Peninsula (see "Depositional Cycles in Unit II," p. 11). The biogenic component is lower in Unit III and at the base of Unit II during relatively low input of terrigenous sediment.

Throughout the core, the most abundant biogenic component is diatoms, which normally account for 10%–30% but locally reach 60% of the sediment (Table T3; Fig. F5). Sponge spicules are also a common component, whereas radiolarians and silicoflagellates represent only minor proportions in some horizons. Foraminifers are very rare.

In general, the mineralogy of the terrigenous component is dominated by lithic fragments, quartz, and feldspar, except for rare glauconite-bearing silt beds. Glauconite, hornblende, mica, opaque minerals, pyroxene, carbonates, and volcanic glass have been identified.

Ice-Rafted Debris

One of the goals of Leg 178 is to extend knowledge of the glacial history of the Antarctic Peninsula. Ice-rafted debris is a ubiquitous component of Units I, II, and III (Table T3; Fig. F5) and locally a substantial part of the flux of terrigenous sediment to the site. Because of the overall fine-grained nature of sediment at Site 1095, ice-rafted debris is readily identified. It occurs as scattered sand grains and granules, as iso-

lated pebbles (lonestones), and as lenses of granules and sand. Ice-rafted debris lithologies are variable but include volcanic (rhyolite and basalt), volcaniclastic, intrusive igneous (granite and granodiorite), and metamorphic rocks. Most or all can be matched to Antarctic Peninsula sources (see papers in Craddock, 1982; Oliver et al., 1983; and Thomson et al., 1991). In the absence of core X-radiographs, a rough estimate of ice-rafted debris abundance and characteristics has been made from visual examination of split cores.

Scattered sand grains and granules are common in Unit I from 2 mbsf downward. Pebbles as much as 5 cm in diameter are particularly common in Cores 178-1095D-2H, 3H, and 5H and include a variety of volcanic and acid to intermediate plutonic rocks, with rare, low-grade metasedimentary rocks. Most pebbles are subrounded to subangular, the largest being rounded.

In general, the number of ice-rafted pebbles (>0.5 cm diameter) at the top of Unit II in Hole 1095B fluctuates but remains high until 205 mbsf at the base of Core 178-1095B-13H (Table **T3**). Most of these cores contain sand and granules and from one to three pebbles. Below 205 mbsf until 426 mbsf (base of Core 178-1095B-36X), cores contain sand, granules, and low numbers of pebbles (Fig. **F5**). Granite and basalt were the only pebble lithologies described from this 221-m-thick interval. In Unit III, below Core 178-1095B-40X, scattered sand and granules are accompanied by gravel clasts representing a wide variety of lithologies (Fig. **F12D, F12E**).

The changing flux of ice-rafted debris through time at Site 1095 cannot be quantified without further study. It is not possible to identify glacial–interglacial cycles simply on the basis of observed downhole ice-rafted debris abundance because this would disregard changes in the rate of background sedimentation. At times of rapid sedimentation, the flux of ice-rafted debris is diluted. Conversely, reduced sedimentation rates result in concentration of ice-rafted debris unrelated to any change in the ice-rafted debris flux itself. This is clearly demonstrated by low content of ice-rafted debris in rapidly deposited turbidite sequences and enhanced content in bioturbated intervals with low sedimentation rates (e.g., Facies M in Unit II; Fig. **F5**).

Depositional Setting and Environmental Interpretation of Site 1095

Unit I

Biogenic-rich facies of Subunit IA are interpreted as interglacial isotope Stages 1–11 because (1) core-top sediment (i.e., Holocene) is biogenic rich, (2) good lithologic correlation can be made with piston cores from this area dated down to Stage 5 by chemostratigraphy (cf. Pudsey and Camerlenghi, 1998), and (3) the diatom *Hemidiscus karstenii* is absent in the second but present in the third biogenic unit down, which corresponds to isotope Stage 7 (Fig. **F6**).

Terrigenous facies are interpreted as glacial stage sediments, with perennial sea ice cover inhibiting biogenic production at the sea surface (and hence food supply to the benthos). Glacial terrigenous supply may have been higher than interglacial, as glacial units are thicker despite negligible biogenic input. The lack of bioturbation in the glacial units, despite low sedimentation rates (2 cm/k.y. down to Stage 7) may be explained by the very low food supply to the benthos. The higher abundance of ice-rafted debris downhole from 5 to 10 mbsf is interpreted as

more ice rafting instead of less background sedimentation, as the glacial intervals maintain the same thickness.

In the absence of consistent cyclicity in biogenic content of Subunit IB, the relationship of the two facies to glacial–interglacial cycles is not self-evident. We suggest that the massive silty clays with scattered sand grains and intermittent foraminifers and diatoms are interglacial, and the laminated clays with silt laminae are glacial. This is consistent with interglacial, ice-free, open-water conditions allowing biogenic productivity and supporting a burrowing benthic fauna, although microfossils are not generally preserved. It is also consistent with the model of Larter and Barker (1991), which predicts that frequent turbidites are generated at the continental shelf edge during glacials, when the ice sheet is at the continental shelf edge.

Units II and III

Given the similarity of lithofacies within Units II and III (e.g., Figs. **F4, F10, F11, F12**), a similar depositional setting is indicated. When considered together, these units provide a record very similar to that of an aggrading distal base-of-slope setting in low latitudes. Cross- and parallel-laminated silt-mud turbidites such as those of Unit II are characteristic of distal and interchannel portions of submarine fan lobes and slopes (cf. Nelson and Maldonado, 1990). A likely depositional setting consists of an interchannel environment such as a levee marginal to active distributary channels (Fig. **F13**; Stow et al., 1990; Alonso and Maldonado, 1990; Nelson et al., 1991), but this must be assessed in the light of other data sets. Facies L_1, L_2, and L_3 clearly represent a facies continuum of muddy turbidites. Transitions from type $T_{C\text{-}D\text{-}E1\text{-}E2\text{-}E3}$ (Facies L_1) to type $TD_{\text{-}E1\text{-}E2\text{-}E3}$ (Facies L_2) and $T_{E1\text{-}E2\text{-}E3}$ (Facies L_3) typically occur downslope and across slope on the lower distal portions of lobes and slopes (Fig. **F11**).

F13. Schematic representation of a distal turbidite depositional setting, **p. 61.**

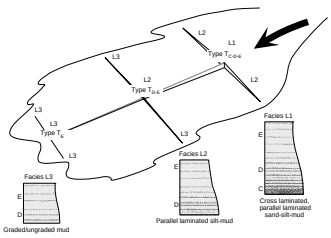

Depositional Cycles in Unit II

The stratigraphic distribution of Facies L_1, L_2, and L_3 in Unit II shows recurring patterns giving rise to a broadly cyclic repetition of facies. Typical "coarsening-upward" cycles comprise a lowermost part dominated by L_2 and L_3 facies. Upward, L_1 and L_2 facies become dominant. In other cases, the sequence of facies occurs in reverse order (L_1, L_2 and L_3), representing an overall "fining-upward" sequence (Fig. **F4**). Those intervals within a cycle of a high frequency of $T_{C\text{-}D\text{-}E}$ turbidites (Facies L_1) indicate higher energy conditions and usually a more proximal setting to the sediment source (Fig. **F13**). Those parts of a cycle dominated by more fine-grained $T_{D\text{-}E}$ turbidites record a more distal setting. These trends provide valuable information regarding environmental conditions and overall depositional energy and have been termed "first-order cycles" by Stow et al. (1990). Two such cycles, of 50- to 100-m thickness, can be identified in Unit II (a, b in Fig. **F5**). The first-order cycles of Unit II, determined from uphole trends in lithofacies types and frequency at Site 1095, correlate approximately with paleomagnetically determined higher depositional rates. Also, the base of the long first-order cycle at 300 mbsf is coincident with an influx of neritic diatoms, which may indicate sediment supply from a more distal environment inshore. Upward in the cycle, as sedimentation rates increase and turbidites become coarser grained (i.e., Facies L_1; Fig. **F4**), diatoms are few

and fragmentary (see "Biostratigraphy," p. 13). Provisionally, first-order cycles of several tens of meters can be interpreted as recording long-term (0.5–1.5 m.y.) phases of enhanced sediment deposition, reflecting sediment supply trends and changing position and dimensions of feeder channels, lobes, or levees along the margin of the Antarctic Peninsula.

Depositional trends in high-latitude glacial settings cannot be interpreted in terms of changes in sea level, in contrast to lower latitude and temperate margins where relative sea-level change, tectonics, and sediment supply control sedimentation. The advance and retreat of continental ice sheets are considered a major factor influencing deposition on high-latitude margins (e.g., Boulton, 1990; Larter and Barker, 1991), and the "relative erosion level" is the ice-sheet base, rather than sea level. In an alternative view of the Antarctic Peninsula margin, Bart and Anderson (1995) suggested that "ice-sheet expansion across the overdeepened inner and outer shelf may only have occurred during extreme sea-level falls," but this is a question of degree rather than a fundamental difference of interpretation. Tectonics has not been a major factor controlling deposition at Site 1095, since ridge-crest collision occurred in the early Oligocene at this section of the margin (see Fig. F7, p. 35, in Barker and Camerlenghi, Chap. 2, this volume). Larter and Barker (1991) estimated >1 km subsidence of the outer shelf off Adelaide Island, where ridge-crest collision occurred more recently (at 16.5 Ma). The shelf break has prograded during deposition of S1 and S2 (by as much as 25 km within Lobe 4 [Larter et al., 1997; Barker and Camerlenghi, Chap. 2, this volume]), which implies only limited changes in margin morphology (see also "Site 1097" and "Shelf Transect" [Sites 1100, 1102, and 1103] chapters).

Well-defined, second-order cycles occur within the first-order cycles in Unit II. These cycles are bounded by Facies M, which records episodes of reduced deposition and the accumulation of ice-rafted debris (Fig. F12D). The second-order cycles can also be seen in color and magnetic susceptibility data (Fig. F7). They may be the stratigraphic expression of high-frequency (possibly 40 and 100 k.y.) glacial–interglacial changes in sediment supply along the Antarctic Peninsula continental margin. The absence of second-order cycles in Unit III at Site 1095 may be significant in understanding glacial history.

The low overall intensity of bioturbation through much of Units II and III suggests near-constant deposition rates and short recurrence intervals between successive turbidity current flows, or bottom conditions that did not favor a significant development of bottom-dwelling fauna, such as a reduced nutrient supply or low oxygen content (see "Lithostratigraphy," p. 4, in the "Site 1096" chapter). The deposits of Unit III show a moderate sedimentation rate of 11 cm/k.y., and most of the deposits of Unit II recorded a rather low mean depositional rate of 6–8 cm/k.y. (Fig. F5), which is close to rates estimated for the same stratigraphic interval penetrated at Deep Sea Drilling Project Site 325 (Hollister, Craddock, et al., 1976). Calculation of the frequency of turbidite events, on the basis of the mean sedimentation rate and thickness of turbidite sequences, yields a recurrence interval of ~0.4–2 turbidity flows/k.y. This frequency should be greater at times of enhanced sediment supply to the margin during the development of the laminated facies and lower for the massive facies. The rate of bioturbation in the deposits thus reflects the interplay between the two controlling factors, sediment supply and oceanographic conditions, during the depositional evolution at Site 1096. Deposition rates decline above

the top of Unit II, which is marked by enhanced concentrations of ice-rafted debris and diamict facies. It is likely that much of the terrigenous fine-grained sediment within Unit I was provided to the water column by dilute turbidity flows as suspension clouds and then deposited by weak bottom currents (e.g., Stow et al., 1990; Rebesco et al., 1996; Pudsey and Camerlenghi, 1998).

BIOSTRATIGRAPHY

The biostratigraphy at Site 1095 was derived from an examination of diatoms, radiolarians, and benthic and planktonic foraminifers. Pliocene to Pleistocene deposits consisted primarily of glacial and interglacial hemipelagic sediments containing foraminifers but only rare intervals of siliceous microfossils. The upper Miocene through lower Pliocene sediments consist mainly of turbidites, together with intervals of hemipelagic sediments containing radiolarians and diatoms and very rare foraminifers. The biostratigraphy of Site 1095 was accomplished using zonations developed for the Southern Ocean (see **"Biostratigraphy,"** p. 9, in the "Explanatory Notes" chapter).

Diatoms

The diatom biostratigraphy of Holes 1095A, 1095B, and 1095C is complex and contains an incomplete record of Pleistocene through upper Miocene datums and events. Many core intervals are barren or have a low abundance and diversity of diatoms. In samples that contain diatoms, reworking of older species is often noted. In spite of the obvious reworking, there is a strong biostratigraphic signal for the early Pliocene and late Miocene (Fig. **F14**). Material used in the biostratigraphic analysis of this site was gathered from core catchers as well as from within the split cores (usually one sample per section).

All datums and their hole/core depths at Site 1095 are listed in Table **T4**. The identification of diatom species at this site follows the taxonomic determinations of Schrader (1976), Akiba (1986), Barron (1985), Akiba and Yanagisawa (1986), Gersonde (1990, 1991), Gersonde and Burckle (1990), Yanagisawa and Akiba (1990), Baldauf and Barron (1991), Harwood and Maruyama (1992), and Gersonde and Bárcena (1998).

The first datum in the zonal scheme is the last occurrence (LO) of *Actinocyclus ingens*. This was noted early in the drilling, in Sample 178-1095A-2H-3, 90 cm (9.8 mbsf). The LO datums of *Thalassiosira elliptipora* and *Fragilariopsis barronii* (178-1095A-3H-6, 94 cm [17.7 mbsf]) were also observed within the *A. ingens* Zone. Zonal boundary datums for the *Thalassiosira kolbei* Zone were not noted, but the LO of *Thalassiosira inura* (which occurs within this zone) was observed at 178-1095A-9H-3, 130 cm (72.6 mbsf). Within the overlap between Holes 1095A and 1095B is the LO of *Fragilariopsis interfrigidaria,* which was last noted in Sample 178-1095B-1H-1, 95 cm (83.9 mbsf) and was absent from 178-1095A-9H-CC (77.8 mbsf). The *Thalassiosira vulnifica* and *T. insigna/vulnifica* Zones were not observed in Hole 1095A. In Hole 1095D, however, we observed some well-preserved specimens of *T. vulnifica* and *T. insigna* in Samples 178-1095D-7H-CC (65.6 mbsf) and 8H-CC (75.1 mbsf). These two core-catcher samples would fall within the *T. insigna/T. vulnifica* Zone because both species are present, but the top and bottom datums for this zone were not noted in Hole 1095D.

F14. Summary of the occurrence of diatoms, radiolarians, and planktonic foraminifers at Site 1095, **p. 62.**

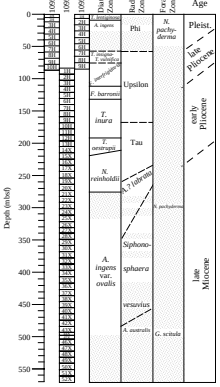

T4. Biostratigraphically useful diatom datums for Site 1095, **p. 123.**

The base of the *F. interfrigidaria* Zone was identified in Sample 178-1095B-3H-CC (111.5 mbsf) with the first occurrence (FO) of *F. interfrigidaria*. This zone, and the earlier *F. barronii* Zone, is well represented in the sediments at this site with abundant and diverse diatom assemblages. The base of the *F. barronii* Zone is marked by the FO of *F. barronii* in Sample 178-1095B-5H-3, 33 cm (124.3 mbsf); co-occurrent with this datum is the FO of *Thalassiosira striata*. The FO of *Thalassiosira complicata* was noted in Sample 178-1095B-6H-CC (140.0 mbsf), and the next biostratigraphically useful datum (FO of *T. inura*) occurs six cores deeper in Sample 178-1095B-12H-4, 41 cm (192.4 mbsf).

The lower two-thirds of Hole 1095B is late Miocene in age. Diatoms are preserved in Cores 178-1095B-15H through 43X. The FO datum of *Thalassiosira oestrupii,* defining the base of the *T. oestrupii* Zone, is found between Samples 178-1095B-14X-4, 133 cm, and 15X-2, 126 cm. The FO of *Fragilariopsis praeinterfrigidaria,* which has been observed later than that of *T. oestrupii* (Harwood and Maruyama, 1992), is in Sample 178-1095B-14X-4, 133 cm (210.8 mbsf). The next sample with a good assemblage of diatoms is from 178-1095B-15X-2, 126 cm (217.5 mbsf). *T. oestrupii* is not found in this sample or in any of the others below, thus placing the FO datum for *T. oestrupii* in this interval (210.8–217.5 mbsf). It is possible that the order in which these two datums occur in this region is reversed compared to other areas of the Southern Ocean. Another datum in this part of the hole is the LO of *Nitzschia donahuensis* in Sample 178-1095B-15X-2, 126 cm (217.5 mbsf). Because the stratigraphic age of this datum is older than that of *T. oestrupii,* the argument for placing this previous zonal boundary between Samples 178-1095B-14X-4, 133 cm, and 15X-2, 126 cm, is reinforced (Table **T4**).

The LO datum for *Actinocyclus ingens* var. *ovalis* is placed in Sample 178-1095B-21X-3, 128 cm (276.7 mbsf). The upper boundary species datum for the *A. ingens* var. *ovalis* Zone (FO of *Thalassiosira oliverana*) was not observed at this site. It would occur just below the *A. ingens* var. *ovalis* LO datum, according to the biostratigraphy of other regions of the Southern Ocean. We noted FO datums of two species (*A. ingens* var. *ovalis* and *T. oliverana* var. *sparsa*) in Sample 178-1095B-28X-5, 104 cm (346.8 mbsf). The FO of *Thalassiosira torokina* is higher in the sedimentary column than its biostratigraphic range would place it, occurring in Sample 178-1095B-23X-CC (301.2 mbsf). After examining additional samples, we may be able to determine that the late FO of *T. torokina* resulted from poor preservation within samples from this period and that intervals of good preservation were not sampled in this preliminary investigation.

The samples in Cores 178-1096B-29X through 45X contained a typical late Miocene assemblage, with a large proportion of *Denticulopsis* species dominating. The species of *Denticulopsis* used as zonal boundary markers in older sediments, *D. dimorpha* and *D. praedimorpha,* were absent from this assemblage. One sieved sample, from Core 178-1095B-37X, contained *Asteromphalus kennetii,* which has an FO age of 10.29 Ma. This datum also helps constrain the age of the lower part of Hole 1095B to the late Miocene.

The neritic diatom *Paralia sulcata* has been observed in samples from Cores 178-1095B-21X through 27X and is especially common in Cores 178-1095B-23X and 24X (290–310 mbsf) (see **"Sedimentation Rates,"** p. 32 [Fig. **F52**]). *Paralia sulcata* is a benthic neritic species that lives on coarse sediment in a relatively low-salinity, shallow-water environment and can easily be transported to deep water. The movement from a shallow-water environment can take place through sediment transport

or by an increased influx of relatively low-salinity water from the shelf. The sporadic presence of delicate benthic diatoms, *Navicula* spp. and *Pinnularia* spp., and of the reworked middle Miocene diatom, *Denticulopsis dimorpha* var. *areolata,* in the same interval suggests shallow-water sediment transport. To account for the observed proportion of *P. sulcata,* it is possible that more of the shelf was in the photic zone and was therefore shallower than today. However, this is a preliminary interpretation based on the shipboard smear-slide observations. Additional future analyses are needed.

Radiolarians

Radiolarians from core-catcher samples at Site 1095 range in age from late Pliocene (Phi Zone) to late Miocene (*Acrosphaera australis* Zone). Occurrences of good to moderately well-preserved radiolarians are sporadic, with long intervals that are barren or have only rare occurrences of radiolarians (Fig. **F15**). Consequently, first and last occurrences of biostratigraphic indicator species can only be estimated. All assemblages are composed of high-latitude species, and no warm-water species were observed. The youngest sediment with stratigraphically useful species is in Sample 178-1095D-3H-CC (27.6 mbsf) indicated by *Triceraspyris antarctica* in the Phi Zone. A relatively diverse assemblage is present in this sample, and *Helotholus vema* does not occur. The shallowest occurrence of *H. vema* is in Sample 178-1095D-4H-CC (37.1 mbsf), indicating a late Pliocene age (Upsilon Zone).

The youngest core-catcher sample in Hole 1095A with biostratigraphically useful radiolarians is 178-1095A-8H-CC (68.3 mbsf), containing *Antarctissa cylindrica, H. vema, Desmospyris spongiosa,* and *Stylatractus universus*. The sediment above this core was barren of radiolarians, so Core 178-1095A-8H-CC is placed within the Upsilon Zone instead of at its upper boundary. However, because *Prunopyle titan* was not present in Sample 178-1095A-8H-CC (but does appear deeper in Hole 1095B), we conclude that the sample is younger than 3.5 Ma. *Prunopyle titan* does not occur in Hole 1095A but does in 1095B, suggesting that Hole 1095A does not penetrate sediments older than 3.5 Ma.

In Sample 178-1095B-3H-CC (111.5 mbsf), *Lampromitra coronata* is present, suggesting an age of at least 3.7 Ma. The common occurrence of *D. spongiosa* implies a Pliocene age within the Upsilon Zone and not reworking. The last occurrence of *H. vema* is in Sample 178-1095B-8H-CC (159.0 mbsf). Because the moderate preservation in Sample 178-1095B-9H-CC seems sufficient for the presence of *H. vema,* the lower boundary of the Upsilon Zone is placed between Samples 178-1095B-8H-CC and 9H-CC (168.5 mbsf).

The top occurrence of *Lychnocanium grande* is in Sample 178-1095B-10H-CC (178.0 mbsf). This species is common in Sample 178-1095B-16H-CC (233.9 mbsf), where its top common occurrence is placed (5.0 Ma, in the Tau Zone; see **"Sedimentation Rates,"** p. 32). In core-catcher samples below Core 178-1095B-18H (243.5–235.1 mbsf), few to no radiolarians were encountered until Sample 178-1095B-29H-CC (359.2 mbsf). Here, fragments of *Siphonosphaera vesuvius* are present, indicating a middle late Miocene age within the *S. vesuvius* Zone. No marker species for the *Amphymenium challengerae* Zone were encountered. The *Acrosphaera*? *labrata* Zone is indicated in Sample 178-1095B-19X-CC (262.7 mbsf) by the presence of *A.*? *labrata* fragments.

F15. Sedimentation rates based on radiolarian occurrences, Site 1095, **p. 63.**

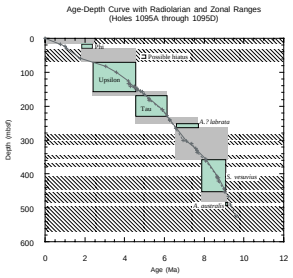

The oldest marker species observed is a fragment of *Cycladophora spongothorax* in Sample 178-1095B-43X-CC (493.4 mbsf). A fragment of *A. australis* is also present. The presence of sponge spicules may indicate increased influence of shelf deposits, which would dilute the oceanic component containing radiolarians. On the other hand, this could be an indication of reworking. These sediments are placed in the *A. australis* Zone, however, because diatom and foraminifer data are consistent with this age; further, none of the several biostratigraphically significant species just below this datum is present. No other biostratigraphically useful specimens were encountered between Sample 178-1095B-44X-CC and the bottom of the hole at 52X-CC.

The sporadic nature of the observed radiolarian biostratigraphic record makes it impossible to estimate a single sedimentation rate for any given time. Nevertheless, a range of sedimentation rates can be generated from the available biostratigraphic data (Fig. **F15**).

Foraminifers

Shipboard analyses of foraminifers at Site 1095 were done using core-catcher and a few additional samples. Rare to abundant planktonic and rare benthic foraminifers were recovered in Cores 178-1095A-1H through 6H (49 mbsf). Preservation of the foraminifers was good to excellent. The planktonic foraminiferal assemblage was dominated by *Neogloboquadrina pachyderma* sinistral, which is characteristic of Pleistocene to upper Miocene sediments in the Southern Ocean (Berggren, 1992). Rare specimens of *N. pachyderma* dextral and *Globigerina bulloides* were also observed in Holes 1095A and 1095D.

Hole 1095B was barren of foraminifers except for two samples. Sample 178-1095B-23X-5, 34–36 cm (298 mbsf), contained a small assemblage consisting of *N. pachyderma* sinistral and several benthic foraminifer species. The preservation was so poor, however, that identification could only be made to genus level. Sample 178-1095B-44X-CC (494 mbsf) contains a better preserved but small planktonic foraminifer assemblage consisting of *Neogloboquadrina continuosa, Globorotalia scitula,* and *Globoturborotalita woodi.* This suggests a middle to late Miocene age and would fall in the *G. scitula* Zone of Berggren (1992).

PALEOMAGNETISM

Split-Core Measurements

Archive halves of all cores recovered at Site 1095 were measured at 4-cm intervals. For Core 178-1095A-1H, the natural remanent magnetization (NRM) was measured after partial alternating field (AF) demagnetization at the 0 (NRM step), 10, 20, and 25 mT. For Cores 178-1095A-2H through 10H and Cores 178-1095B-1H through 8H, measurements were obtained after partial AF demagnetization at 0, 10, 20, and 30 mT (Tables **T5, T6, T7, T8, T9, T10, T11, T12, T13, T14, T15,** all also in ASCII format in the **TABLES** directory). For Cores 178-1095B-9H through 52X and Hole 1095C, the AF demagnetization commenced at 20 mT (Tables **T11, T12, T13, T14, T15, T16, T17, T18,** all also in ASCII format in the **TABLES** directory). The decision to start demagnetization at 20 mT was justified by the coercivity of the drill-string overprint and the need to maintain a constant core flow through the paleomagnetics laboratory. For Hole 1095D, the AF demagnetization scheme was

T5. Split-core paleomagnetic measurements for Hole 1095A before demagnetization, **p. 125.**

T6. Split-core paleomagnetic measurements for Hole 1095A after 10-mT demagnetization, **p. 126.**

T7. Split-core paleomagnetic measurements for Hole 1095A after 20-mT demagnetization, **p. 127.**

T8. Split-core paleomagnetic measurements for Hole 1095A after 25-mT demagnetization, **p. 128.**

T9. Split-core paleomagnetic measurements for Hole 1095A after 30-mT demagnetization, **p. 131.**

T10. Split-core paleomagnetic measurements for Hole 1095A, results from 25- and 30-mT demagnetization, **p. 132.**

T11. Split-core paleomagnetic measurements for Hole 1095B before demagnetization, **p. 133.**

T12. Split-core paleomagnetic measurements for Hole 1095B after 10-mT demagnetization, **p. 134.**

T13. Split-core paleomagnetic measurements for Hole 1095B after 20-mT demagnetization, **p. 135.**

T14. Split-core paleomagnetic measurements for Hole 1095B after 30-mT demagnetization, **p. 136.**

altered to 0, 10, and 20 mT (Table T19, T20, T21, T22, T23, all also in ASCII format in the TABLES directory) to preserve the remanence for future U-channel studies. Besides providing access to the unprocessed data, we include processed data from each hole (Tables T5, T6, T7, T8, T9, T10, T11, T12, T13, T14, T15, T16, T17, T18, T19, T20, T21, T22, T23), for which processing consists of removing results from within 8 cm of the ends of each core section (these are anomalous owing to magnetic edge effects) and from drilling-disturbed intervals. In addition, the raw data are available in the Ocean Drilling Program database.

In all holes, the magnetization of the cores contained a steep, downward component, which simulated a reversed polarity direction at low (0–10 mT) demagnetization levels (Fig. F16A). In addition, either a radial overprint or other biases, perhaps instrumental, resulted in nearly all of the declinations having a bias toward 0° (Fig. F16B), even after demagnetization.

Discrete Samples

Discrete samples were collected from the working halves of cores to carry out full AF demagnetization up to fields as large as 80 mT (Tables T24, T25, T26, all also in ASCII format in the TABLES directory). Stepwise demagnetization up to high fields is used (1) to reveal the peak field necessary to clean the remanence vector of the drill-string overprint, (2) to assess the stability of the remanence vector, (3) to determine how many magnetization components are present, and (4) to estimate the direction and uncertainty of the characteristic remanent magnetization (ChRM, i.e., the highest coercivity component that is stable) of each sample through principal component analysis (PCA). We also conducted very preliminary rock magnetic investigations, which mainly were restricted to anhysteretic remanent magnetization and susceptibility measurements. These measurements were made to estimate a preliminary relative paleointensity record at Site 1095 and to assess the quality of this record for postcruise research.

Demagnetization revealed that the drill-string overprint could be mostly or wholly removed by partial AF demagnetization at 20 or 30 mT and that the characteristic remanence was very stable up to the 60-mT demagnetization step (Fig. F17). A few discrete samples have three components of magnetization: a low-coercivity drill-string overprint that is removed with ~10-mT demagnetization, a second component that is removed between 10 and 50 mT, and a third high-coercivity component that is stable during demagnetization up to 80 mT (Fig. F18). These samples typically come from silty intervals, and the medium-coercivity component is consistent with adjacent samples that are fine grained. Hence, this medium-coercivity component is probably the primary remanent magnetization in these silty intervals. A small number of samples gave no stable magnetization direction.

Inclinations calculated from PCA of the discrete sample measurements agree very well with the inclinations from the magnetically cleaned split cores, except in a few samples as noted above (Fig. F19). A computer program was written to automate the PCA. The program iteratively searched for the demagnetization steps that minimized the size of the maximum angular deviation angle, which measures how well the vector demagnetization data fit a line. The program requires that at least four demagnetization steps be used, never uses steps lower than 10 mT, does not require that the best-fit PCA line pass through the origin (the "free" option of standard PCA), and generally favors high-coerciv-

T15. Split-core paleomagnetic measurements for Hole 1095B, results from 30-mT demagnetization, p. 137.

T16. Split-core paleomagnetic measurements for Hole 1095C before demagnetization, p. 138.

T17. Split-core paleomagnetic measurements for Hole 1095C after 20-mT demagnetization, p. 139.

T18. Split-core paleomagnetic measurements for Hole 1095C after 30-mT demagnetization, p. 140.

T19. Split-core paleomagnetic measurements for Hole 1095D before demagnetization, p. 141.

T20. Split-core paleomagnetic measurements for Hole 1095D after 10-mT demagnetization, p. 142.

T21. Split-core paleomagnetic measurements for Hole 1095D after 20-mT demagnetization, p. 143.

T22. Split-core paleomagnetic measurements for Hole 1095D after 30-mT demagnetization, p. 144.

T23. Split-core paleomagnetic measurements for Hole 1095D, results from 30-mT demagnetization, p. 145.

ity components over low-coercivity components in samples with multicomponent magnetizations.

For the 302 samples analyzed, 201 give maximum angular deviation angles that fall between 0° and 5°, and 54 give angles between 5° and 10° (Table **T27,** also in ASCII format in the **TABLES** directory). These 255 samples have very well-constrained ChRMs, whereas those with higher maximum angular deviation angles should be treated with caution. In general, samples with low intensities give larger maximum angular deviation angles and more uncertain ChRM directions (Fig. **F19C, F19D**). An additional 36 samples were collected from Core 178-1095B-34X to examine the behavior of the field during Chron 4r.2r (see **"Identification of Cryptochron 4r.2r-1 in Hole 1095B,"** p. 19), with 31 of these having maximum angular deviation angles <5°.

Magnetostratigraphy

Results obtained from Holes 1095A and 1095B form a near-continuous paleomagnetic data set for the upper 450 mbsf. The magnetostratigraphy was constructed from records of the inclination and intensity of remanence. Declination was not used in the magnetostratigraphic record because the cores were unoriented, because of the bias in the declination mentioned above (Fig. **F16B**), and because the declination contributes little to the total paleomagnetic vector, which is very steep at Site 1095. The overall quality of the paleomagnetic record is very good, with clear magnetic polarities characterized by steep inclinations (averages = +73°, –71°) approaching the geocentric axial dipole value of ±78° expected at 67°S.

The inclination record provided a reliable magnetostratigraphy down to 460 mbsf and comprised 208 m of APC and 252 m of XCB core (Figs. **F20**, **F21**; Table **T28**). The Brunhes/Matuyama (0.78 Ma) boundary occurs in Hole 1095A at ~17.1 mbsf (Section 178-1095A-3H-6), and the Jaramillo Subchron (0.99–1.07 Ma) between 23.1 and 29.1 mbsf. The Jaramillo Subchron is not observed in Hole 1095D, possibly destroyed by core flow-in or masked by the drill-string overprint. The short interval of normal polarity observed between 40.8 and 41.2 mbsf in Hole 1095A may be associated with the Cobb Mountain Event (1.2 Ma). The polarities of underlying sediments show a succession of two large normal periods interrupted by a shorter reversed interval. This in turn suggests a record of Chron C2An instead of C2n and the possibility of a hiatus in the sedimentary sequence between 50 and 65 mbsf. Seismic stratigraphy suggested an unconformity at ~60 mbsf coincident with a prominent lithostratigraphic boundary (see **"Seismic Stratigraphy,"** p. 33, and **"Lithostratigraphy,"** p. 4). The reversal at ~58.8 mbsf has been interpreted as the termination of the Olduvai (1.77 Ma). It is probably underlain by a hiatus such that the onset of the Olduvai and all of Chron C2r was lost.

The discontinuous core recovery at the base of Hole 1095B prevented a confident identification of the sparse directions from 480 to 560 mbsf. Downhole logging using the GHMT provided a complete polarity stratigraphy at the base of Hole 1095B (see **"Downhole Measurements,"** p. 27). When a 5-m offset was applied to the logging depth scale, the locations of polarity transitions observed in the core and in the drill hole agreed extremely well. The logging record confirmed that the polarity transition observed in the core at 460.7–461.04 mbsf is the termination of Chron C4Ar.1n. The deepest event that could be confi-

F16. Inclinations and declinations from Holes 1095A and 1095B, **p. 64.**

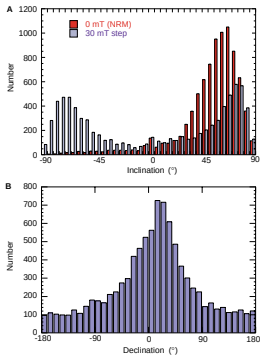

T24. Discrete sample NRM and AF demagnetization results for Hole 1095A, **p. 146.**

T25. Discrete sample NRM and AF demagnetization results for Hole 1095B, **p. 147.**

T26. Discrete sample NRM and thermal demagnetization results for samples from Hole 1095B, **p. 148.**

F17. Orthogonal projection, change in intensity, and equal-area projection of the remanence vector, **p. 65.**

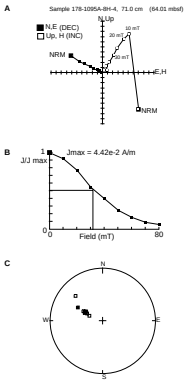

dently identified in the paleomagnetic data is the termination of Chron C4Ar.2n (9.58 Ma) at 522.7–522.9 mbsf.

Identification of Cryptochron 4r.2r-1 in Hole 1095B

Interpretation of the magnetostratigraphy from the onset of Chron 4Ar up to the onset of Chron 2An is fairly simple, with the exception of an extra normal polarity event near the base of Chron 4r.2r (Fig. F22) that is not shown in most geomagnetic polarity time scales (GPTSs). Cande and Kent (1992a, 1995) have, however, placed a geomagnetic event in the lower part of Chron 4r.2r, which they refer to as Cryptochron C4r.2r-1.

Cryptochrons are geomagnetic events of short duration (<20 k.y.), which may represent full polarity reversals, directional changes in the field that are incomplete reversals (such as some excursions), geomagnetic intensity variations, or some combination of these. Most of the cryptochrons listed by Cande and Kent (1992a, 1992b, 1995) were identified from the small-scale magnetic anomalies (referred to as "tiny wiggles") observed in marine magnetic anomaly profiles.

Neither the nature nor the duration of a cryptochron can be uniquely ascertained from marine magnetic anomaly profiles alone. Hence, observing one of these events in a magnetostratigraphic record has important implications for geomagnetism and for future refinement of the GPTS.

By identifying the normal polarity interval between 399.9 and 404.8 as Cryptochron 4r.2r-1, we obtained a pattern of reversals that fits the GPTS very well and gives fairly constant sedimentation of 6–11 cm/k.y. for the interval from 450 to 325 mbsf. Within this interval, the interpreted magnetostratigraphy agrees very well with the biostratigraphy. Given these two observations, we were confident in the interpretation, and thus decided to investigate further the nature of the cryptochron.

We conducted detailed AF and thermal demagnetization experiments on 36 discrete samples that span the cryptochron (Figs. F23, F24, F25, F26). These confirmed that the magnetizations within the normal polarity cryptochron and the bounding reversed polarity intervals are fairly simple, with the drill-string overprint being removed by demagnetization at ~10 mT or 250°C. Beyond this, the demagnetization data reveal univectorial behavior, except in transition intervals and a few other intervals that have low relative paleointensity.

Thermal demagnetization reveals that ~80% of magnetization decays between 275° and 425°C, which indicates that the dominant remanence-carrying mineral is titanomagnetite. Another 10% of the total magnetization is removed between 525° and 625°C, which suggests the presence of magnetite and possibly hematite. The remanence present above the 580°C step could result from the temperature of the oven being inaccurate by 20°–40°C because the sample is completely demagnetized above the 600°C step. In any case, after removal of the drill-string overprint, the remanence-carrying minerals for a single sample all give the same direction.

The simple demagnetization behavior and the agreement between discrete and split-core measurements indicate that the split-core results after 30 mT provide an accurate, detailed record of the cryptochron. First, the inclination record indicates that the cryptochron is a full geomagnetic reversal. The declinations, on the other hand, are meaningless in these XCB cores because core deformation produces biscuits (pieces of core) that are azimuthally unoriented with respect to one

F18. Vector end-point diagram showing the removal of the drill string overprint for Sample 178-1095B-4H-4, 71 cm, p. 66.

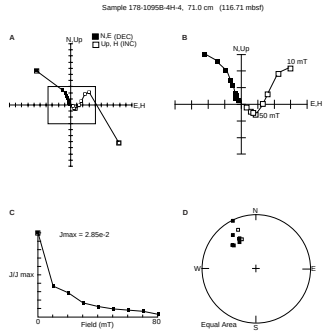

F19. Inclinations measured on archive halves and discrete samples, p. 67.

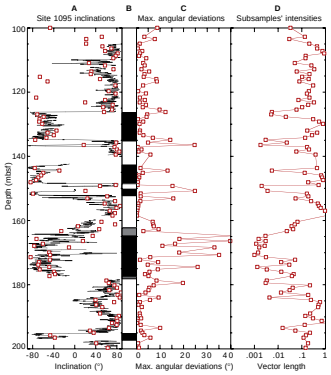

T27. Results from principal component analysis of discrete paleomagnetic samples, p. 151.

F20. Inclination of the magnetization vector vs. depth for Holes 1095A, 1095B, and 1095D after AF demagnetization, p. 68.

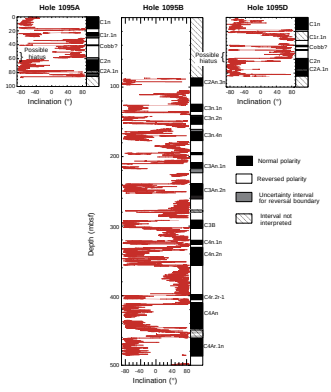

another. Because of the steepness of the inclination at this site, however, the normal and reversed directions must be nearly antipodal even in the absence of declination observations. Second, the relative paleointensity record, derived by dividing the intensity (after 30-mT demagnetization) by the multisensor track (MST) susceptibility, shows that the cryptochron is also a zone of low paleointensity, at least with respect to adjacent chrons (Fig. F27). Third, the transition zones between the normal polarity cryptochron and adjacent reversed polarity intervals are relatively sharp, each spanning 20–30 cm or ~2–4 k.y. The paleointensity collapses to zero within the transition zones but recovers within a few thousand years. Fourth, given that sedimentation rates are between 6 and 11 cm/k.y., the duration of the cryptochron is 45–82 k.y., several times larger than the 16 k.y. estimated by Cande and Kent (1995) from marine magnetic anomalies. Of course, all these interpretations are preliminary, and more work is planned to investigate these properties and alternative magnetostratigraphic interpretations.

F21. Intensity of the magnetization vector vs. depth for Holes 1095A, 1095B, and 1095D after AF demagnetization, p. 69.

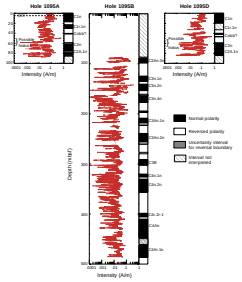

T28. Depths of geomagnetic reversals in Holes 1095A, 1095B, and 1095D, p. 156.

ORGANIC GEOCHEMISTRY

As required by safety regulations, headspace gas analyses at Site 1095 were performed immediately upon recovery on one sample from each core, for a total of 60 analyses (Table T29). Inorganic carbon concentrations were measured on one sample per section for a total of 160 samples (Table T30), whereas total carbon was measured on a small subset of only 23 samples because of a limited supply of oxygen for elemental analyses.

Volatile Hydrocarbons

Headspace methane concentrations did not exceed background levels in Hole 1095A, except for the slightly elevated value (125 ppm) obtained for the uppermost sample at ~1 mbsf (Table T29). Significant amounts of methane and trace amounts of ethane first appeared at ~170 mbsf in Hole 1095B (Table T29; Fig. F28). No heavier gases (C_{3+}) could be detected by the natural gas analyzer, and the methane/ethane ratio remained stable throughout Hole 1095B (Table T29). The minor amounts of gas detected lie well within the limits for safety and pollution risk. The observed methane and ethane probably originated biogenically (Claypool and Kvenvolden, 1983), as indicated by the absence of heavier hydrocarbon gases and the downhole decrease of interstitial water sulfate concentration through the same interval (see "Inorganic Geochemistry," p. 21).

F22. Inclinations from split cores and from discrete samples, p. 70.

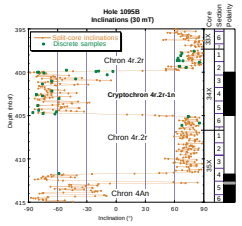

F23. Vector end-point diagram from the reversed polarity interval above Cryptochron 4r.2r-1, p. 71.

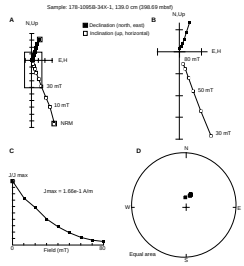

F24. Vector end-point diagram from the transition zone between the cryptochron and reversed polarity interval, p. 72.

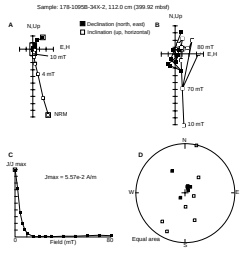

Inorganic Carbon and Elemental Analysis

Measured inorganic carbon and calculated calcium carbonate concentrations generally remain <0.16 wt% and <1.3 wt%, respectively, at Site 1095 (Table T30). A few thin intervals with carbonate contents of >1.3 wt% appear to correlate with intervals where foraminifers are observed (see "Biostratigraphy," p. 13). Total carbon and organic carbon concentrations also remain quite low, at <0.6 wt% and <0.5 wt%, respectively (Table T30). The small variations detected in inorganic and organic carbon at Site 1095 occurred both in laminated and bioturbated intervals and cannot be attributed to any specific sediment type. The generally low values show no obvious downhole trend and reflect low

biological productivity of carbonaceous material, postdepositional dissolution of carbonate, and a high input of terrigenous sediment.

INORGANIC GEOCHEMISTRY

Interstitial Water Chemistry

We squeezed 22 whole-round core samples for interstitial water at Site 1095 (Table T31). Two samples were taken from each of the first two cores in Hole 1095A, targeting alternating gray barren and brown biogenic lithologies, interpreted respectively as glacial and interglacial sedimentary units. Otherwise, single samples were taken from every third core in Holes 1095A and 1095B, as recovery permitted and regardless of lithology. Interstitial water chemistry did not exhibit any systematic differences in composition between inferred glacial and interglacial intervals, which suggests that diffusion and slow sedimentation suffice to smooth out any possible effects resulting from meter-scale lithologic variability. Chloride concentrations decrease slightly (2.6%) with depth (Fig. F29) but show no obvious signs of mixing between different water masses; therefore, any stronger trends seen in profiles of other dissolved constituents should reflect chemical reaction processes.

Organic-Matter Degradation

The interstitial water chemistry at Site 1095 (Fig. F29) shows clear evidence for active diagenesis of buried organic matter, although the predominantly terrigenous sediment contains only low amounts of organic carbon (<0.4 wt%; see "Organic Geochemistry," p. 20). Dissolved manganese increases sharply with depth to a maximum concentration (120 µM) at 25 mbsf, reflecting dissolution of Mn oxides under suboxic conditions. Directly below this zone, dissolved sulfate and manganese decrease steadily with depth as a result of sulfate reduction and accompanying precipitation of sulfide minerals. Manganese reaches a minimum concentration (10 µM) near 160 mbsf, at the base of the sulfate reduction zone, where sulfate decreases to zero and significant concentrations of methane and ethane first arise (see "Organic Geochemistry," p. 20; Fig. F30). In addition, other dissolved by-products of organic matter decay, such as alkalinity, ammonium, and phosphate, all increase steadily with depth in the upper sediment column. Alkalinity reaches maximum concentrations (≥7.0 mM) between 80 and 170 mbsf, then decreases steadily with depth to a minimum concentration (1.2 mM) at the bottom of Hole 1095B, whereas ammonium reaches maximum concentrations (>1250 µM) in a broad zone between 220 and 420 mbsf, then decreases by one-third at greater depths. Unlike alkalinity and ammonium, phosphate reaches maximum concentrations (≥7.0 µM) between 5 and 25 mbsf, decreases somewhat erratically with depth through the sulfate reduction zone, and maintains a constant concentration (≈3.0 µM) below. Note that dissolved fluoride decreases sharply between the surface and 100 mbsf and also maintains a constant concentration (8–10 µM) at greater depths. The coincident uptake of phosphate and fluoride by the sediment could reflect precipitation of authigenic apatite, although in disseminated amounts too small to detect, and the constant phosphate and fluoride concentrations at depth could correspond to equilibrium values with respect to this mineral phase (Jahnke et al., 1983; Schuffert et al., 1994).

F25. Vector end-point diagram from a sample within Cryptochron 4r.2r-1, p. 73.

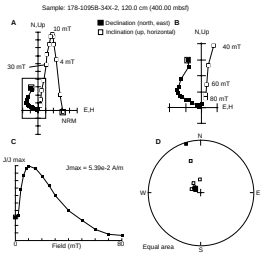

F26. Vector end-point diagram for a thermally demagnetized sample within Cryptochron 4r.2r-1, p. 74.

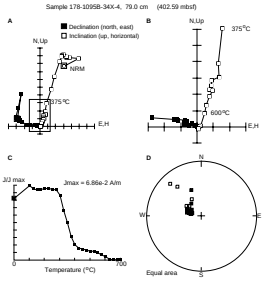

F27. Intensity and MST susceptibility for the interval 395–414 mbsf, p. 75.

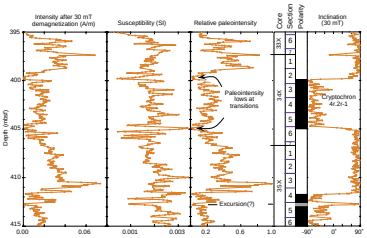

T29. Results of headspace monitoring of hydrocarbon gases, p. 157.

T30. Results of total and inorganic carbon analyses, p. 158.

Silica, Carbonate, and Silicate Diagenesis

Other inorganic processes such as dissolution of biogenic silica and carbonate, reprecipitation of authigenic silica and carbonate phases, diagenesis of clay and feldspar minerals, and possibly even reactions with underlying basaltic crust probably influence the chemical composition of interstitial water at Site 1095. Dissolved silica increases exponentially with depth and achieves maximum concentrations of nearly 1.1 mM, or approximately the solubility limit of opal-A (Kastner et al., 1977), in two separate zones from 100 to 200 mbsf and 300 to 400 mbsf (Fig. F29). These zones coincide roughly with sedimentary intervals where siliceous microfossils occur in greatest abundance (see "Biostratigraphy," p. 13; Fig. F14). Slightly lower dissolved silica concentrations characterize the interval from 200 to 300 mbsf, and silica decreases again at depths below 400 mbsf. We infer that biogenic opal dissolves principally between 0 and 100 mbsf, with substantial dissolution occurring even in the uppermost meter of sediment because the first interstitial water sample has a relatively high silica concentration (nearly 400 µM) compared to typical deep-ocean values (<200 µM). We also infer that authigenic silica precipitates somewhere below 400 mbsf, and we cannot exclude the possibility that certain silica phases may recrystallize between 100 and 400 mbsf.

In general, dissolved calcium concentrations increase, and dissolved magnesium concentrations decrease downhole throughout all depth intervals at Site 1095 (Fig. F29). Noticeable inflections in the gradients of calcium and magnesium occur at depths of ~160 and 400 mbsf. These inflections suggest the possible existence of specific reaction horizons at these depths and the involvement of multiple processes in controlling the behavior of calcium and magnesium. Possible mechanisms invoked previously to explain similar observations at many other ocean drilling sites include replacement of calcite by dolomite, formation of authigenic smectite and other clay minerals, and alteration of basaltic basement rocks (cf. Lawrence et al., 1975; Gieskes and Lawrence, 1976; Perry et al., 1976). The first potential reaction horizon coincides with the base of the sulfate reduction zone and thus could reflect ongoing dolomite formation because dissolved sulfate can inhibit this process (Baker and Kastner, 1981). Initial smear-slide and X-ray diffraction (XRD) analyses, however, have not revealed any dolomite occurrences at Site 1095. Moreover, the sediments generally contain low amounts (<0.1 wt%) of inorganic carbon (see "Organic Geochemistry," p. 20; Table T30), such that only small amounts of replacement dolomite could possibly form. Considering the predominantly fine-grained, carbonate-poor, terrigenous nature of the sediment recovered at Site 1095, clay mineral reactions probably exert the strongest influence on the observed calcium and magnesium profiles. The steady decrease of dissolved potassium with depth to near-zero concentration at the bottom of Hole 1095B supports this assessment. Strontium concentrations remain constant at ~90 µM (seawater levels) from 0 to 54 mbsf, then increase steadily to 145 µM by 296 mbsf. This increase suggests that minor dissolution of trace carbonates may occur in this interval. Magnesium concentrations below 400 mbsf would extrapolate to near zero at the inferred basement depth of ~1240 m (see "Seismic Stratigraphy," p. 33) and thus may represent a diffusion gradient resulting from basalt alteration. Similar extrapolation of the much steeper calcium gradient, however, gives an unlikely concentration of >300 mM at base-

F28. Methane distribution at Site 1095, p. 76.

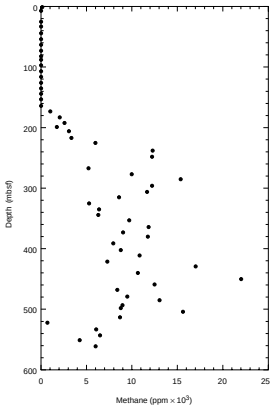

T31. Results of interstitial water analyses for Holes 1095A and 1095B, p. 161.

F29. Profiles of interstitial water chemistry in Holes 1095A and 1095B, p. 77.

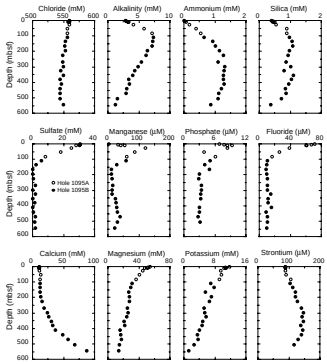

F30. Calcium carbonate distribution at Site 1095, p. 78.

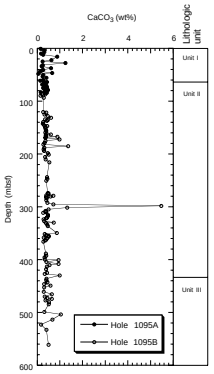

ment. As such, the observed increase in calcium below 400 mbsf must have another cause.

X-Ray Diffraction Mineralogy

A total of 22 samples were analyzed by XRD for both bulk and clay mineralogy at Site 1095. In five cores, two samples were taken where alternating colors were interpreted as possible barren glacial and biogenic interglacial intervals. Most unpaired samples were taken from presumed glacial intervals. All samples were found to consist primarily of quartz, feldspar, and a mixture of clay minerals. The clays consist of chlorite, illite, and a poorly defined phase with a broad and variable diffraction peak between 6° and 9° 2θ that shifted after glycolation (Fig. F31). This phase is tentatively identified as a mixed-layer clay, most likely mixed smectite-illite in varying proportions. Traces of amphibole were also detected in all samples.

The relative abundances of quartz and feldspar, as measured by the ratio of their principal diffraction peaks, remain nearly constant among all samples, but clay mineral abundances vary significantly. In bulk-sediment samples, the 3.19-Å plagioclase diffraction peak ranges consistently between 30% and 45% of the height of the 3.34-Å quartz peak (Table T32). Considerable variability among the clays, however, is demonstrated by the widely varying intensity of the 7-Å chlorite peak. This appears to be a real feature of the mineral abundances, not an artifact of sample preparation, because bulk samples with low chlorite/quartz intensity ratios also have low relative intensities of chlorite in their clay-sized fractions (Table T33). Relative abundances of the three clay minerals are illustrated in Figure F32. Chlorite/illite values vary by a factor of four, with the highest values generally occurring below 128 mbsf. Mixed-layer/illite ratios also vary by a factor of four but show no obvious trend with depth. Chlorite/mixed-layer clay ratios show the greatest degree of variability, with the lowest values generally obtained for biogenic-rich samples from presumed interglacial intervals (see "Lithostratigraphy," p. 4). Thus, the greatest variability among clays may occur between alternating sedimentary facies instead of as a function of age or burial depth.

X-Ray Fluorescence and Trace-Element Chemistry

Trace-element concentrations were measured by X-ray fluorescence on splits of the 22 bulk-sediment samples analyzed by X-ray diffraction (Table T34). Most of the measured elements exhibit peak concentrations in the uppermost 50 mbsf, typically between 40 and 100 mbsf, and then concentrations decrease by 20% to 30% with depth. For example, Rb concentrations exceed 100 ppm in the uppermost 50 mbsf but average about 85 ppm from 90 to 500 mbsf. The generally similar patterns observed for Nb, Zr, Y, Zn, Rb, Ni, Cr, and Ce could reflect greater dilution with depth by quartz or biogenic opal, but available data suggest otherwise. Bulk-sediment XRD analyses show a tendency toward lower quartz concentrations with depth (Table T32), and sedimentological analyses (see "Lithostratigraphy," p. 4) show a distinct decrease in preservation of biogenic opal with depth.

Barium exhibits a similar decrease in concentration with depth, except for three samples with distinctly high concentrations from the interglacial intervals at 5, 18, and 28 mbsf (1400, 970, and 880 ppm Ba, respectively). These interglacial intervals contain 60% to 100% more

F31. X-ray diffractograms of clay-sized fractions of sediment from Sample 178-1095A-4H-5, 85–88 cm, p. 79.

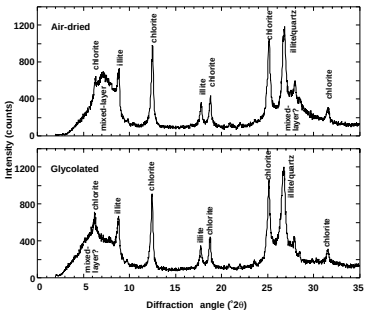

T32. Relative intensities of X-ray diffraction peaks from bulk mineral samples, p. 162.

T33. Relative intensities of X-ray diffraction peaks from clay mineral samples, p. 163.

F32. Ratios between X-ray diffraction intensities of selected peaks for chlorite and mixed-layer clays, p. 80.

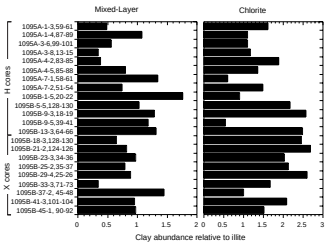

T34. Trace-element chemistry of bulk sediment, Holes 1095A and 1095B, p. 164.

barium than corresponding glacial intervals from the same cores. Sediments can concentrate barium from seawater during decomposition of organic matter (Dymond et al., 1992), and elevated barium in interglacial intervals probably reflects increased biogenic productivity in the surface water at Site 1095. Note, however, that no barium peak occurs with the interglacial interval at 128 mbsf because barite dissolves readily in anoxic sediments, and a diagenetic barium front should occur at the base of the sulfate reduction zone (Brumsack and Gieskes, 1983; von Breymann et al., 1990). More-detailed analyses of barium in these sediments could prove useful in characterizing productivity cycles of the Pleistocene.

PHYSICAL PROPERTIES

Whole-Core Measurements

MST

Natural gamma-ray emission (NGR), magnetic susceptibility, gamma-ray attenuation porosity evaluator (GRAPE, a density proxy), and *P*-wave velocity were measured on whole-round core sections (see **"Physical Properties,"** p. 20, in the "Explanatory Notes" chapter). All measurements were made to the base of the APC cores in Holes 1095A, 1095B, and 1095D to depths of 87.70 mbsf (Core 178-1095A-10H), 203.10 mbsf (Core 178-1095B-13H), and 84.68 mbsf (Core 178-1095D-9H), respectively. Whole-core *P*-wave measurements were degraded in quality below 203.10 mbsf in Hole 1095B because of drilling disturbance associated with XCB coring and the slightly smaller diameter of the core relative to that of the core liner.

Magnetic Susceptibility

Whole-core magnetic susceptibility was measured at 2-cm intervals (averaged over 2 s at each point). The raw data values range from 0 to 1400×10^{-5} SI units (see data **on CD-ROM and the World Wide Web**; Fig. **F33**). Low-pass filtered data are presented with depth and age scales in Figures **F34**, and **F35**, respectively. After low-pass filtering (Fig. **F34**), susceptibility shows a positive correlation with the GRAPE density data. The filtered susceptibility also shows an excellent positive correlation with core intervals rich in silt turbidites (see **"Lithostratigraphy,"** p. 4). In addition, magnetic susceptibility measurements were taken at 1-cm intervals using the Bartington magnetic sensor on three split cores (Cores 178-1095A-8H and 178-1095D-1H and 2H) with the aim of obtaining a more detailed susceptibility record to correlate with previously studied piston cores from the same sediment drift (Pudsey and Camerlenghi, 1998).

GRAPE Bulk Density

Gamma-ray attenuation was measured at 2-cm intervals (averaged over 2 s at each point). The raw data range from 0.5 to 2.5 g/cm³ (see data **on CD-ROM and the World Wide Web**; Fig. **F33**). After low-pass filtering, which aids in cleaning the raw data, the range narrows to 0.9–2.0 g/cm³ (Figs. **F34**, **F35**).

F33. Raw data for NGR, GRAPE density, magnetic susceptibility, and *P*-wave velocity, **p. 81.**

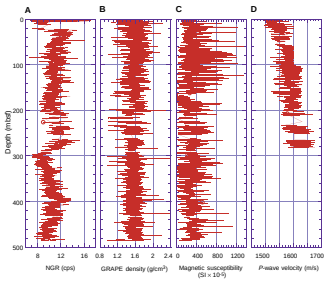

F34. Filtered NGR, GRAPE density, and magnetic susceptibility data using a Gaussian filter, **p. 82.**

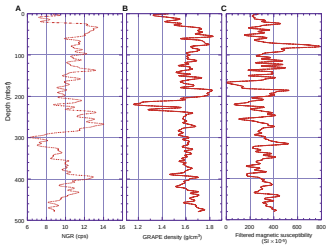

F35. Filtered NGR, GRAPE density, and magnetic susceptibility data vs. age, **p. 83.**

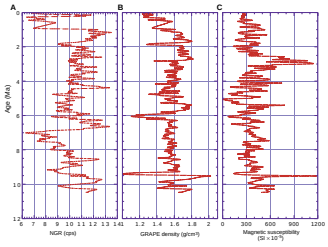

Density estimated from GRAPE data rises to 1.82 g/cm³ at ~50 mbsf, then falls to ~1.6 g/cm³ at ~100 mbsf. The depth of this density drop corresponds closely to the base of lithostratigraphic Unit I (49.3 mbsf, Core 178-1095A-7H-1) (see "Lithostratigraphy," p. 4). Below 100 mbsf, the density is broadly constant at ~1.6 g/cm³, but it drops to between 1.2 and 1.4 g/cm³ at ~205 mbsf, which is potentially attributable to the switch to XCB coring (Core 178-1095B-14X-1, 205.0 mbsf) and a zone of intermittent poor core recovery (between 200 and 295 mbsf). However, the drop in density corresponds to a drop in the downhole logging density (see "Downhole Measurements," p. 27) and to a reflection in the vertical seismic profile (VSP) seismic records (see "Seismic Stratigraphy," p. 33). GRAPE-estimated density remains constant at ~1.6 g/cm³ down to ~380 mbsf, where it gradually increases to reach ~1.7 g/cm³ at ~480 mbsf. At this depth, the record is truncated by poor core recovery.

Superimposed on these broad trends are peaks in the filtered data that show a positive correlation with the magnetic susceptibility data and correspond to intervals rich in silt laminae (see "Magnetic Susceptibility," p. 24).

P-wave Velocities

Whole-core *P*-wave measurements were recorded continuously only down to 281.54 mbsf (Core 178-1095B-21X) in Hole 1095B, after which sediment disturbance, related to XCB coring, was too great for measurements to be reliable. Raw *P*-wave velocity data include short (1–5 cm) runs of high values close to the ends of core sections and several unrealistically low values (~1100 m/s). The anomalously high values at the section ends may result from core disturbance as well as from the influence of the core caps, and thus they were removed. The raw data set is on CD-ROM and the World Wide Web, and the cleaned data, which omit anomalously high and low values, are presented in Figure F33.

MST *P*-wave velocity increases downhole, matching the increase in bulk density indicated by the index properties (compare Figs. F33 and F36). Superimposed on this velocity trend are peaks that correlate with core intervals rich in silt laminae (see "Lithostratigraphy," p. 4). Velocities continue to increase below 200 mbsf. This change is unlikely to be an artifact of XCB coring (core disturbance should cause a decrease in velocities). Broad trends in the velocities agree well with in situ interval velocity estimates obtained from the WST (see "Downhole Measurements," p. 27).

F36. Filtered GRAPE bulk density and index properties (MAD) bulk density, and water content, p. 84.

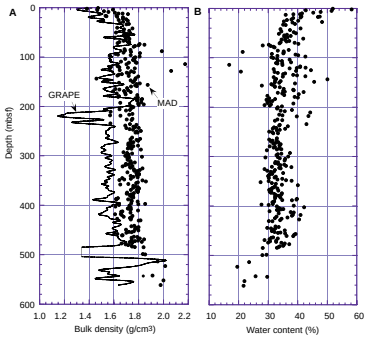

Natural Gamma Radiation

Whole-core natural gamma-ray emissions (averaged over 15 s) were counted at 15-cm intervals. The change to XCB coring caused no alteration in the signal. The raw data set is on CD-ROM and the World Wide Web and is presented in Figure F33.

The filtered gamma-ray count (Figs. F34, F35) shows an overall decrease with depth. Between 270 and 300 mbsf, the gamma-ray count decreases sharply from ~13.5 to 7 cps, which is not matched in the downhole log measurements (see "Downhole Measurements," p. 27). Neither this decrease nor the less pronounced variability in the record correlates with other physical properties, the downhole log data, or the lithostratigraphic record. The low at 280–300 mbsf matches an interval

of low sedimentation rate, but this is not repeated elsewhere in the record and is not associated with a higher biogenic component.

Split-Core Measurements

Index Properties

Gravimetric and volumetric determinations of index properties were made for 60 samples from Hole 1095A and 273 samples from Hole 1095B. One sample was taken per core section. Samples were not taken in the reconstituted sediment surrounding biscuits in the XCB cores or in regions of flow-in in the APC cores. Wet mass, dry mass, and dry volume were measured, and from these measurements percentage water weight, porosity, dry density, bulk density, and grain density were calculated (see **"Physical Properties,"** p. 20, in the "Explanatory Notes" chapter; data **on CD-ROM and the World Wide Web**).

A comparison of bulk density values from the GRAPE and the index properties bulk density values (Fig. **F36**) shows a positive correlation, in which the GRAPE bulk density is constant at ~1.6 g/cm^3 from 100 mbsf downward, and the index properties bulk density is constant at 1.75 g/cm^3 from the same depth. The index properties grain density measurements are seen to decrease slightly with depth (Fig. **F37**). Therefore, the steady bulk density downhole is attributed to compaction and/or diagenetic processes.

Porosity decreases downhole linearly between 20 and 500 mbsf from ~60% to 56% (Fig. **F37**); similarly, the bulk water content (Fig. **F36**) decreases from 38% to 32% within the same depth range. This decrease with depth is expected and can be attributed to increased compaction under load.

Discrete P*-wave Velocities*

Discrete *P*-wave measurements using all three sensors (PWS1, PWS2, and PWS3) of the velocity-strength system were made on cores from Site 1095. The upper 80 m of Cores 178-1095D-1H through 9H were soft enough to use the penetrative transducer pairs of PWS1 (direction of measurement = longitudinal, spacing of transducers = 69.5 mm) and PWS2 (direction of measurement = transversal, spacing of transducers = 34.8 mm). The PWS1 and PWS2 transducers were placed in a cross-like pattern at the same depth location to allow an evaluation of sediment anisotropy. Additionally, Hamilton Frame measurements (PWS3) were performed at the center of the cross formed by the PWS1 and PWS2 transducer imprints to assess the variability between all three transducers. Results of all three measurements are shown to the same depth scale in Figure **F38** (average measurement separation = 1.8 m). Except for a two-data-point excursion at 20 m, all velocity values are in close agreement. We observe a more consistent difference in velocity between the longitudinal (PWS1) and transverse (PWS2) direction. Within the upper 50 m, the transversal *P*-wave velocity is in general slightly smaller than the longitudinal velocity. The average anisotropy index for the upper 50 m is –0.0038 (see **"Physical Properties,"** p. 20, in the "Explanatory Notes" chapter for the equation). Below 50 mbsf, the transverse velocity generally exceeds the longitudinal velocity, expressed in a positive average anisotropy index of 0.012.

Hamilton Frame (PWS3) measurements (average measurement separation = 1.7 m) were made on Cores 178-1095D-1H through 9H and 178-1095B-14X through 52X, spanning the interval from 210 to 560 mbsf (Fig. **F38**). No discrete *P*-wave velocities are recorded for the depth

F37. Index properties porosity and MAD grain density, **p. 85.**

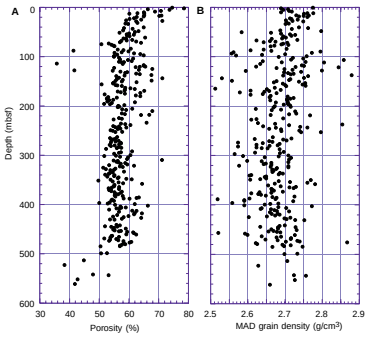

F38. PWS1, PWS2, and PWS3 measurements vs. depth, **p. 86.**

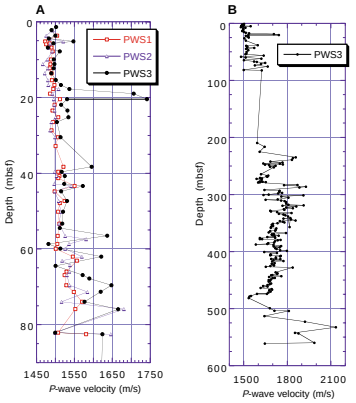

interval 83–210 mbsf. The strong increase in *P*-wave velocity below 500 mbsf can be correlated with an increase in density (Fig. F34) and is therefore thought to represent a real feature. Data presented on CD-ROM and the World Wide Web include corrections made to data from the depth intervals 56.52–82.52 mbsf and 359.3–414.84 mbsf. The error resulted when the distance readings of the transducer heads lost calibration and were corrected by linearly shifting the depths of the data sections.

DOWNHOLE MEASUREMENTS

Logging Operations

After coring had reached target depth at 570.2 mbsf, Hole 1095B was filled with viscous mud, reamed, and flushed of debris. We ran one full pass and a shorter repeat pass of the TC tool string (the hostile environment natural gamma-ray sonde [HNGS], accelerator porosity sonde [APS], HLDS, and dual induction tool [DIT]), two full passes of the GHMT string (natural gamma-ray tool [NGT], susceptibility magnetic sonde, and nuclear magnetic resonance sonde), and performed a velocity checkshot survey using the WST (see Fig. F39; also see "Downhole Measurements," p. 25, in the "Explanatory Notes" chapter). Logging operations started at 1030 hr on 22 February and finished at 0030 hr on 24 February (Table T35).

During hole preparation, the sea state worsened to wave heights of 2–3 m combined with swells of 2.5–4 m (period = 10–14 s), which proved problematic for logging operations. All tool strings had to be lowered through the pipe slowly (~1000 m/hr instead of the usual 3000m/hr), especially in the upper part, to prevent cable slip when the ship heaved downward. The ship's heave was large enough to cause the wireline heave compensator to hit its limit switches (maximum extent = 6 m) within a few minutes of being switched on, so we decided to run the TC without heave compensation. At the start of the repeat TC run, the caliper arm of the HLDS broke off, and the DIT failed. Subsequently, the swell reduced enough for the GHMT and WST to be run with the heave compensator on.

Log Quality

Borehole caliper measurements showed that the hole was typically 16–18 in (40–45 cm) in diameter, with some zones of wider washout beyond the maximum caliper extent of 18.5 in (47 cm) (Fig. F40). The washed-out zones resulted in poor contact with the borehole wall and hence negative spikes in the density log and positive spikes in the porosity log (e.g., 280–310 mbsf and 175–205 mbsf). Although some of the sections of excessive hole diameter are probably caused by drill bit rotation at the same depth for a length of time (e.g., in between taking cores), there is also a lithologic control. The deeper penetrating logs, such as medium resistivity and magnetic susceptibility, are much less affected by changing borehole diameter.

Because the hole fills with debris falling from the borehole wall over time, logging-tool runs vary in the depths that they reach. The TC, which was the first tool string to be run, reached the bottom of the hole, and the GHMT reached to within 13 m of bottom. The WST, the last logging run, reached 43 m from bottom.

F39. Graphic summary of downhole logging operations at Hole 1095B, p. 87.

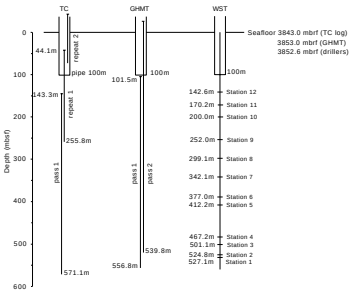

T35. Summary of logging operations, p. 165.

F40. Downhole logs from Hole 1095B, p. 88.

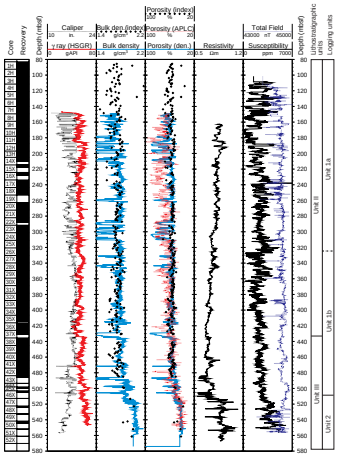

The natural gamma logs from TC and GHMT runs were only partially repeatable. This is a result of the two different tools used to measure natural gamma: the HNGS on the TC corrects for borehole diameter and potassium in the borehole fluid, whereas the NGT on the GHMT does not. The HNGS logs are shown in Figure F41. However, the depth control on the GHMT runs was better than on the TC runs because of the heave compensation. The HNGS is the more sensitive of the two, hence its results are presented in Figures F40 and F41. The erroneous spikes in the HNGS logs were probably caused by measuring sediment previously activated by the neutron source in the porosity (APS) tool located below the HNGS during high heave.

The absolute values of density and density-derived porosity match well the index physical properties of the cores, apart from the anomalous log density lows at washouts (Fig. F40). The APS porosity measurements also match the index properties porosity values, except in the wide-diameter intervals.

The pattern in the magnetic susceptibility log matches well the MST susceptibility record (Fig. F42), but with a depth offset of between 4 and 6 m for the logged interval. The location of the seafloor is apparent in the natural gamma log of the second GHMT run, and it is unlikely that the wireline stretched 5 m between 110 and 0 mbsf. The origin of the depth mismatch probably lies in using the core seafloor depth obtained from the mudline in Hole 1095A and applying it to Hole 1095B, where core recovery started at only 83 mbsf. The correlation between Holes 1095A and 1095B over the 5 m of nominal overlap is unclear, and a 5-m offset is possible.

F41. Downhole logs from the HNGS natural gamma tool on the TC tool string, p. 89.

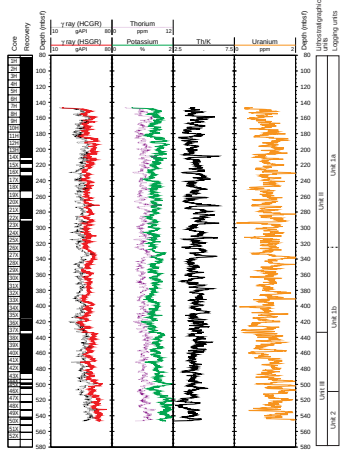

F42. Comparison of susceptibility logs from the two passes of the GHMT, p. 90.

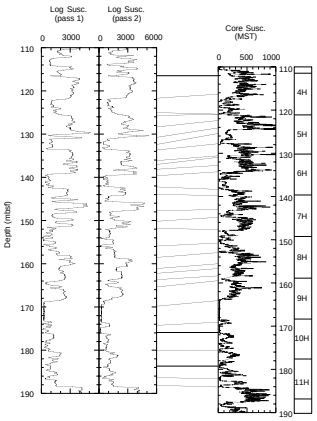

Logging Units

The sedimentary sequence could be divided into two units on the basis of changes in the character of the downhole logs (Figs. F40, F41).

Unit 1: 100 (Base of Pipe) to 510 mbsf

The overall trend we expect in the logs is one of compaction: porosity decreasing downhole, and consequent increasing density, resistivity, and sonic velocity. However, in Unit 1, density and porosity have no overall downhole gradient. Only below 460 mbsf do the logs begin to show the more normal compaction trend. This could be a result of increasing downhole proportion of diatoms and radiolarians, whose skeletons maintain porosity. The resistivity actually decreases downhole, although the trend becomes similar to that of the porosity and density logs when increasing downhole temperature is considered (resistivity decreases with increasing temperature).

Within Unit 1, we can define two subunits on the basis of the susceptibility log. Both subunits show a downhole increase in the base level of susceptibility variations, with a boundary marked by a (downhole) step decrease at 325 mbsf. Toward the top of both subunits, the amplitude of susceptibility variation reaches a maximum. The lower subunit contains a pattern that repeats about three times. Each repetition is ~40 m thick and shows a steady uphole increase in resistivity, density, and natural gamma, topped by a sharp decrease; porosity and susceptibility behave in the opposite way.

Unit 2: 510–570 mbsf (Total Depth)

The transition from Unit 1 to Unit 2 is marked by a step increase in density, resistivity, natural gamma, and susceptibility; porosity decreases to ~40%. Below the boundary, density and porosity maintain fairly steady values; in contrast, resistivity and susceptibility show a slight increase in variability.

Log-Lithology Comparison

The natural gamma and resistivity logs respond to variations in lithology. High natural gamma levels indicate higher clay, mica, and K-feldspar contents in the sediment. Susceptibility is governed principally by the concentration of magnetic minerals in the sediment, the most important of which is magnetite, which occurs mostly in the detrital fraction. From comparison of susceptibility with the core lithology (Fig. F43), the sediments that are richer in silt layers have higher susceptibility. In Figure F43, the natural gamma peaks seem to occur in about the same places as, but slightly higher up the log than, the susceptibility peaks, both marking intervals of increased terrigenous input.

F43. Core lithology compared to magnetic susceptibility and natural gamma logs at Hole 1095B, p. 91.

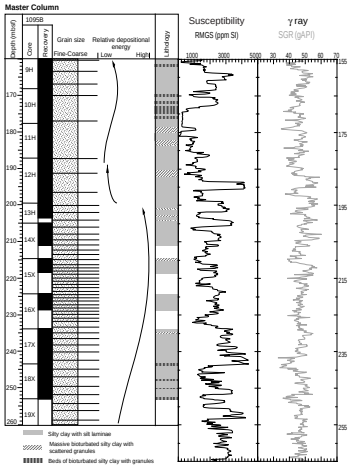

Magnetic Polarity Stratigraphy from the GHMT

The total magnetic field (MAGB) and magnetic susceptibility (RMGS) measurements from the GHMT tool string were analyzed in tandem to construct a logged magnetic polarity stratigraphy (see "Downhole Measurements," p. 25, in the "Explanatory Notes" chapter). This GHMT polarity sequence matches well the polarity zones based on split-core inclination measurements (see "Paleomagnetism," p. 16), after the 5-m downward shift of the core depth scale is considered.

The GHMT polarity sequence enables the core polarities to be extended into the interval of very low core recovery below ~480 mbsf. The interval from 491 to 523 mbsf (486–518 mbsf in terms of core depths) is reversed polarity; from below that to the base of the logs (556 mbsf) is normal polarity with two or three shorter reversed polarity events. The short reversed polarity interval at 546–548 mbsf in Figure F44 probably corresponds to the reversed interval between C5n.1n and C5n.2n (9.88–9.92 Ma) (Cande and Kent, 1995). By extrapolation downward at the implied sedimentation rate (13.5 cm/ky), an age of 10.1 Ma is determined for the base of the cored hole (570.2 mbsf).

F44. Polarity stratigraphy from the GHMT tool string, p. 92.

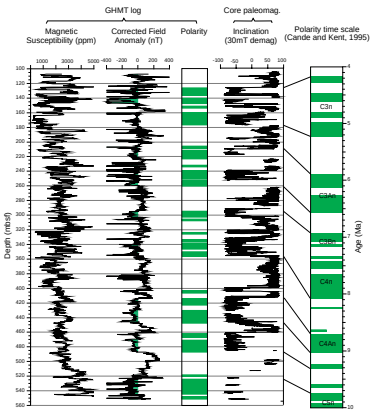

Velocity Checkshot Survey

One-way sonic traveltimes from a Generator Injector (GI) gun (at the surface) to the WST (in the borehole) were recorded at 12 depth stations between 527 and 142 mbsf to give a depth-to-traveltime conversion and interval velocities. Although the station spacing was not close enough for the survey to be a full zero-offset vertical seismic profile, we could nevertheless identify strong reflectors below the logged interval. Details of the survey are given in "Seismic Stratigraphy," p. 33.

Temperature Log

The Lamont-Doherty temperature-logging tool recorded the temperature of the fluid in Hole 1095B during the first pass of the TC tool

string (Fig. F45). These measurements underestimate the formation temperature, as the fluid did not have time to equilibrate to the formation temperature. A temperature of 19°C was recorded at the bottom of the hole (570 mbsf); thus, the temperature gradient could be at least 33°C/km. Both downhole and uphole curves show a constant offset of ~0.5°C because the borehole continued to re-equilibrate during acquisition.

OCEANOGRAPHY: SEABED MOORING[3]

Mooring ST-3, recovered from the *Polar Duke* on 20 February while Hole 1095B was being drilled, was the third deployed within the Sediment Drifts of the Antarctic Offshore (SEDANO) program, funded by the Programma Nazionale di Ricerche in Antartide with the participation of the British Antarctic Survey and aimed at describing the modern deep oceanographic circulation in the vicinity of Drift 7. Results of two previous moorings have been described by Camerlenghi et al. (1997a) and are summarized (and a related CTD section shown) in "Regional Oceanography," p. 6, in Barker and Camerlenghi (Chap. 2, this volume).

The two previous moorings, located along slopes of the drift, had shown slow, steady current flow, parallel to seabed contours. The mooring recovered during operations of Leg 178 was composed of two rotor-type current meters, 8 and 60 m above the seafloor. It was positioned in a more distal location than the previous moorings but along the same bathymetric contour (~3550 m [Fig. F46]), with the aim of observing seafloor current dynamics where the relief of the drift was minimal and obtaining information higher above the seafloor to constrain the thickness of the Ekman boundary layer.

Figure F47 shows a progressive vector diagram of the unfiltered time series (11.5 months from March 1997 to February 1998) provided by the two meters, produced by initial processing on board the *JOIDES Resolution*. Close to the seabed (8 m) the mean current flow direction is westward, tangential to the bathymetric contour; 60 m from the seafloor, however, the mean flow direction is to the south-southwest, angled ~80° counterclockwise from the direction at the lower mooring. The upper mean flow is faster (5.2 cm/s) than the lower (4.0 cm/s). It can be inferred that the lower meter lies within the Ekman layer, whereas the upper one lies above it.

Despite the overall difference in flow direction, there is some coherence between flow variabilities of the two time series. Highest flow velocities are found in both series in June and August 1997, concomitant with variations in flow direction, probably reflecting the passage of mesoscale eddies with strong barotropic properties that induce recirculation down to the seabed. The typical length scale of the June eddy is smaller than the August one, but both eddies have the same duration at depth. These barotropic perturbations lead to maximal current intensity at the seafloor, so that fine-grained sediment suspensions can be transported southwestward. The lowest mean current velocity along this contour is found in the most distal part of the drift (at ST-03) where the topographic control on flow direction and intensity is expected to be lowest. The generally low mean flow velocities are in agreement with preliminary results of the optical characteristics of the bottom-water masses, which suggests a virtual absence of a permanent nepheloid layer overlying Drift 7. The regional oceanography is therefore compat-

F45. Temperature log from Hole 1095B, p. 93.

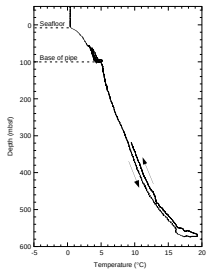

F46. Location map of the moorings on Drift 7, p. 94.

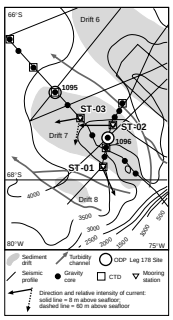

F47. Vector diagram of unfiltered meter data from Mooring ST-03, p. 95.

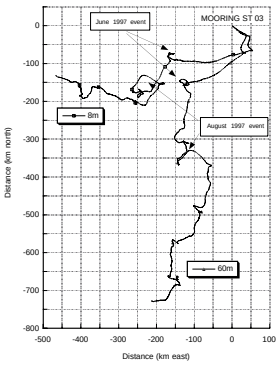

[3]Contributed by R. Laterza, A. Giorgetti, and A. Crise, Osservatorio Geofisico Sperimentale, P.O. Box 2011, Trieste Opicina 34016, Italy.

ible with modern and ancient interglacial sedimentation composed almost exclusively of biogenic material, with minor clay particles of either bottom current or eolian origin. Textural analysis on late Pleistocene sediments from Drift 7 (Pudsey and Camerlenghi, 1998) implied that small differences in grain size between glacial and interglacial sediments do not reflect dramatic glacial–interglacial changes in bottom-water flow. Therefore, the main factor controlling glacial–interglacial changes in sediment composition appears to be the sediment source.

COMPOSITE DEPTHS

Based on correlation between magnetic susceptibility, NGR, GRAPE, *P*-wave velocity, and color spectral reflectance data, a record extending from late Miocene up to the present was obtained with ~85% recovery in the upper 200 mbsf of three holes drilled at Site 1095 (Hole 1095C was not used). A composite section to the base of the hole was developed (see **"Composite Depths,"** p. 23, in the "Explanatory Notes" chapter). The base of the Site 1095 composite section is at 561.91 mcd (561.37 mbsf in Hole 1095B). Continuity of the stratigraphic section was confirmed from the mudline to 92.03 mcd (87.41 mbsf in Hole 1095A and 91.49 mbsf in Hole 1095B). Below this depth, successive cores from Hole 1095B were depth corrected by addition of the offset.

The depth offsets that were used for the composite depth section for Site 1095 are given in Table **T36**. Table **T36** shows the depth offset values (in meters) that must be applied to the depths scale (mbsf) in order to optimally align all cores from every hole at a given site. Each depth offset value refers to the depth increment that must be added to (or subtracted from) each core so that a composite spliced record can be constructed. Depth offset values (Fig. **F48**) typically increase with increasing depth because they are cumulative depth corrections determined for each core.

At Site 1095, whole-core, high-resolution measurements were taken every 2 cm for magnetic susceptibility, GRAPE density, and *P*-wave velocity and every 15 cm for NGR for all cores in Holes 1095A, 1095B, and 1095D. *P*-wave data were not measured for XCB cores. GRAPE and magnetic susceptibility data, which proved to be the most useful for correlation, are displayed on the composite depth scales in Figure **F49**. Additional measurements of spectral reflectance on the core were done at a 5-cm interval with the Minolta color scanner. Initially, all data sets for each hole were visually and quantitatively compared to check their consistency. Subsequently, GRAPE density measurements (see **"Physical Properties,"** p. 24) and magnetic susceptibility (as the most continuous and consistent data sets) were used as the primary parameters to determine depth offsets for the composite depth section. All other parameters were useful to check the hole-to-hole correlation. No smoothing or culling was applied to the data.

Correlation between all data sets was very good, at least for all combined depths up to 480 mcd. The magnetic susceptibility was inversely (the first 55 mcd) and directly (the remaining data sets) correlated with the reflectance parameters (except for the L* parameter). Hole 1095A magnetic susceptibility correlated with chromaticity parameter a*, whereas Hole 1095B correlated better with chromaticity parameter b*. The spliced section, however, was built using the same chromaticity parameter a* for all holes for consistency.

T36. Depth offsets of the Site 1095 mcd scale relative to mbsf depth, **p. 166.**

F48. Depth offsets of the Site 1095 mcd scale relative to mbsf depth, **p. 96.**

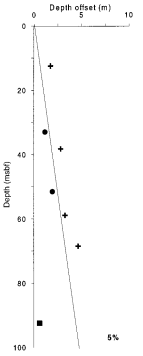

F49. GRAPE density and magnetic susceptibility data from Site 1095 on the mcd scale, **p. 97.**

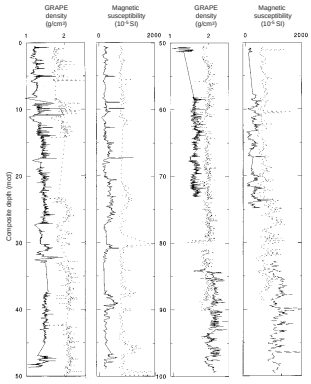

The overlap between adjacent holes was documented throughout the comparative analyses (cross correlation) between the cores. It was found that the cores in Hole 1095D recovered a signal similar to those in Hole 1095A. The MST and reflectance record was, however, more expanded in Hole 1095A (at least in the upper two cores), which most likely reflects a change in sedimentation rate instead of a correlation stretching effect. This was confirmed by sedimentological analysis (see "Sedimentation Rates," p. 32). For this reason, the cores from Hole 1095D were predominantly used to build the spliced section.

In addition, it was noted (Fig. F50) that the magnetic susceptibility, the reflectance parameters (except for L*), and the GRAPE density showed a correlated cyclic pattern in the raw data, which is better preserved in the upper 200 mcd. The same cyclic pattern is observed in the *P*-wave data (values in the 1450–1700 m/s range). The relative agreement of different sedimentary features in adjacent holes was excellent. However, minor stretching and compression in the cores were unavoidable. Much of this distortion occurred on a scale of <1 m. Core stretching of the decimeter to centimeter scale would be required to align all sedimentary features. Because the Splicer software does not allow such adjustment, the cores in which the wavelength of the cyclical pattern was similar were chosen to build the spliced section (which must be considered preliminary; see "Composite Depths," p. 23, in the "Explanatory Notes" chapter).

Following the construction of composite depth sections for the site, single spliced records were built as described in "Composite Depths," p. 23, in the "Explanatory Notes" chapter. The tie points for the Site 1095 splice are given in Table T37. Plots of spliced reflectance and magnetic susceptibility data are shown in Figure F51.

SEDIMENTATION RATES

A sedimentary section, 570 m thick, extending from the Holocene to the upper Miocene (~10.1 Ma), was recovered at Site 1095. Recovery was essentially continuous to 480 mbsf. Sedimentation rates were determined using magnetostratigraphy from Holes 1095A and 1095B in combination with diatom and radiolarian datums. Sedimentation rates are assumed to be constant between datums and are calculated by taking the slope of the depth-age curve between successive points. In this case, the sedimentation rates were calculated from the depth-age fixes (Fig. F52; Tables T38, T39, T40) by fitting linear regression lines to selected intervals of the combined magnetic and biostratigraphic data sets.

The depth of a geomagnetic polarity transition is defined as the depth at which the inclination changes sign. Many transitions were assigned a large uncertainty interval where the transition itself was lost in a gap between cores or within a disturbed interval (see Table T28). The center of the uncertainty interval was used in calculating sedimentation rates. Biostratigraphic datums were assigned when a clear FO or LO could be determined through examination of sediment samples. No FO or LO was determined when the occurrence bordered an interval barren of biogenic material.

Sedimentation rates determined from polarity transitions and diatom and radiolarian datums are given in Tables T38, T39, and T40 and illustrated in Figures F53 and F54. Rates derived from paleomagnetic data show a change from Hole 1095A to 1095B, with a lower sedimen-

F50. Correlated cyclic pattern of GRAPE density, magnetic susceptibility, and other data, p. 98.

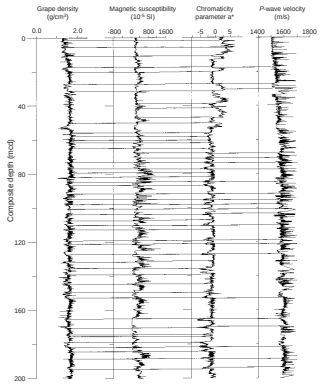

T37. Spliced cores for Holes 1095A, 1095B, and 1095D, p. 168.

F51. Spliced records of magnetic susceptibility and chromaticity parameter a*, p. 99.

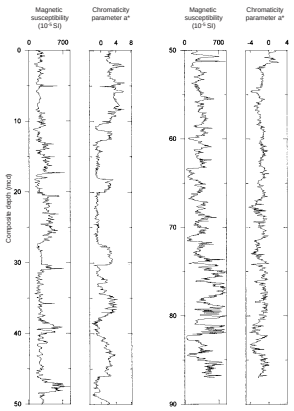

F52. Depth-age profile determined from geomagnetic reversals and diatom and radiolarian datums, p. 100.

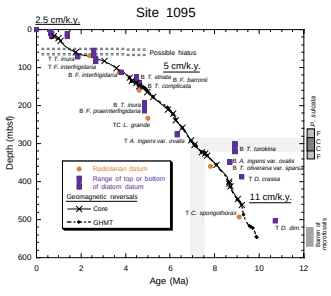

T38. Sedimentation rates calculated from geomagnetic polarity transition data, p. 169.

tation rate in Hole 1095A over the last 3.04 m.y. The lower sedimentation rate indicates a decrease in sediment deposition between 60 and 83 mbsf. The possibility of a hiatus between 50 and 65 mbsf is discussed in "Paleomagnetism," p. 16. Seismic stratigraphy suggested an unconformity at ~60 mbsf coincident with a prominent lithostratigraphic boundary (see "Seismic Stratigraphy," p. 33, and "Lithostratigraphy," p. 4). The paleomagnetic and biostratigraphic data are in excellent agreement for the upper 200 m of this section. Below 200 mbsf, the biostratigraphic data bracket the depth-age curve derived from magnetostratigraphy. The combined data sets yield a smooth depth-age profile down to 480 mbsf. This curve is continued down to 551 mbsf in the GHMT logging data and extrapolated to 570 mbsf. The overall trend is an uphole decrease in sedimentation rate from ~11 cm/k.y. near the base of the hole to 2.5 cm/k.y. at the top.

SEISMIC STRATIGRAPHY

Site 1095 is situated on the distal northeast flank of sediment Drift 7 (Rebesco et al., 1996, 1997). The drift is perpendicular to the margin and is bounded by channels (Fig. F2; see "Background and Scientific Objectives," p. 1). Previous seismic stratigraphic interpretations of the Antarctic Peninsula drifts can be found in Rebesco et al. (1996, 1997) and in McGinnis et al. (1997). Rebesco et al. (1996) identify six acoustic units, M1 through M6, above oceanic basement. Sites 1095 and 1096 were selected to sample the four upper acoustic units, M1 through M4, interpreted to correspond to two stages in the evolution of the drift: a drift maintenance stage (M1 and M2) and a drift growth stage (M3 and M4). Site 1095 penetrated to a depth of 570 mbsf recovering sediments from Units M1 to M4.

The existing MCS profiles across Site 1095, collected by the Osservatorio Geofisico Sperimentale of Trieste (Fig. F1A; also see "Seismic Stratigraphy," p. 29, in the "Explanatory Notes" chapter and "Appendix," p. 24, and Fig. AF1, p. 59, both in the "Leg 178 Summary" chapter), have been examined to establish the seismic stratigraphy. Physical properties measurements from cores and results from downhole logging are used to correlate the section at Site 1095 with the seismostratigraphic units and to assign true depth to seismic reflectors. At each site, the acoustic units are described and tied where possible to the other drill sites.

Seismic Models and Correlations

Density/Velocity Model

Bulk densities for the formation have been derived from MST GRAPE measurements with a 2-cm spatial resolution, index properties measurements (1.5-m spatial resolution), and lithodensity logging data (HLDS, measurement separation ~15 cm [Fig. F55]). The results from index properties measurements agree very well with the in situ properties from the downhole logging. Compared to these two data sets, the GRAPE densities show generally lower values. This difference increases dramatically (~0.3 g/cm^3) when the coring method changes from APC to XCB at 205 mbsf at the top of Core 178-1095B-14X, probably from the larger air/water gap between liner and core and the higher degree of core disturbance produced by the XCB. Two different density models

T39. Sedimentation rates calculated from radiolarian datums, p. 171.

T40. Sedimentation rates calculated from diatom datums, p. 172.

F53. Sedimentation rate vs. depth determined from geomagnetic polarity transitions, p. 101.

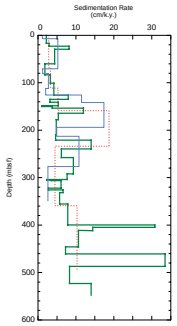

F54. Sedimentation rate vs. age determined from geomagnetic polarity transitions, p. 102.

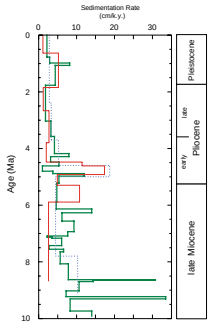

F55. Comparison of different density data sets for Site 1095, p. 103.

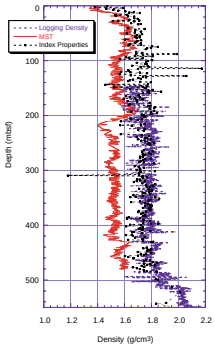

have been tested using (1) only index properties data and (2) a combination of GRAPE density (0–150 mbsf) and downhole logging data (150–560 mbsf).

Three differently derived velocities are available. The MST logger provided continuous data (4-cm spatial resolution) down to 200 mbsf (within the APC-cored part of the holes) and only sparse data between 200 and 280 mbsf. Single Hamilton Frame (PWS3) measurements (one every section) provide high-quality data for the deeper parts of Site 1095. In Figure F56, MST data, interval velocities derived from a downhole seismic experiment (using the WST and a 2500-cm³ two-chamber GI air gun), and the Hamilton Frame measurements are plotted for comparison. Most of the MST-derived *P*-wave velocities are slightly higher than the interval velocities from the downhole seismic experiment, believed to provide the most accurate results (Hardage, 1985). Two different velocity models have been tested. The first model uses MST data (0–209 mbsf) and Hamilton Frame data (209–543 mbsf); the second model also combines MST and Hamilton Frame data but from different depth intervals (PWS3 = 0–80 mbsf, 209–560 mbsf, and MST = 80–209 mbsf).

Source Signals

Two differently derived signals of the GI gun that was actually used during the seismic site survey were employed for the seismic models. Six randomly chosen traces were extracted from a digital far-field recording of multiple firing of the gun in water (recording distance ~300 m) (Fig. F57C). The signals were brought in phase, then stacked and resampled at 0.5 ms using a cubic interpolation function (Fig. F57A). The signal (wavelength = 10 ms) contains a continuous-energy spectrum up to 350 Hz (Fig. F57B).

A second source signal was generated by extracting strong, coherent seafloor reflections from the MCS profile across the drill site. The signal was processed as for the far-field signature (above) (Fig. F57D, F57F). The seafloor signal has a much longer wavelength (40 ms) and consists of a negative onset followed by two positive excursions and a final negative one (Fig. F57D). The derived signal has a dominant frequency range of 10 to 250 Hz (Fig. F57E). Differences between the frequency spectra of the signals could be explained by the low-pass filter effect of a long path through seawater and the uppermost seafloor sediments and by anti-alias filtering applied during data acquisition.

VSP and Traveltime Depth Models

The results from 12 geophone stations of a downhole seismic experiment have been processed to a six-trace VSP section (Fig. F58). Additionally, the traveltime information was used to compare a standard traveltime/depth relationship (Carlson et al., 1986) to a second-order polynomial extrapolation, a linear extrapolation, and a combined linear-polynomial model (Fig. F59). The polynomial model, the Carlson et al. (1986) relationship, and the combined polynomial-linear model show good agreement and allow the depth to oceanic basement at 650 ms one-way traveltime to be estimated as 1250 mbsf (Fig. F58). VSP reflectors should be compared to the multichannel reflectors and tied to depth. Unfortunately, the low number of stations (12) and their wide spacing (average: 33 m) prevent this. The chosen station spacing introduces a low-pass anti-alias filter (~25 Hz) and greatly reduces the cover-

F56. Comparison of MST, downhole logging, and index properties velocities, p. 104.

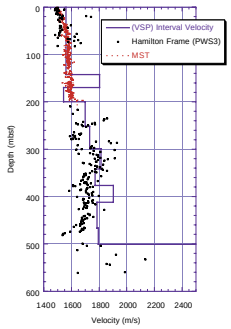

F57. Source signals and their characteristics, p. 105.

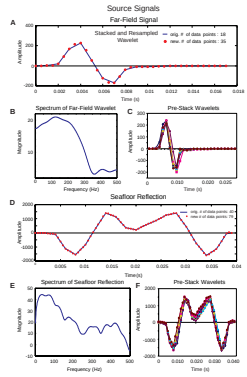

F58. Seismostratigraphic interpretation of Site 1095 and display of the VSP traces, p. 106.

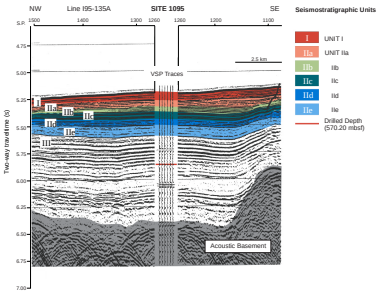

F59. Traveltime depth models for Site 1095, p. 107.

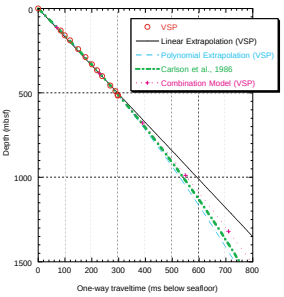

age up the hole. As a result, only strong reflectors from the lower part of the drilled section and below are visible in the stacked VSP section. One of these reflectors, for example, belongs to the sediment/basalt interface (Fig. F58). The WST deployment at Site 1095 was mainly designed to provide a checkshot survey (i.e., one-way traveltimes to stations at known depths in the hole and interval velocities between those stations).

Synthetic Seismograms

The raw velocity and density data were carefully evaluated and corrected for obvious artifacts. In the case of the MST, the 1.5-m core section end-effects (in *P*-wave velocity and density data) and density lows caused by core disturbance were removed. The velocity and density data were preprocessed and cleaned in 20-m sections according to the methods described in "Seismic Stratigraphy," p. 29, in the "Explanatory Notes" chapter. Special care was taken with anomalous density values within the downhole logging data caused by overwidened hole sections. These artificial density lows have been manually removed. Model A data (index properties density, PWS3 and MST velocity) were resampled at a 0.8-m spatial resolution. For Model B (logging and MST density, PWS3 and MST velocity), the data resolution was degraded to 0.6-m spacing. Each acoustic impedance model was convolved with the far-field and seafloor signals. The velocity/density data, the impedance curve, the reflectivity coefficients, and two unfiltered synthetic seismograms are displayed for each model (Figs. F60 [Model A], F61 [Model B]). A depth axis is displayed next to the time scale to allow convenient traveltime/depth conversions.

The most eye-catching difference between synthetic traces is not caused by the differences in the velocity and density data but by the different source signals used for the convolution. The higher frequency content of the far-field signal and its shorter signal length result in a higher frequency, more detailed synthetic trace. Figure F62 depicts a comparison of the two trace spectra from Model A and the corresponding spectra of the signals used. Because shape and frequency range are nearly identical, there was no major loss in information during data subsampling and interpolation.

Comparison of Synthetic Seismograms and Digital Reflection Seismic Profiles

All four calculated synthetic traces are interpolated to a 1-ms resolution (1000 Hz) and subsequently filtered using a high-order, zero-phase equi-ripple band-pass filter (pass band = 20–110 Hz, attenuation = 60–70 dB, filter order = 170–220 [Fig. F63]). Five of these traces are then shown together with 42 traces of the field seismic profile (Figs. F64, F65, F66, F67). A zero-phase Butterworth band-pass filter (pass band = 10–110 Hz) and a 150-ms automatic gain recovery window were applied to the sorted and stacked data set. Additionally, the total time window and the delay were reduced, and the 2-ms data were interpolated to 1 ms to match the time resolution of the synthetic trace. The optimal filter parameters were adjusted to values used during the actual processing of the precruise survey data. Different amounts of time-invariant gain were applied to equalize the overall amplitude appearance of the field and synthetic traces. Possible tie lines connect synthetic and survey

F60. Unfiltered synthetic seismograms for far-field and seafloor signals, Model A, p. 108.

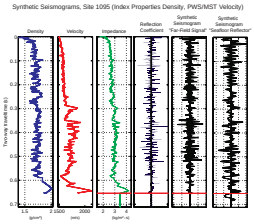

F61. Unfiltered synthetic seismograms for far-field and seafloor signals, Model B, p. 109.

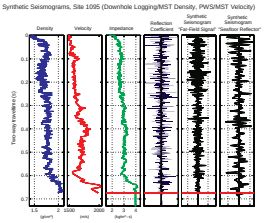

F62. Comparison of the input and output frequency spectra, Model A, p. 110.

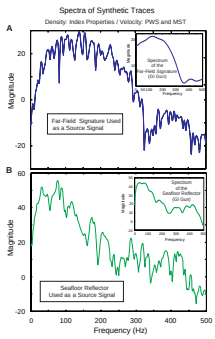

F63. Filter characteristics used to filter synthetic trace of Model A, p. 111.

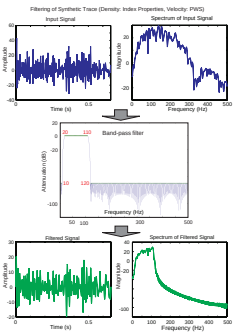

reflectors. Because of polarity changes within the synthetic, correlation between positive and negative half-cycles are possible.

Each data set has its own problem zones that show poor or no correlation with the survey data. For example, a zone of strong reflections between 300 and 350 mbsf appears in all four synthetic runs but does not fit the survey data. The best working preliminary model is Model A (index properties density and PWS3 velocity) in combination with the seafloor reflection as a source signal (Fig. F65).

Both velocity models allow an accurate time/depth conversion. The two-way traveltime to the base of Hole 1095B (~654 ms) is defined within 20 ms (see Table T41). The extrapolated VSP curve of Figure F59 has been used to create the table. Most of the important reflectors and seismostratigraphic boundaries show up within the synthetic seismograms.

Correlation of VSP, Seismostratigraphic Units, and the Analogue Seismic Section

In Figure F58, the six-trace VSP section and the analogue seismic data are shown at the same scale. The boundaries of the major seismostratigraphic units and the maximum penetration time are marked. The slight time offset (10–20 ms) below seafloor between the analogue and the digital data can be partly explained by the negative onset of the seafloor reflector.

Seismic Units

Direct comparison between the multichannel records and the synthetic seismogram, the physical properties data, and the lithologic units suggests subdivision of the seismic units (Figs. F58, F68, F69).

1. Seismic Unit I (0–64 mbsf). In seismic profiles parallel and perpendicular to the margin, seismic Unit I consists of parallel and subparallel high-amplitude continuous reflectors that alternate with lower amplitude and more disrupted reflectors (Figs. F68, F69). Alternation between higher and lower amplitude reflector packages is more evident in the sub-bottom 3.5-kHz profile collected on site approach (see Fig. F3). Seismic Unit I has relatively uniform thickness that suggests a sheet-drape geometry. Its base at the site location is marked by a strong high-amplitude reflector that locally has an erosional character (Figs. F58, F69, F70) (see "Lithostratigraphy," p. 4, and "Paleomagnetism," p. 16).
2. Seismic Unit II (64–338 mbsf). Seismic Unit II is characterized by variable amplitude and discontinuous reflectors (Figs. F68, F69). Five acoustic subunits (i.e., Subunit IIa, IIb, IIc, IId, and IIe) have been distinguished. Subunit IIa (64–~107 mbsf) is characterized by high-amplitude, continuous to disrupted reflectors. Subunit IIa also has localized internal reflection truncations and onlaps. Subunit IIb (107–149 mbsf) consists of high-amplitude reflectors that thin to the northwest and the northeast (Figs. F68, F69) and become thicker toward the base of the continental slope. Subunit IIc (149–214 mbsf) is marked by very strong couplets of high-amplitude reflectors that correspond to an increase in formation velocity (i.e., from 1550 to 1700 m/s) as recorded during VSP (see "Downhole Measurements," p. 27). Subunit IId (214–

F64. Comparison of synthetic traces for Model A (far-field) and digital data of line I95-135A, p. 112.

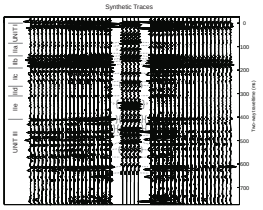

F65. Comparison of synthetic traces for Model A (seafloor) and digital data of line I95-135A, p. 113.

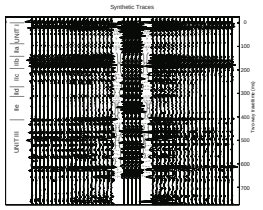

F66. Comparison of synthetic traces for Model B (far-field) and digital data of line I95-135A, p. 114.

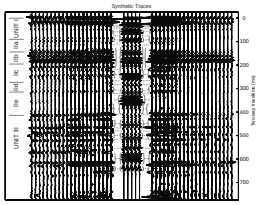

F67. Comparison of synthetic traces for Model B (seafloor) and digital data of line I95-135A, p. 115.

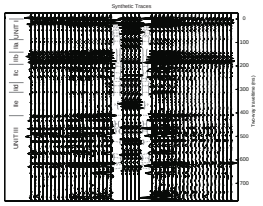

T41. TWT and depth to base of seismic units at Site 1095, p. 173.

250 mbsf) is characterized by high-amplitude, continuous reflectors. Subunit IIe (250–338 mbsf) has reflectors of low amplitude and continuity, corresponding to a downhole decrease in formation velocities in the VSP record (see "Downhole Measurements," p. 27).

3. Seismic Unit III (338–570 mbsf, and continuing to beneath the cored section). This unit is typified by a sequence of reflectors with very high amplitude and continuity (Figs. F68, F69). The lowermost sampled part of Unit III also corresponds to a rapid increase downhole in velocity and density in the logging and physical properties data (see "Downhole Measurements," p. 27, and "Physical Properties," p. 24). The base of seismic Unit III has not been determined, but it may be associated with a change in the character of reflectors at about 800 ms and coincides with a strong reflector on the traces in the VSP profile (Fig. F58).

Interpretation

The acoustic stratigraphy, in conjunction with the drilling data, places constraints on the age of depositional events for the distal continental rise sequences (Fig. F70). Several general observations can be made from the seismic profile across the distal drift site.

Seismic Unit I has been interpreted to show hemipelagic drape. The upper 50 m of seismic Unit I correlates with lithologic Unit I (see "Lithostratigraphy," p. 4). Lithologic Unit I is characterized by fine-grained, diatom-bearing silty clay and clay, alternating with silty clay with sand grains. These deposits are believed to form by the slow sedimentation of biogenic-rich facies as hemipelagites in a regime of weak bottom currents. Seismic Unit I extends ~10 m deeper than lithologic Unit I, in a transitional interval characterized by an increase in ice-rafted debris in the laminated silt and mud facies. The base of Unit I is marked by a reflector that is locally an erosional unconformity. The depth of this unconformity correlates with a hiatus in the magnetostratigraphic record (see "Paleomagnetism," p. 16).

Seismic Unit II includes much of lithostratigraphic Unit II (see "Lithostratigraphy," p. 4). Lithostratigraphic Unit II has repetitive successions of turbiditic sediments and structureless bioturbated intervals containing enhanced concentrations of ice-rafted debris (see "Lithostratigraphy," p. 4). Truncation and onlap of reflectors in seismic Subunit IIa, and the mostly horizontal parallel and subparallel reflectors below seismic Subunit IIa, are both compatible with overbank turbidite deposition from a nearby channel. At ~435 mbsf within seismic Unit III, there is a downward lithologic transition from turbidites to the finer grained parallel-laminated siltstones and claystones that characterize lithologic Unit III (see "Lithostratigraphy," p. 4). The type of ice-rafted debris also changes downcore from scattered sand, granules, and small pebbles (i.e., a few millimeters) in lithologic Unit II to large-size pebbles (centimeter size) in lithologic Unit III. The more uniform sedimentary succession of lithologic Unit III is compatible with the regular reflector pattern below.

The ages assigned to the seismic units recognized at Site 1095 (Fig. F70; Table T41) are based on preliminary paleomagnetic data from cores (see "Paleomagnetism," p. 16). Seismic Unit I is Pleistocene in age (0–1.7 Ma). The base of seismic Unit I corresponds to a possible hiatus in the paleomagnetic data (see "Paleomagnetism," p. 16). Seismic

F68. MCS profile across Site 1095 parallel to the margin, p. 116.

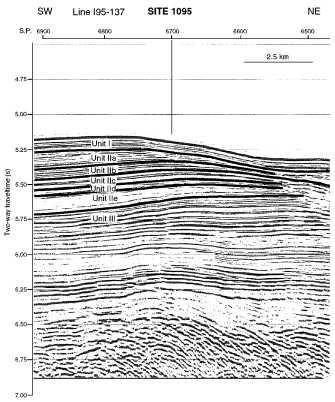

F69. MCS profile across Site 1095 perpendicular to the margin, p. 117.

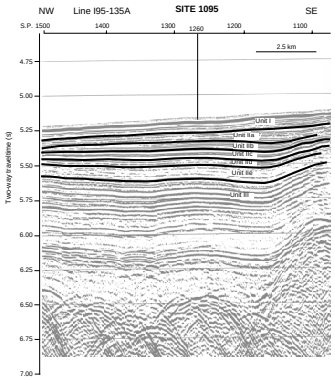

F70. Seismic section over Site 1095 showing seismic units, depths, and ages, p. 118.

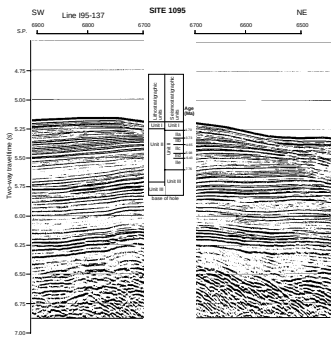

Unit II is Pliocene to late Miocene in age (1.7 Ma or older, depending on the extent of the hiatus, to 7.76 Ma). The Pliocene–Miocene transition occurs within Subunit IIc. Seismic Unit III is older than 7.76 Ma.

At Site 1095, seismic Units M1 to M4 of Rebesco et al. (1997) were drilled. The base of seismic Units IIa and IId correlate with the unit boundaries M1/M2 and M2/M3, respectively. The bottom of the hole reached the boundary between seismic Units M3 and M4.

REFERENCES

Akiba, F., 1986. Middle Miocene to Quaternary diatom biostratigraphy in the Nankai trough and Japan trench, and modified lower Miocene through Quaternary diatom zones for middle-to-high latitudes of the North Pacific. *In* Kagami, H., Karig, D.E., Coulbourn, W.T., et al., *Init. Repts. DSDP,* 87: Washington (U.S. Govt. Printing Office), 393–481.

Akiba, F., and Yanagisawa, Y., 1986. Taxonomy, morphology and phylogeny of the Neogene diatom zonal marker species in the middle-to-high latitudes of the North Pacific. *In* Kagami, H., Karig, D.E., Coulbourn, W.T., et al., *Init. Repts. DSDP,* 87: Washington (U.S. Govt. Printing Office), 483–554.

Alonso, B., and Maldonado, A., 1990. Late Quaternary sedimentation of the Ebro turbidite systems (Northwestern Mediterranean): two styles of deep-sea deposition. *Mar. Geol.,* 95:353–377.

Baker, P.A., and Kastner, M., 1981. Constraints on the formation of sedimentary dolomite. *Science,* 213:215–216.

Baldauf, J.G., and Barron, J.A., 1991. Diatom biostratigraphy: Kerguelen Plateau and Prydz Bay regions of the Southern Ocean. *In* Barron, J., Larsen, B., et al., *Proc. ODP, Sci. Results,* 119: College Station, TX (Ocean Drilling Program), 547–598.

Barker, P.F., 1982. The Cenozoic subduction history of the Pacific margin of the Antarctic Peninsula: ridge crest-trench interactions. *J. Geol. Soc. London,* 139:787–801.

Barron, J.A., 1985. Miocene to Holocene planktic diatoms. *In* Bolli, H.M., Saunders, J.B., and Perch-Nielsen, K. (Eds.), *Plankton Stratigraphy:* Cambridge (Cambridge Univ. Press), 763–809.

Bart, P.J., and Anderson, J.B., 1995. Seismic record of glacial events affecting the Pacific margin of the Northwestern Antarctic Peninsula. *In* Cooper, A.K., Barker, P.F., and Brancolini, G. (Eds.), *Geology and Seismic Stratigraphy of the Antarctic Margin.* Am. Geophys. Union Antarct. Res. Ser., 68:75–96.

Berggren, W.A., 1992. Neogene planktonic foraminifer magnetobiostratigraphy of the southern Kerguelen Plateau (Sites 747, 748, and 751). *In* Wise, S.W., Jr., Schlich, R., et al., *Proc. ODP, Sci. Results,* 120 (Pt. 2): College Station, TX (Ocean Drilling Program), 631–647.

Berggren, W.A., Kent, D.V., Swisher, C.C., III, and Aubry, M.-P., 1995. A revised Cenozoic geochronology and chronostratigraphy. *In* Berggren, W.A., Kent, D.V., Aubry, M.-P., and Hardenbol, J. (Eds.), *Geochronology, Time Scales and Global Stratigraphic Correlation*. Spec. Publ.—Soc. Econ. Paleontol. Mineral. (Soc. Sediment. Geol.), 54:129–212.

Boulton, G.S., 1990. Sedimentary and sea level changes during glacial cycles and their control on glaciomarine facies architecture. *In* Dowdeswell, J.A., and Scourse, J.D. (Eds.), *Glacimarine environments: processes and sediments*. Geol. Soc. Spec. Publ., 53:15–52.

Brumsack, H.J., and Gieskes, J.M., 1983. Interstitial water trace-metal chemistry of laminated sediments from the Gulf of California, Mexico. *Mar. Chem.,* 14:89–106.

Camerlenghi, A., Crise, A., Pudsey, C.J., Accerboni, E., Laterza, R., and Rebesco, M., 1997a. Ten-month observation of the bottom current regime across a sediment drift of the Pacific margin of the Antarctic Peninsula. *Antarct. Sci.,* 9:426–433.

Camerlenghi, A., Rebesco, M., and Pudsey, C.J., 1997b. High resolution terrigenous sedimentary record of the sediment drifts on the Antarctic Peninsula Pacific margin. *In* Ricci, C.A. (Ed.), *The Antarctic Region: Geological Evolution and Processes*. Init. Results, SEDANO Progr., *Terra Antarct.,* 705–710.

Cande, S.C., and Kent, D.V., 1992a. A new geomagnetic polarity time scale for the Late Cretaceous and Cenozoic. *J. Geophys. Res.,* 97:13917–13951.

Cande, S.C., and Kent, D.V., 1992b. Ultrahigh resolution marine magnetic anomaly profiles: a record of continuous paleointensity variations? *J. Geophys. Res.,* 97:15075–15083.

Cande, S.C., and Kent, D.V., 1995. Revised calibration of the geomagnetic polarity timescale for the Late Cretaceous and Cenozoic. *J. Geophys. Res.,* 100:6093–6095.

Carlson, R.L., Gangi, A.F., and Snow, K.R., 1986. Empirical reflection travel time versus depth and velocity versus depth functions for the deep-sea sediment column. *J. Geophys. Res.,* 91:8249–8266.

Claypool, G.E., and Kvenvolden, K.A.,1983. Methane and other hydrocarbon gases in marine sediment. *Annu. Rev. Earth Planet Sci.,* 11:299–327.

Craddock, C. (Ed.), 1982 . *Antarctic Geoscience:* Madison (Univ. Wisconsin Press).

Dymond, J., Suess, E., and Lyle, M., 1992. Barium in deep-sea sediment: a geochemical proxy for paleoproductivity. *Paleoceanography,* 7:163–181.

Gersonde, R., 1990. Taxonomy and morphostructure of Neogene diatoms from the Southern Ocean, ODP Leg 113. *In* Barker, P.F., Kennett, J.P., et al., *Proc. ODP, Sci. Results,* 113: College Station, TX (Ocean Drilling Program), 791–802.

Gersonde, R., 1991. Taxonomy and morphostructure of late Neogene diatoms from Maud Rise (Antarctic Ocean). *Berichte zur Polarforschung,* 59:141–171.

Gersonde, R., and Bárcena, M.A., 1998. Revision of the late Pliocene–Pleistocene diatom biostratigraphy for the northern belt of the Southern Ocean. *Micropaleontology,* 44:84–98.

Gersonde, R., and Burckle, L.H., 1990. Neogene diatom biostratigraphy of ODP Leg 113, Weddell Sea (Antarctic Ocean). *In* Barker, P.F., Kennett, J.P., et al., *Proc. ODP, Sci. Results,* 113: College Station, TX (Ocean Drilling Program), 761–789.

Gersonde, R., Hodell, D.A., Blum, P., et al., 1999. *Proc. ODP, Init. Repts.,* 177 [CD-ROM]. Available from: Ocean Drilling Program, Texas A&M University, College Station, TX 77845-9547, U.S.A.

Gieskes, J.M., and Lawrence, J.R., 1976. Interstitial water studies, Leg 35. *In* Hollister, C.D., Craddock, C., et al., *Init. Repts. DSDP,* 35: Washington (U.S. Govt. Printing Office), 407–426.

Hardage, B.A., 1985. Vertical seismic profiling: a measurement that transfers geology to geophysics. *In* Berg, O.R., and Woolverton, D.G. (Eds.), *Seismic Stratigraphy II: An Integrated Approach.* AAPG Mem., 26: 13–36.

Harwood, D.M., and Maruyama, T., 1992. Middle Eocene to Pleistocene diatom biostratigraphy of Southern Ocean sediments from the Kerguelen Plateau, Leg 120. *In* Wise, S.W., Jr., Schlich, R., et al., *Proc. ODP, Sci. Results,* 120: College Station, TX (Ocean Drilling Program), 683–733.

Heinrich, H., 1988. Origin and consequences of cyclic ice rafting in the northeast Atlantic Ocean during the past 130,000 years. *Quat. Res.,* 29:142–152.

Hollister, C.D., Craddock, C., et al., 1976. *Init. Repts., DSDP,* 35: Washington (U.S. Govt. Printing Office).

Jahnke, R.A., Emerson, S.R., Roe, K.K., and Burnett, W.C., 1983. The present day formation of apatite in Mexican continental margin sediments. *Geochim. Cosmochim. Acta,* 47:259–266.

Kastner, M., Keene, J.B., and Gieskes, J.M., 1977. Diagenesis of siliceous oozes, I. Chemical controls on the rate of opal-A to opal-CT transformation—an experimental study. *Geochim. Cosmochim. Acta,* 41:1041–1059.

Larter, R.D., and Barker, P.F., 1991. Neogene interaction of tectonic and glacial processes at the Pacific margin of the Antarctic Peninsula. *In* Macdonald, D.I.M. (Ed.), *Sedimentation, Tectonics and Eustasy.* Spec. Publ. Int. Assoc. Sedimentol., 12:165–186.

Larter, R.D., Rebesco, M., Vanneste, L.E., Gamboa, L.A.P., and Barker, P., 1997. Cenozoic tectonic, sedimentary and glacial history of the continental shelf west of Graham Land, Antarctic Peninsula. *In* Cooper, A.K., Barker, P.F., and Brancolini, G. (Eds.), *Geology and Seismic Stratigraphy of the Antarctic Margin* (Pt. 2). Antarct. Res. Ser., 71:1–27.

Lawrence, J.R., Gieskes, J.M., and Broecker, W.S., 1975. Oxygen isotope and cation composition of DSDP pore waters and the alteration of Layer II basalts. *Earth Planet. Sci. Lett.,* 27:1–10.

McGinnis, J.P., Hayes, D.H., and Driscoll, N.W., 1997. Sedimentary processes across the continental rise of the southern Antarctic Peninsula. *Mar. Geol.,* 141:91–109.

Nelson, C.H., and Maldonado, A. (Eds.), 1990. *The Ebro Continental Margin, Northwestern Mediterranean Sea*. Mar. Geol., Spec. Iss., 95:57–442.

Nelson, C.H., Maldonado, A., Barber, J.H., Jr., and Alonso, B., 1991. Modern sand-rich and mud-rich siliciclastic aprons, alternative base-of-slope turbidite systems to submarine fans. *In* Weimer, P., and Link, M. (Eds.), *Seismic Facies and Sedimentary Processes of Modern and Ancient Submarine Fans:* New York (Springer Verlag), 171–190.

Oliver, R.L., James, P.R., and Jago, J.B. (Eds.), 1983. *Antarctic Earth Science:* Cambridge (Cambridge Univ. Press).

Pemberton, S.G., McEachern, J.A., and Frey, R.W., 1992. Trace fossil facies models: environmental and allostratigraphic significance. *In* Walker, R.G., and James, N. (Eds.), *Facies Models: Response to Sea Level Change:* St. Johns, Newfoundland (Geol. Assoc. Canada), 42–72.

Perry, E.A., Jr., Gieskes, J.M., and Lawrence, J.R., 1976. Mg, Ca and O^{18}/O^{16} exchange in the sediment-pore water system, Hole 149, DSDP. *Geochim. Cosmochim. Acta,* 40:413–423.

Pickering, K.T., Hiscott, R., and Hein, F.J., 1989. *Deep-marine Environments: Clastic Sedimentation and Tectonics:* London (Unwin Hyman).

Piper, D.J.W., 1978. Turbidite muds and silts on deepsea fans and abyssal plains. *In* Stanley, D.J., and Kelling, G. (Eds.), *Sedimentation in Submarine Canyons, Fans and Trenches:* Stroudsburg, PA (Dowden, Hutchinson and Ross), 163–175.

Pudsey, C.J., and Camerlenghi, A., 1998. Glacial-interglacial deposition on a sediment drift on the Pacific margin of the Antarctic Peninsula. *Antarct. Sci.,* 10:286–308.

Rebesco, M., Camerlenghi, A., and Zanolla, C., in press. Bathymetry and morphogenesis of the continental margin west of the Antarctic Peninsula. *Terra Antarct.*

Rebesco, M., Larter, R.D., Barker, P.F., Camerlenghi, A., and Vanneste, L.E., 1997. The history of sedimentation on the continental rise west of the Antarctic Peninsula. *In* Barker, P.F., and Cooper, A.K. (Eds.), *Geology and Seismic Stratigraphy of the Antarctic Margin* (Pt. 2). Am. Geophys. Union Antarct. Res. Ser. 71:29–49.

Rebesco, M., Larter, R.D., Camerlenghi, A., and Barker, P.F., 1996. Giant sediment drifts on the continental rise of the Antarctic Peninsula. *Geo-Mar. Lett.,* 16:65–75.

Schrader, H.-J., 1976. Cenozoic planktonic diatom biostratigraphy of the Southern Pacific Ocean. *In* Hollister, C.D., Craddock, C., et al., *Init. Repts. DSDP,* 35: Washington (U.S. Govt. Printing Office), 605–671.

Schuffert, J.D., Jahnke, R.A., Kastner, M., Leather, J., Sturz, A., and Wing, M.R., 1994. Rates of formation of modern phosphorite off western Mexico. *Geochim. Cosmochim. Acta,* 58:5001–5010.

Stow, D.A.V., Amano, K., Balson, P.S., Brass, G.W., Corrigan, J., Raman, C. V., Tiercelin, J.-J., Townsend, M., and Wijayananda, N.P., 1990. Sediment facies and processes on the Distal Bengal Fan, Leg 116. *In* Cochran, J.R., Stow, D.A.V., et al., *Proc. ODP, Sci. Results,* 116: College Station, TX (Ocean Drilling Program), 377–396.

Stow, D.A.V., and Piper, D.J.W., 1984. Deep-water fine-grained sediments: facies models. *In* Stow, D.A.V., and Piper, D.J.W. (Eds.), *Fine-Grained Sediments: Deep-Water Processes and Facies*. Geol. Soc. Spec. Publ. London, 15:611–645.

Stow, D.A.V., and Townsend, M.R., 1990. X-ray techniques and observations on distal Bengal Fan sediments cored during Leg 116. *In* Cochran, J.R., Stow, D.A.V., et al., *Proc. ODP, Sci. Results,* 116: College Station, TX (Ocean Drilling Program), 5–14.

Thomson, M.R.A., Crame, J.A., and Thomson, J.W. (Eds.), 1991. *Geological Evolution of Antarctica:* Cambridge, U.K. (Cambridge Univ. Press).

von Breymann, M.T., Emeis, K.-C., and Camerlenghi, A., 1990. Geochemistry of sediments from the Peru upwelling area: results from Sites 680, 682, 685, and 688. *In* Suess, E., von Huene, R., Emeis, K.-C., et al., *Proc. ODP, Sci. Results,* 112: College Station, TX (Ocean Drilling Program), 491–503.

Yanagisawa, Y., and Akiba, F., 1990. Taxonomy and phylogeny of three marine diatom genera, *Crucidenticula, Denticulopsis,* and *Neodenticula*. *Chishitsu Chosasho Geppo* [*Bull. Geol. Surv. Jpn.*], 41:197–301.

Figure F1. A. Bathymetric map (from Rebesco et al., in press) and the main morphologic elements of Drifts 6 and 7 and the adjacent continental slope. Thin lines indicate the location of site-survey multichannel seismic (MCS) reflection profiles. The box around Site 1095 refers to Figure **F1B,** p. 44. (Continued on next page.)

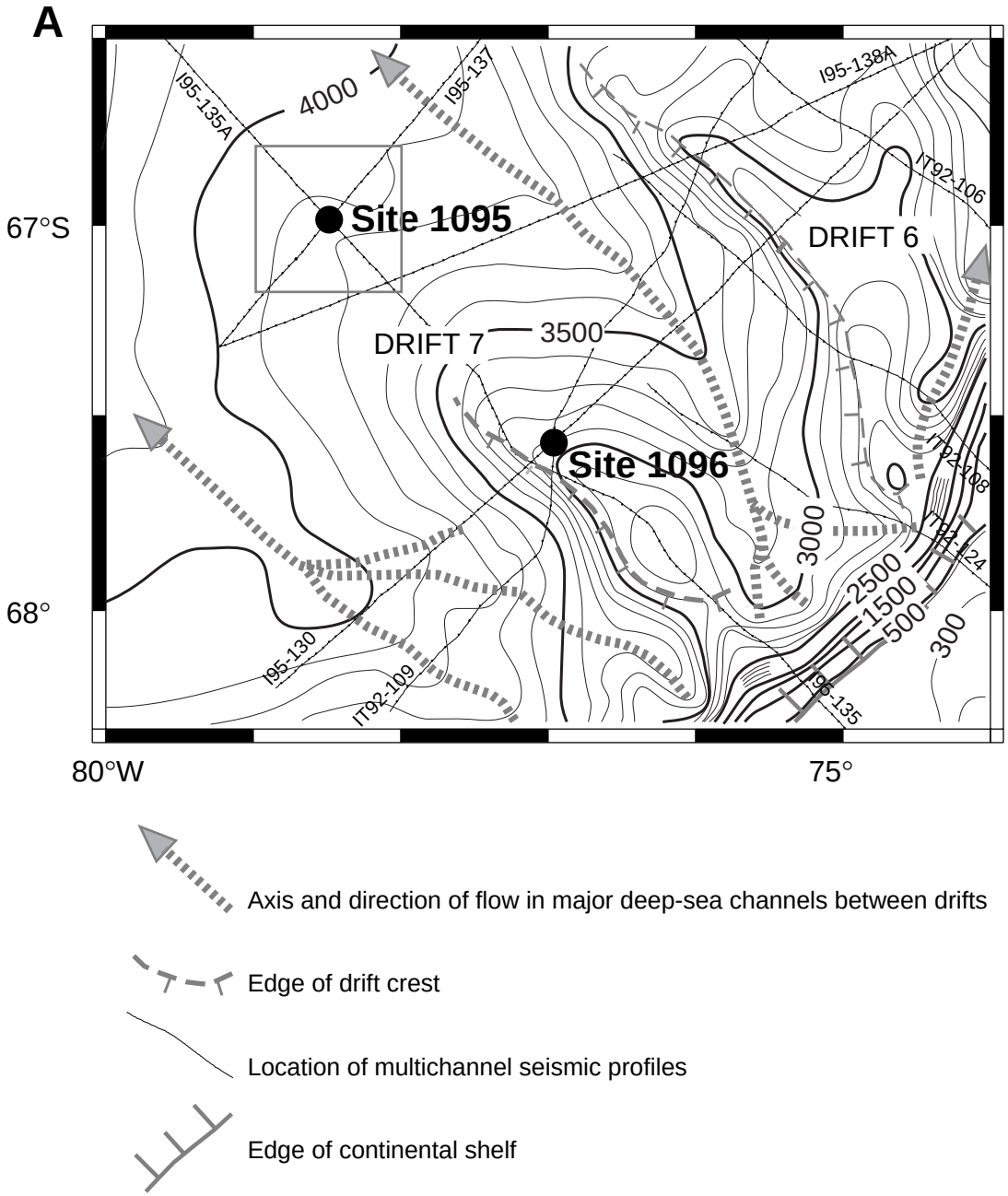

Figure F1 (continued). B. Location of Site 1095 on two crossing MCS reflection profiles (I95-135A and I95-137) and the 3.5-kHz profiles (bold lines) acquired with the *JOIDES Resolution* to locate the site and during transit toward Site 1096.

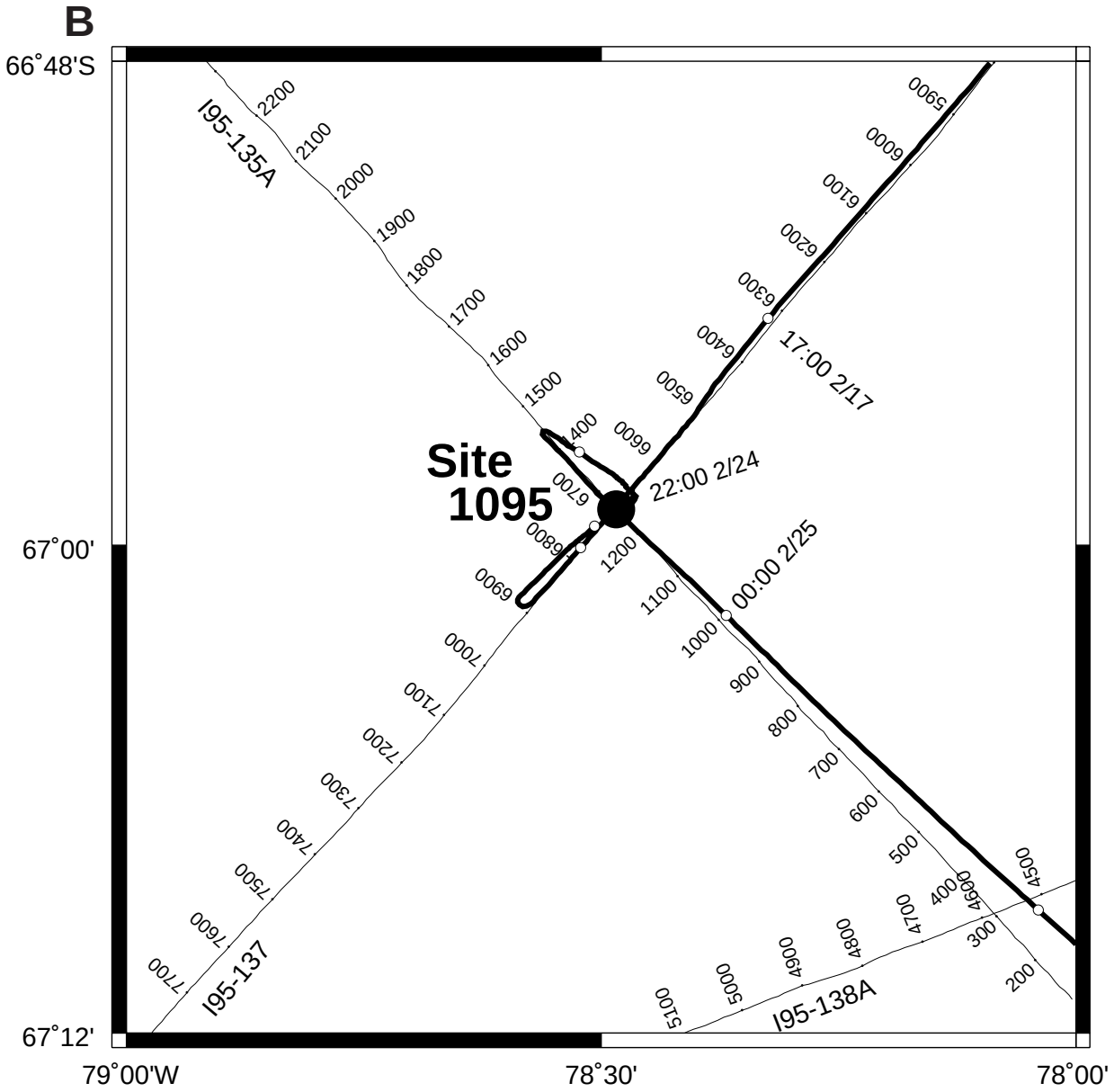

Figure F2. Part of MCS reflection profile I95-137 across Site 1095.

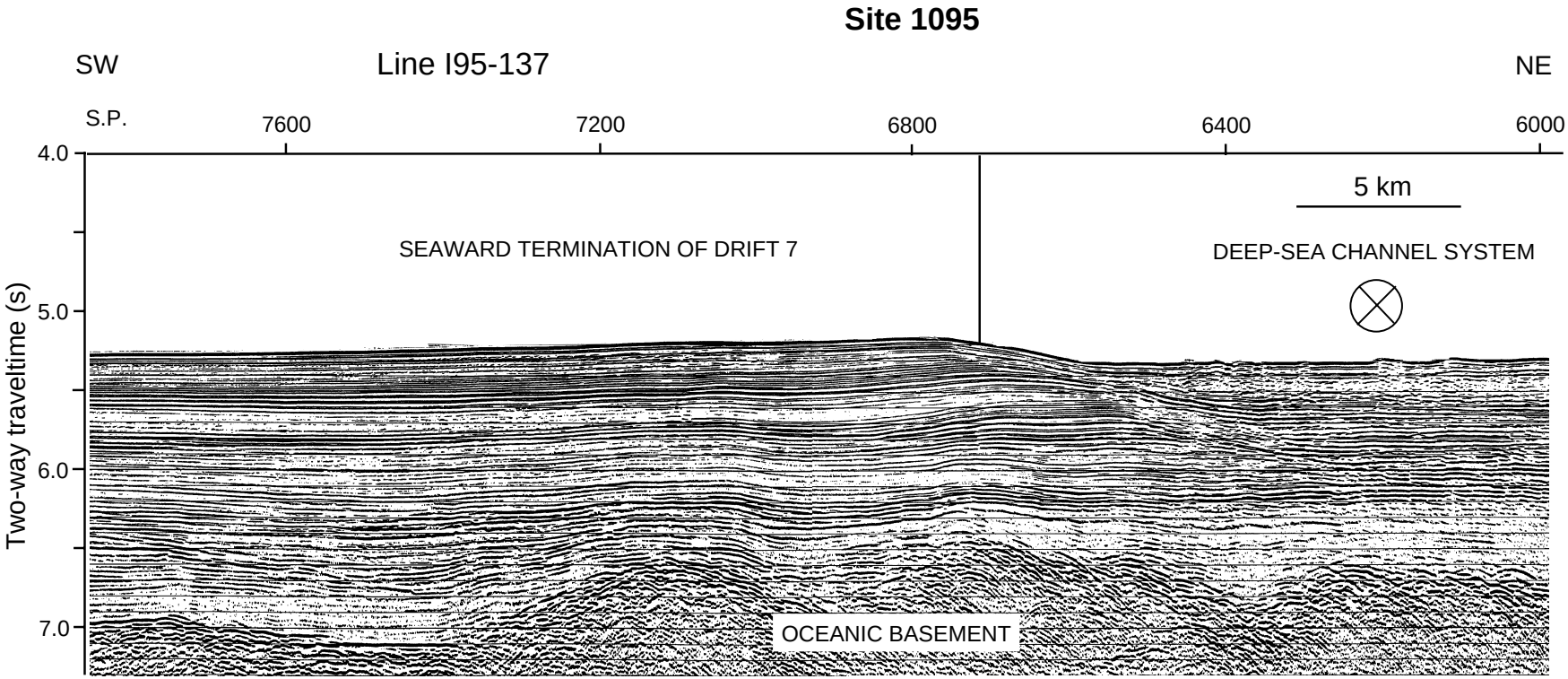

Figure F3. The 3.5-kHz sub-bottom profile across Site 1095 (located in Fig. F1B, p. 44), acquired during site approach. Bedding in the upper 20 m is parallel to the seafloor. The site is located on the gentle northwest flank of Drift 7.

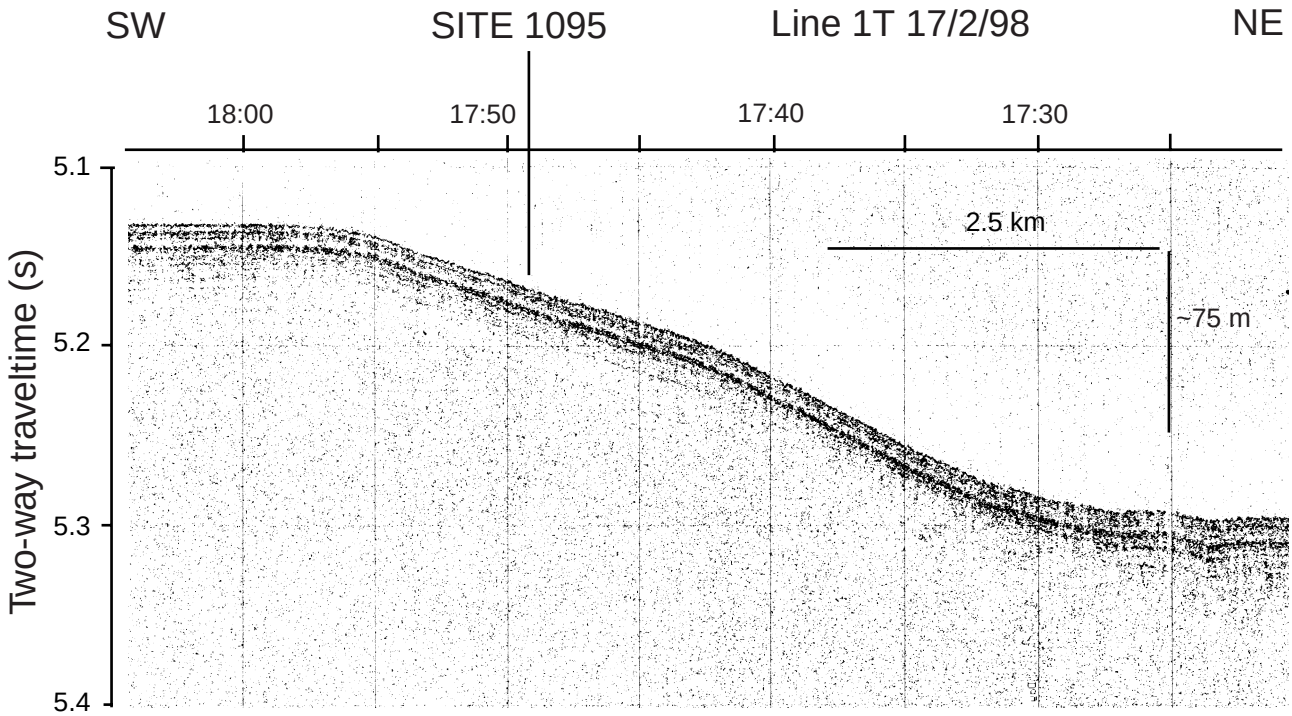

Figure F4. Simplified schematic lithostratigraphy of Site 1095 showing dominant lithology, intensity of bioturbation, and distribution of turbidite Facies L_1, L_2, and L_3 (see Figs. **F10, F11, F12**). Arrows show broad trends in frequency of sand and silt laminations and facies types, which are attributed to long-term "first-order" cycles in Unit II (see Fig. **F5,** p. 49). Shorter term, "second-order" cycles, interpreted as glacial–interglacial, are defined top and bottom by intensely bioturbated intervals. These climatically driven cycles are superimposed on the long-term cycles. Well-developed glacial–interglacial cycles of Unit I are highlighted in Figure **F6,** p. 50. See interpretation and discussion in the text. (Continued on next page.)

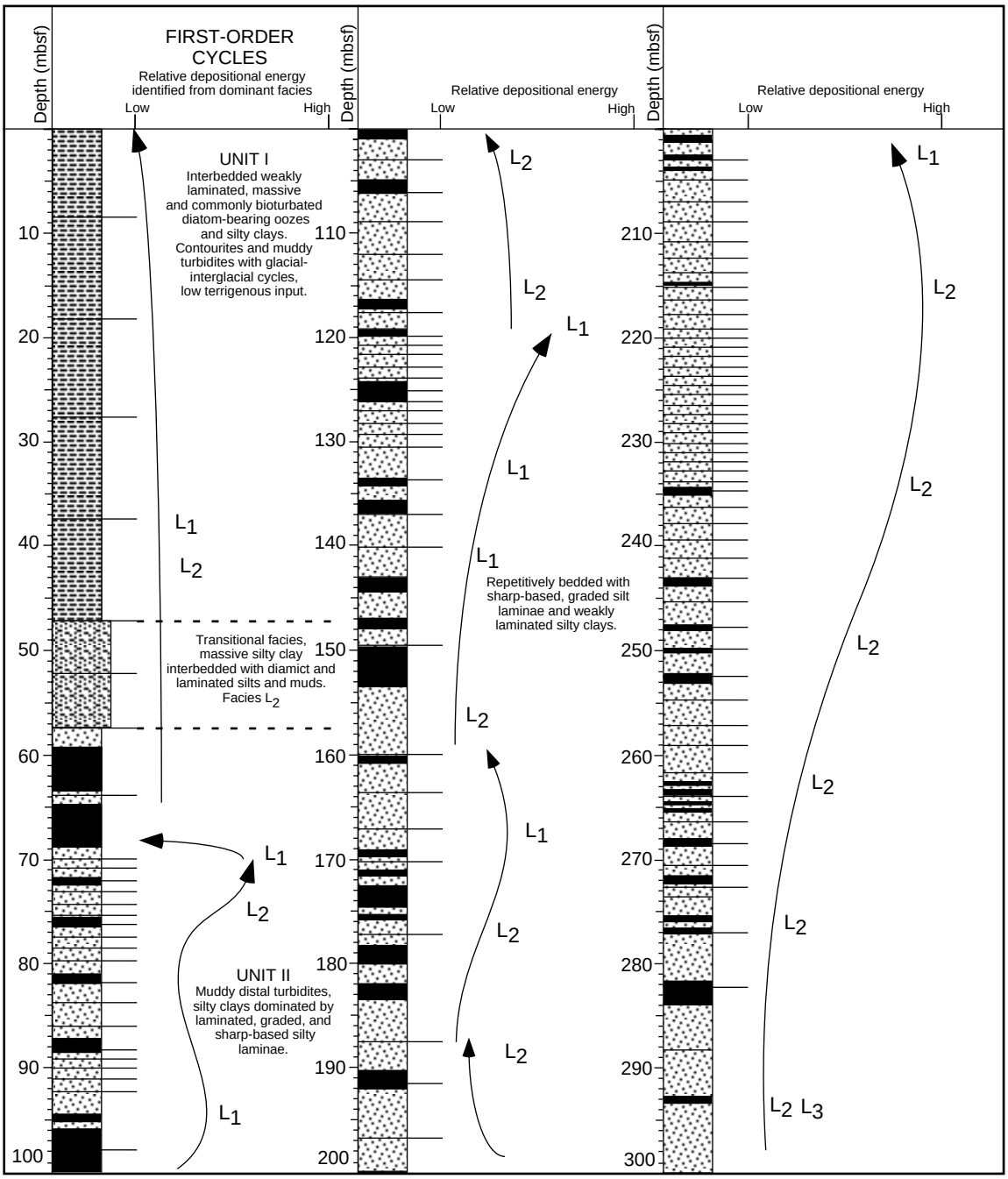

Figure F4 (continued).

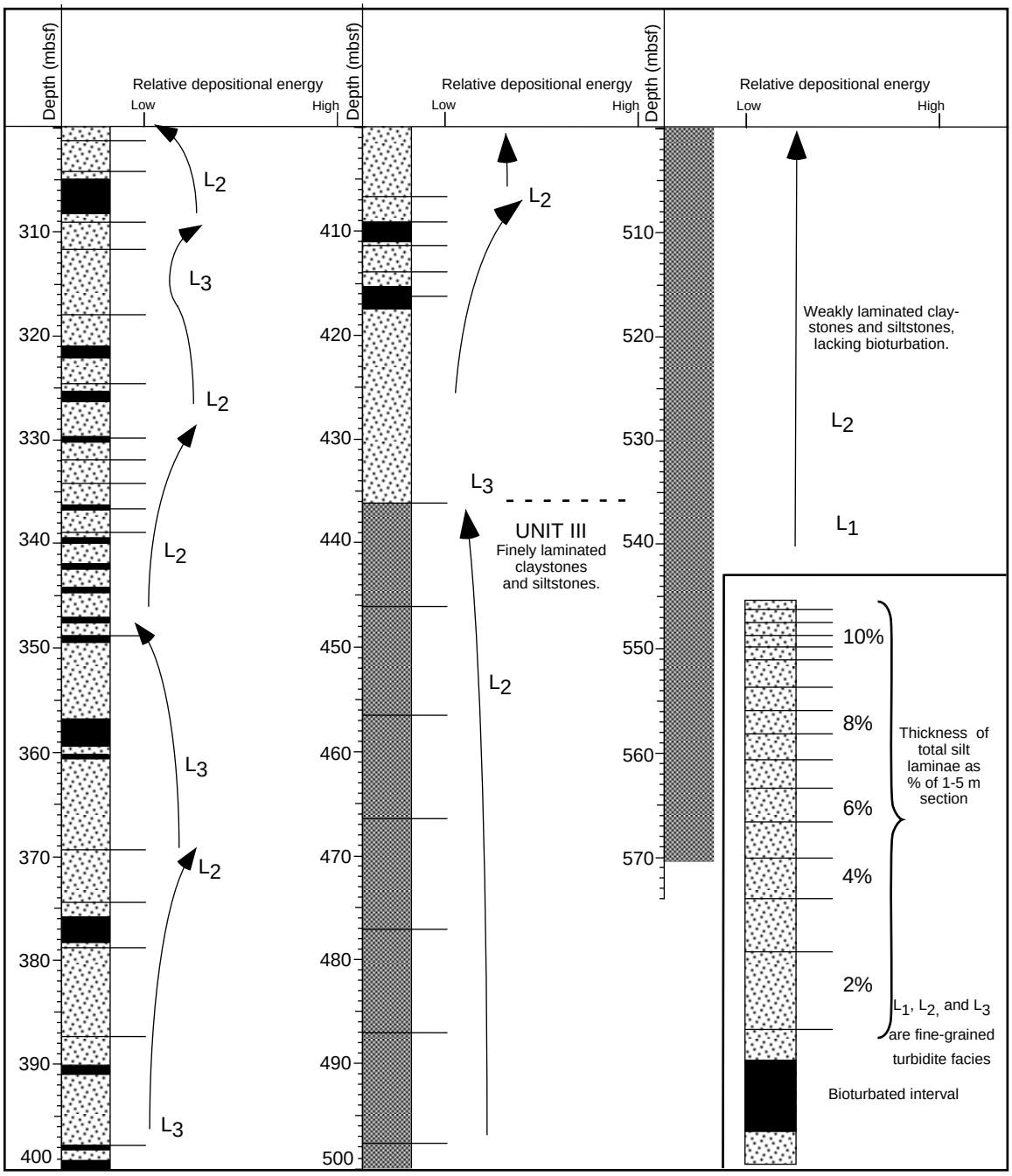

Figure F5. Comparison of downhole sedimentological data from smear slides for Site 1095. Data points (joined by lines in the three left-hand columns) are unevenly spaced: in the second column, both a straight line and a spline curve were used to join points. Linear sedimentation rate derived from paleomagnetic data. First-order cycles identified in Unit II are derived from frequency of occurrence and type of the different turbidite facies identified in Figure **F4**, p. 47.

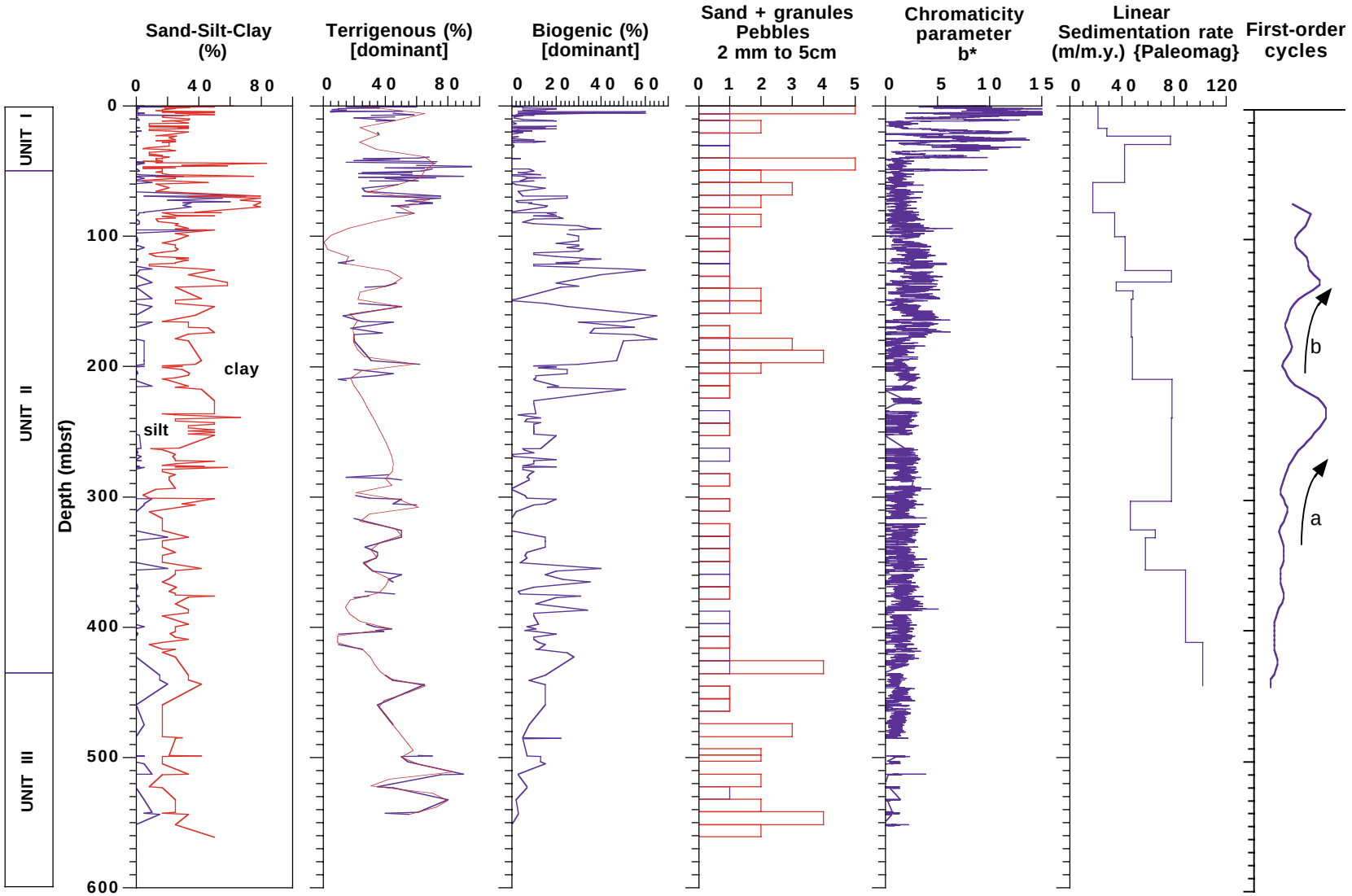

Figure F6. Alternation of diatomaceous facies and terrigenous facies, showing a general relationship to chromaticity parameters a* and b* and to magnetic susceptibility in Subunit IA. Lithologic column is drawn from Hole 1095D; note good correlation with Hole 1095A. IRD = ice-rafted debris.

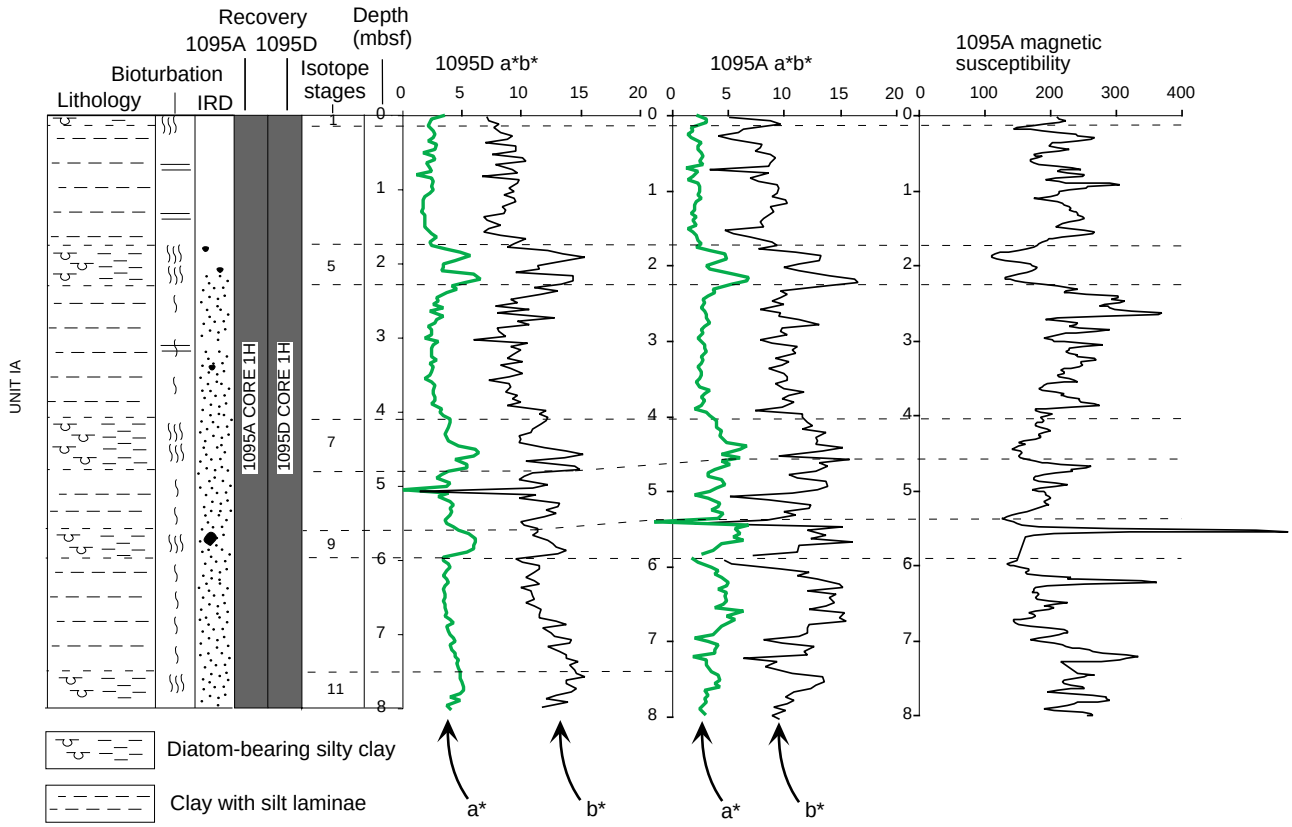

Figure F7. Alternation of silty clay with scattered sand grains, and clay with silt laminae in Subunit IB. There is not a consistent relationship with chromaticity parameters a* and b*. Note the marked decrease in color variability downcore near the base of Subunit IB.

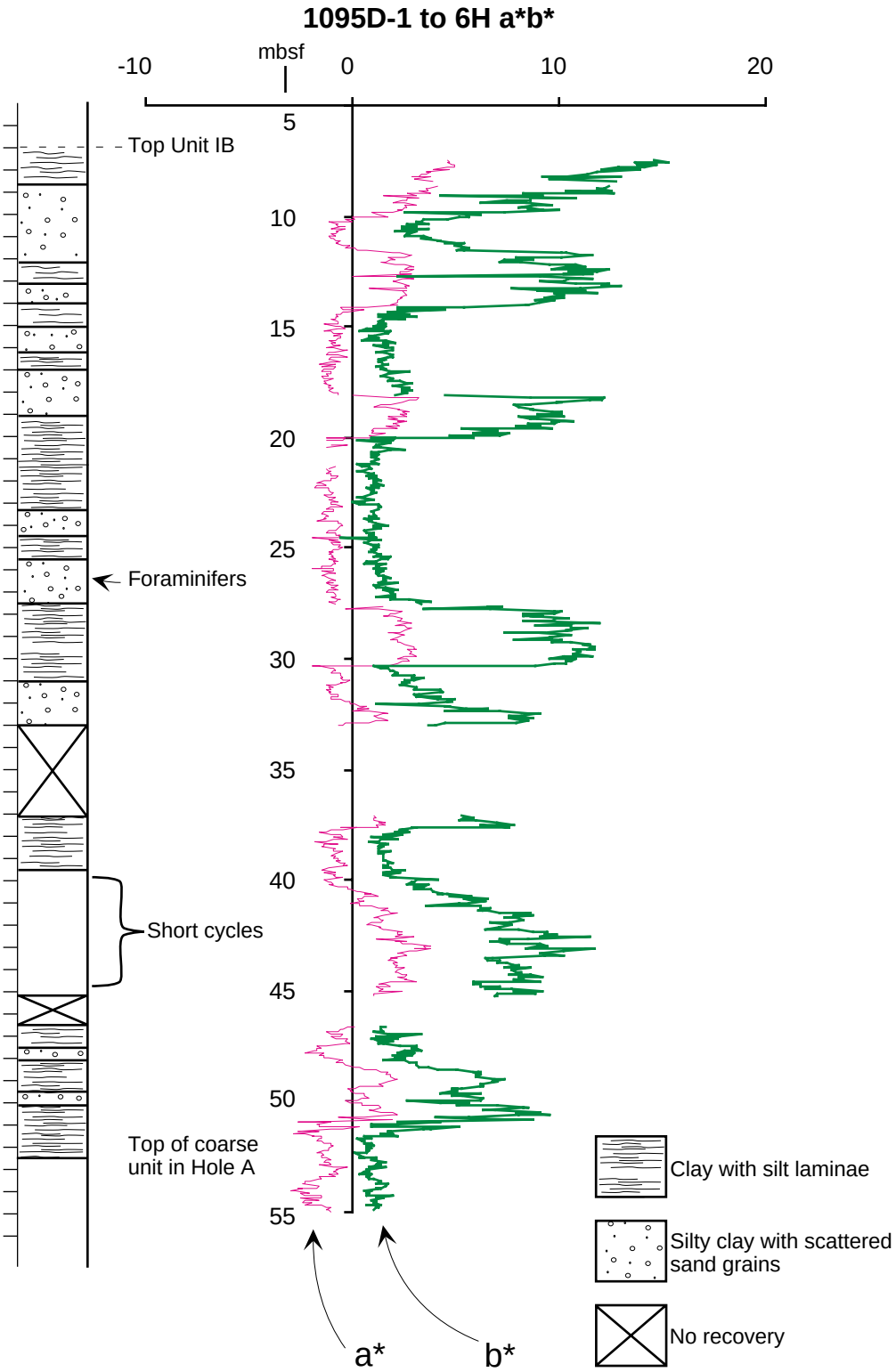

Figure F8. Burrow-mottled silty clay with dispersed sand grains and foraminifers. Interval 178-1095A-5H-1, 78–102 cm.

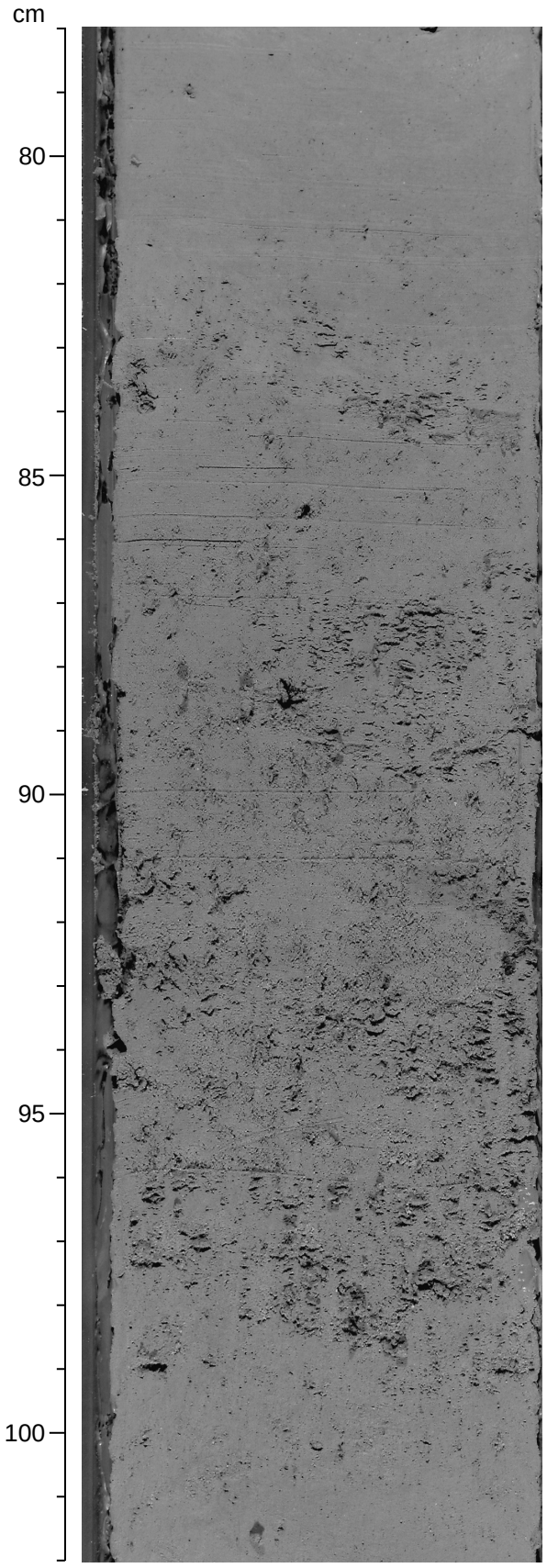

Figure F9. Clay with silt laminae 1–8 mm thick. Silt laminae have sharp bases and are weakly graded. Microfaults disrupt the laminae at 43 and 51–55 cm. These facies are interpreted as muddy turbidites (interval 178-1095A-5H-5, 40–60 cm) (cf. Figs. **F10,** p. 54, **F11,** p. 57).

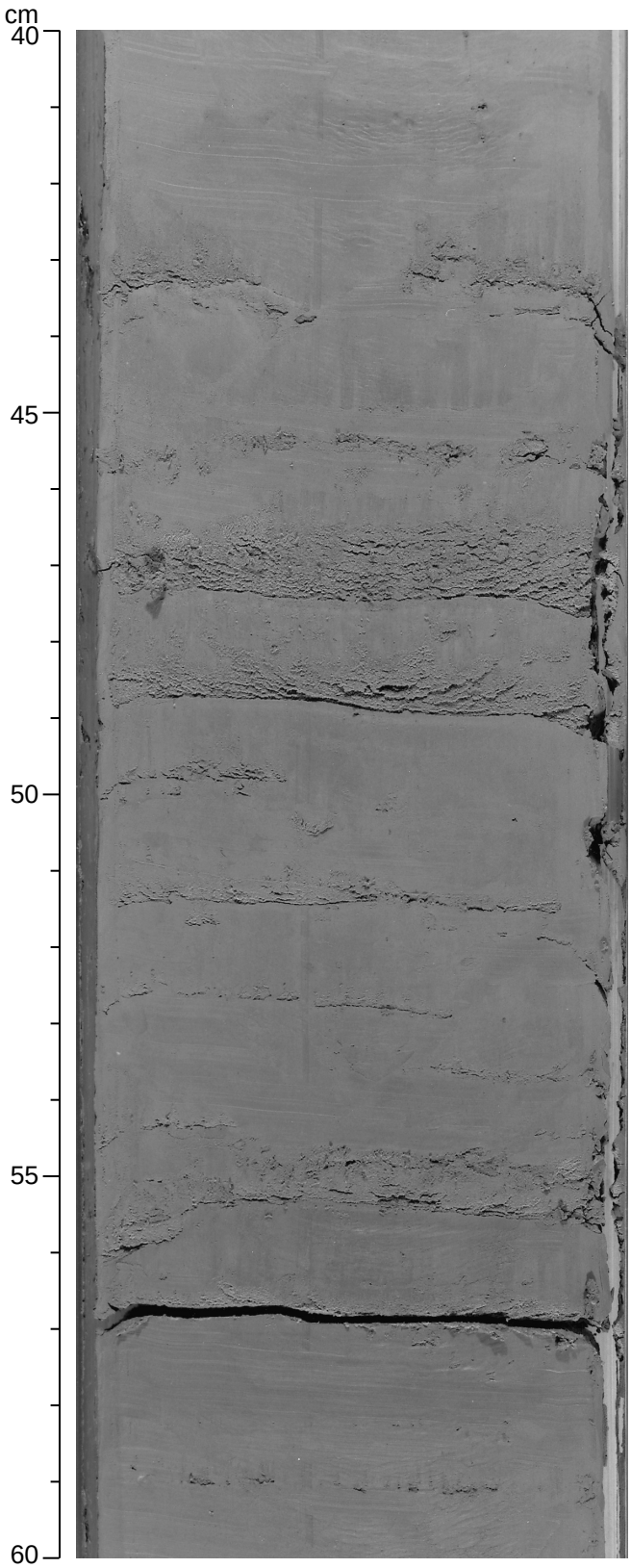

Figure F10. Representative photographs of lithofacies in Unit II. See Figure F11, p. 57, for facies types. **A.** Facies L_1 (interval 178-1095B-1H-5, 33–57 cm). **B.** Facies L_2 with fault (interval 178-1095B-3H-3, 15–40 cm). (Continued on next two pages.)

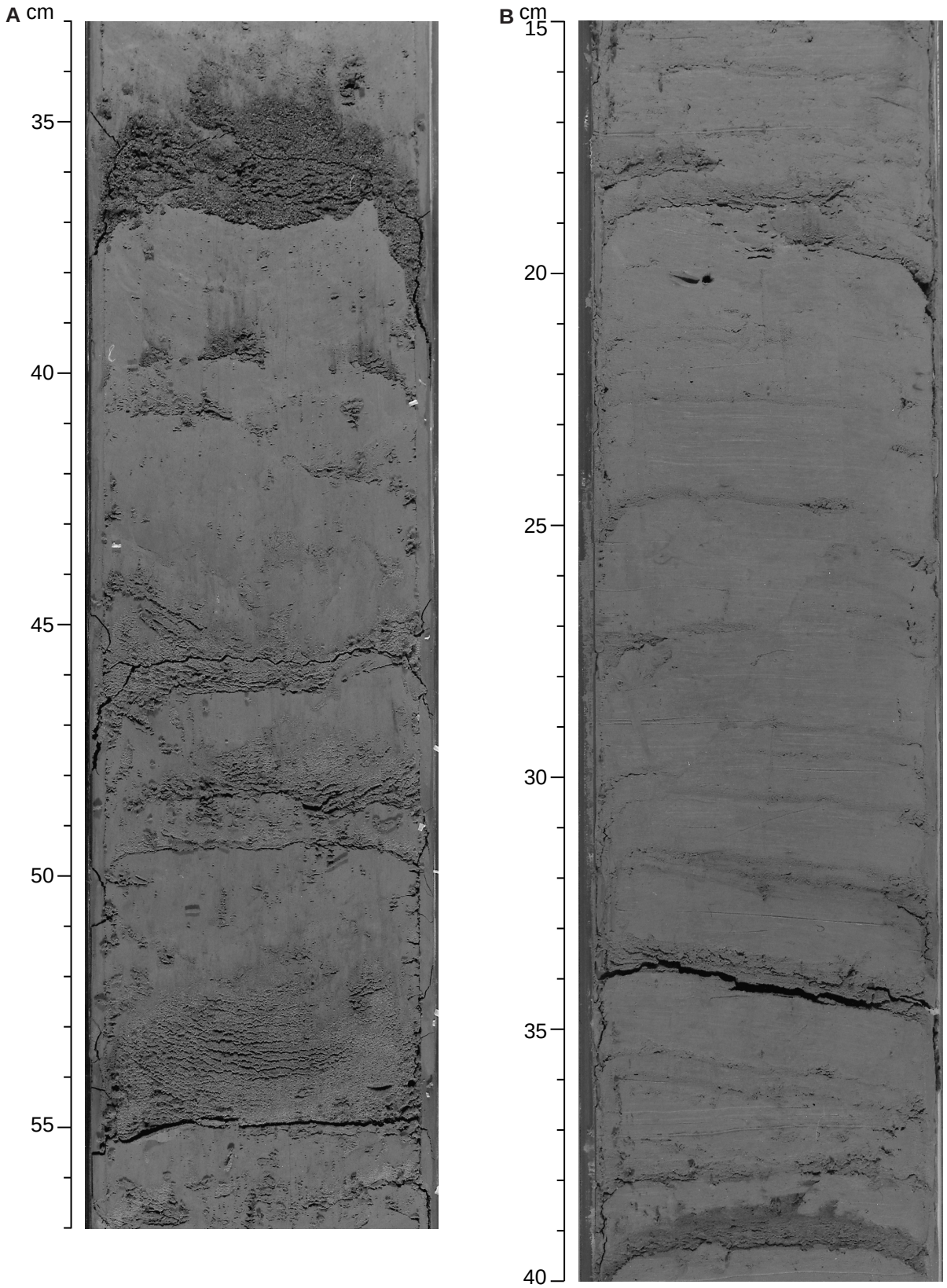

Figure F10 (continued). **C.** Facies L_1 (interval 178-1095B-4H-2, 6–26 cm). **D.** Facies M (interval 178-1095B-7H-6, 58–88 cm).

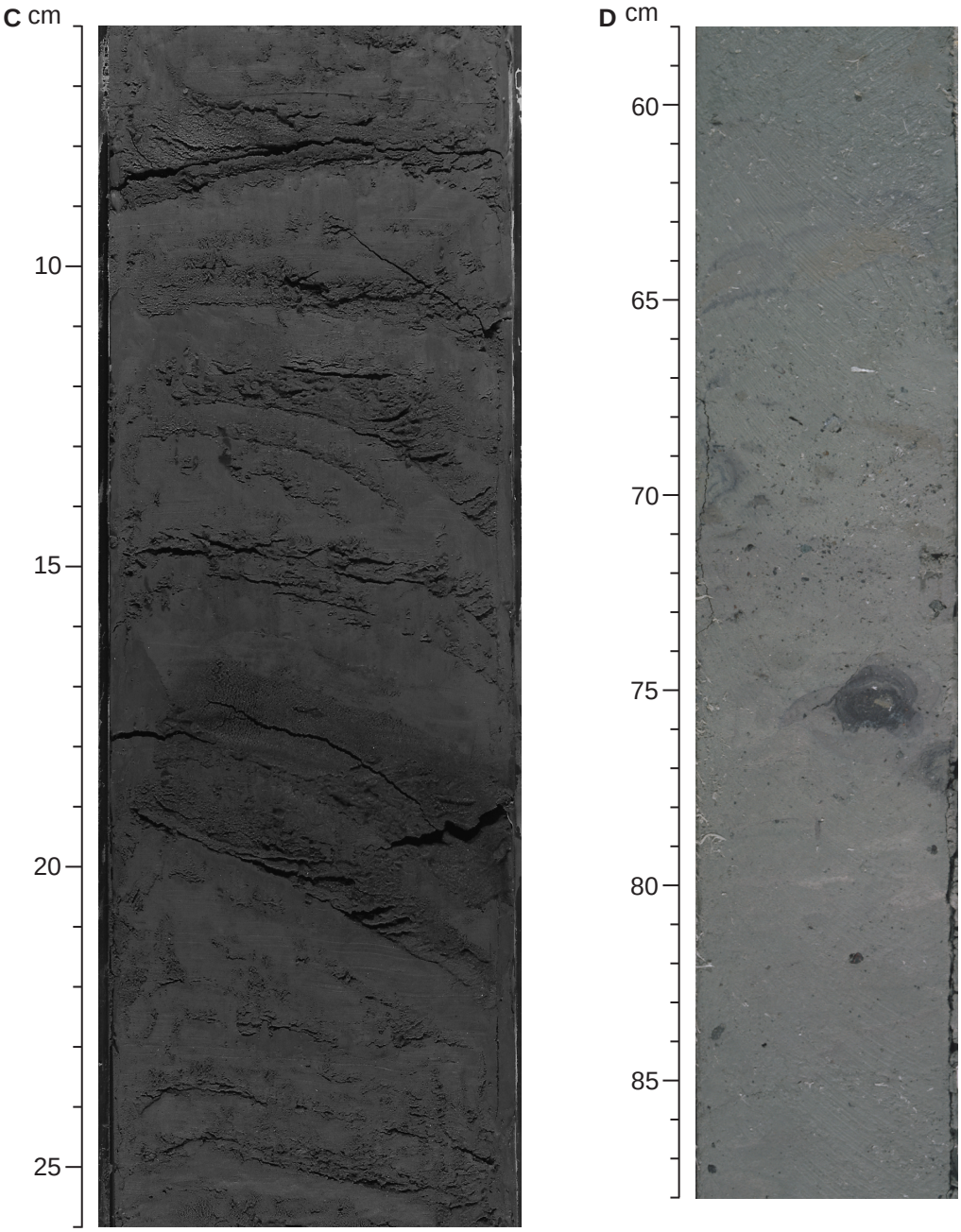

Figure F10 (continued). E. Contact between Facies L_1 and M, second-order cycle boundary (interval 178-1095B-10H-4, 28–48 cm). **F.** Facies L_3 (interval 178-1095B-25X-5, 90–115 cm).

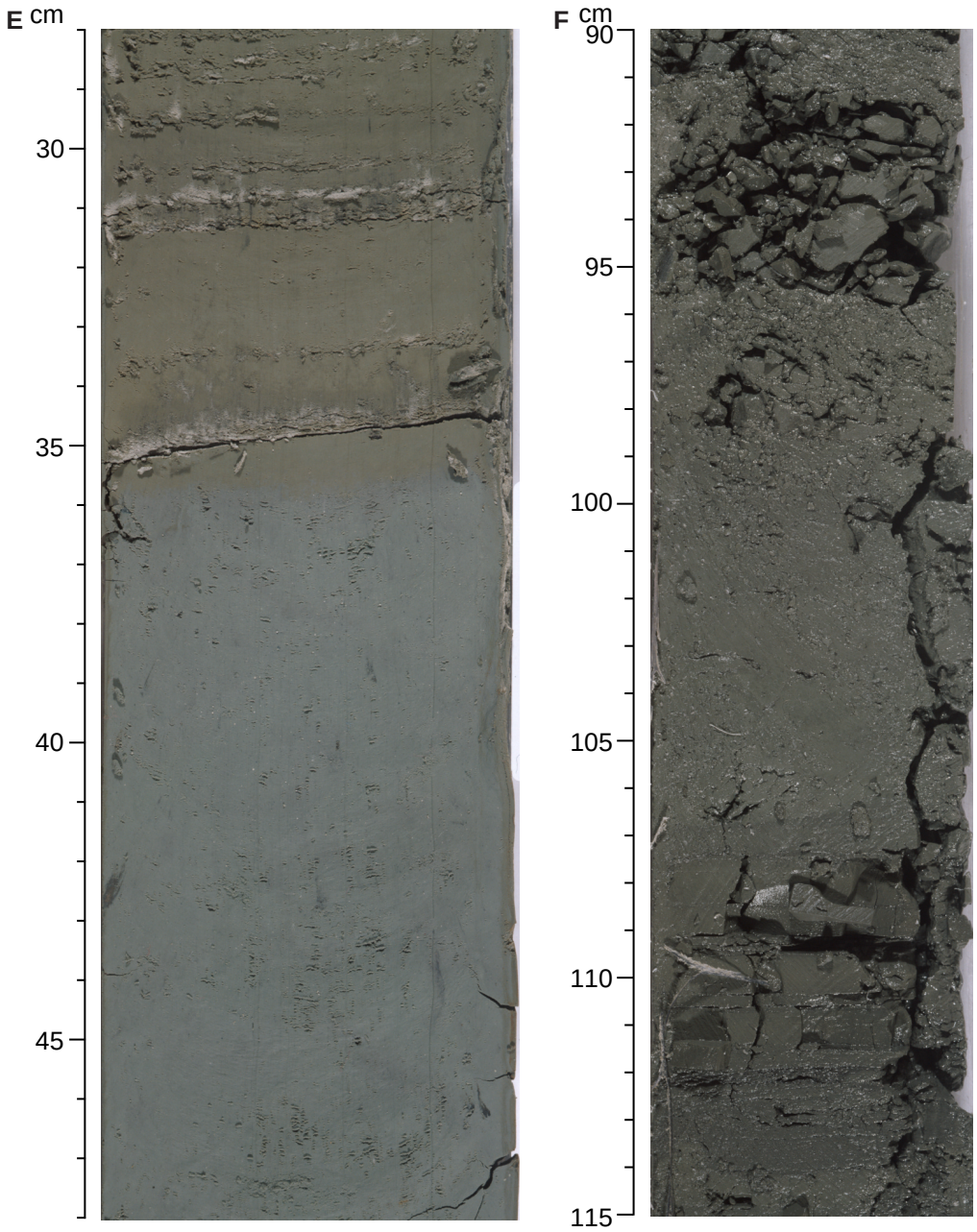

Figure F11. Schematic representation of internal structure of Facies L_1–L_3 recognized at Site 1095 compared with Piper's (1978) descriptive scheme for muddy turbidites. These facies form a downslope and across-slope continuum in fine-grained turbidity currents (see Fig. **F13,** p. 61). Facies L_3 represents the most fine-grained type of muddy turbidite at Site 1095, which corresponds to the most distal fine-grained component of turbidity flows (see Fig. **F13,** p. 61). All three facies may pass upward into hemipelagic muds (hemipelagic division; H). Intensity of bioturbation, amount of ice-rafted debris, and thickness of hemipelagic division at bed tops depends on the recurrence interval of turbidity currents.

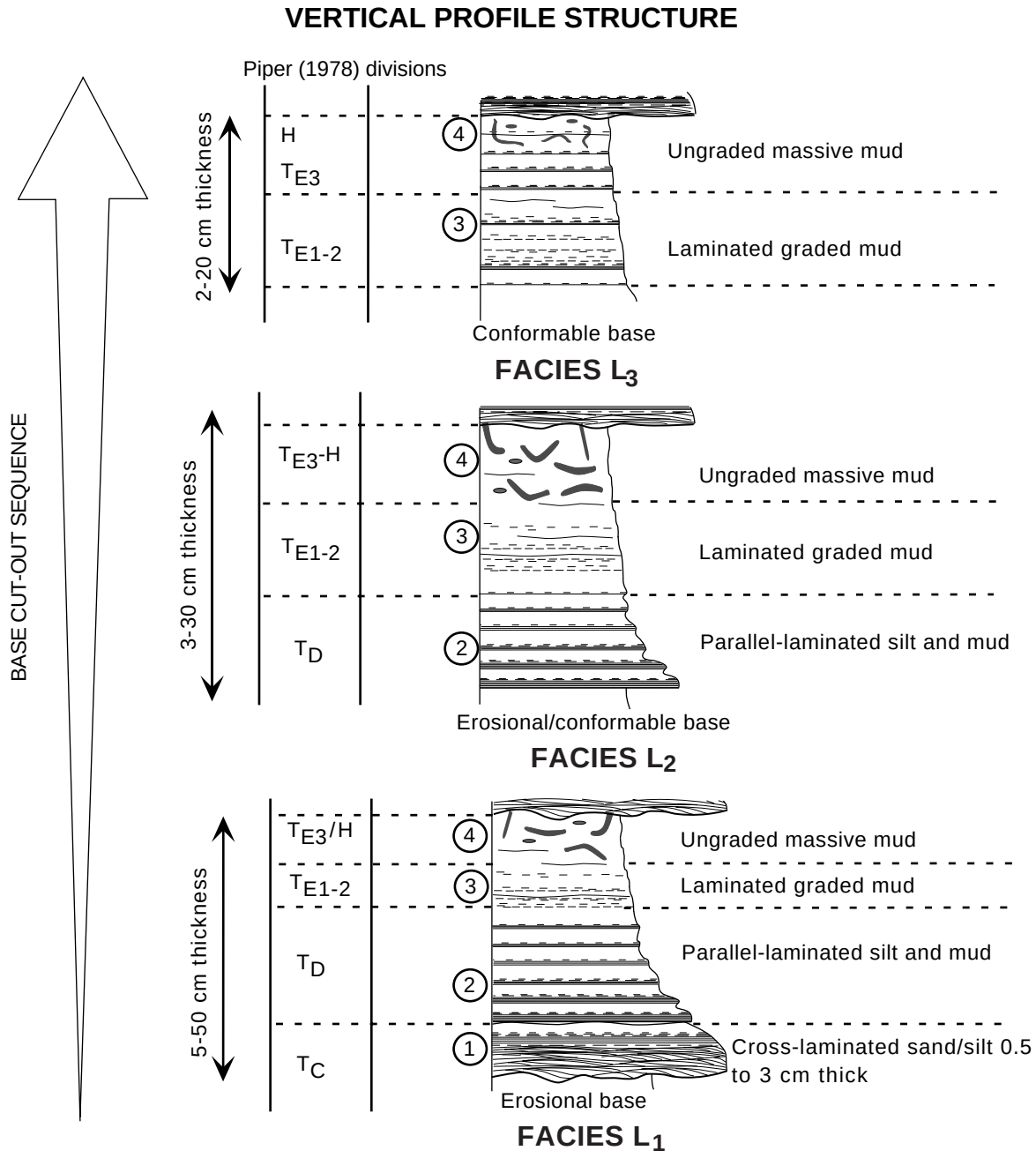

Figure F12. Lithofacies types in Unit III. See Figure F11, p. 57, for detailed facies descriptions. **A.** Facies L_1 and L_2 (interval 178-1095B-43X-2, 67–90 cm). (Continued on next two pages.)

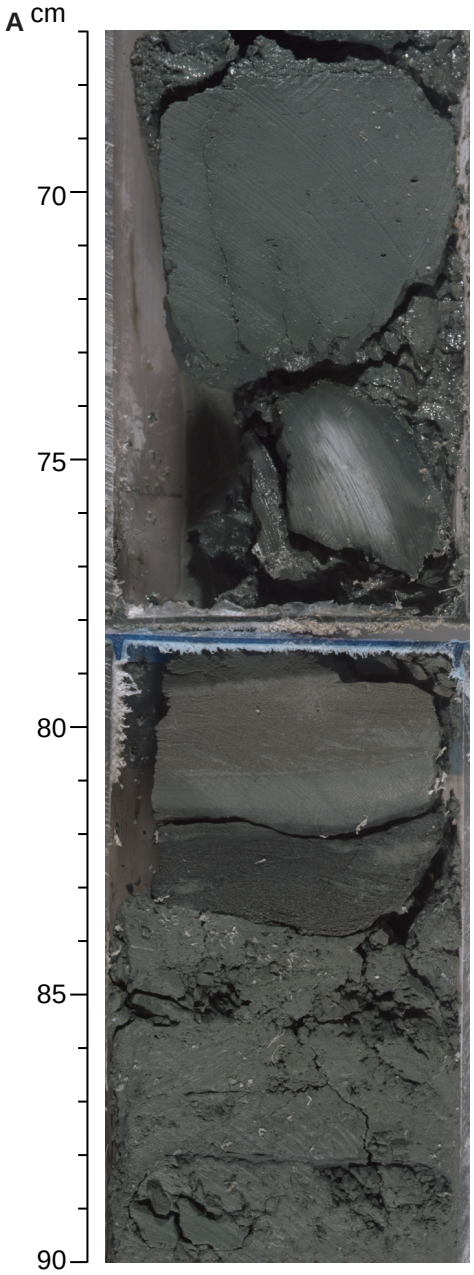

Figure F12 (continued). B. Burrowed facies (interval 178-1095B-39X-1, 50–55 cm). **C.** Facies L_2 (interval 178-1095B-51X-1, 60–80 cm).

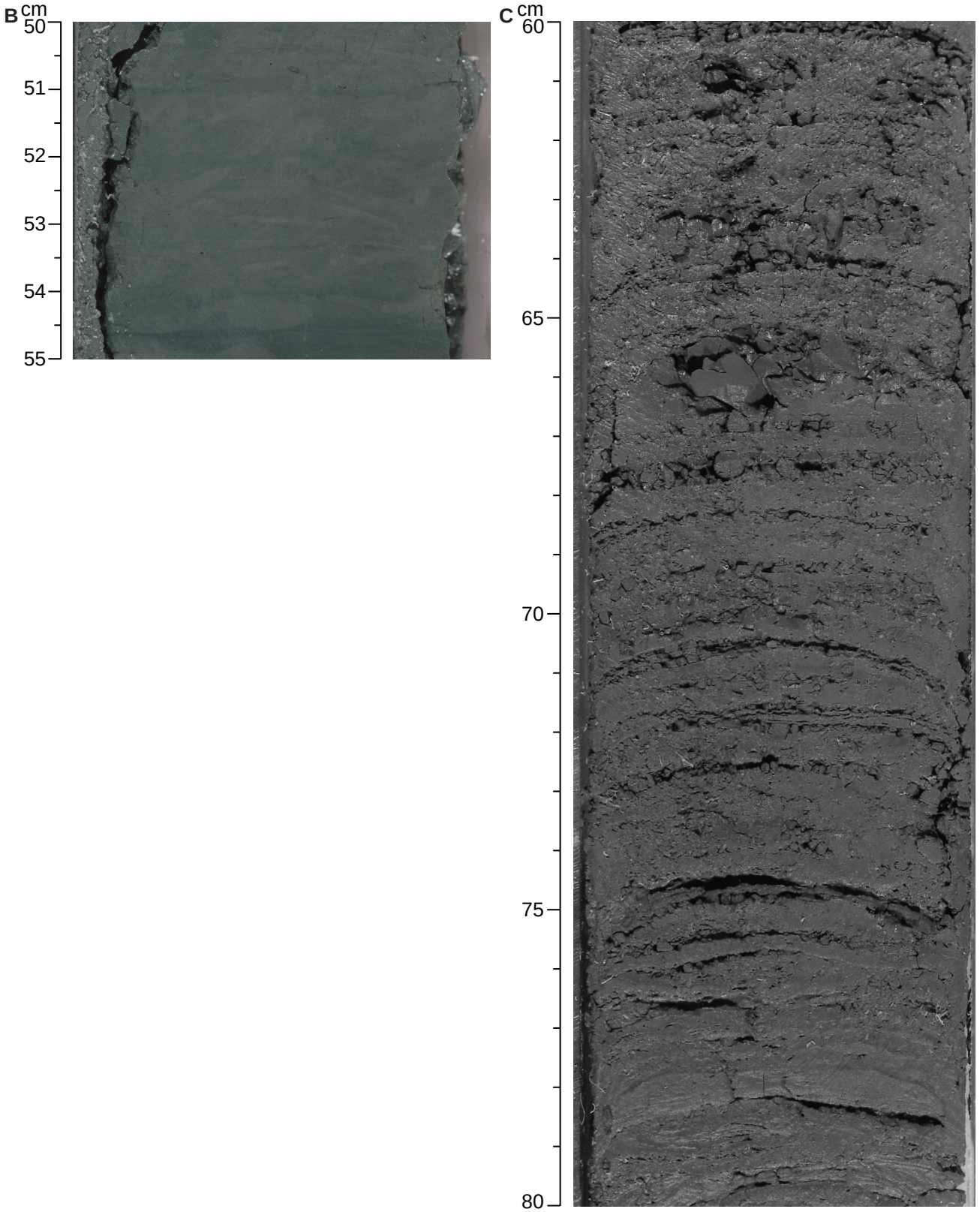

Figure F12 (continued). D. Facies L_3 with ice-rafted debris (interval 178-1095B-51X-1, 0–25 cm). **E.** Facies L_3 with ice-rafted debris (interval 178-1095B-52X-1, 40–60 cm).

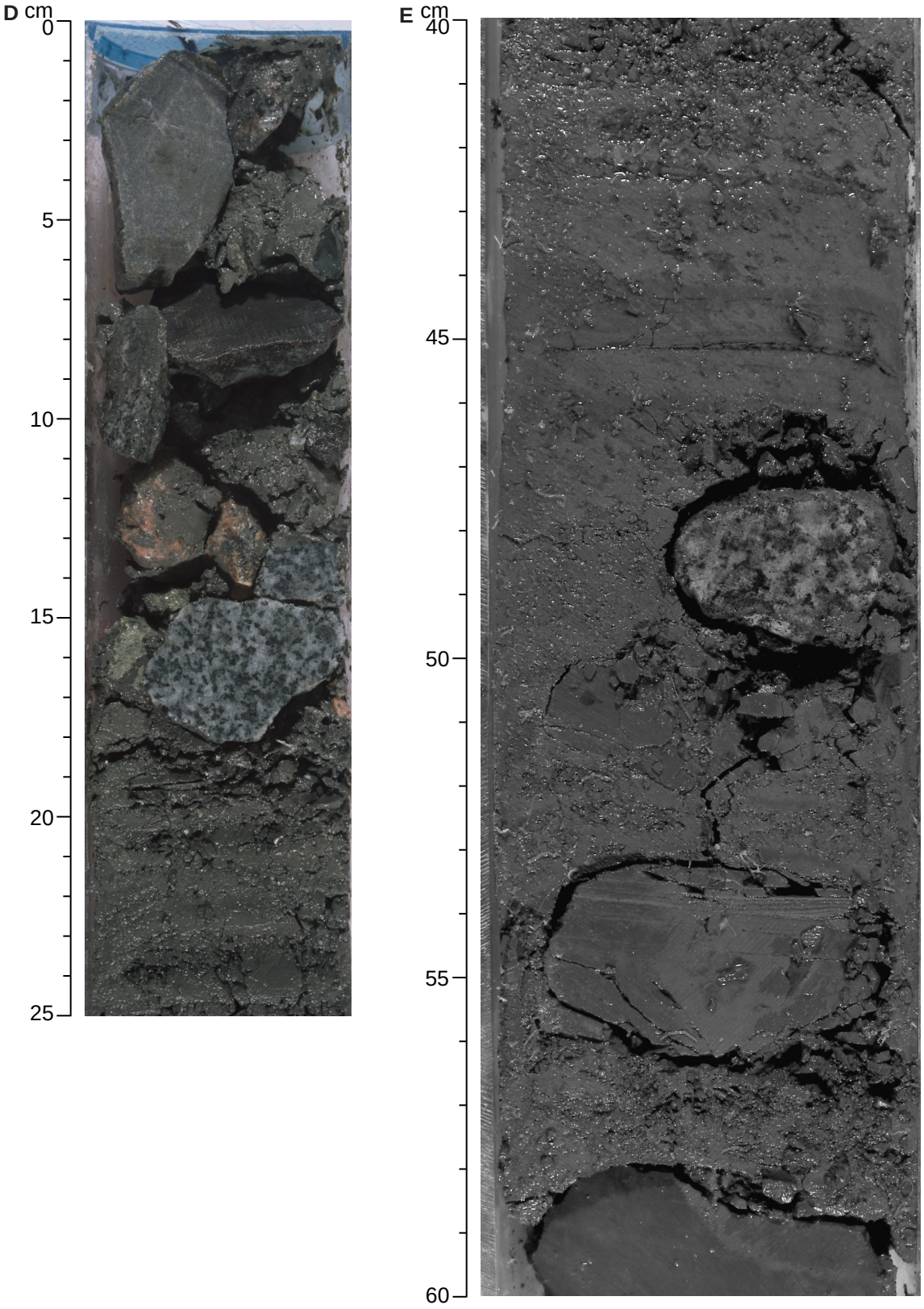

Figure F13. Schematic representation of a distal turbidite depositional setting showing the downslope and across-slope distribution of turbidite facies (L_1, L_2, and L_3) recognized at Site 1095. This setting occurs marginal to main feeder channels on the lower basinal portions of submarine fan and slopes.

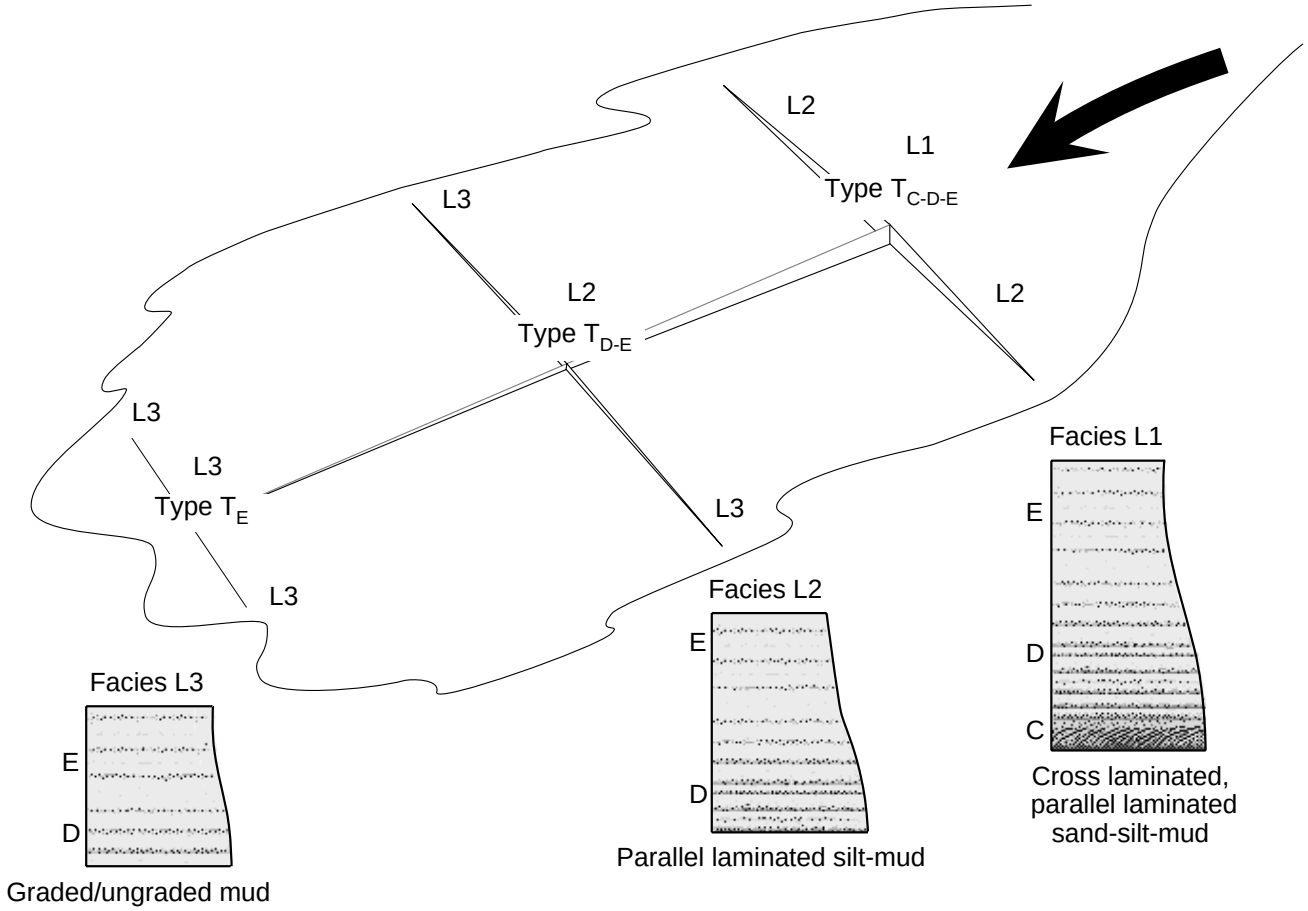

Figure F14. A summary of the occurrence of diatoms, radiolarians, and planktonic foraminifers at Site 1095. Solid boundary lines carry more confidence than dashed boundary lines. Stippled intervals are barren of microfossils.

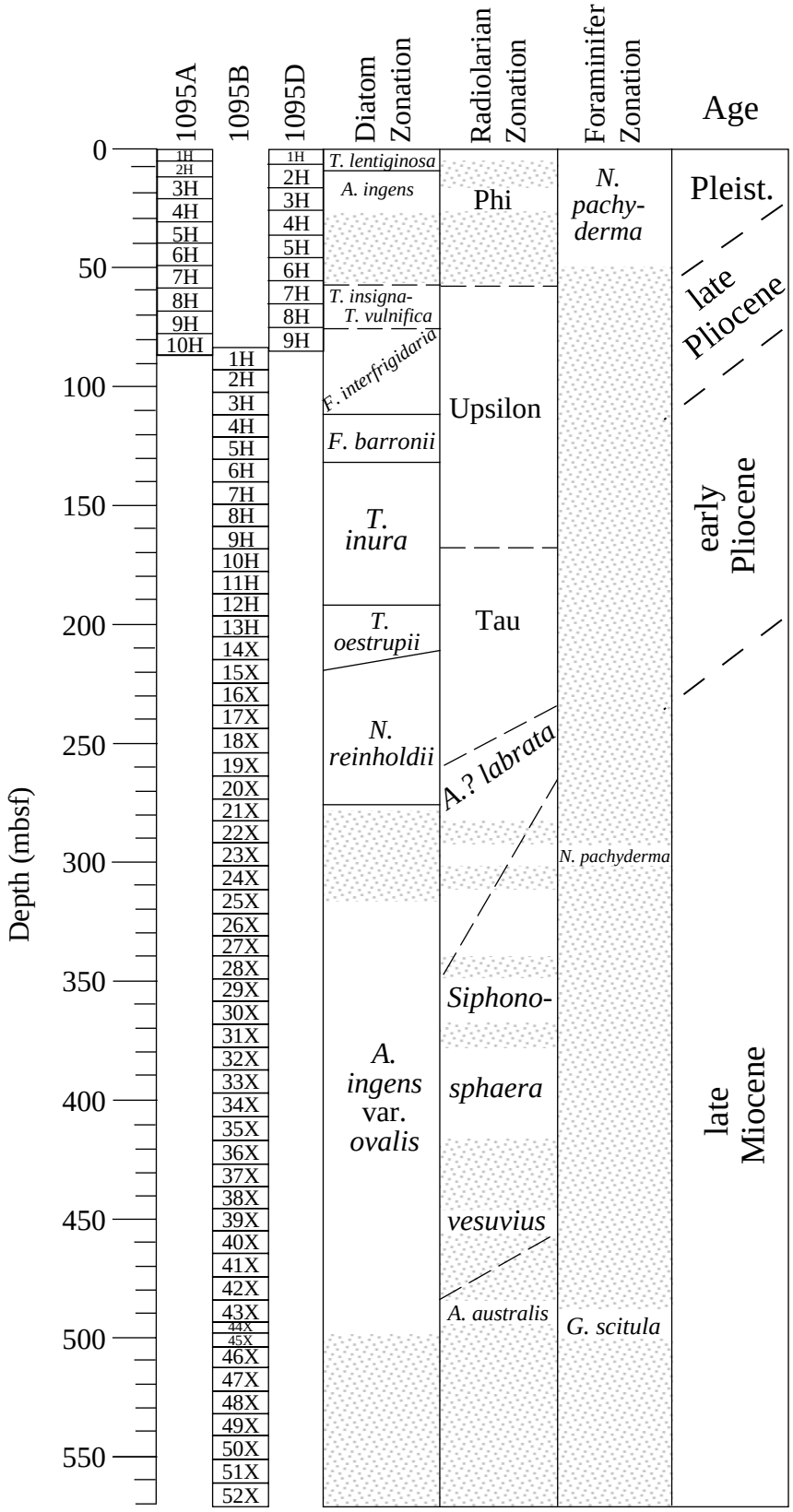

Figure F15. Sedimentation rates based on radiolarian occurrences, Site 1095. Areas enclosed by boxes = age-depth where species in a given zone were observed. Remaining, unboxed shaded areas = range of possible ages for a given depth; diagonal lines = barren intervals, solid line = sedimentation rate based on paleomagnetic data measured directly from the cores, dotted line = logging magnetic data.

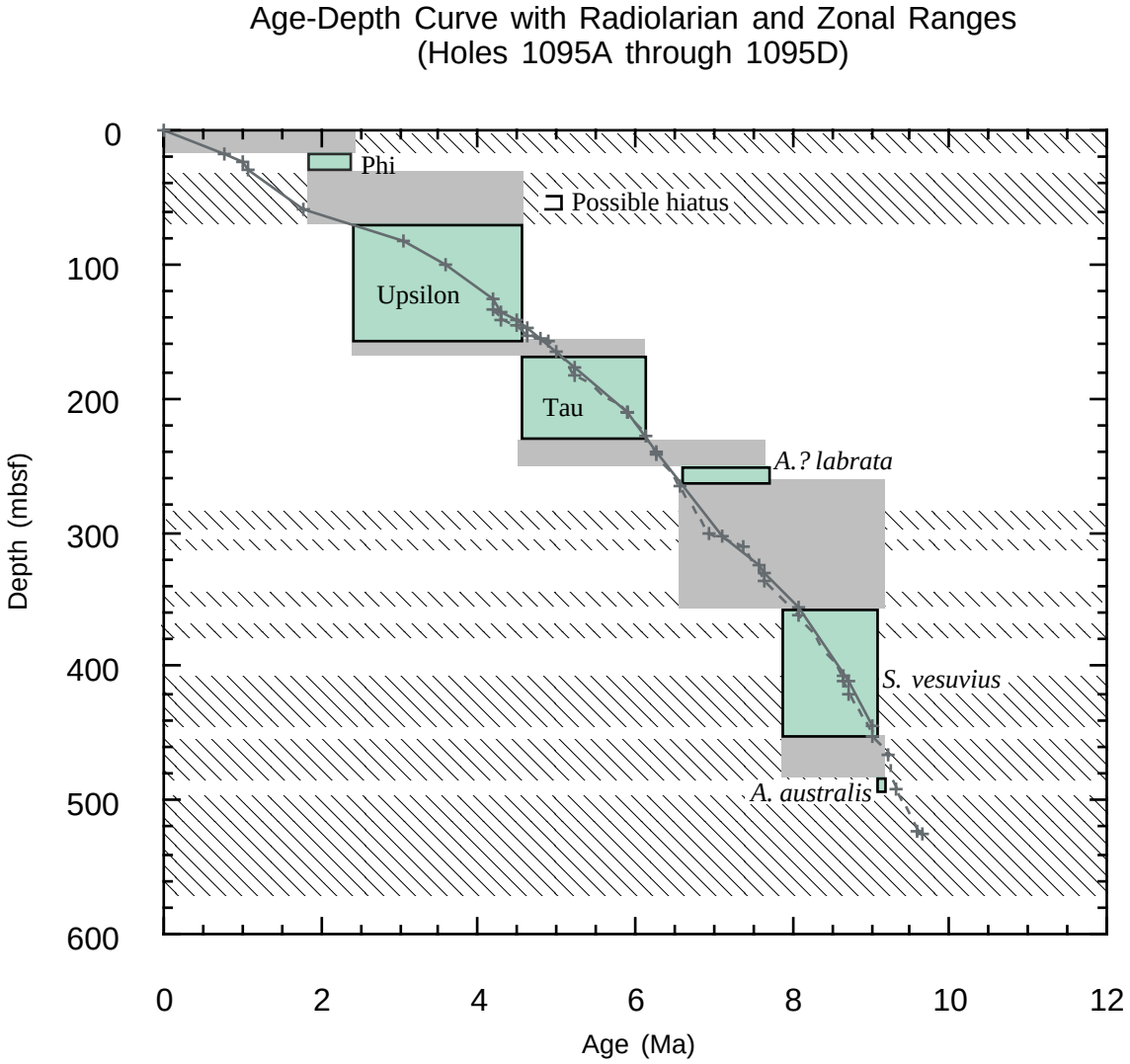

Figure F16. A. Inclinations from Holes 1095A and 1095B at the 0-mT (NRM) and 30-mT demagnetization step. The overprint is steeply inclined downward, mimicking a reversed polarity in the NRM. **B.** Declinations from Holes 1095A and 1095B after 30-mT demagnetization. Although these cores are not oriented, there is a strong bias toward zero declination, which suggests a radial component to the remaining overprint.

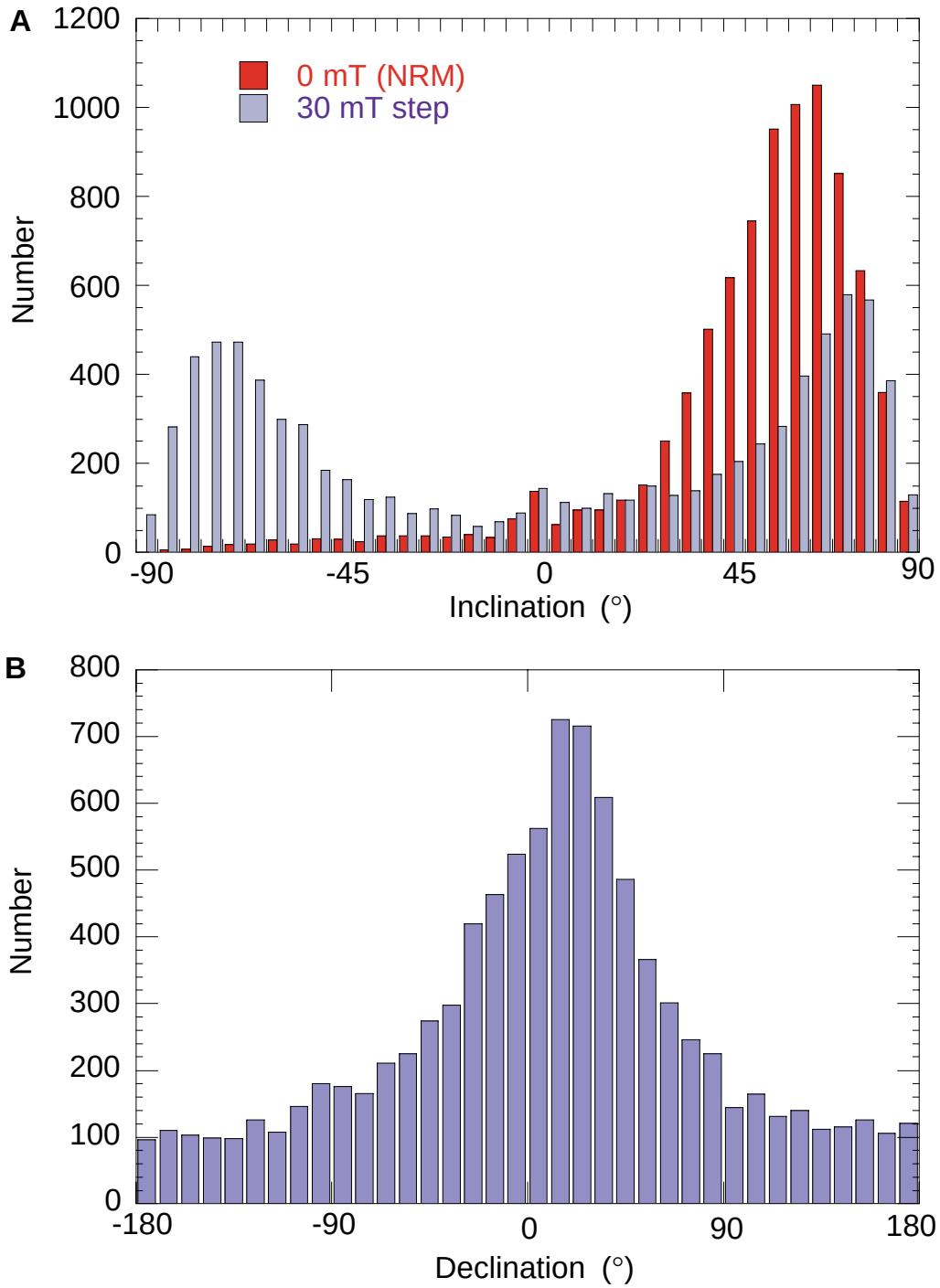

Figure F17. A. Orthogonal projection of the end-points of the remanence vector for Sample 178-1095A-8H-4, 71 cm (64.01 mbsf). Open and solid symbols represent the vertical and horizontal projection, respectively. The steeply inclined drill-string overprint has been removed at the 10-mT demagnetization step. **B.** Change in the intensity of remanence, normalized to the 0-mT (NRM) intensity, during AF demagnetization. The mean destructive field (MDF) is 32 mT. **C.** Equal-area projection of the remanence vector during AF demagnetization. DEC = declination, INC = inclination.

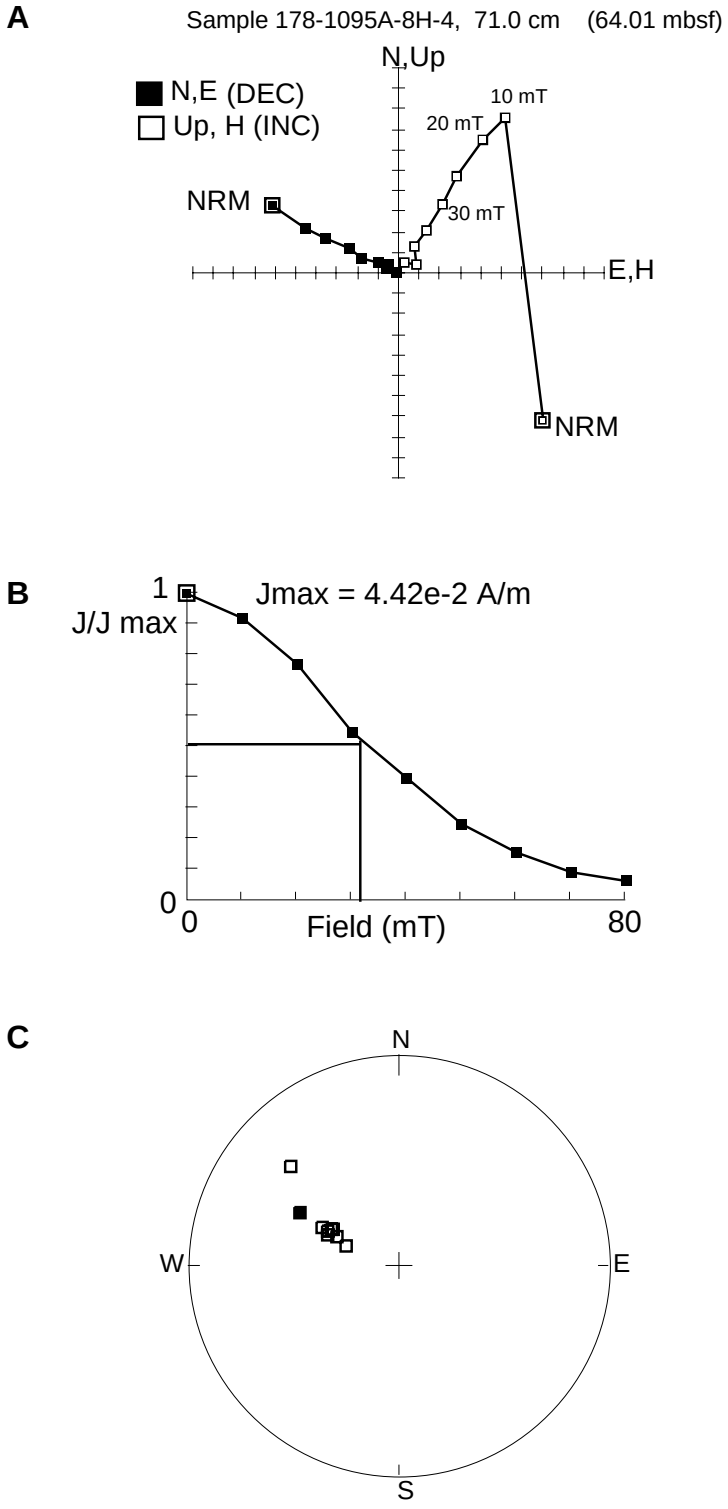

Figure F18. A. Vector end-point diagram showing the removal of the drill-string overprint at the 10-mT step for Sample 178-1095B-4H-4, 71 cm (166.71 mbsf). **B.** Enlarged view of the boxed region from A. A second component with a reversed polarity magnetization is removed between 10 and 50 mT. We interpret this as the primary remanence and construe the remaining normal polarity component as a probably more recent overprint. **C.** Change in the intensity of remanence during AF demagnetization. **D.** Equal-area projection of the remanence vector during AF demagnetization. DEC = declination, INC = inclination.

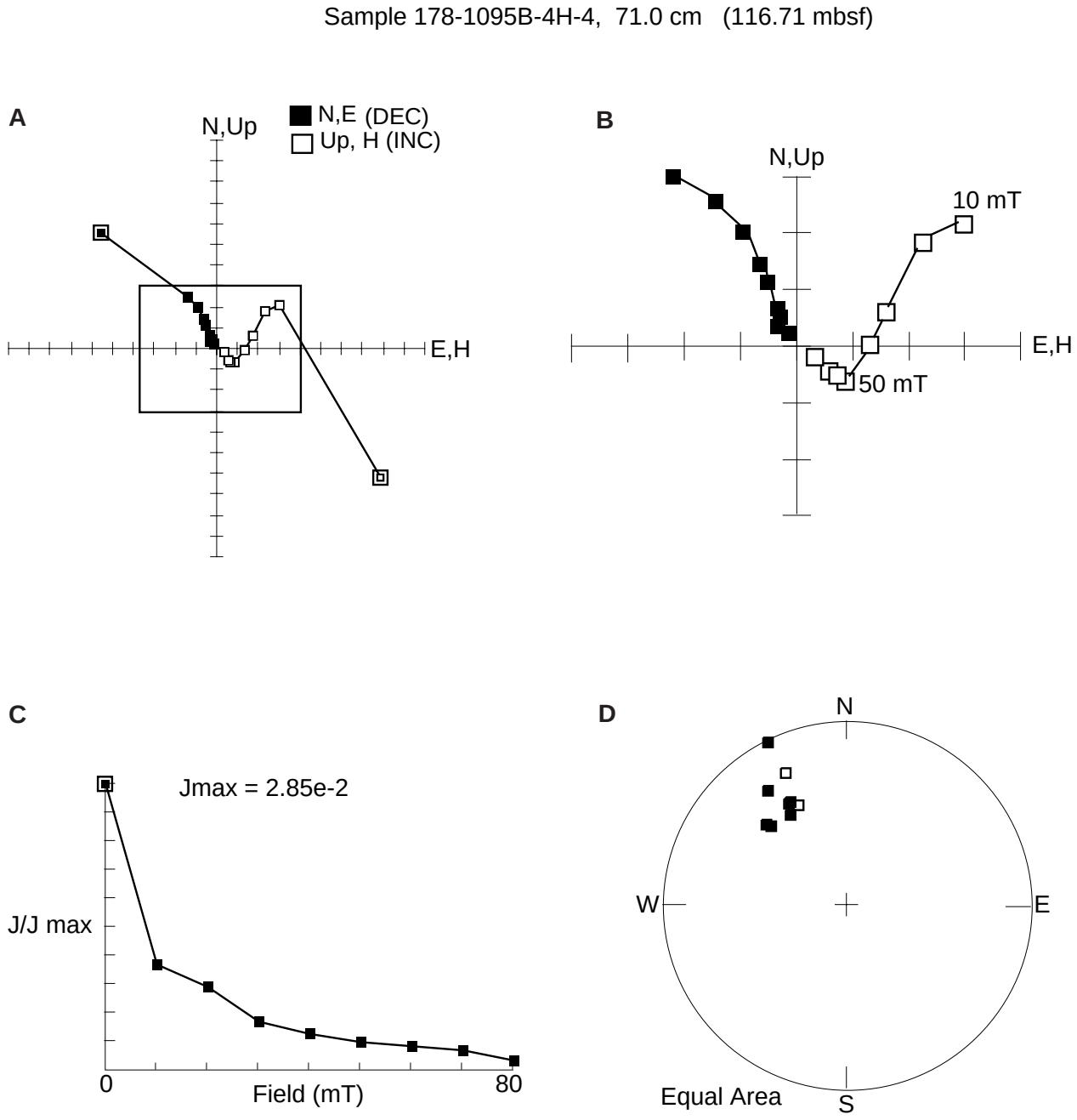

Figure F19. A. Inclinations measured on archive halves (solid line) and discrete samples (open boxes). **B.** Interpreted magnetostratigraphy (see legend in Fig. F20, p. 68). **C.** Maximum angular deviation angles for discrete subsamples. **D.** Vector length for discrete subsamples from PCA, where the vector length is the distance from the origin (zero magnetization) to the center of magnetization (analogous to the center of mass) for the measurements used to compute the PCA best-fit vector. This is a measure of the intensity of the best-fit vector.

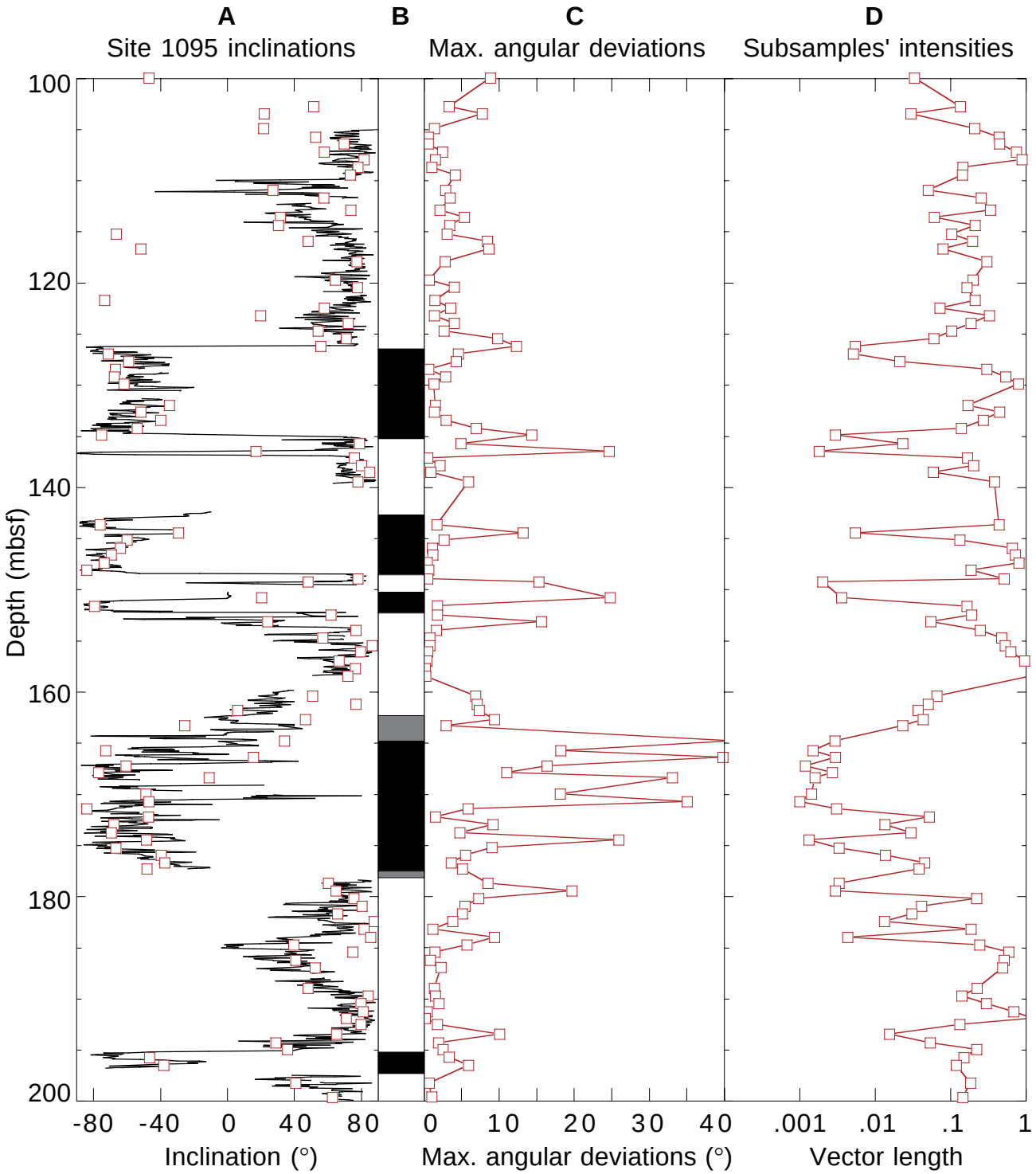

Figure F20. Inclination of the magnetization vector vs. depth (mbsf) for Holes 1095A, 1095B, and 1095D after AF demagnetization at 25 to 30, 30, and 20 mT, respectively. Magnetostratigraphy is based on Berggren et al. (1995).

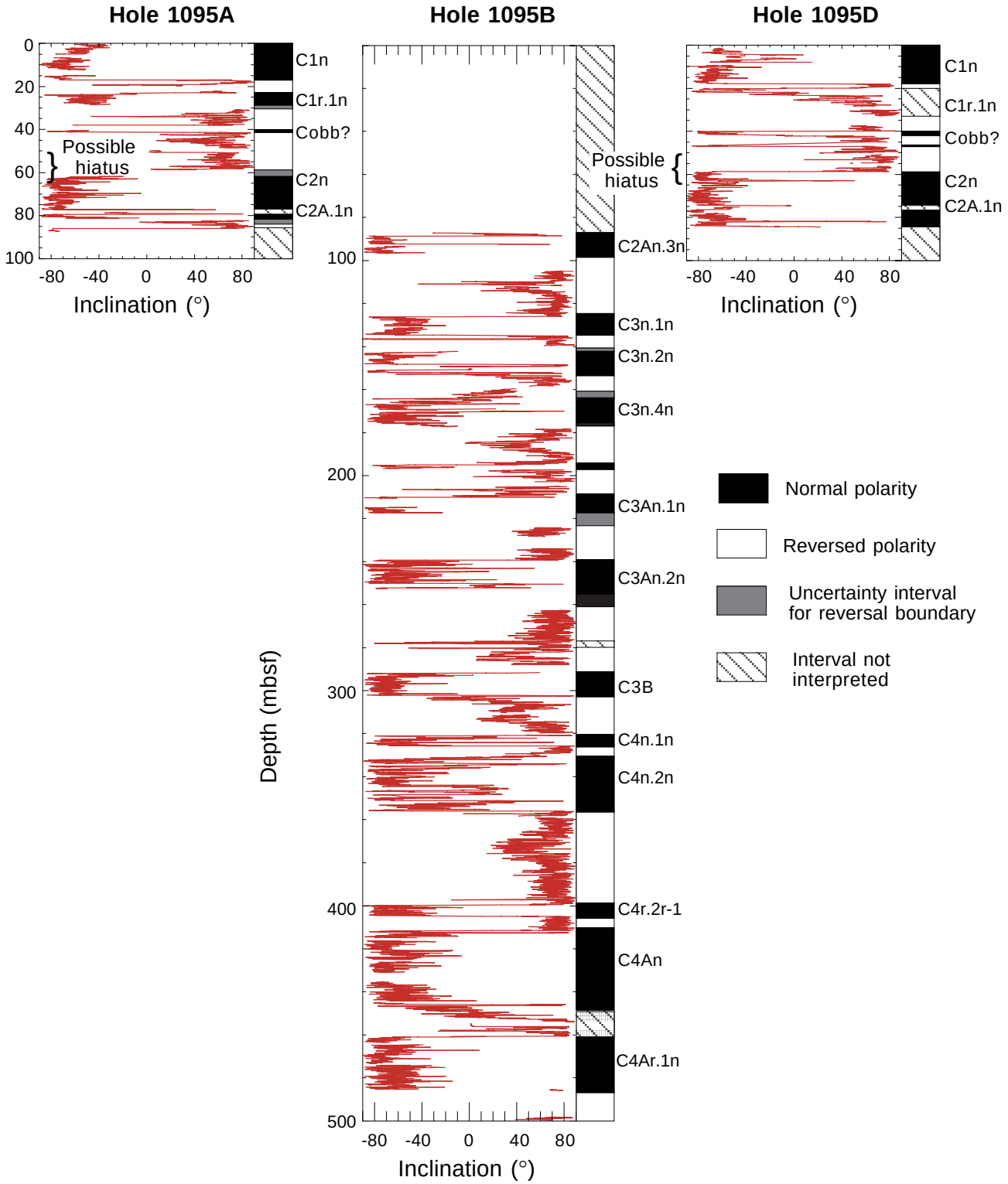

Figure F21. Intensity of the magnetization vector vs. depth (mbsf) for Holes 1095A, 1095B, and 1095D after AF demagnetization at 25 to 30, 30, and 20 mT, respectively. Magnetostratigraphy is based on Berggren et al. (1995).

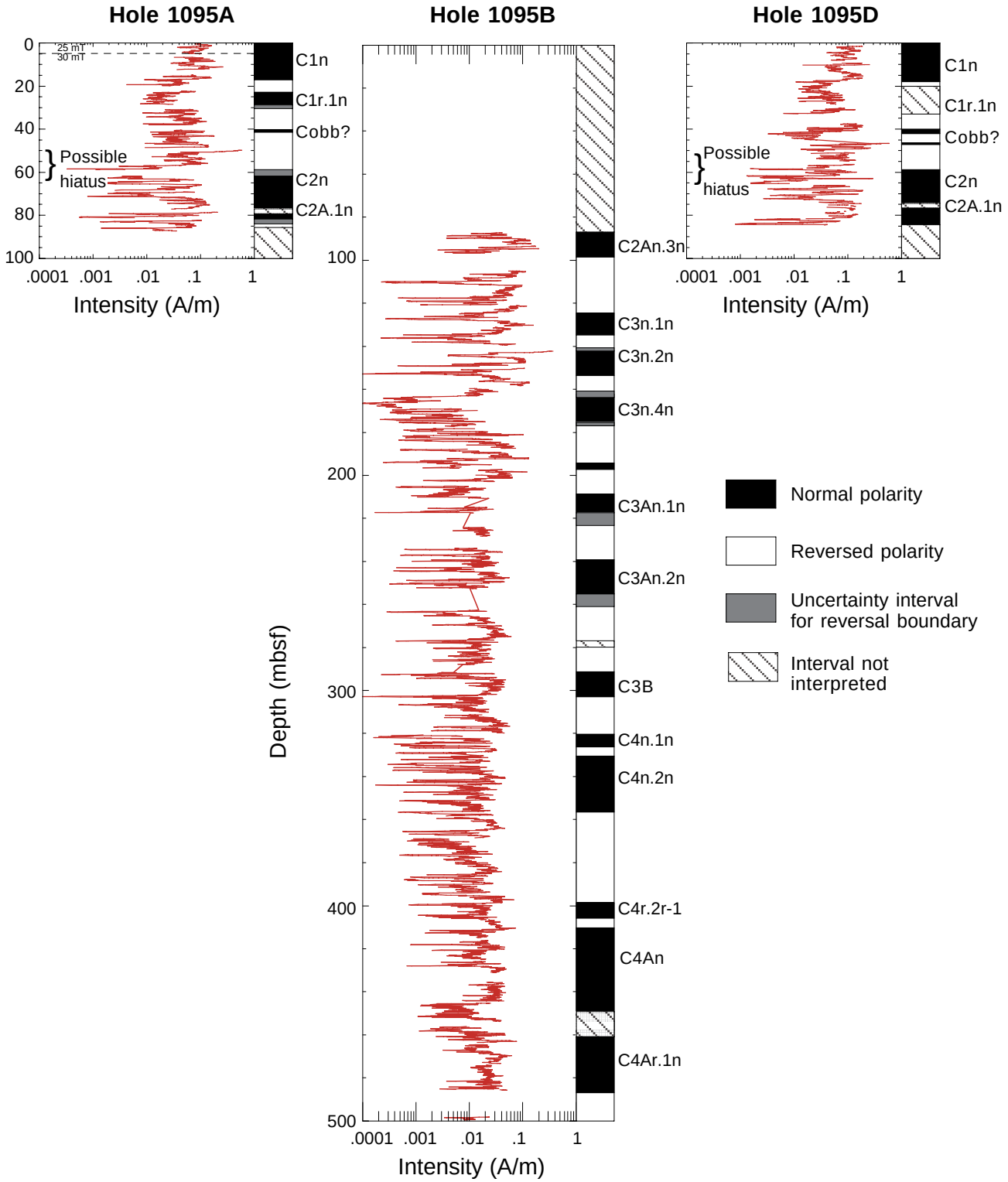

Figure F22. Inclinations from split cores (line connecting small dots) and from discrete samples (squares) for an interval that possibly records Cryptochron 4r.2r-1.

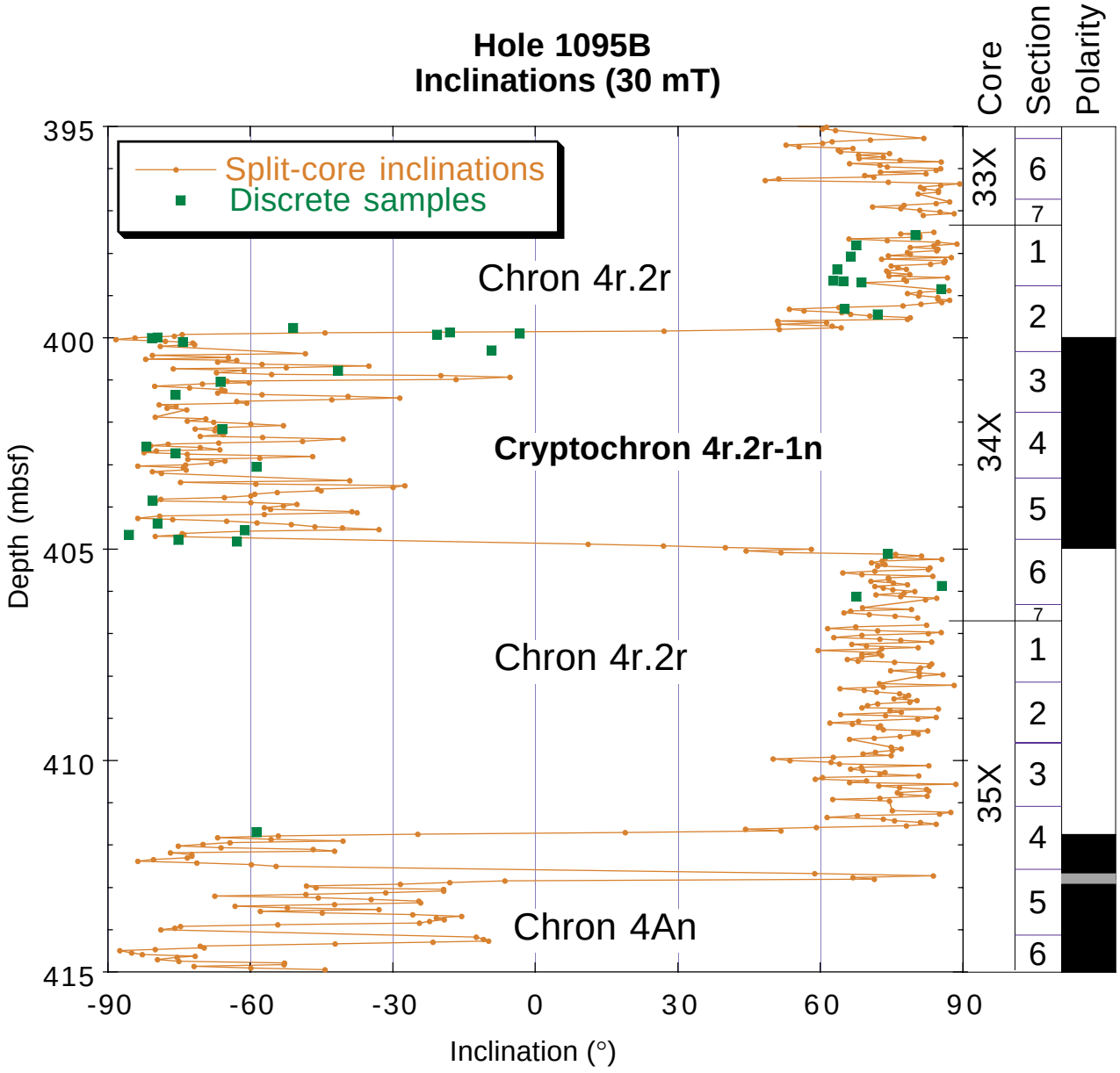

Figure F23. A. Vector end-point diagram for a sample from the reversed polarity interval directly above Cryptochron 4r.2r-1 (Sample 178-1095B-34X-1, 139 cm [398.69 mbsf]). **B.** Enlarged view of the boxed region from A. **C.** Change in the intensity of remanence during AF demagnetization. **D.** Equal-area projection of the remanence vector during AF demagnetization.

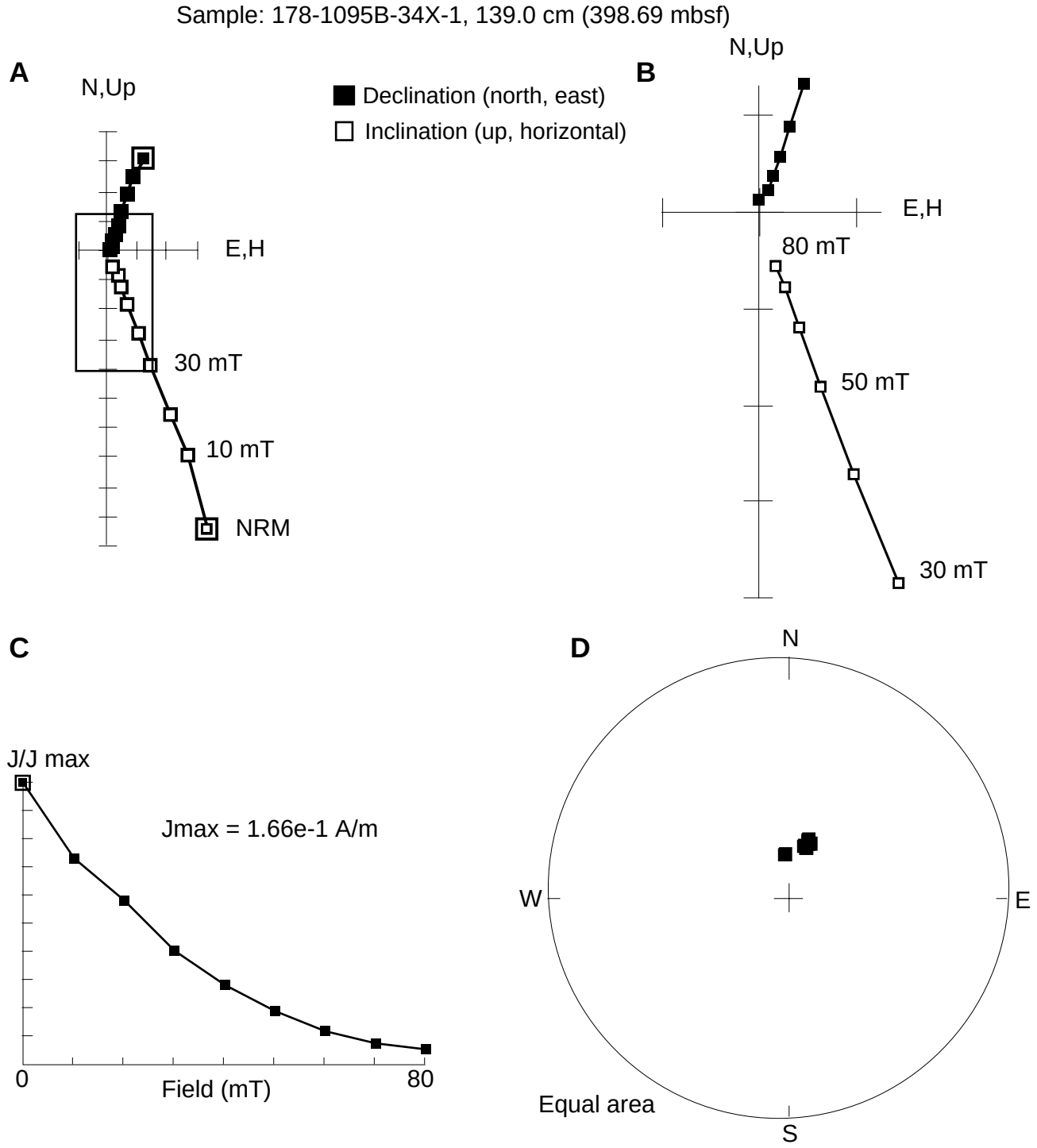

Figure F24. A. Vector end-point diagram for a sample from within the transition zone between the cryptochron and the reversed polarity interval directly above it (Sample 178-1095B-34X-2, 112 cm [399.92 mbsf]). **B.** Enlarged view of the boxed region from A, which illustrates that virtually no magnetization is contained within the sample after the drill-string overprint is removed. **C.** Change in the intensity of remanence during AF demagnetization. **D.** Equal-area projection of the remanence vector during AF demagnetization.

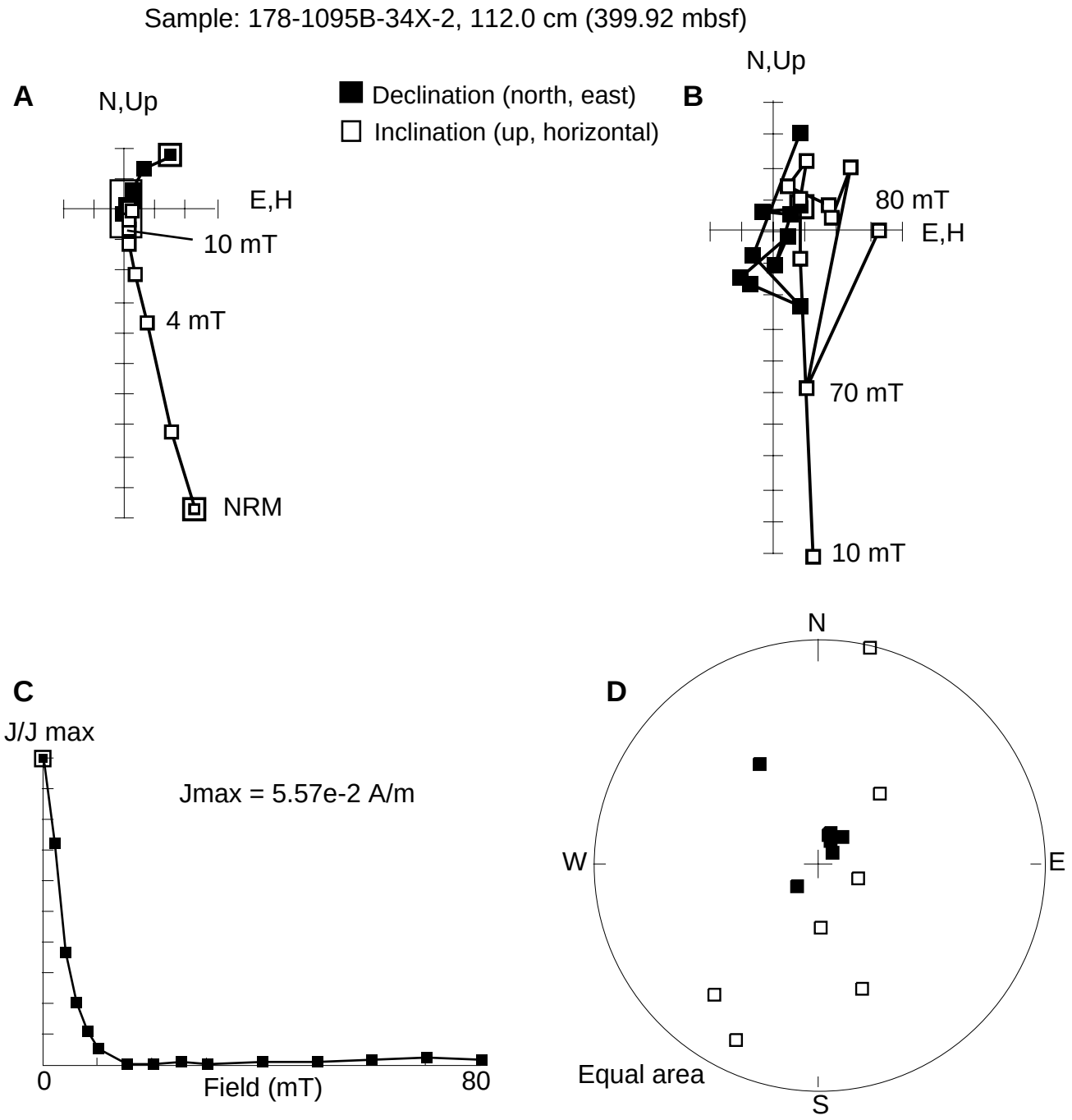

Figure F25. A. Vector end-point diagram for a sample from within Cryptochron 4r.2r-1 that illustrates a primary normal polarity direction after removal of the drill-string overprint (Sample 178-1095B-34X-2, 120 cm [400 mbsf]). **B.** Enlarged view of the boxed region from A. **C.** Change in the intensity of remanence during AF demagnetization. **D.** Equal-area projection of the remanence vector during AF demagnetization.

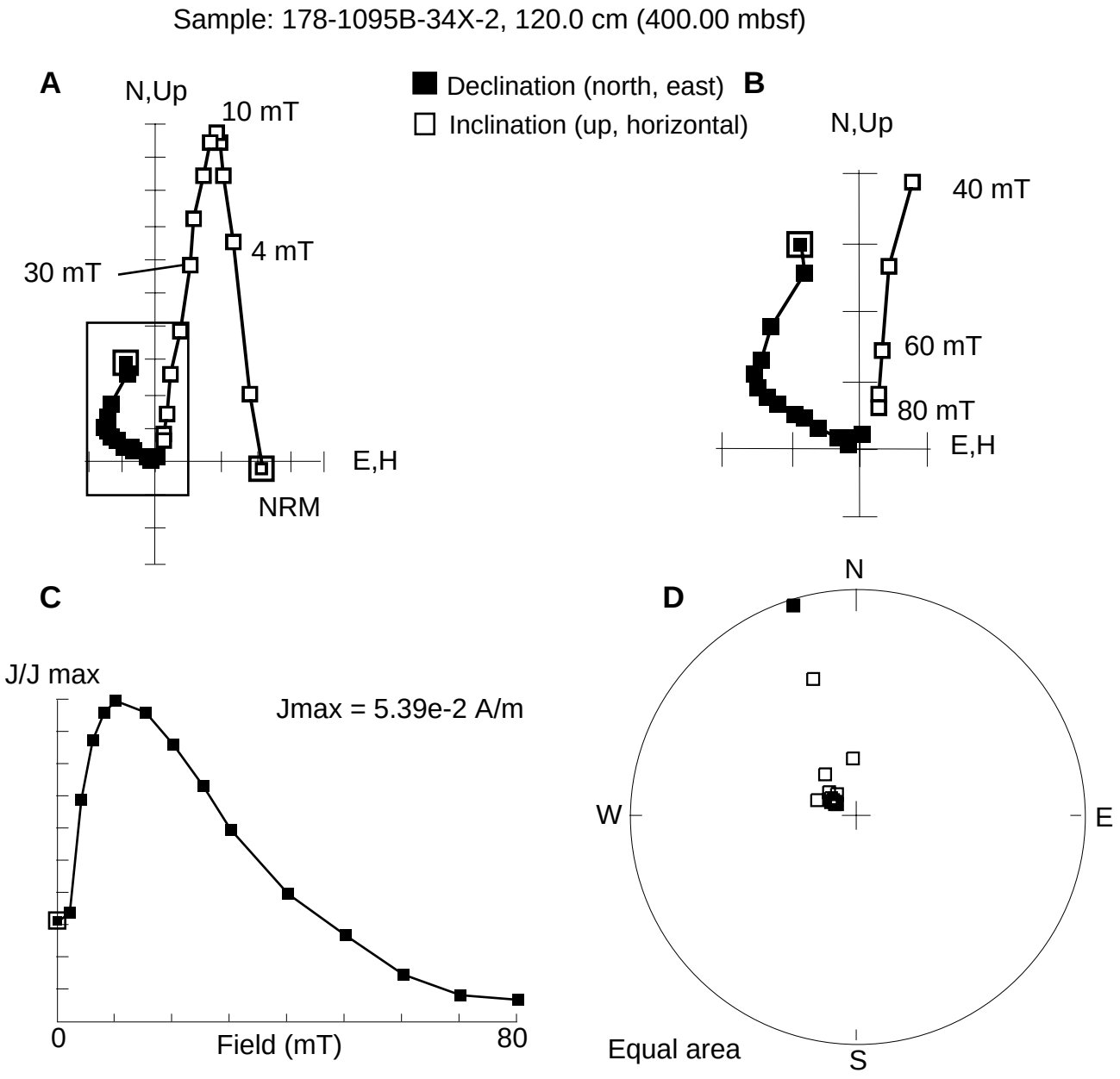

Figure F26. A. Vector end-point diagram for a thermally demagnetized sample from within Cryptochron 4r.2r-1 that illustrates a primary normal polarity direction after removal of the drill-string overprint (Sample 178-1095B-34X-4, 79 cm [402.59 mbsf]). **B.** Enlarged view of the boxed region from A. **C.** Change in the intensity of remanence during AF demagnetization. **D.** Equal-area projection of the remanence vector during AF demagnetization.

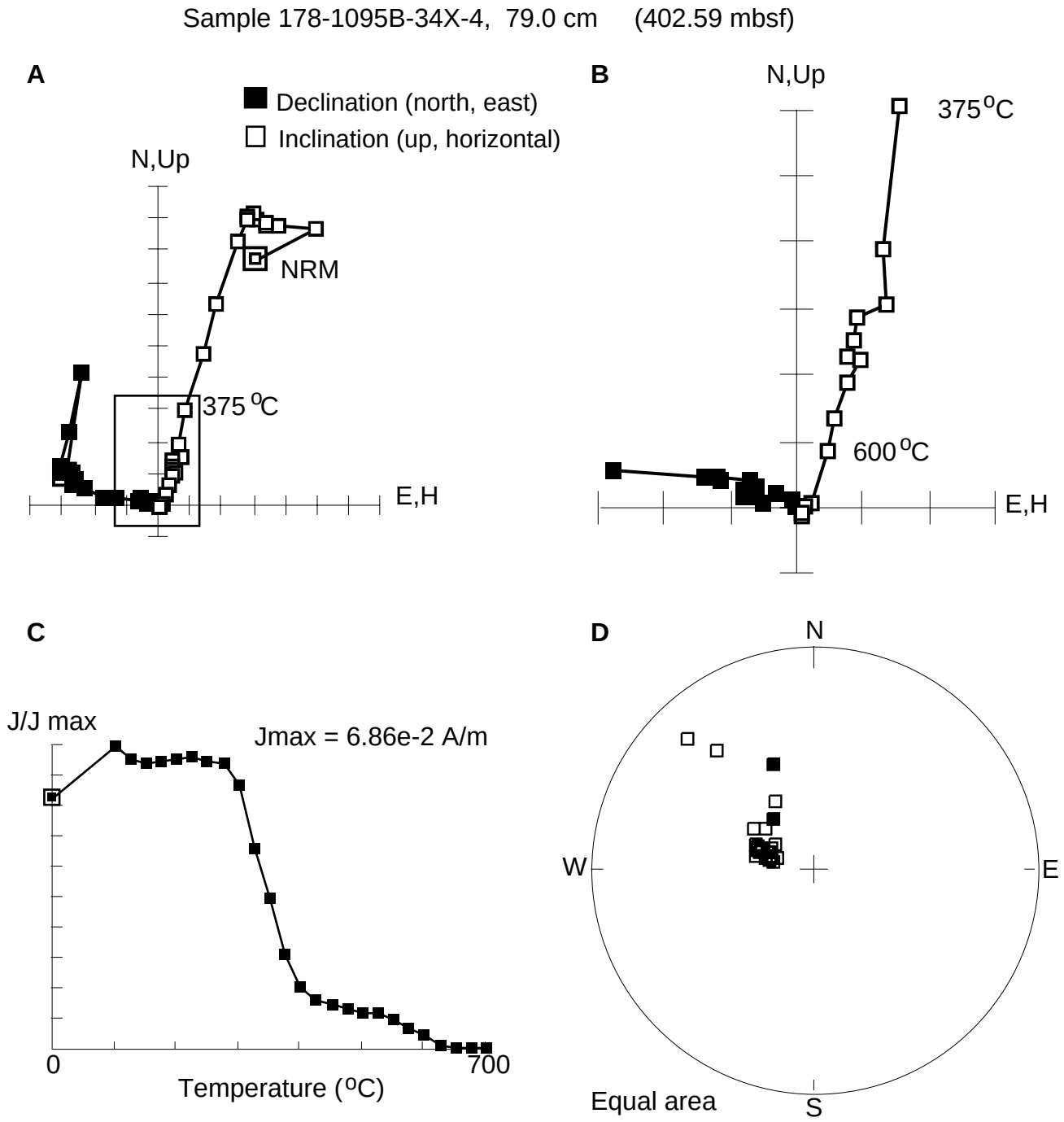

Figure F27. The intensity (after 30-mT demagnetization) and MST susceptibility are shown for the interval from 395 to 414 mbsf, which includes Cryptochron 4r.2r-1. These were used to compute the relative paleointensity record, which illustrates a gradual decay in the field before the cryptochron, a collapse to zero in the transition zone, a return to stable but low paleointensity during the cryptochron, and another collapse to zero in the transition zone. Following this collapse, the geomagnetic field intensity recovered to a value similar to that at the onset of Chron 4r.2r.

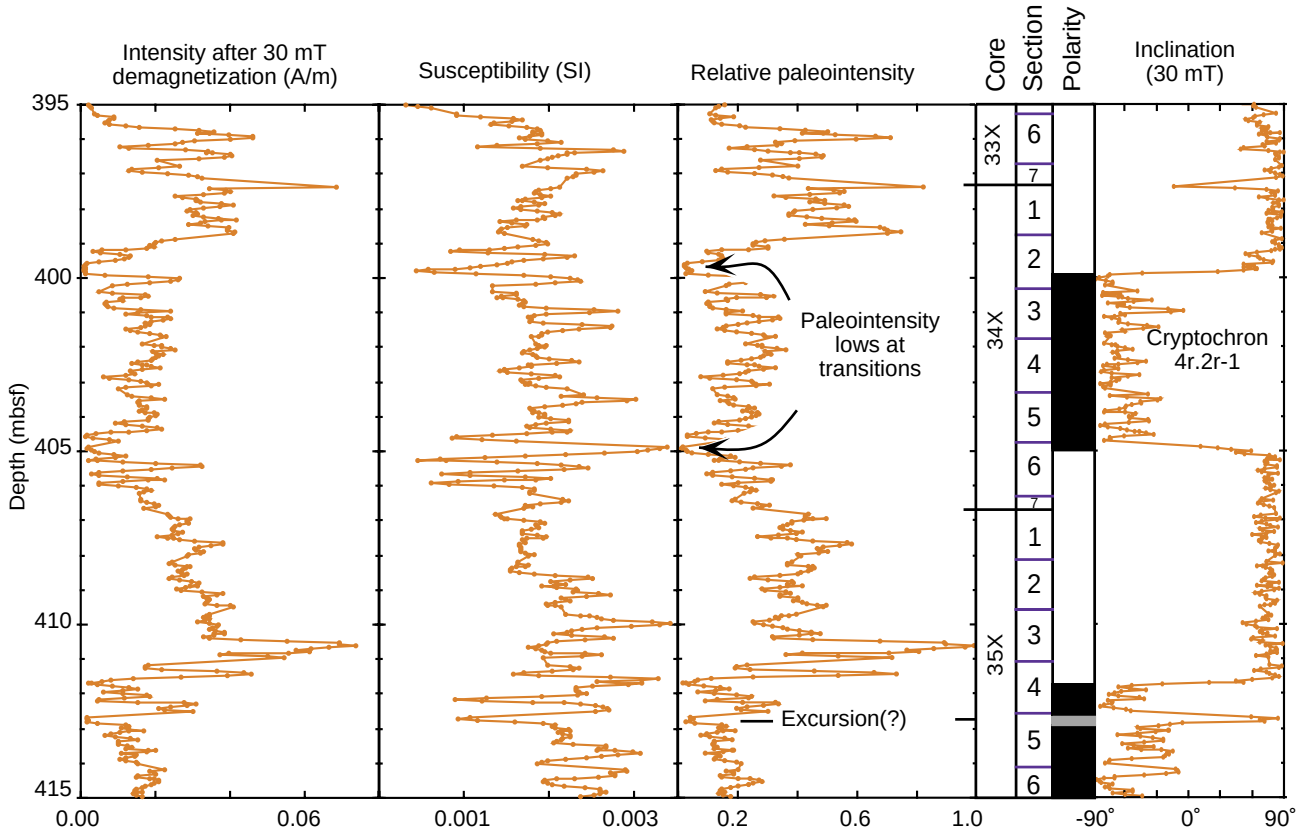

Figure F28. Methane distribution at Site 1095.

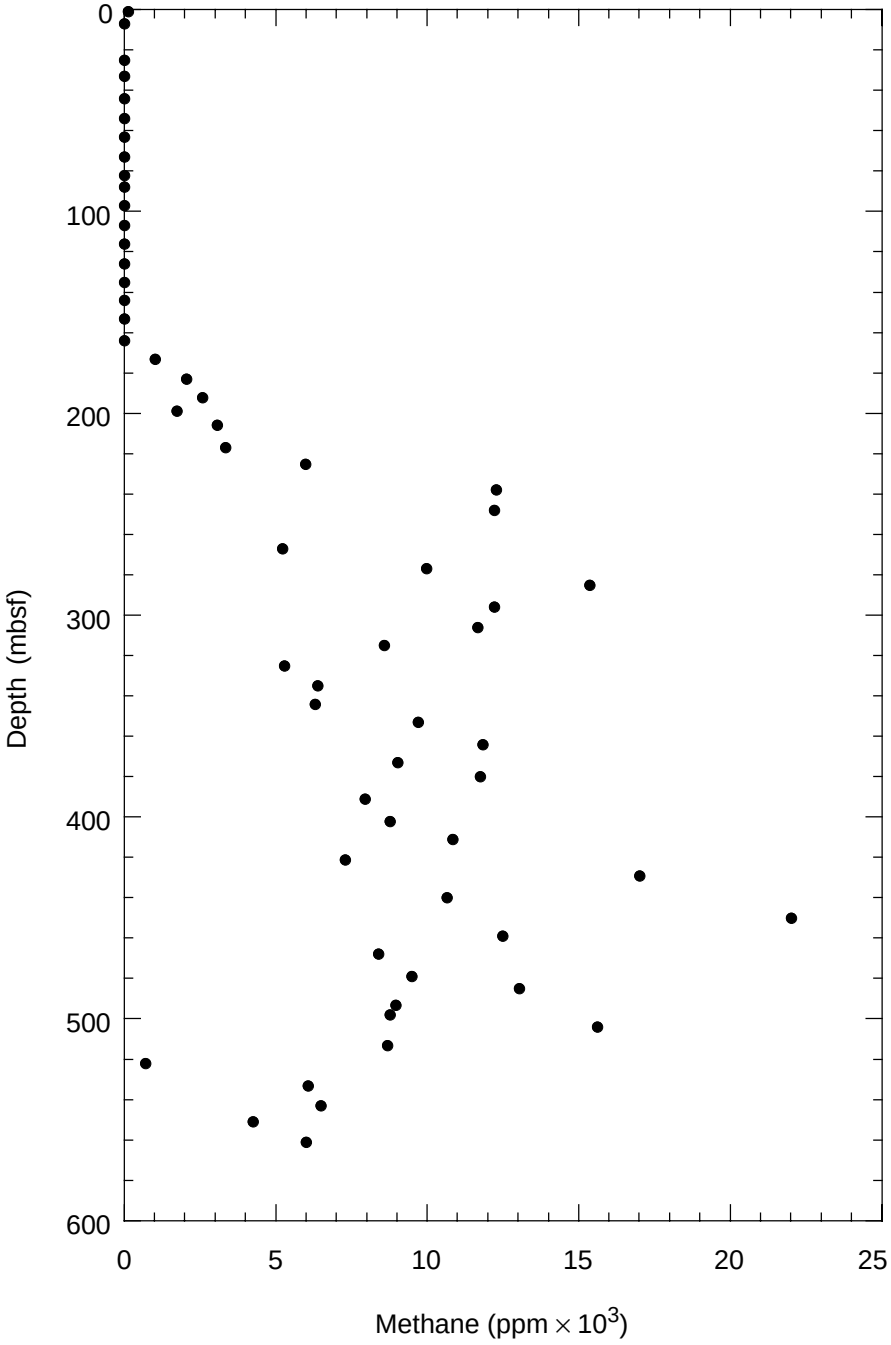

Figure F29. Profiles of interstitial water chemistry in Holes 1095A (open circles) and 1095B (solid circles).

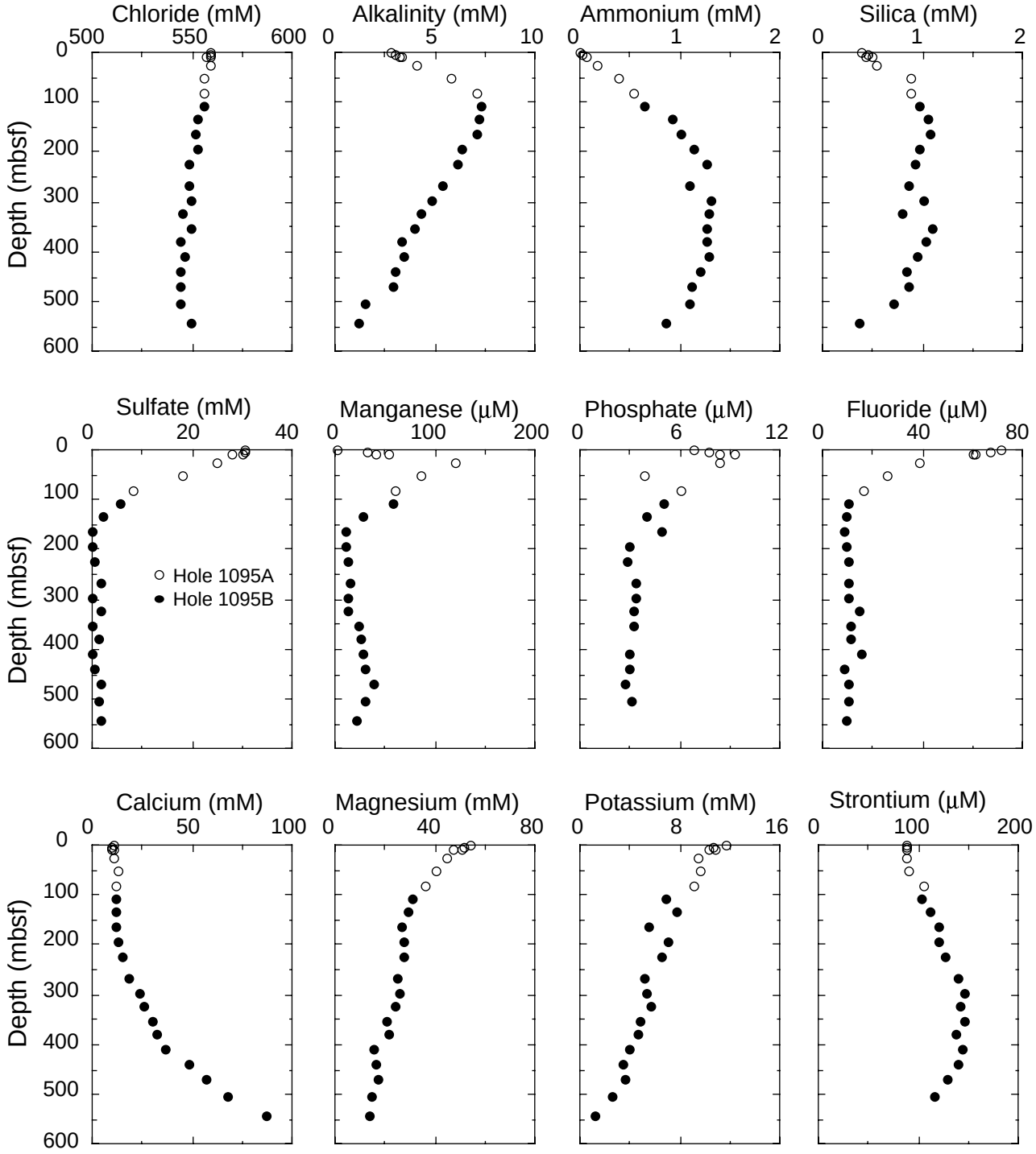

Figure F30. Calculated calcium carbonate distribution at Site 1095.

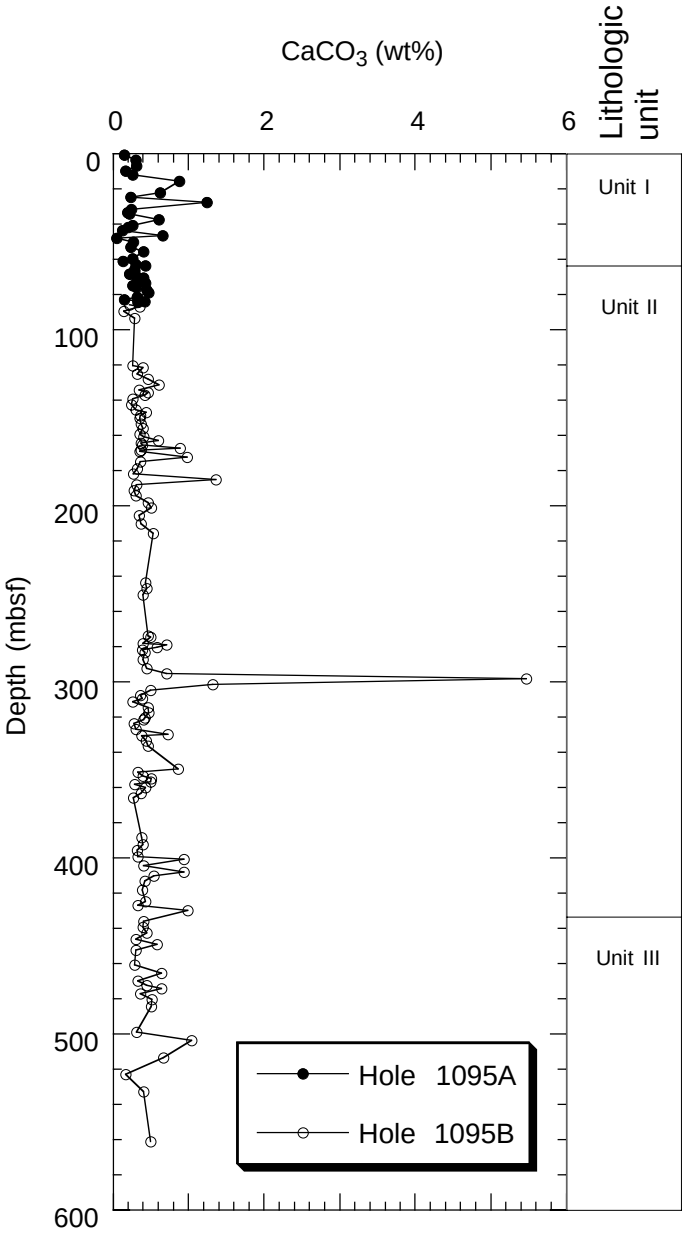

Figure F31. X-ray diffractograms of clay-sized fractions of sediment from Sample 178-1095A-4H-5, 85–88 cm. The broad hump between 6° and 9° 2θ represents a mixed-layer smectite-illite. Note the shift of this peak to lower angles upon glycolation.

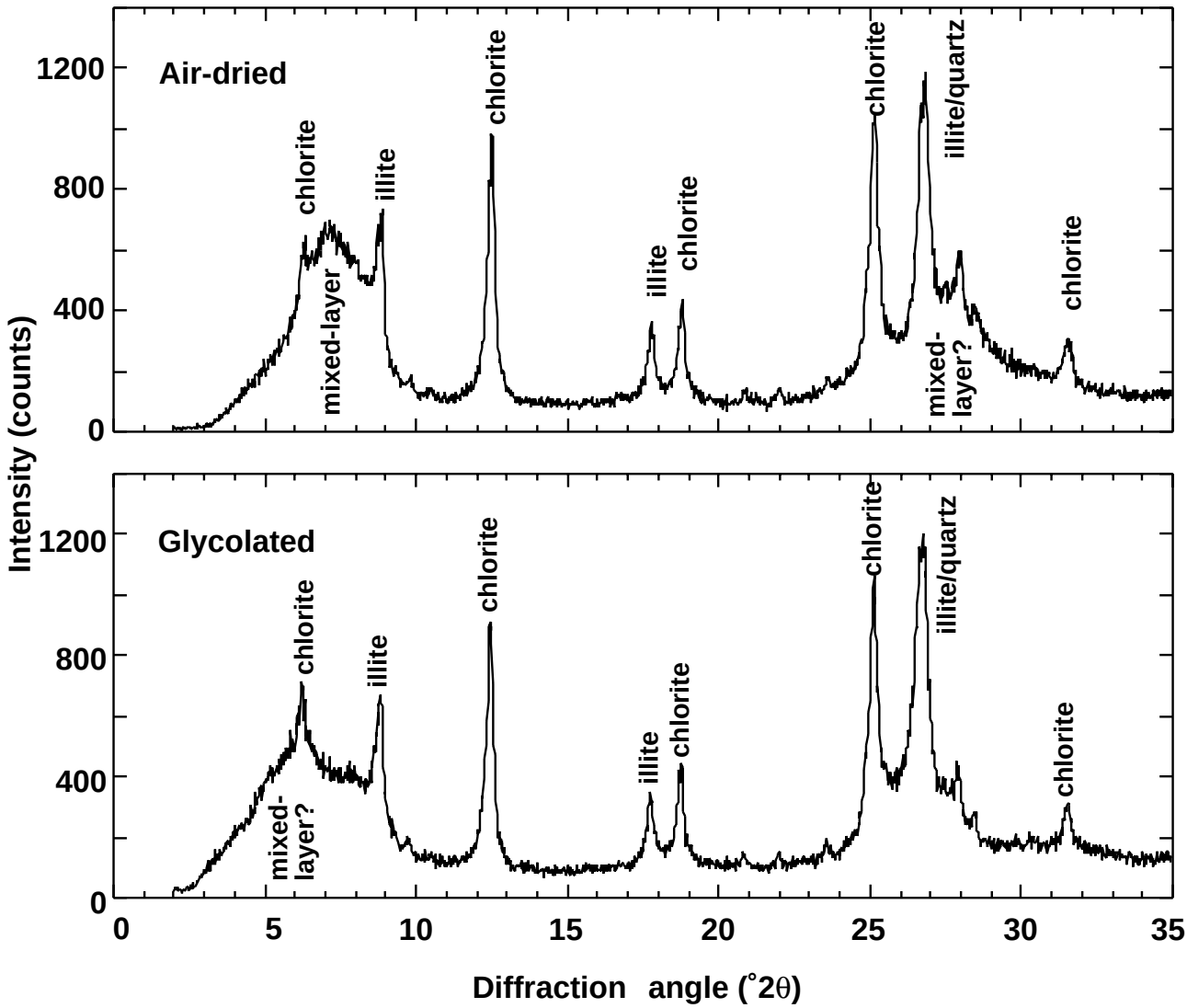

Figure F32. X-ray diffraction intensity ratios among selected peaks for chlorite (7 Å), illite (5 Å), and mixed-layer (~12 Å) clays in clay-sized sediment fractions from Site 1095. Peak height ratios reflect relative differences but not absolute concentrations.

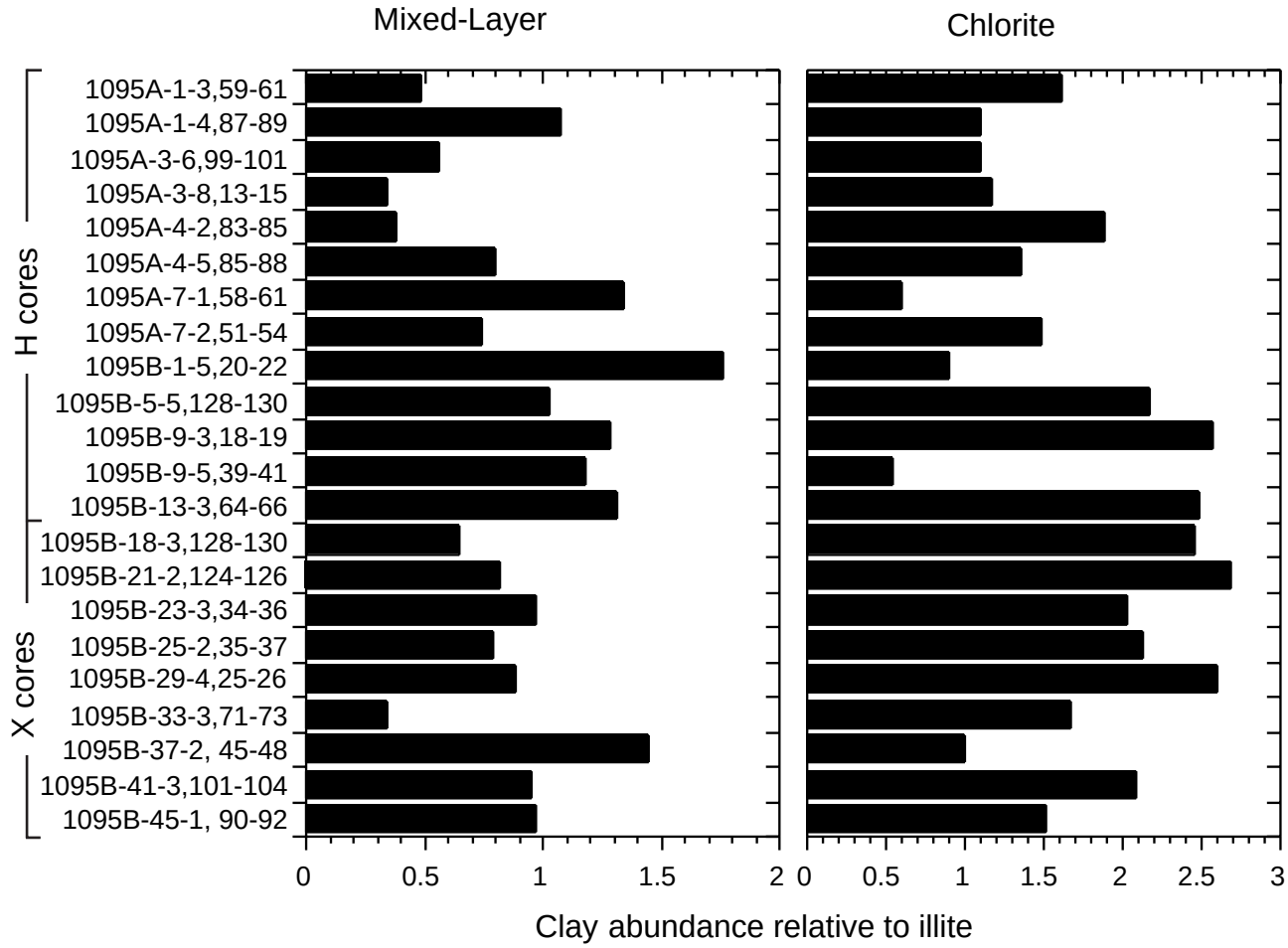

Figure F33. Raw data for **(A)** NGR, **(B)** GRAPE density, **(C)** magnetic susceptibility, and **(D)** *P*-wave velocity. GRAPE data were truncated outside 1.2–2.5 g/cm^3, and the magnetic susceptibility data were truncated outside the range 0–1400 × 10^{-5} SI to remove noise.

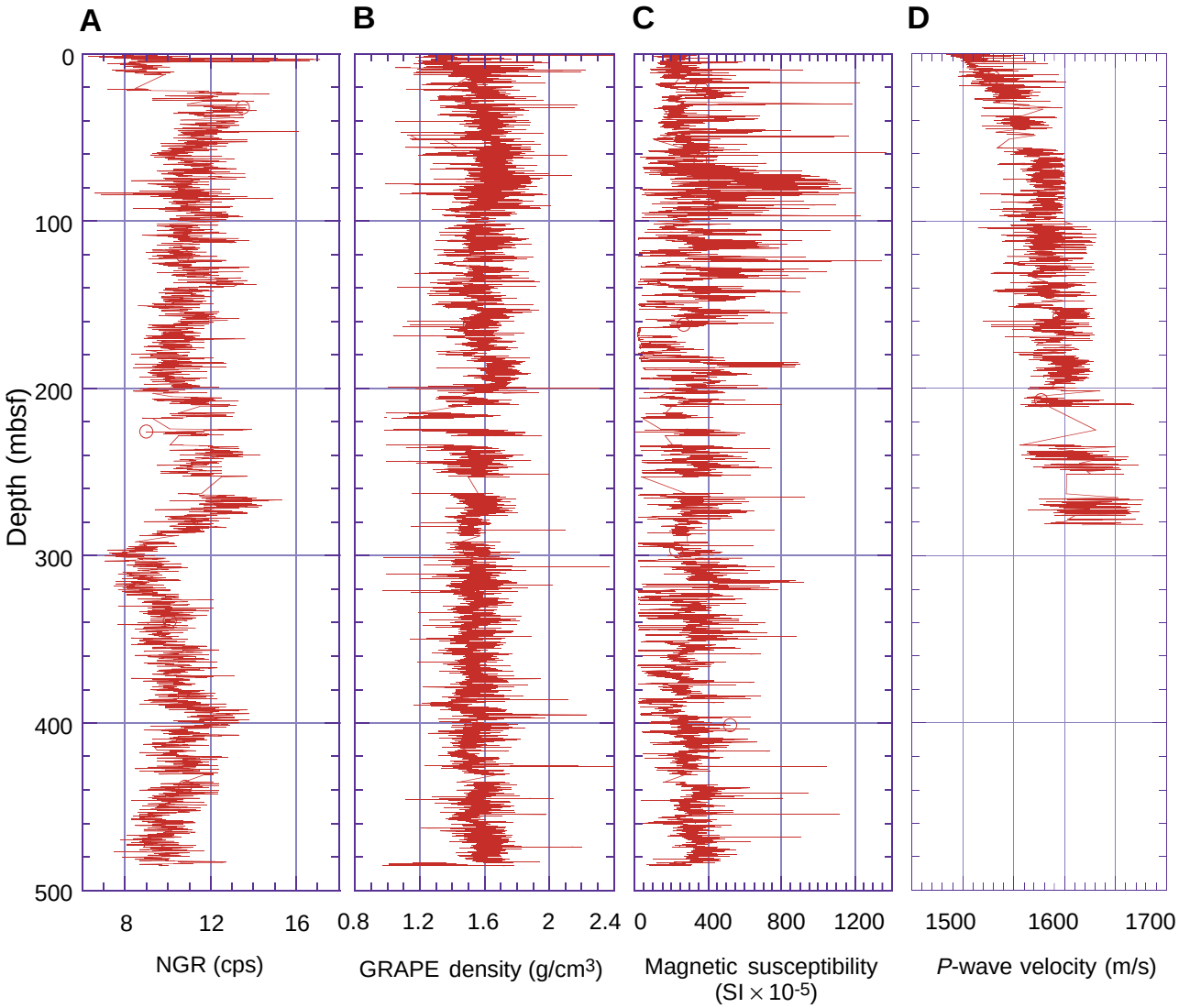

Figure F34. Filtered **(A)** NGR, **(B)** GRAPE density, and **(C)** magnetic susceptibility data, using a Gaussian filter to remove high frequencies. The filter was centered at ~10 m, with a high-frequency truncation point at ~1 m.

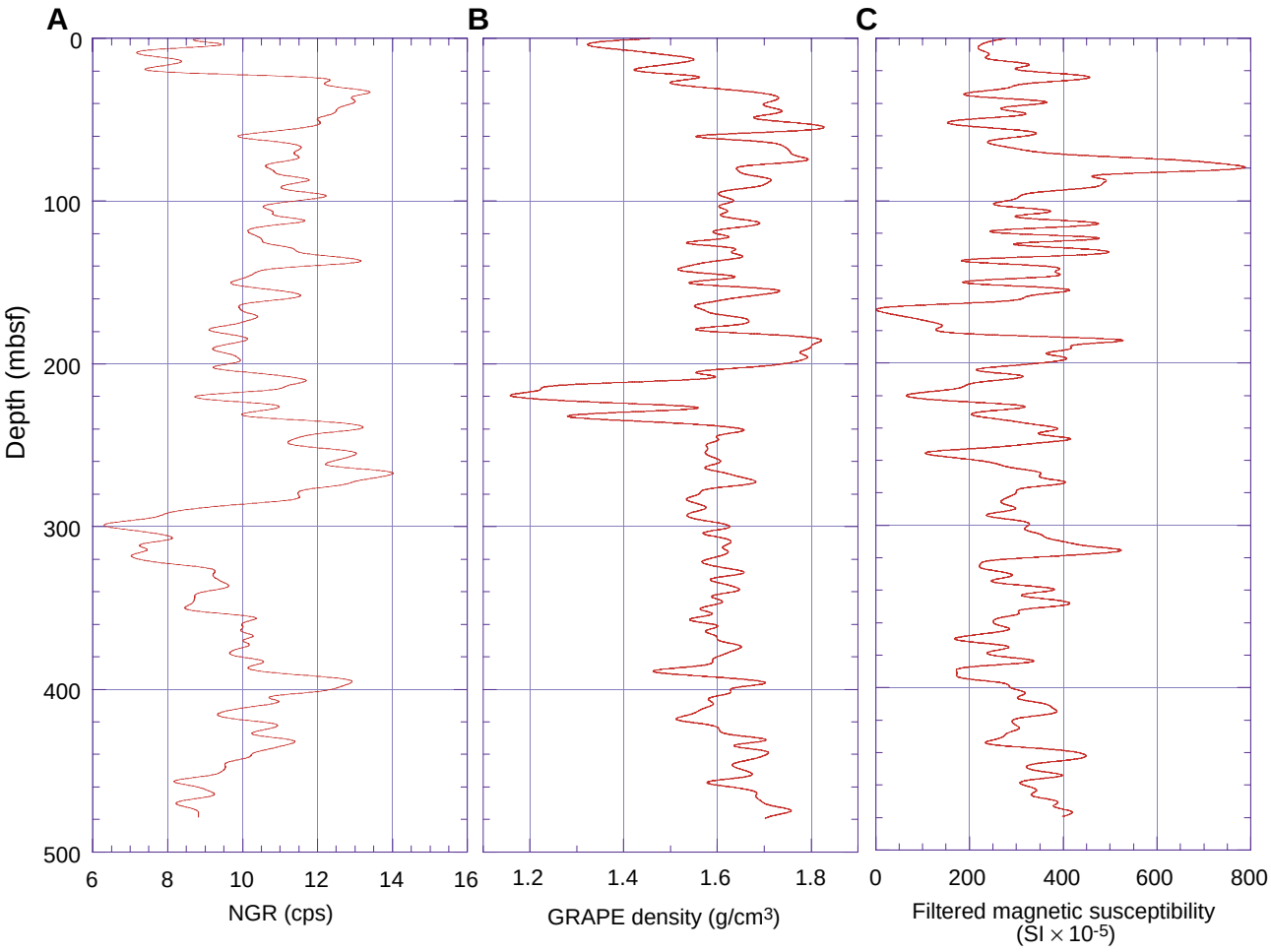

Figure F35. Filtered **(A)** NGR, **(B)** GRAPE density, and **(C)** magnetic susceptibility data vs. age produced using paleomagnetic events from cores and downhole logs. The data were smoothed after rescaling, as in Figure **F34**, p. 82.

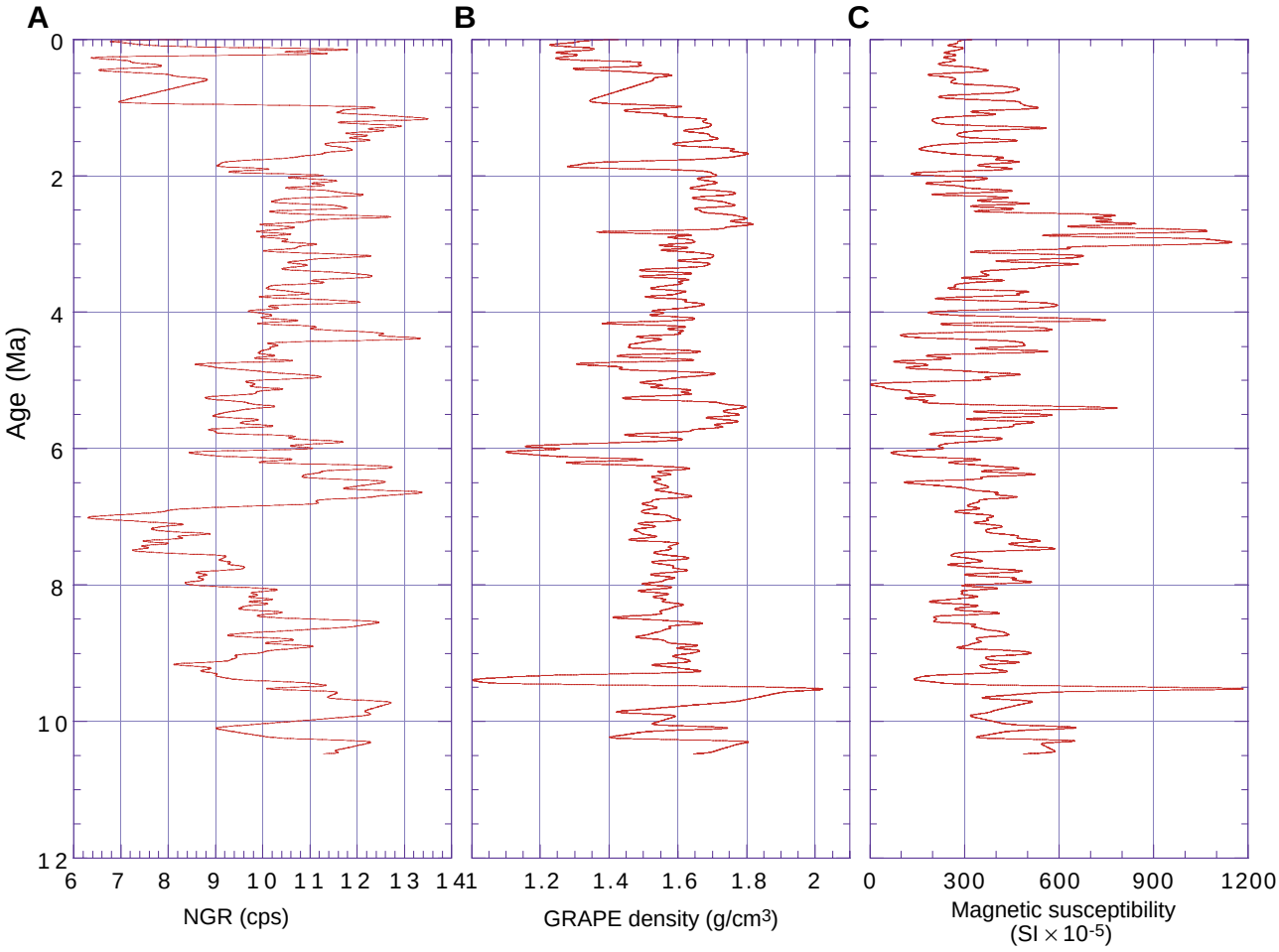

Figure F36. A. Filtered GRAPE bulk density and index properties (MAD) bulk density. **B.** Water content. MAD = moisture and density.

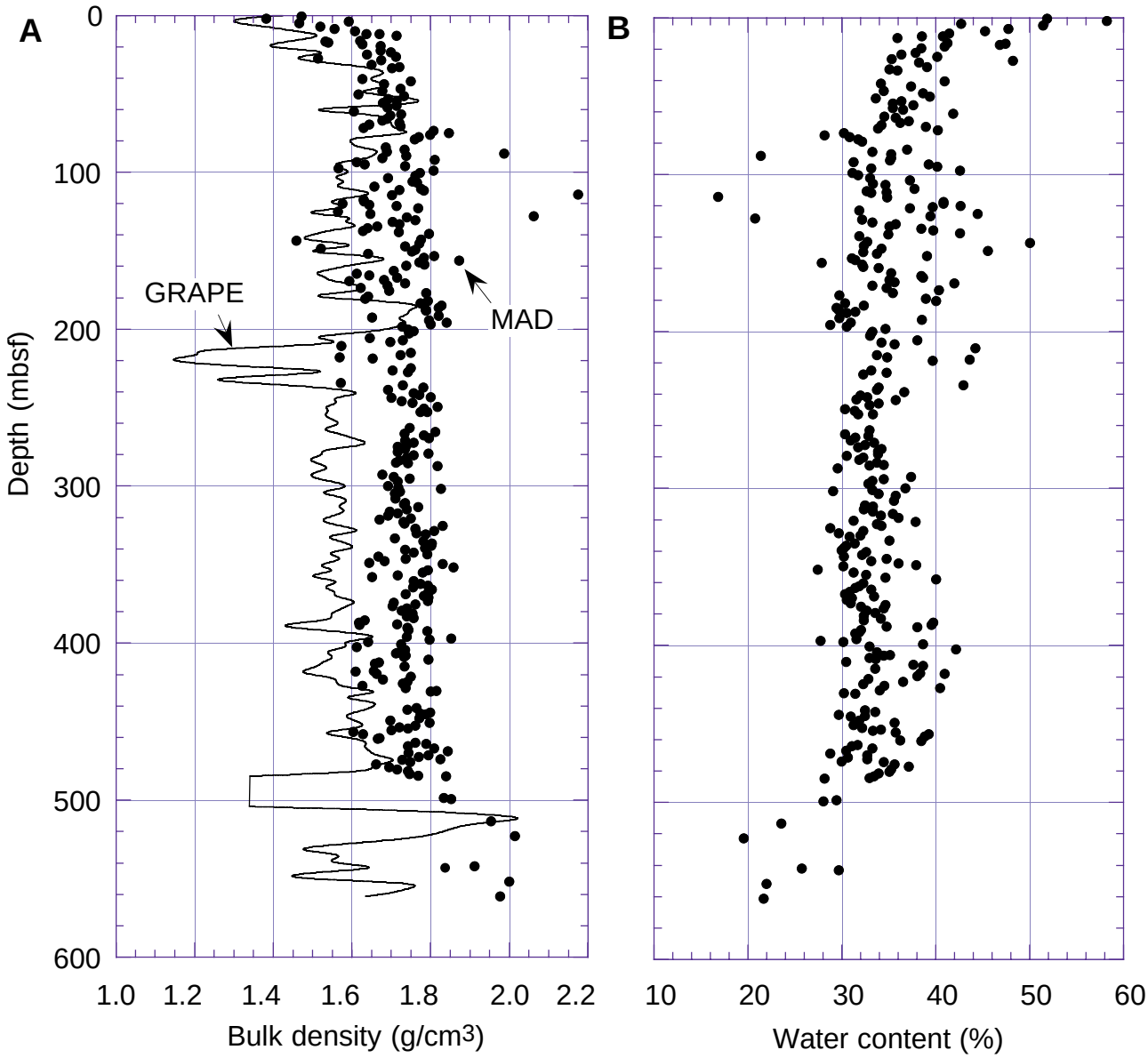

Figure F37. Index properties **(A)** porosity and **(B)** MAD grain density. MAD = moisture and density.

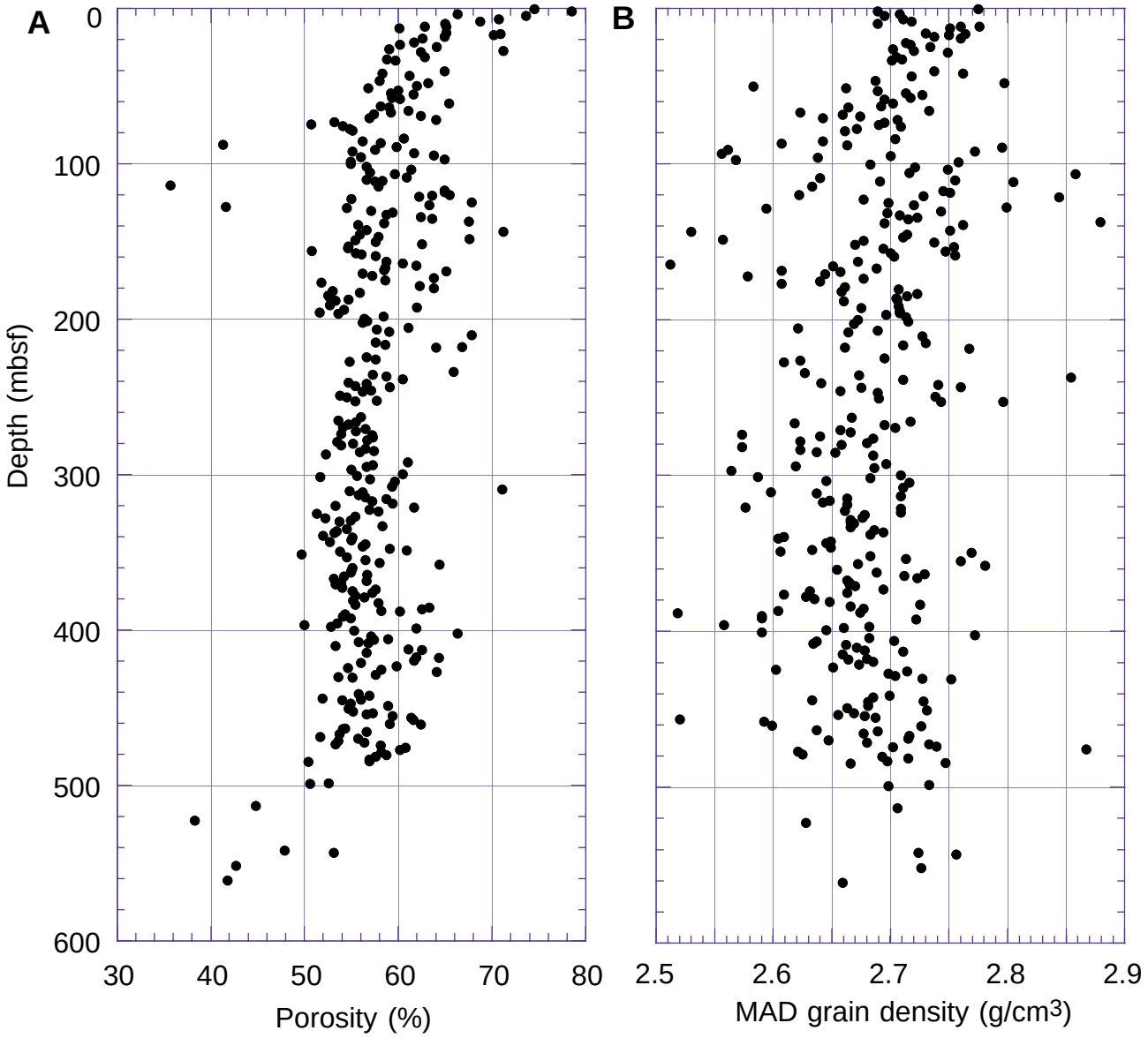

Figure F38. A. Discrete *P*-wave velocity. PWS1, PWS2, and PWS3 measurements vs. depth in the upper part of Site 1095. **B.** Complete PWS3 data set vs. depth at Site 1095.

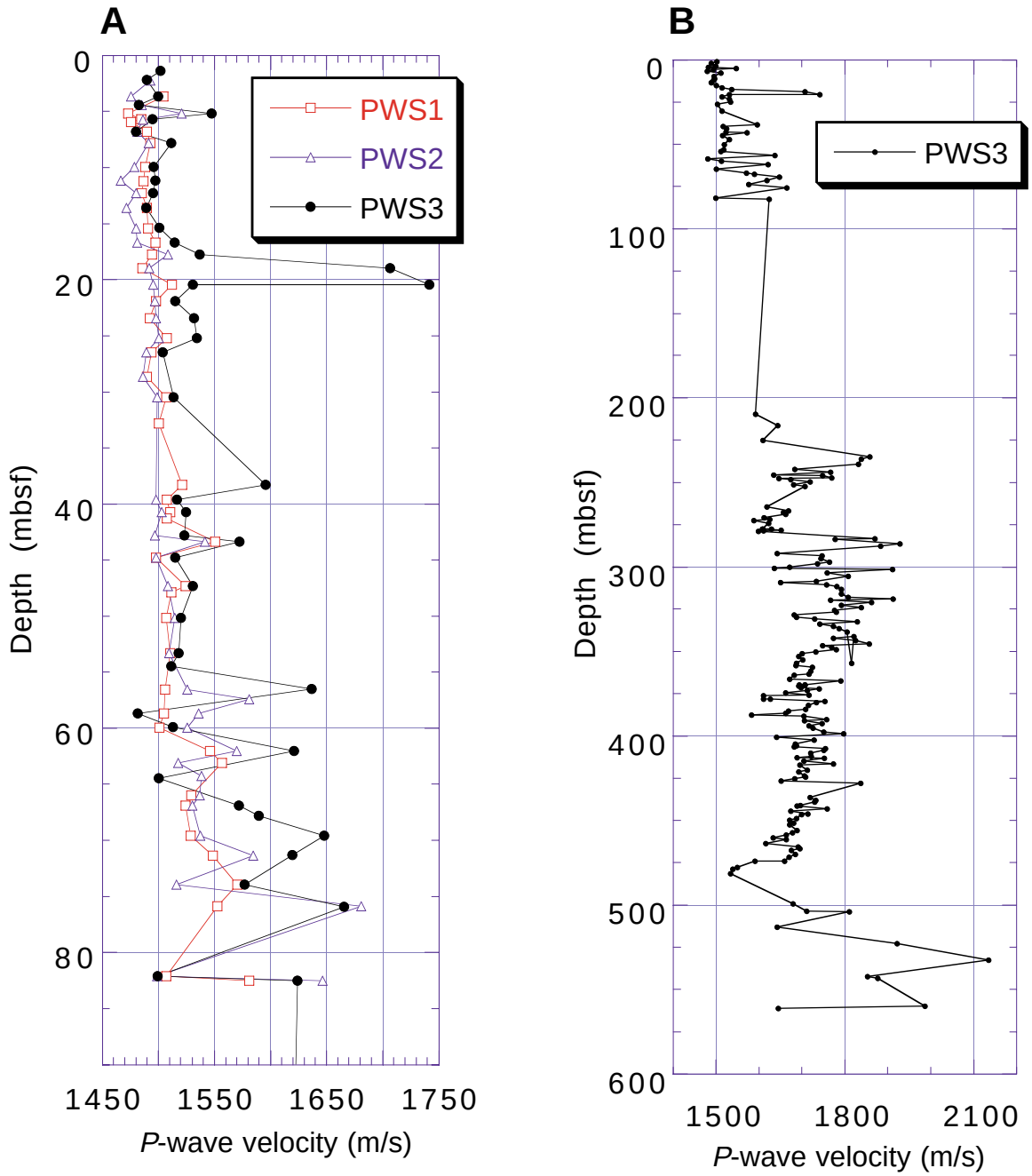

Figure F39. Graphic summary of downhole logging operations at Hole 1095B. Seafloor was picked on the basis of the step in natural gamma activity at the sediment/water boundary.

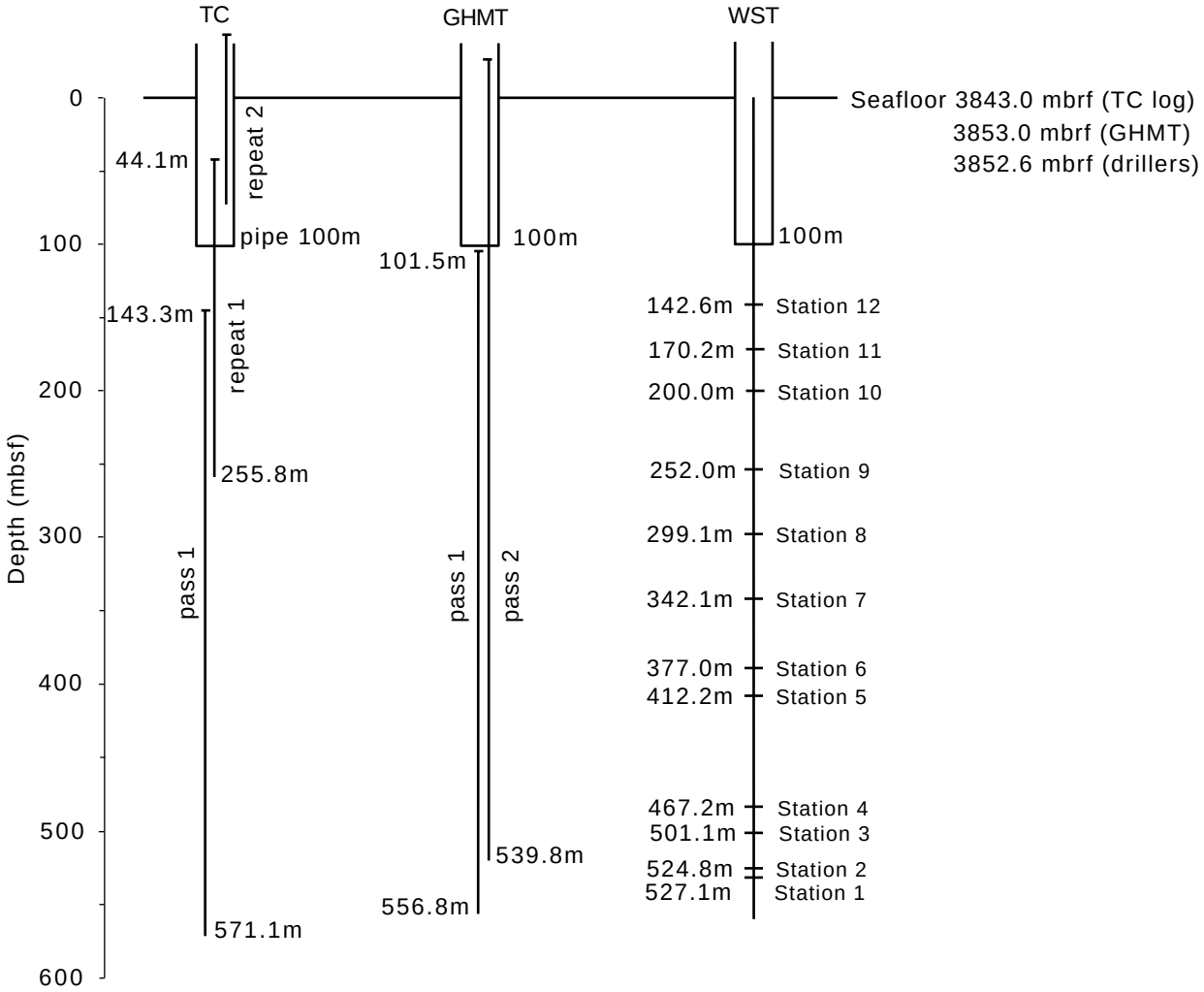

Figure F40. Downhole logs of hole diameter, total natural gamma (HSGR), bulk density (RHOM), porosity (APLC), resistivity (IMPH), magnetic susceptibility (RMGS), and total magnetic field (MAGB) from Hole 1095B, with core measurements of bulk density and porosity (index properties). Depth adjustments have been applied to bring all logs to a common measurement position below the seafloor. Dashed lines in the resistivity and magnetic logs outline downhole trends (see **"Downhole Measurements,"** p. 27).

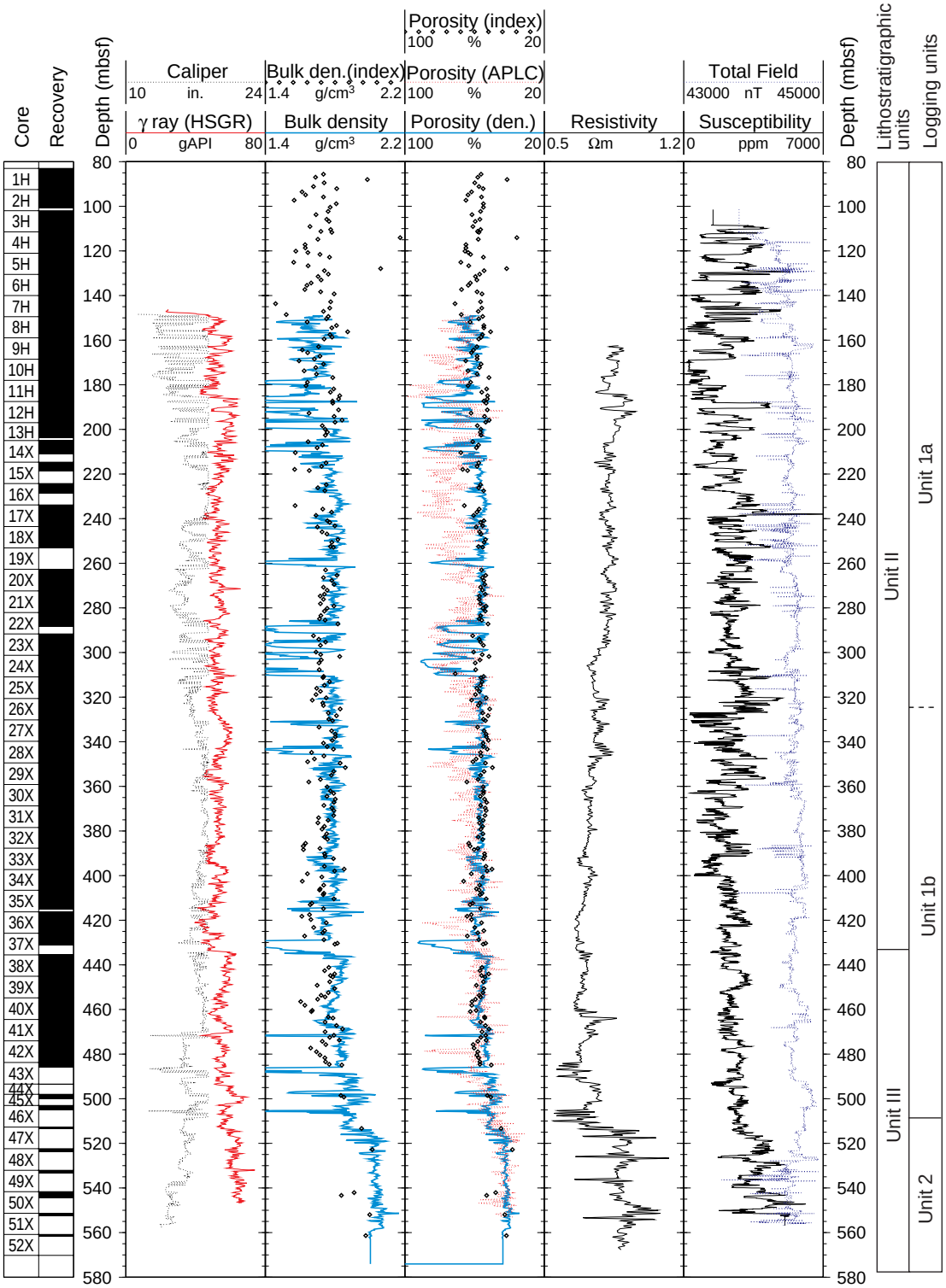

Figure F41. Downhole logs from the HNGS natural gamma tool on the TC tool string. Depth adjustments have been applied to bring all logs to a common measurement position below the seafloor.

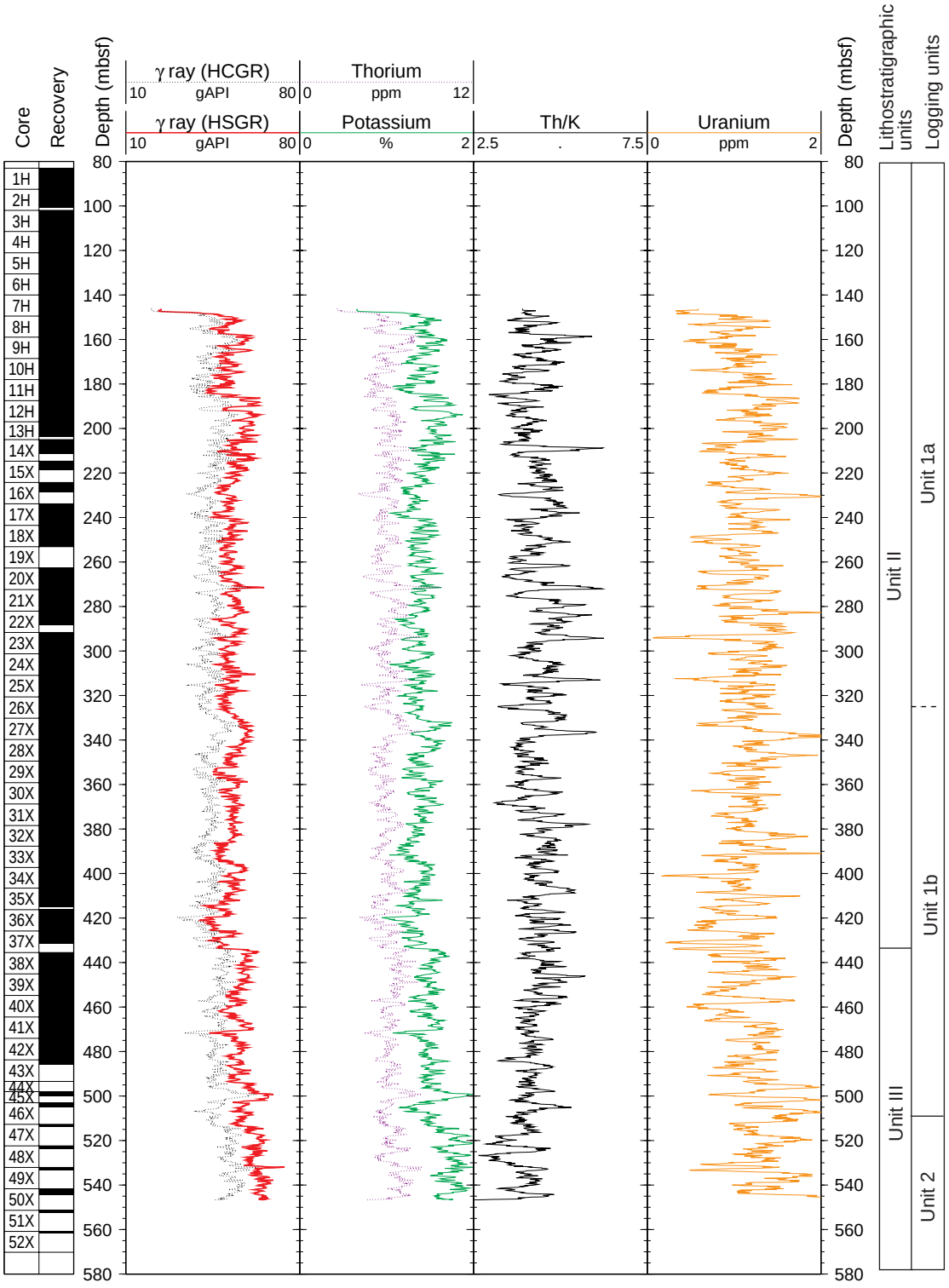

Figure F42. Comparison of susceptibility logs from the two passes of the GHMT with the core MST susceptibility measurements, for the interval 110–190 mbsf. The small discrepancies between the two susceptibility logs are likely caused by oscillations in the vertical motion of the tool.

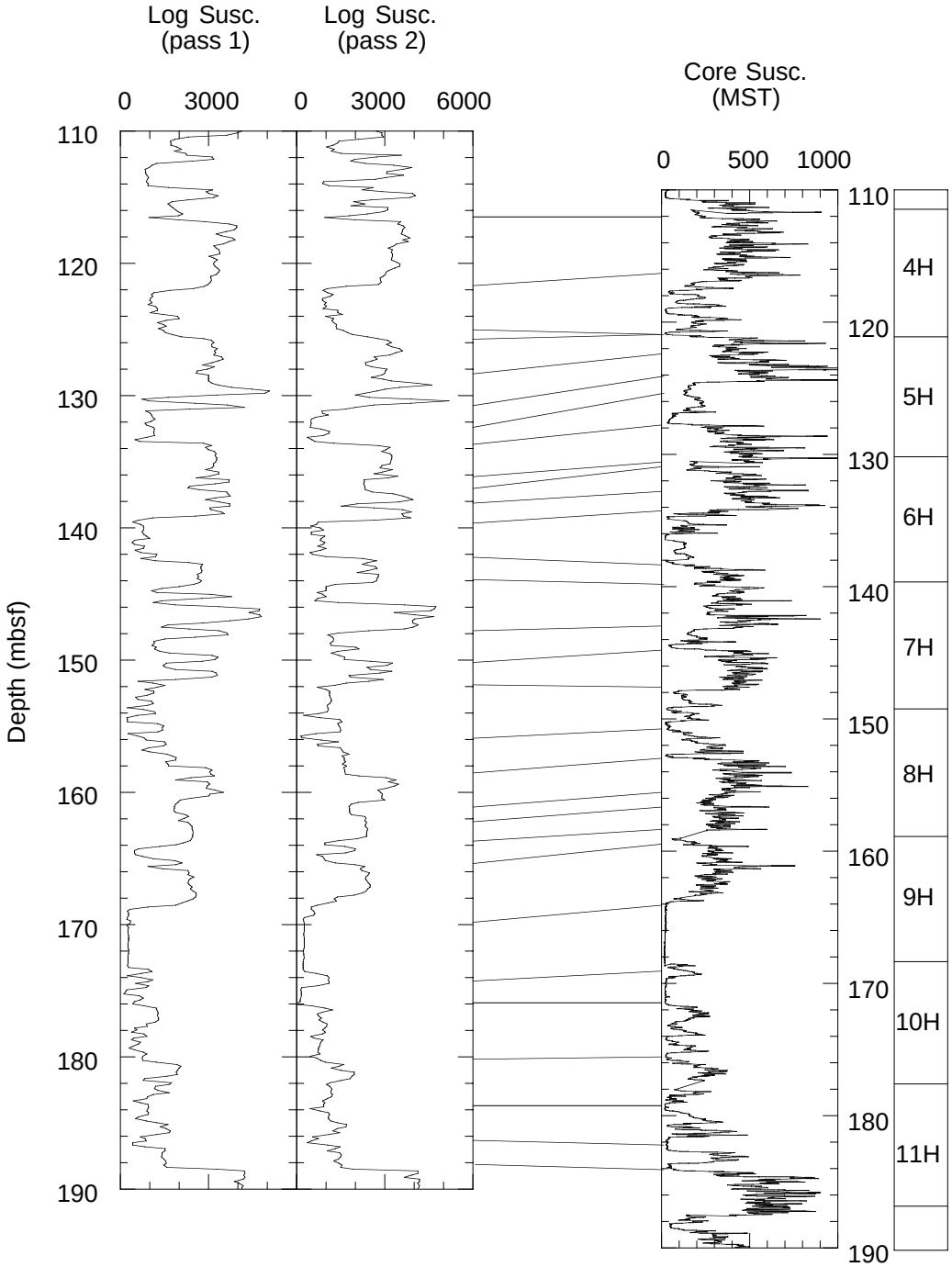

Figure F43. Core lithology compared to magnetic susceptibility (RMGS) and natural gamma (SGR) logs from the GHMT logging run at Hole 1095B over a 100-m-long interval.

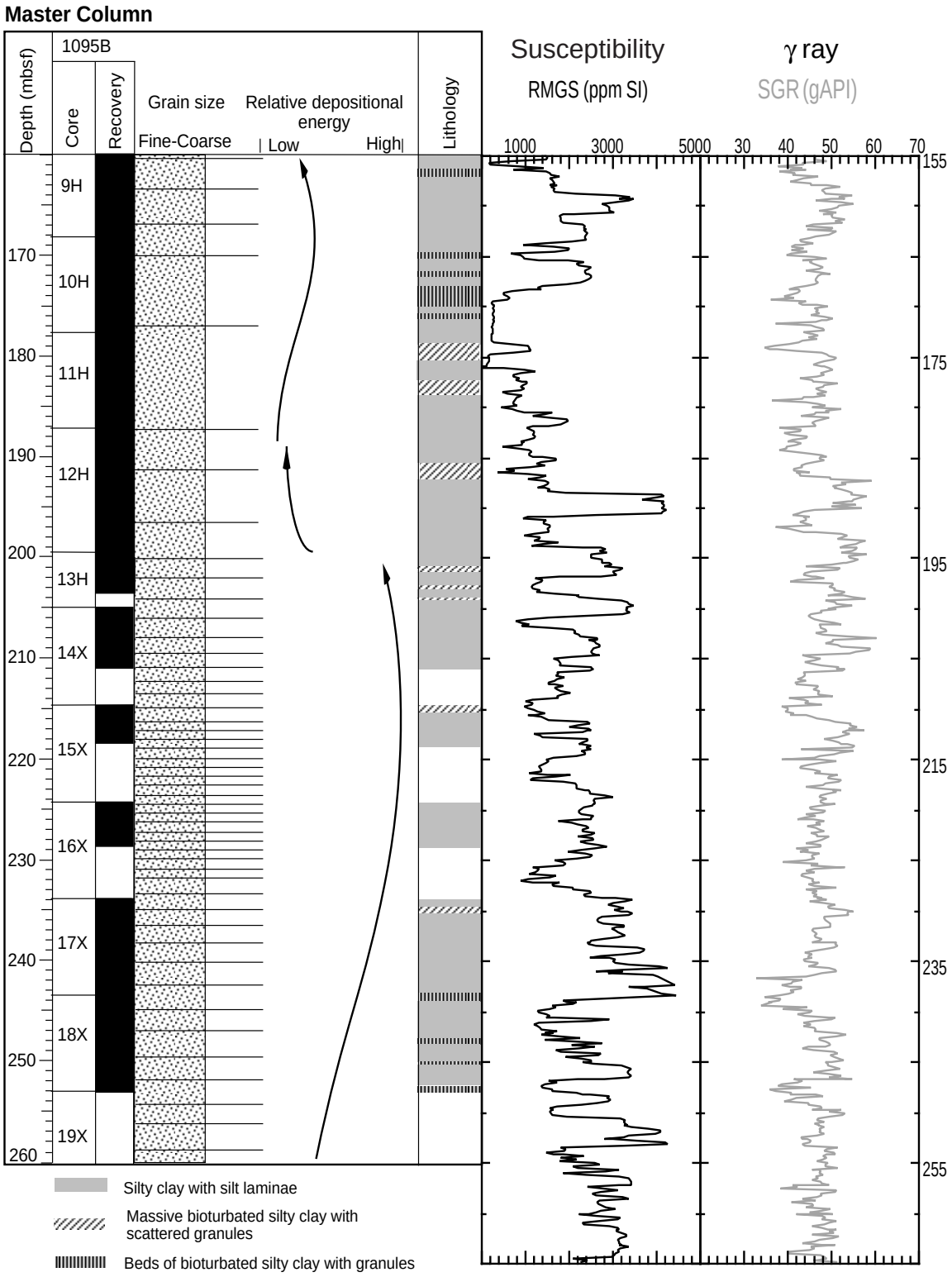

Figure F44. Polarity stratigraphy from the GHMT tool string: susceptibility (RMGS), magnetic field anomaly resulting from the remanence (generated by subtracting from the total field measurement [MAGB] the Earth's field, the field produced by the BHA, and the field caused by the sediment's induced magnetization), inferred polarity (normal polarity corresponds to negative remanence anomaly), the magnetic inclination from core, and the polarity stratigraphy of Cande and Kent (1995). Age assignments, except those from below 480 mbsf, are those proposed in **"Paleomagnetism,"** p. 16. Log depths have been reduced by 5 m in this figure to aid comparison with core depths.

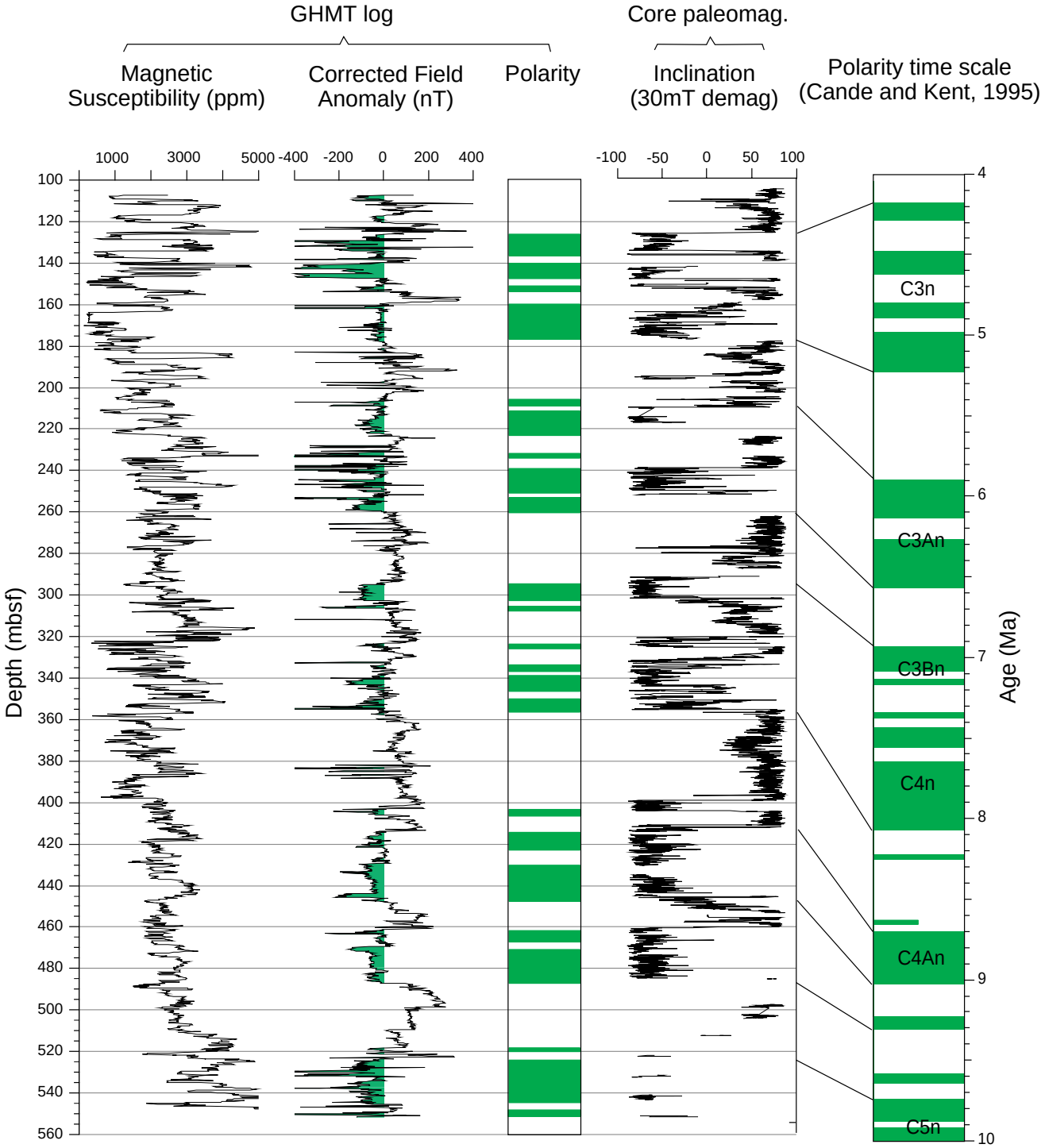

Figure F45. Temperature log from Hole 1095B, taken during the TC run (see "Temperature Log," p. 29).

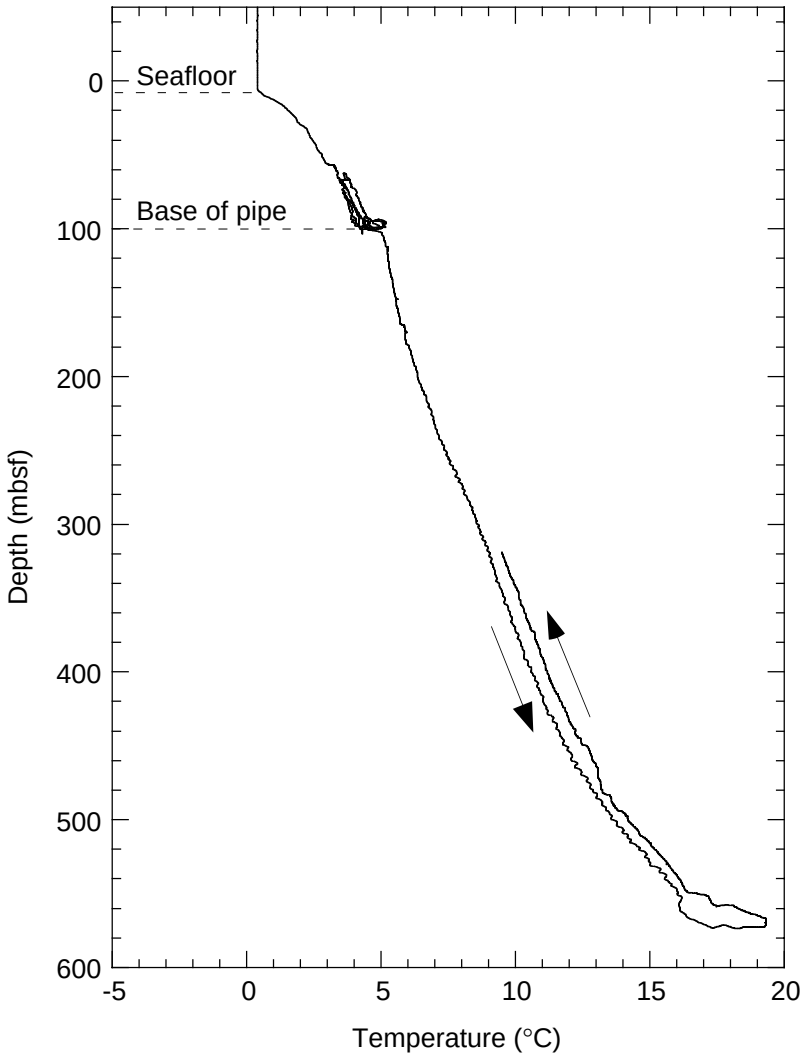

Figure F46. Location map of the moorings on Drift 7, indicating CTD stations, gravity cores, seismic profiles of the SEDANO program, and Leg 178 sites. Directions and relative intensities of mean currents are indicated by arrows.

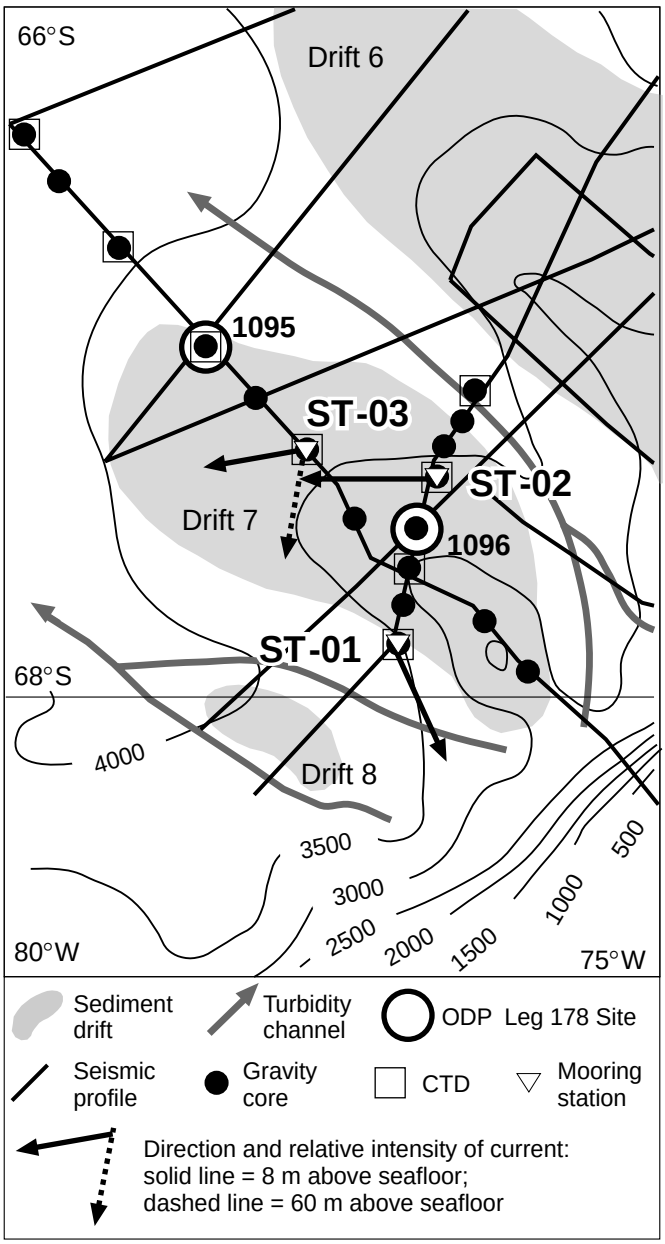

Figure F47. Progressive vector diagram of unfiltered current meter data from Mooring ST-03, at 8 and 60 m above the seafloor. Mooring ST-03 is located in Figure F46, p. 94.

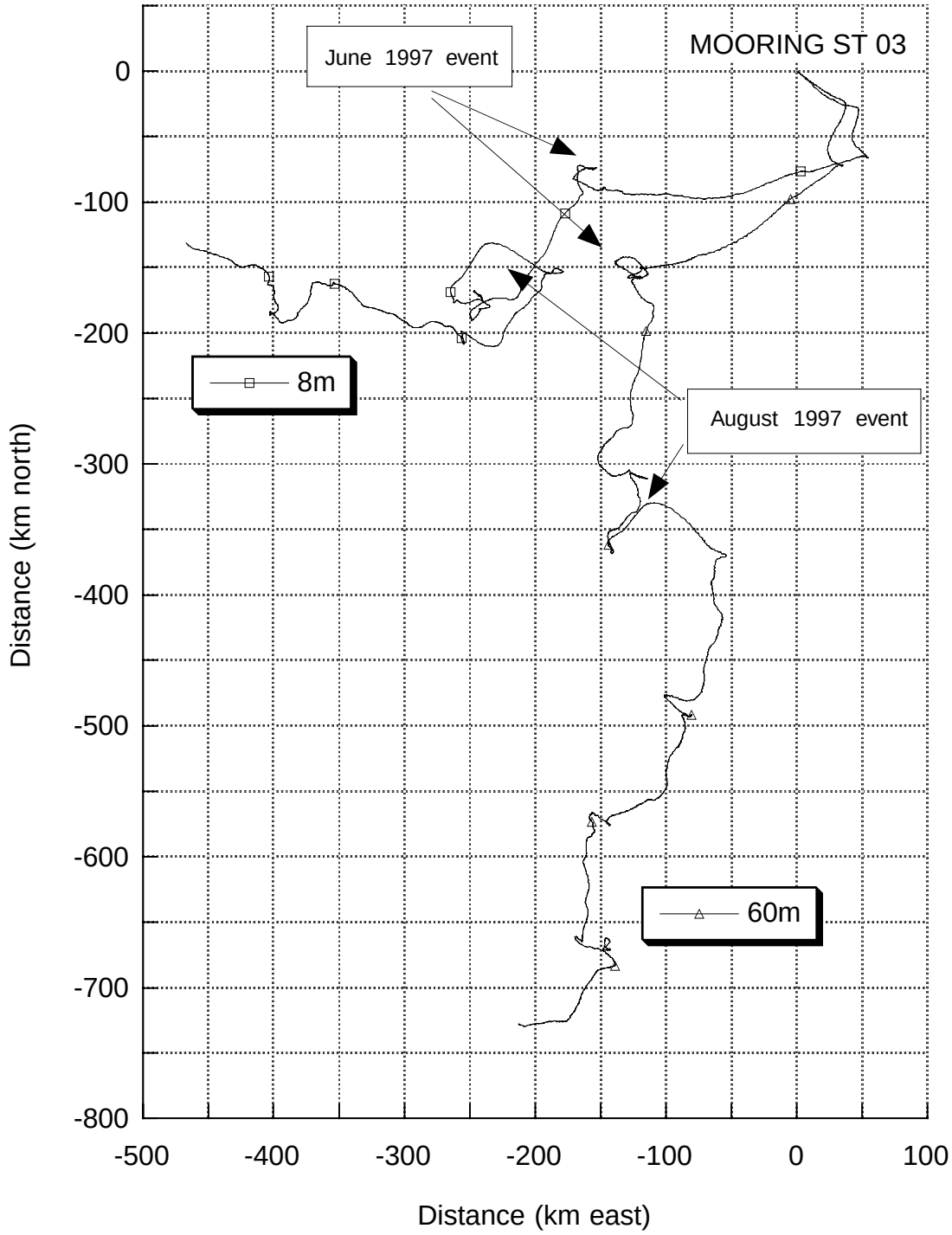

Figure F48. Depth offsets of Site 1095 mcd scale relative to mbsf depth, illustrating the growth of the composite depth scale. Crosses = Hole 1095A, circles = Hole 1095D, square = Hole 1095B.

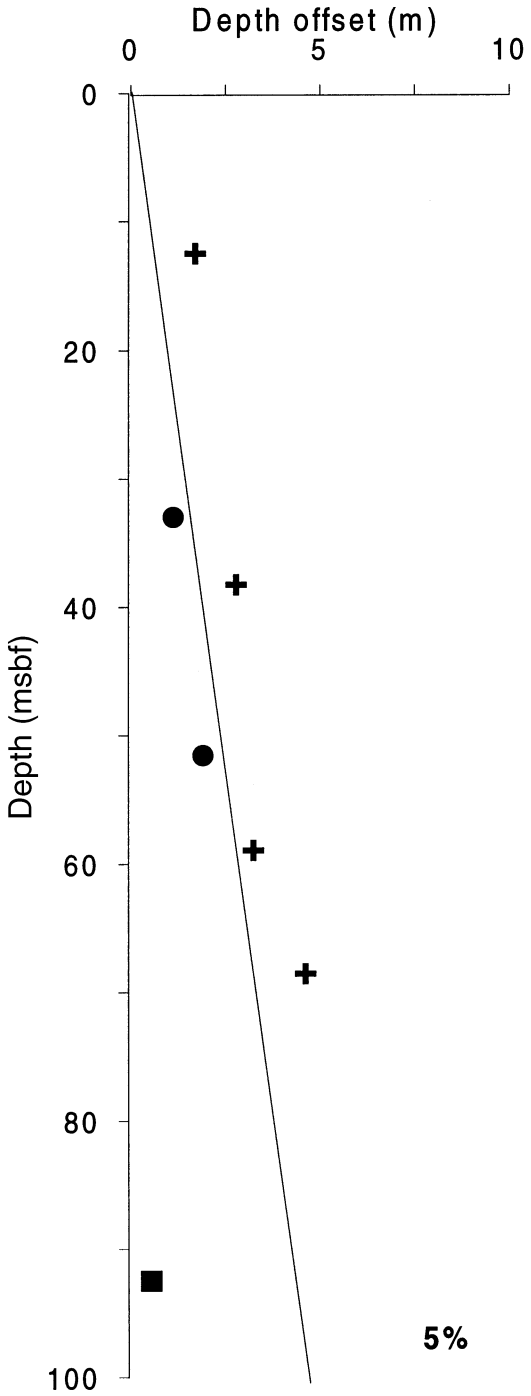

Figure F49. GRAPE density and magnetic susceptibility data from Site 1095 on the mcd scale. Records for Holes 1095A (dotted) and 1095B (dashed) have been horizontally offset from the record for Hole 1095D (solid) for display purposes. Therefore, values given on the horizontal scale are only correct for Hole 1095D.

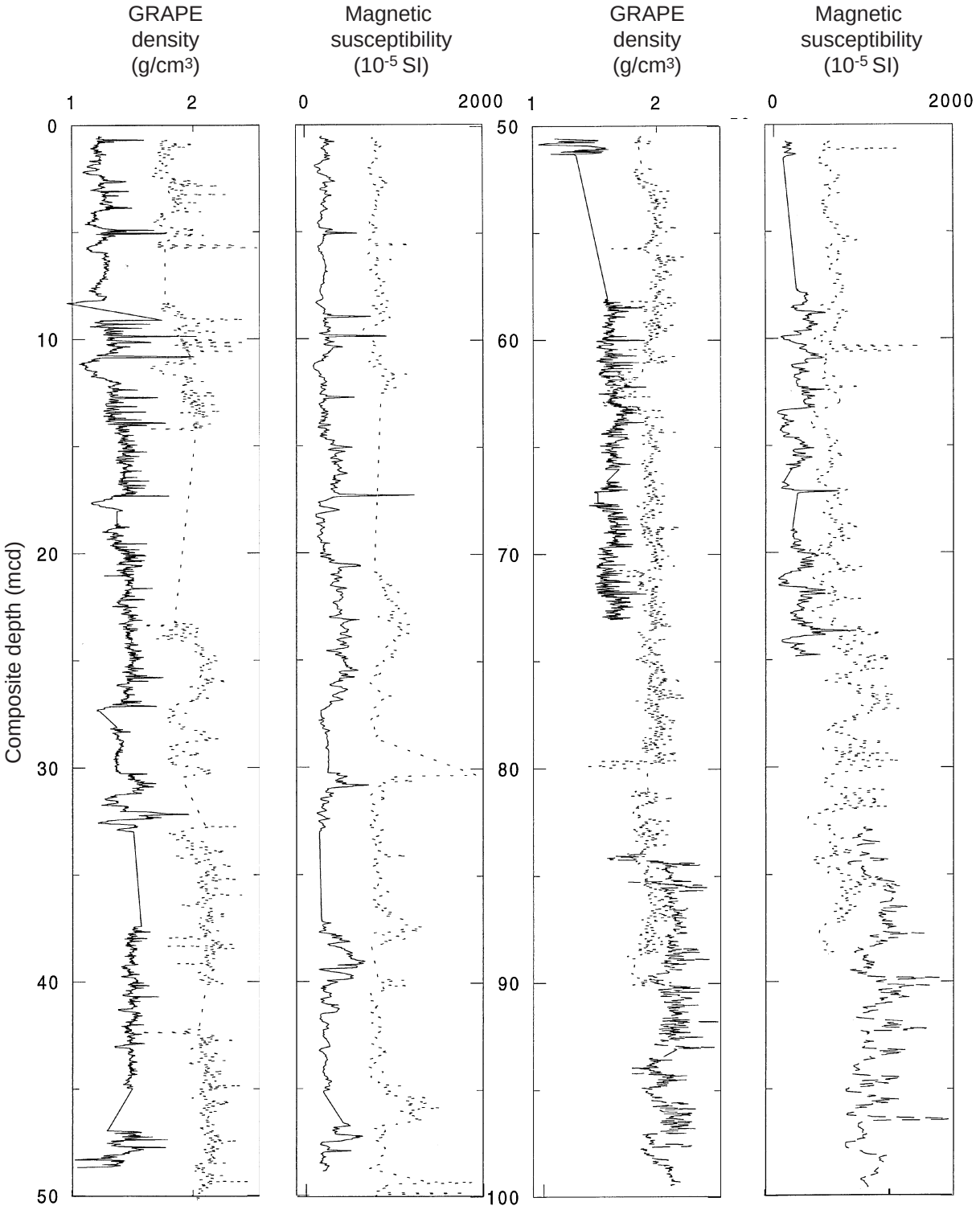

Figure F50. Correlated cyclic pattern of GRAPE density, magnetic susceptibility, chromaticity parameter a*, and *P*-wave data. Composite depths are preliminary (see **"Composite Depths,"** p. 23, in the "Explanatory Notes" chapter).

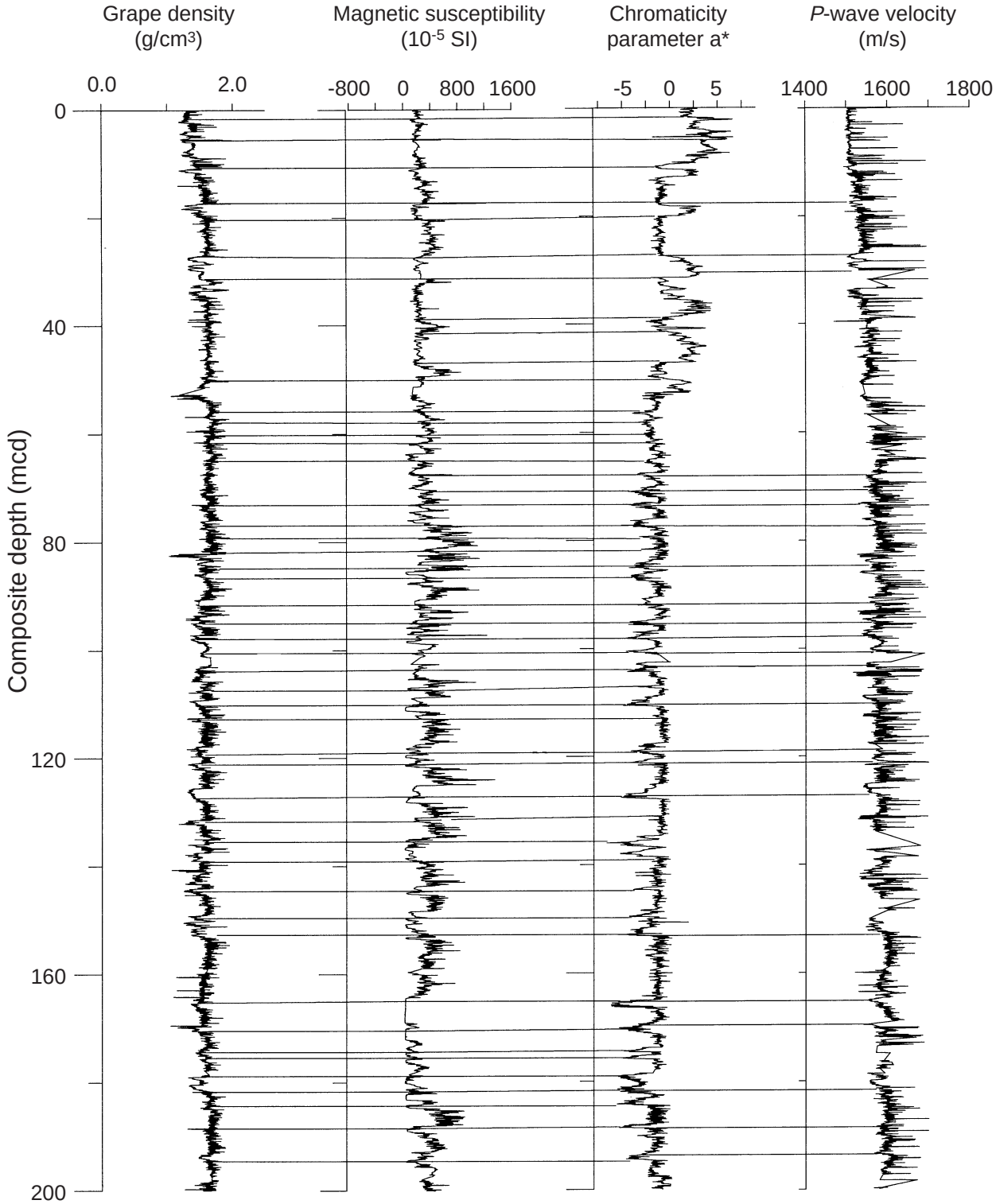

Figure F51. Spliced records of magnetic susceptibility and chromaticity parameter a* for Site 1095. Tie points for forming the splice are given in Table T37, p. 168.

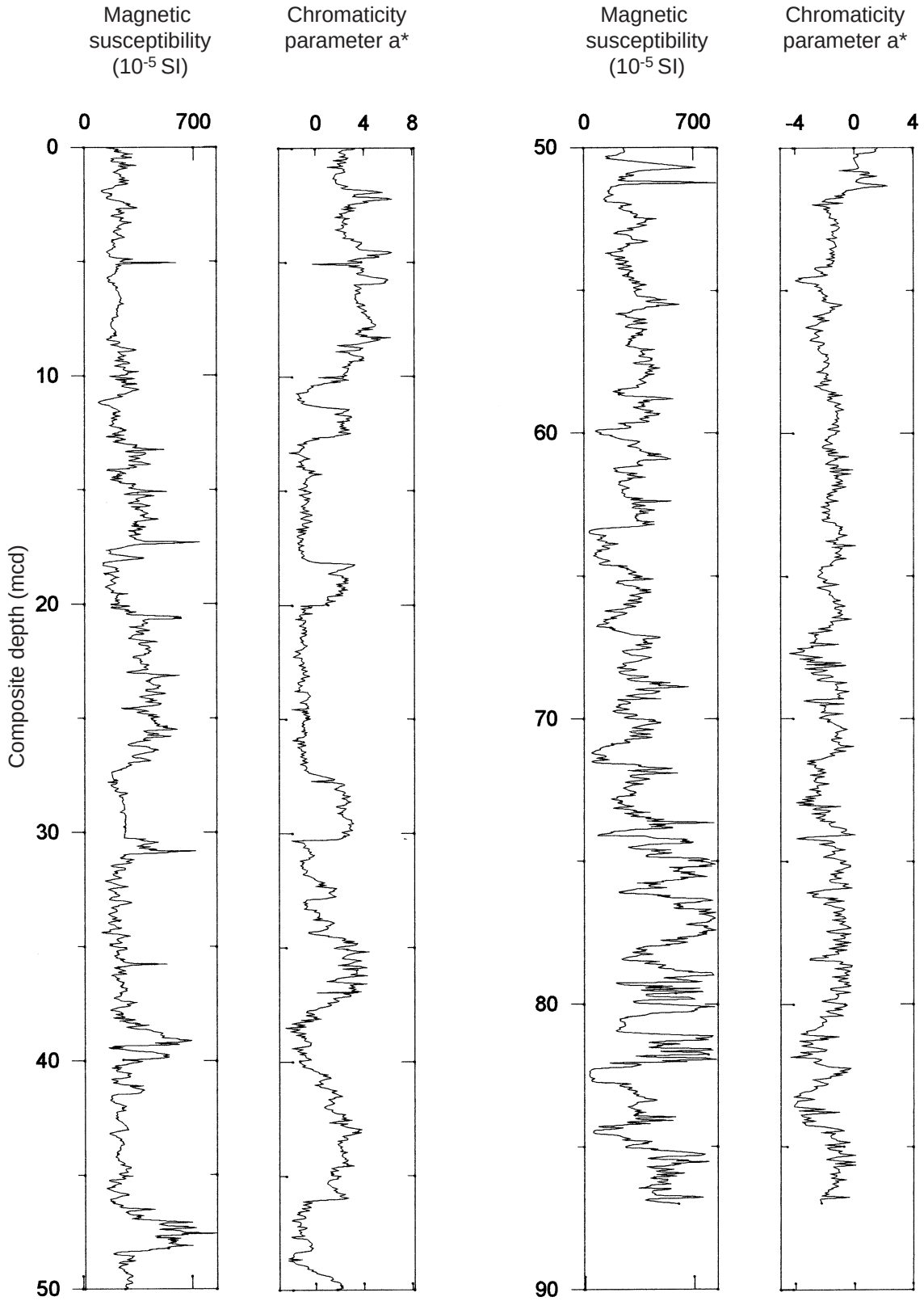

Figure F52. Depth-age profile determined from geomagnetic reversals and diatom and radiolarian datums. Paleomagnetic data were drawn from analysis of split-cores (× symbols) and GHMT logging data (diamonds). Separate curve fits for split-core (thin line) and GHMT data (heavy broken line) are interpolations that pass through all data points within the individual data set and match the slopes at those points. Intervals of diatom datums are marked with a box indicating the distance between the samples used to define the LO or FO interval. *P. sulcata* abundance is indicated by gray shaded bars. Radiolarian datums are indicated with a circle. In labels indicating species identity, T = last occurrence, B = first occurrence, and TC = top common occurrence. The hole is barren of microfossils below ~520 mbsf. Mean sedimentation rates (underlined) determined for three intervals show an uphole decrease.

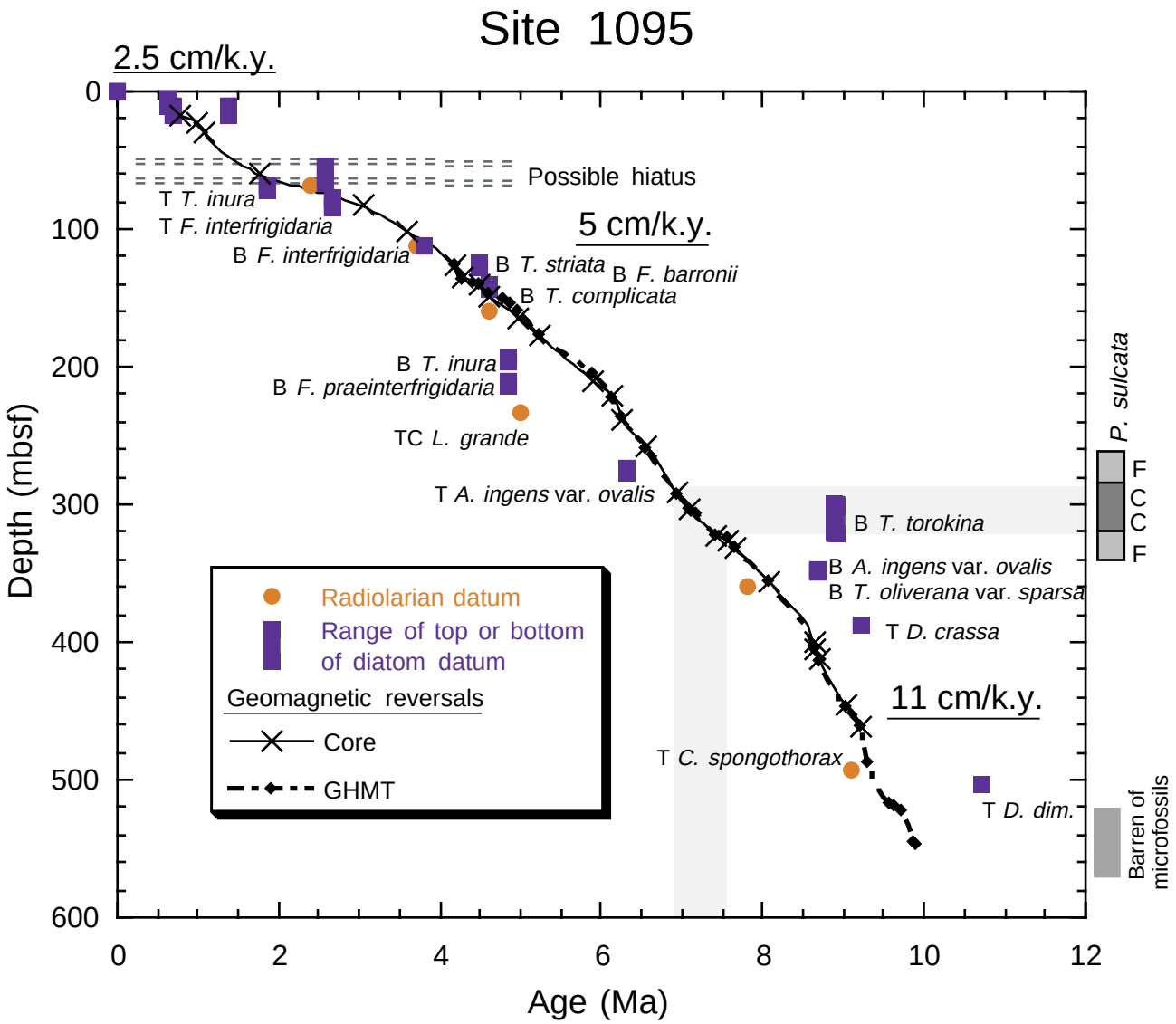

Figure F53. Sedimentation rate (cm/k.y.) vs. depth (mbsf) determined from geomagnetic polarity transitions and diatom and radiolarian datums for Site 1095. The data are given in Tables **T38,** p. 169, **T39,** p. 171, and **T40,** p. 172. The heavy line represents paleomagnetic data from the combined core and GHMT data set, the dashed line indicates radiolarian data, and the thin line is diatom data. The abrupt spike in the paleomagnetic data at ~400 mbsf corresponds to an interval that has been interpreted as a cryptochron and whose absolute age and duration is not well known (see **"Paleomagnetism,"** p. 16).

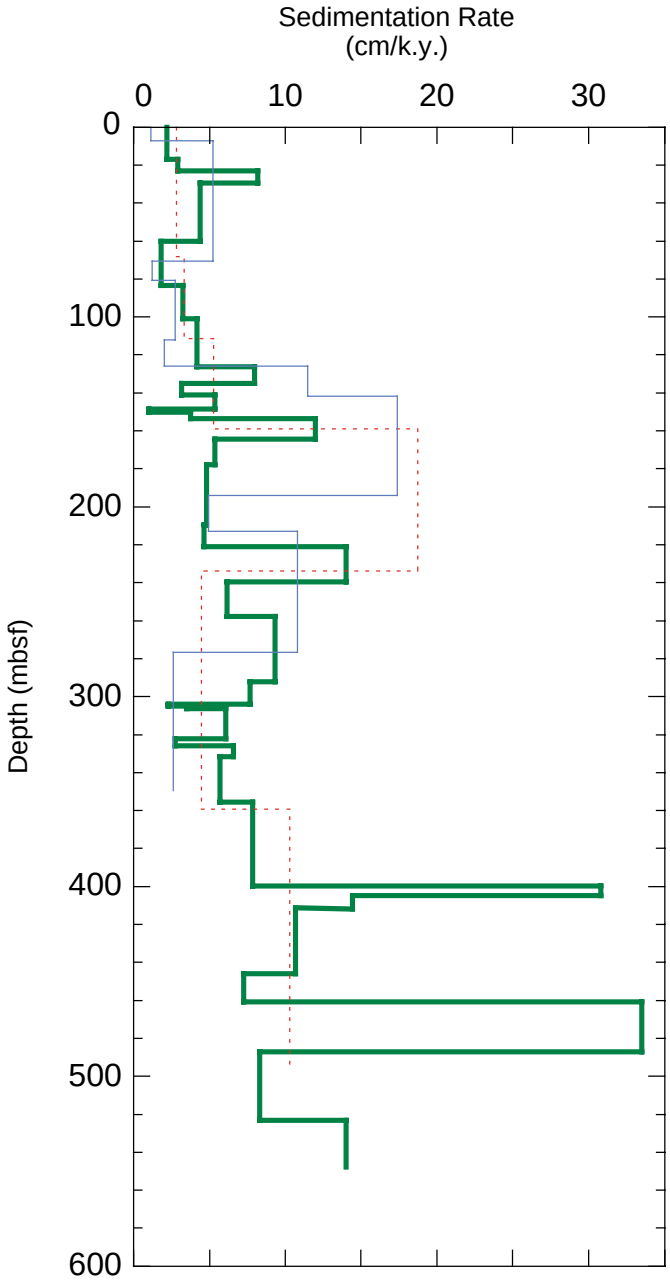

Figure F54. Sedimentation rate (cm/k.y.) vs. age (Ma) determined from geomagnetic polarity transitions and diatom and radiolarian datums for Site 1095. The top of the hole was assigned an age of zero. The data are given in Tables **T38,** p. 169, **T39,** p. 171, and **T40,** p. 172. The heavy line represents paleomagnetic data from the combined core and GHMT data set, the dashed line indicates radiolarian data, and the thin line is diatom data. The abrupt spike in the paleomagnetic data at 8.635–8.651 Ma corresponds to an interval that has been interpreted as Cryptochron C4r.2r-1. However, the age of this event is based on sparse data from marine magnetic anomalies (see **"Paleomagnetism,"** p. 16).

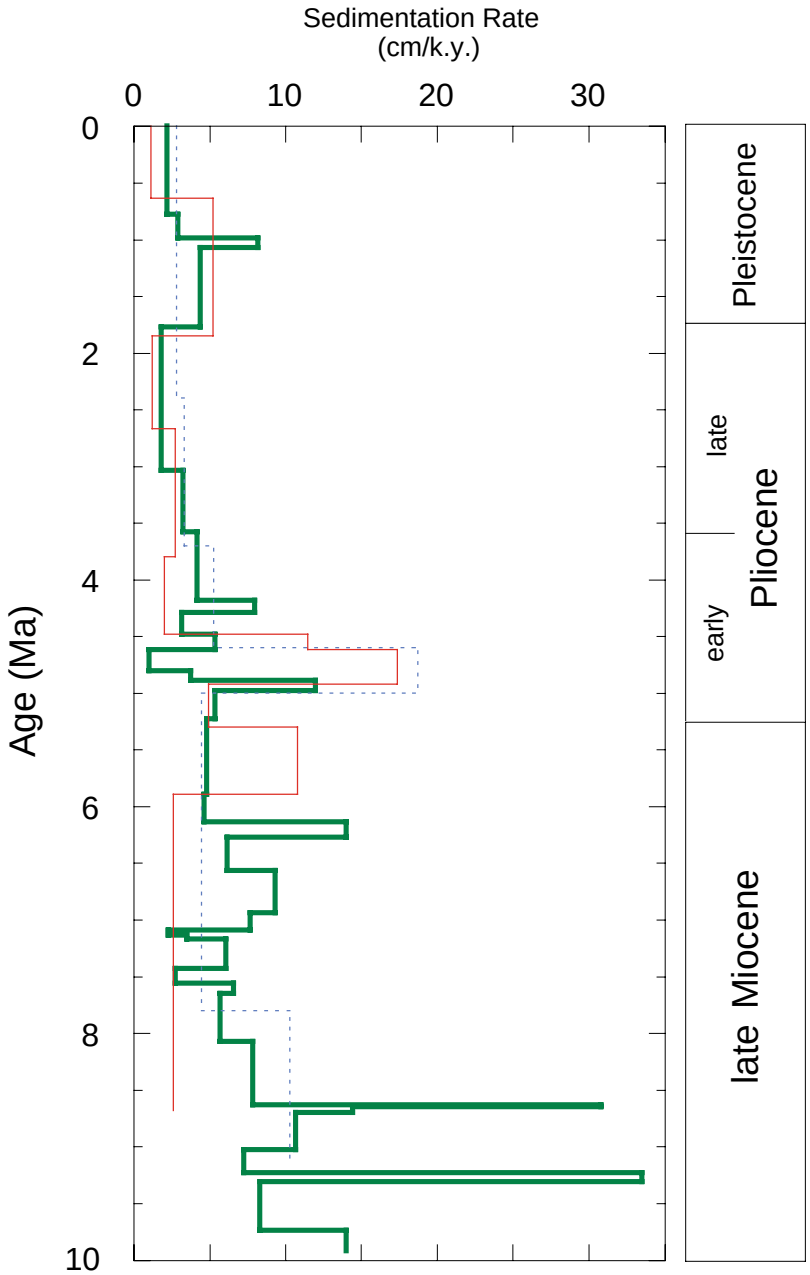

Figure F55. Comparison of different density data sets for Site 1095.

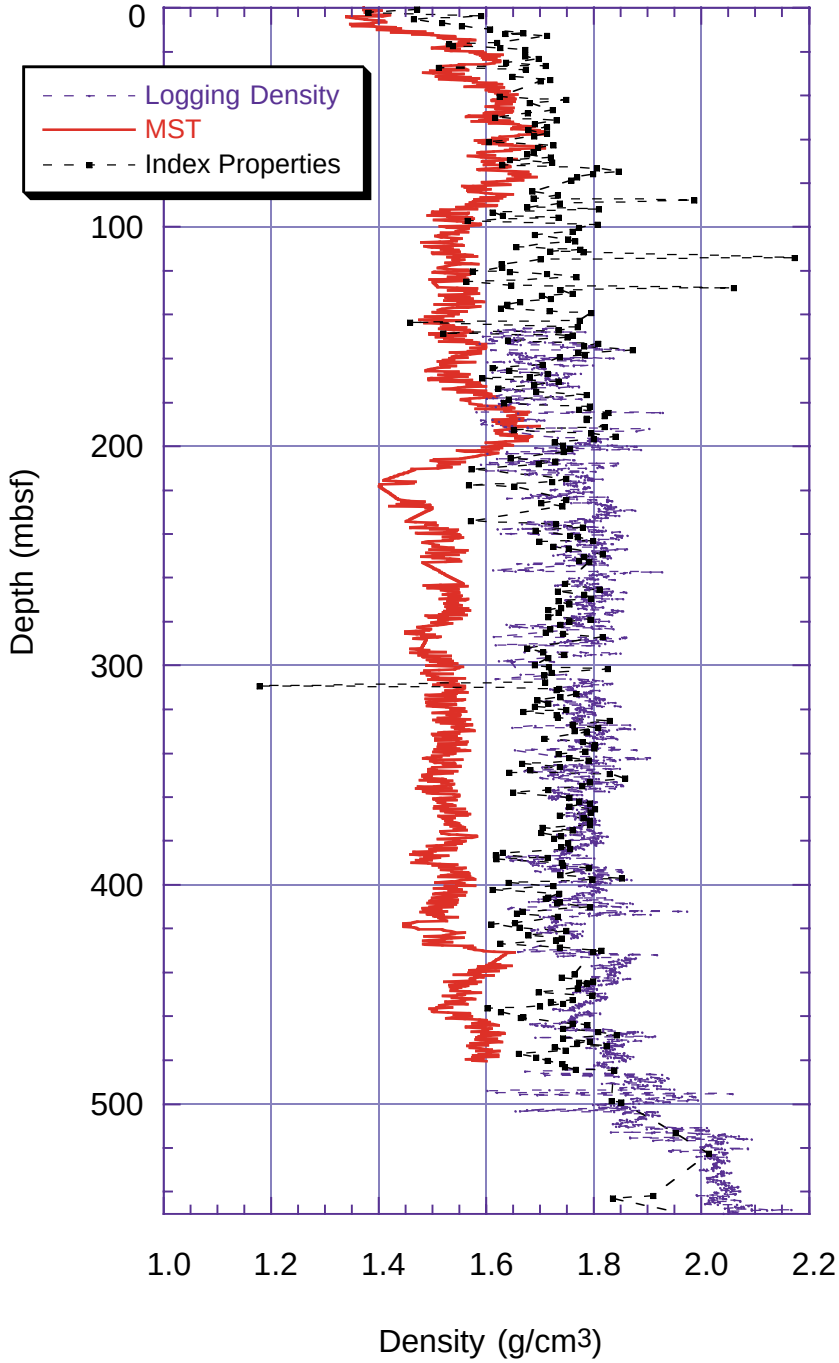

Figure F56. Comparison of MST, downhole logging, and index properties velocities used for different modeling approaches, Site 1095.

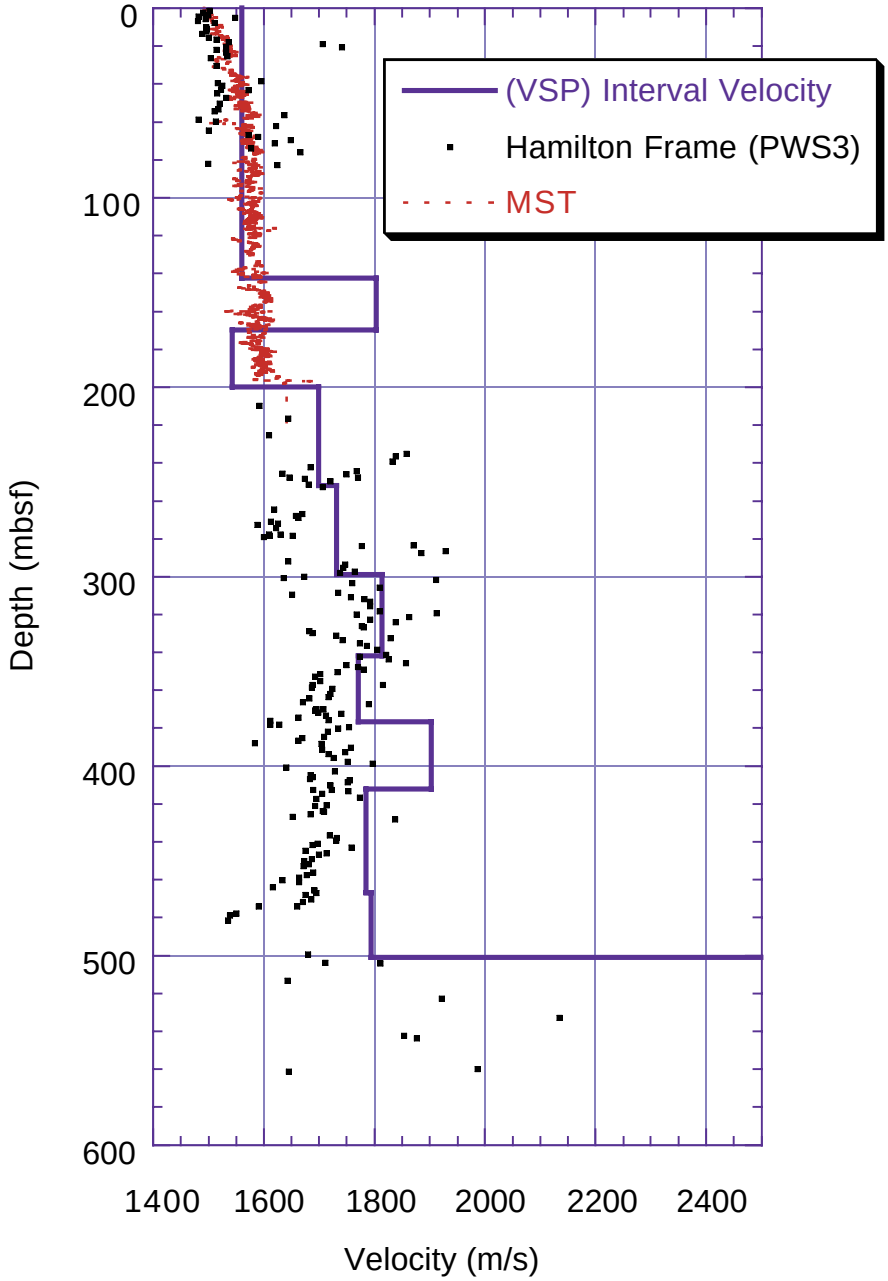

Figure F57. Source signals and their characteristics.

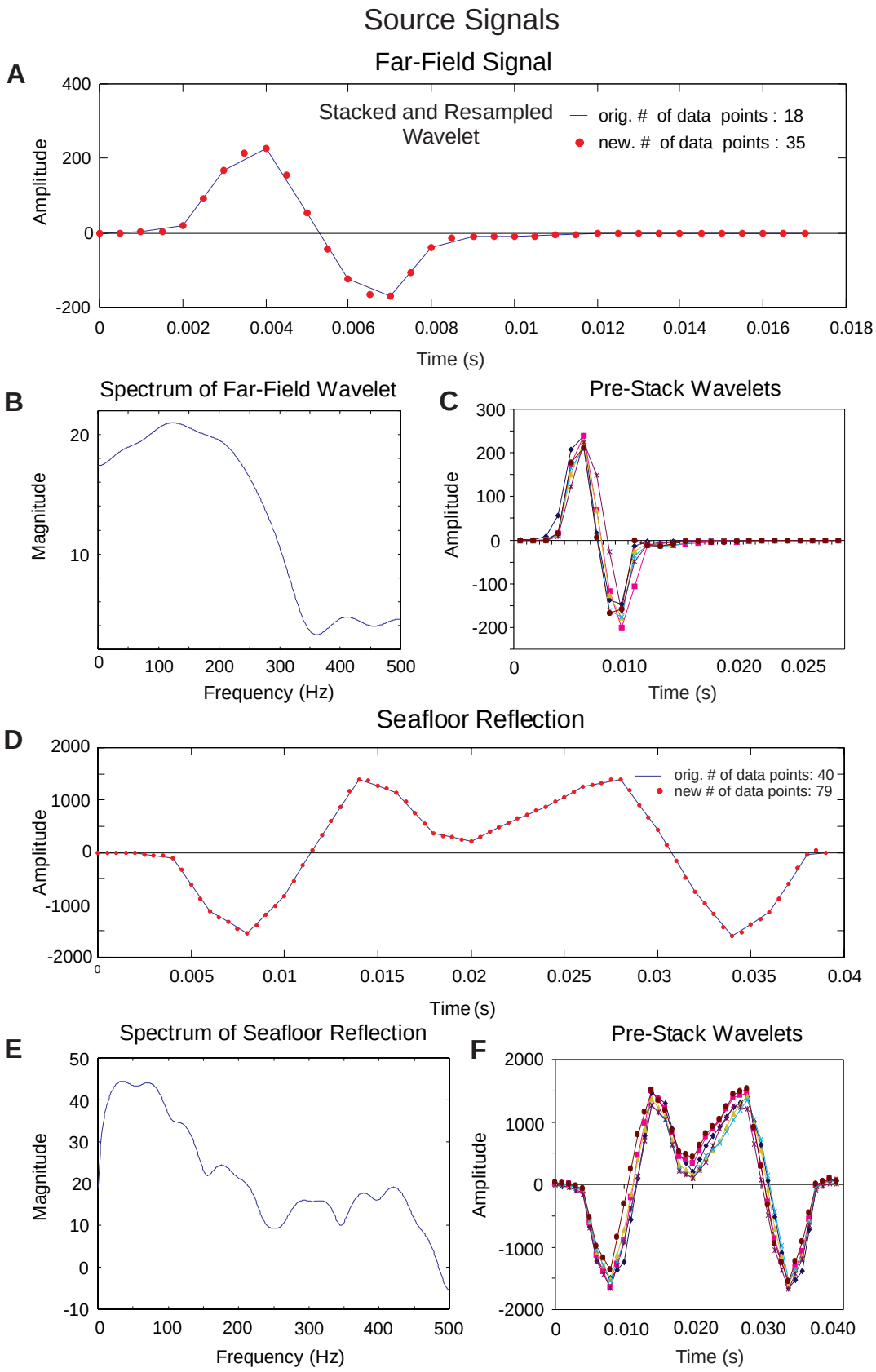

Figure F58. Seismostratigraphic interpretation of Site 1095 and display of the VSP traces.

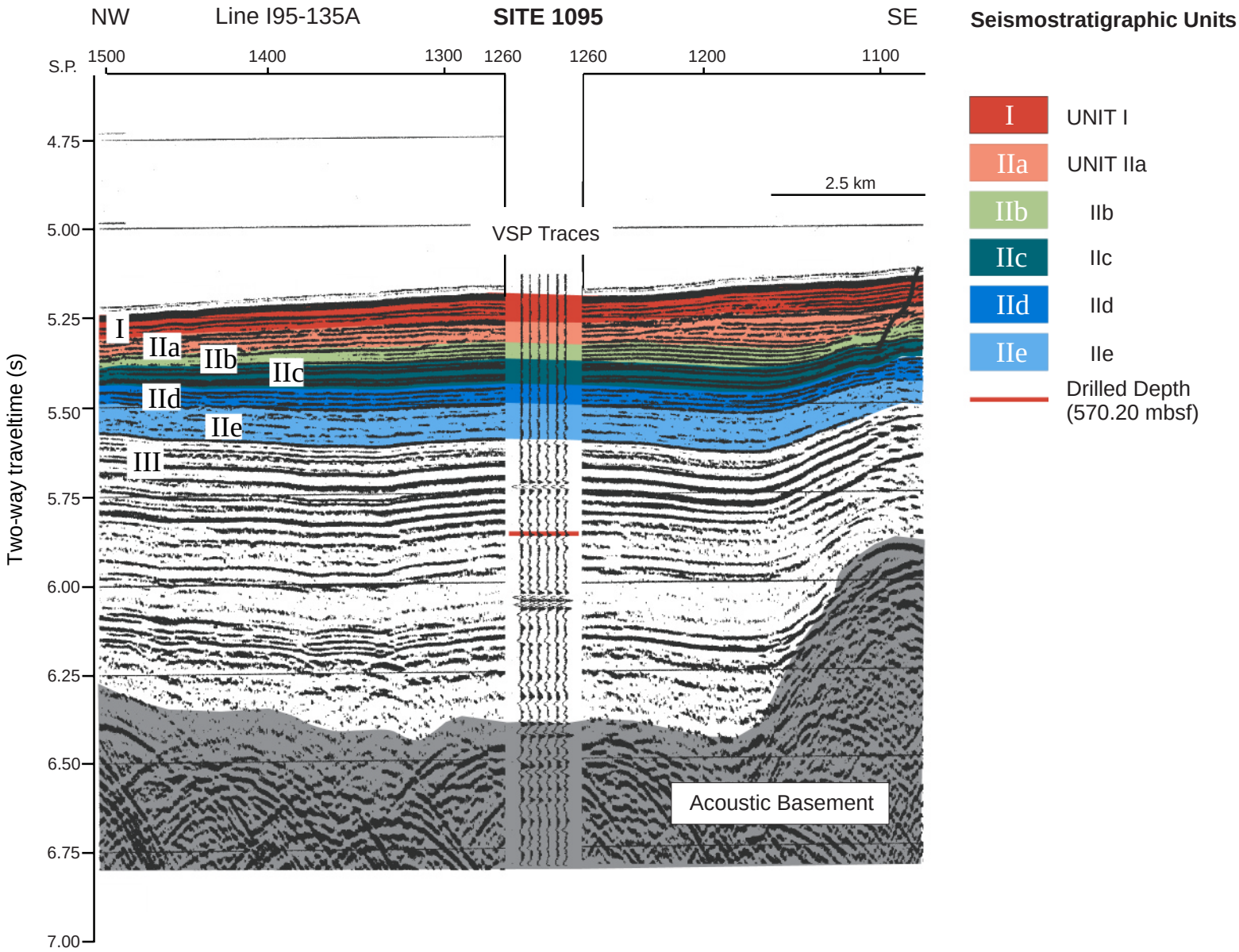

Figure F59. Traveltime depth models for Site 1095. The Carlson et al. (1986) approximation and the observed traveltime during the VSP experiment are in good agreement.

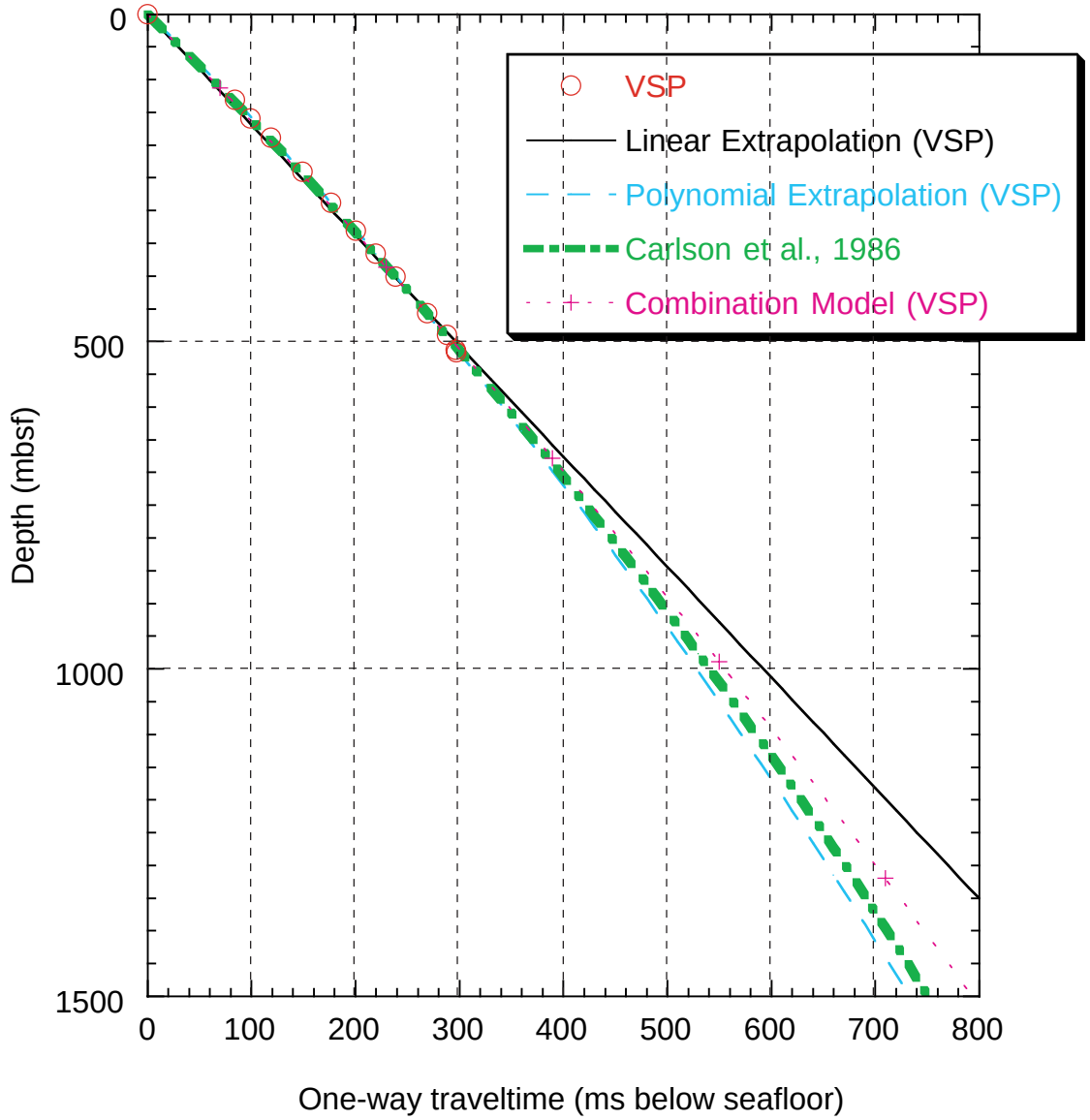

Figure F60. Unfiltered synthetic seismograms for far-field and seafloor signals (Model A).

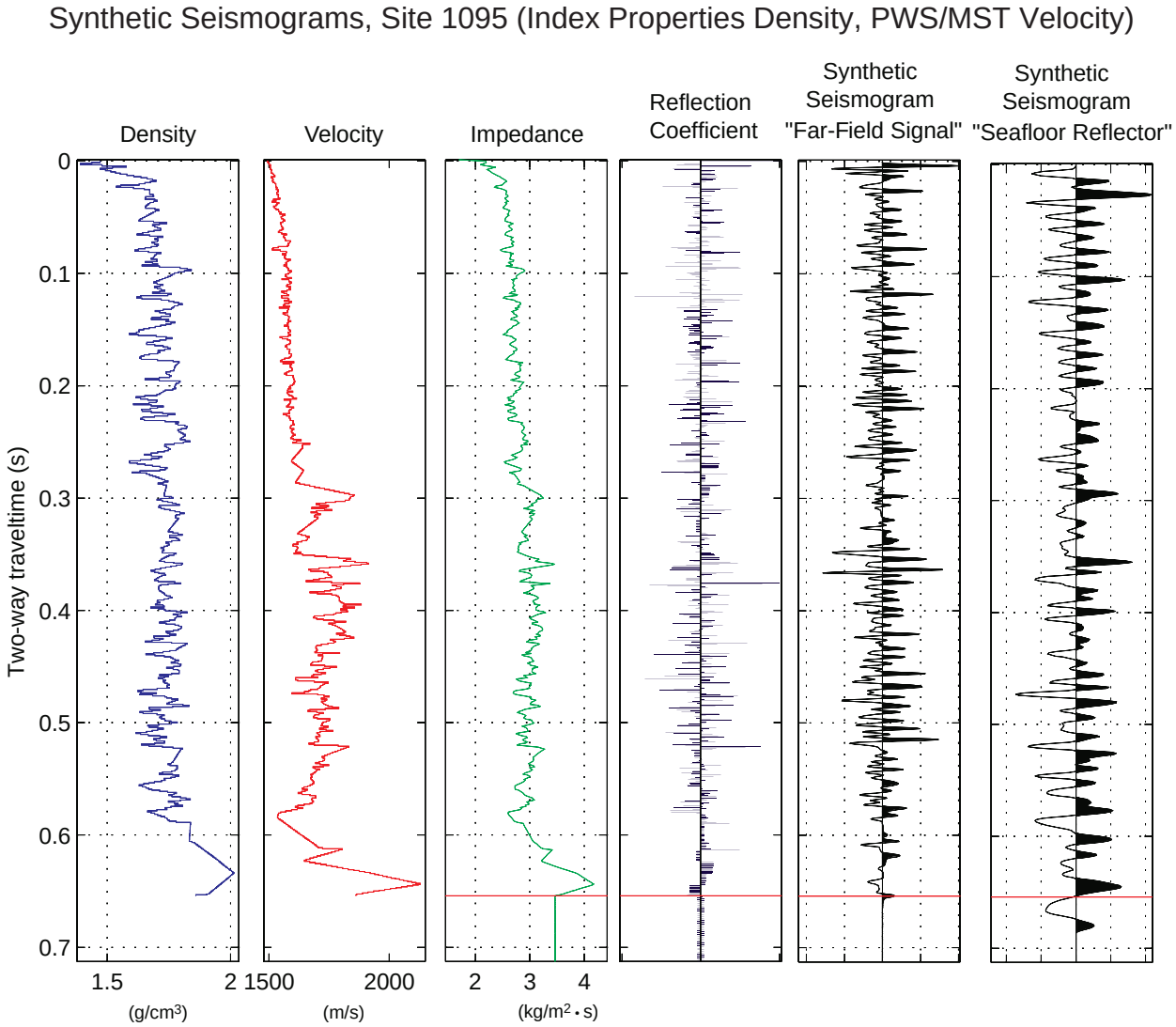

Figure F61. Unfiltered synthetic seismograms for far-field and seafloor signals (Model B).

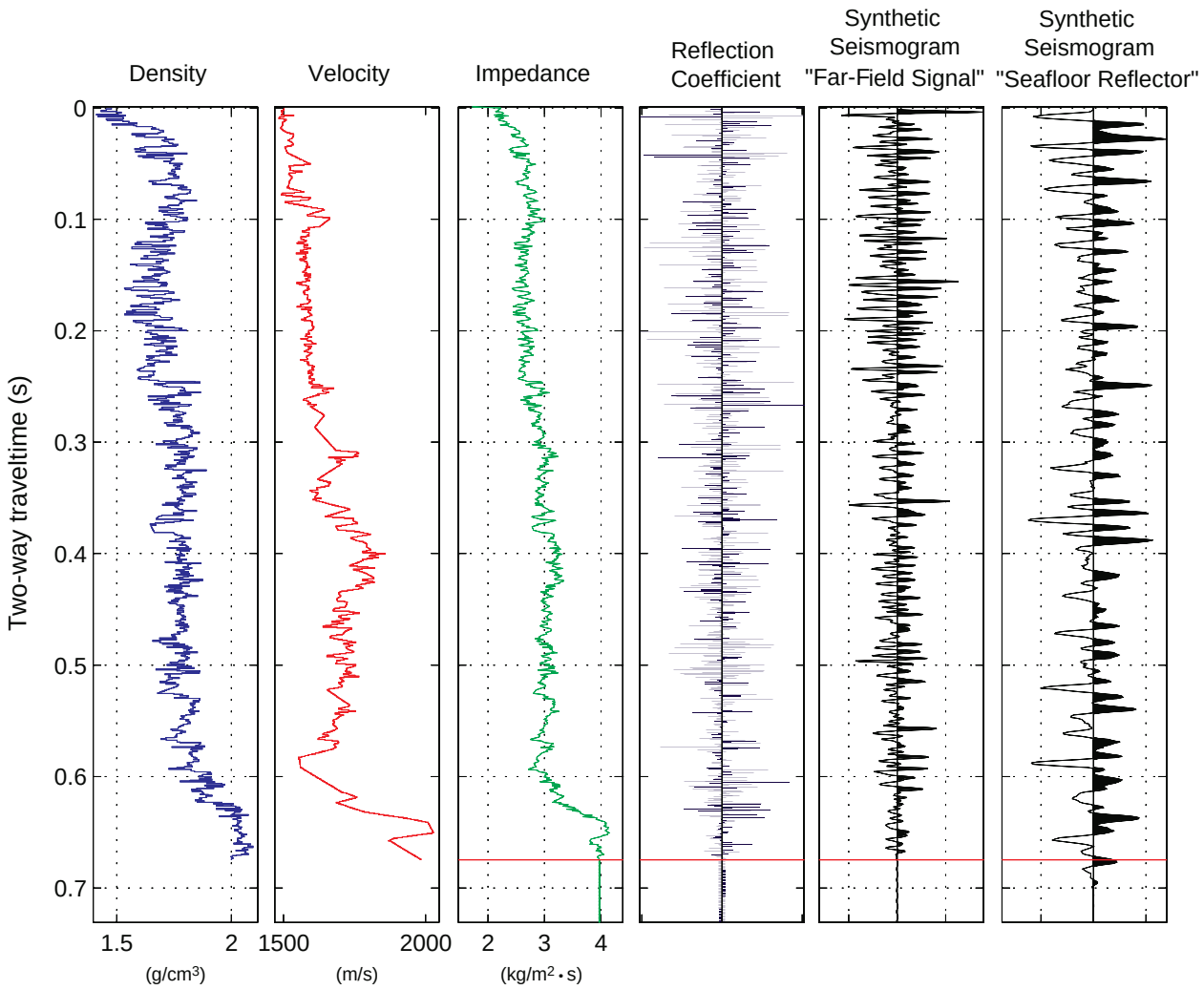

Figure F62. Comparison of the input and output frequency spectra of Model A.

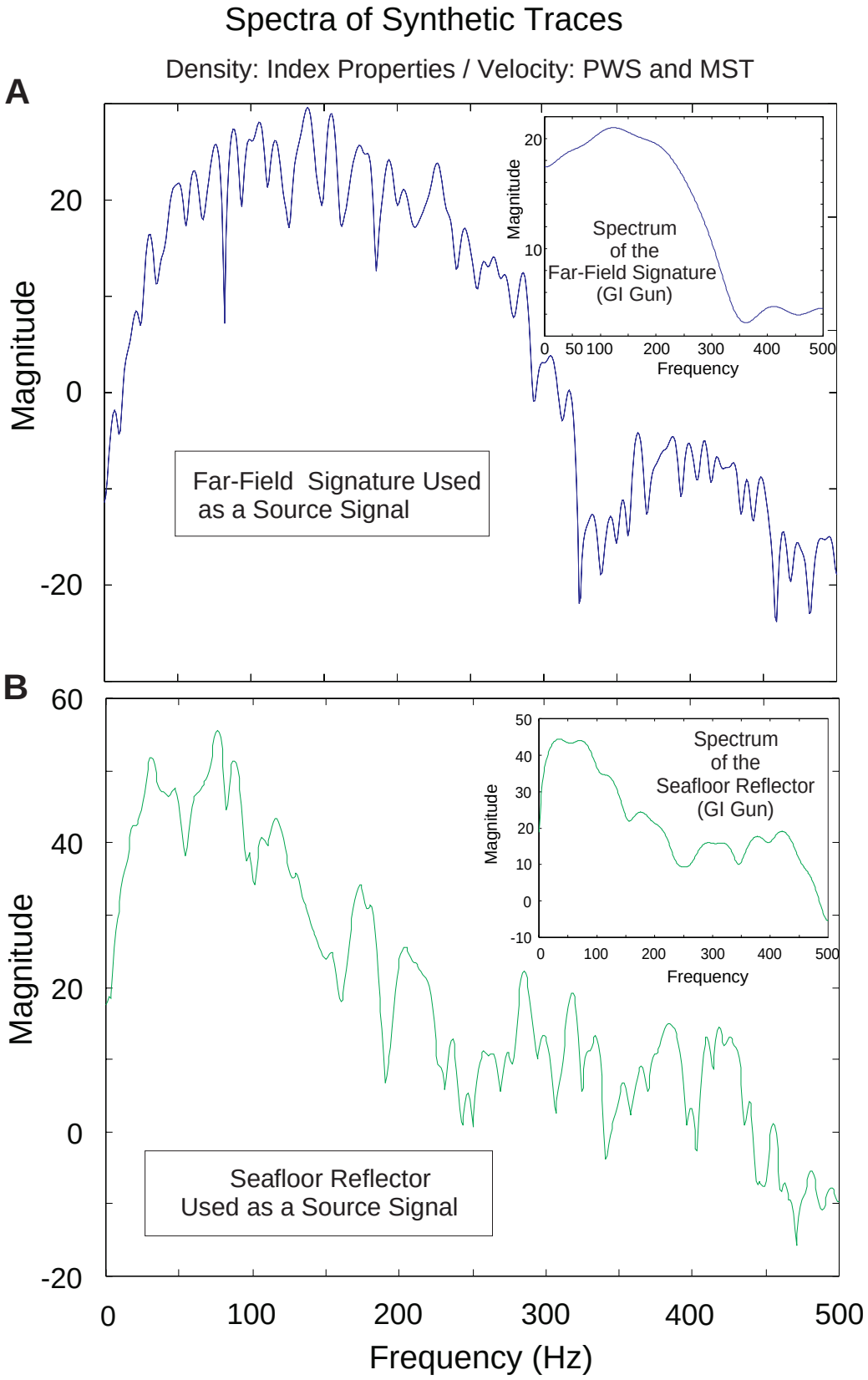

Figure F63. Filter characteristics used to filter the synthetic trace of Model A (far-field source signal).

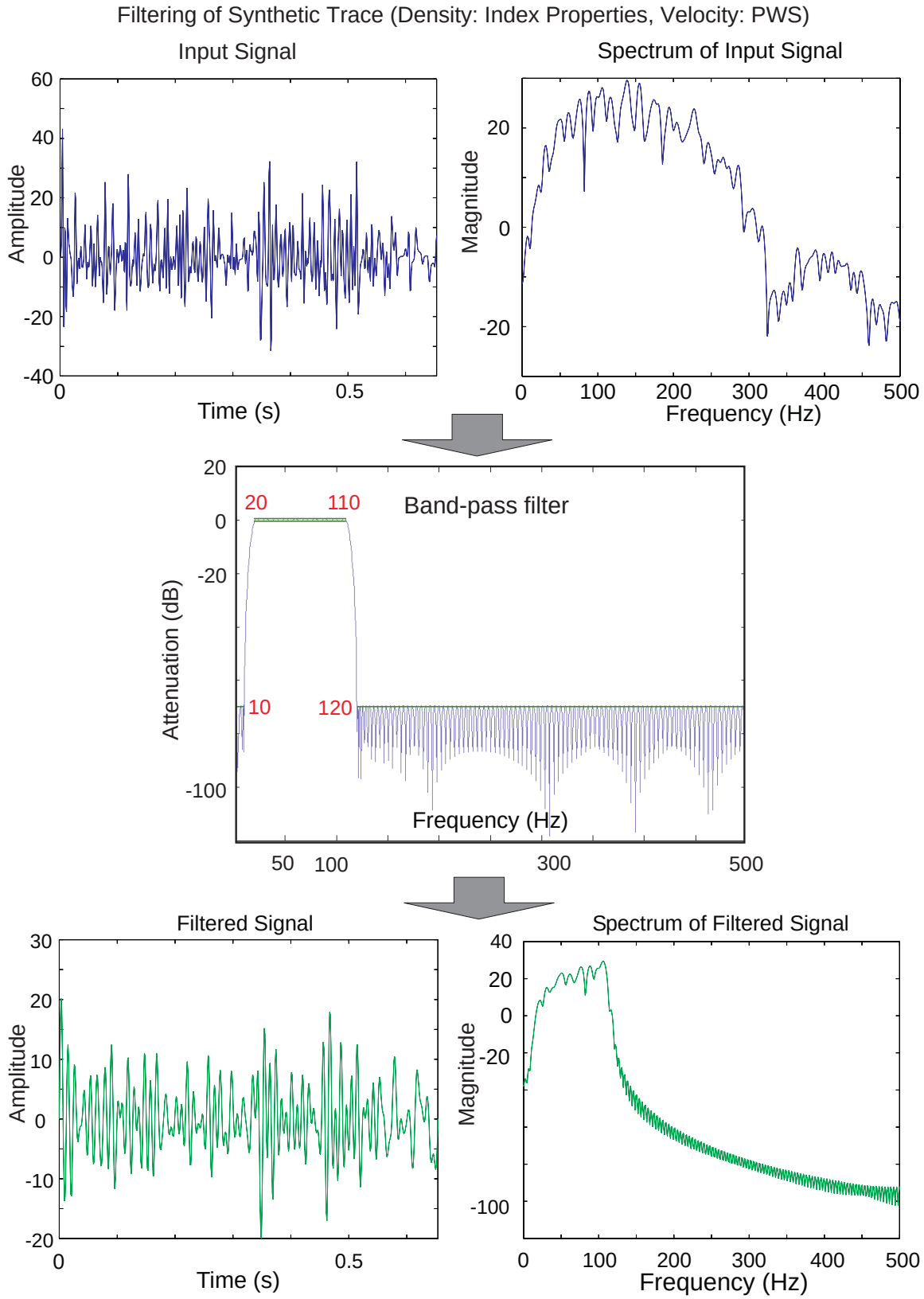

Figure F64. Comparison of the synthetic traces for Model A (far-field source signal) and digital data of survey line I95-135A.

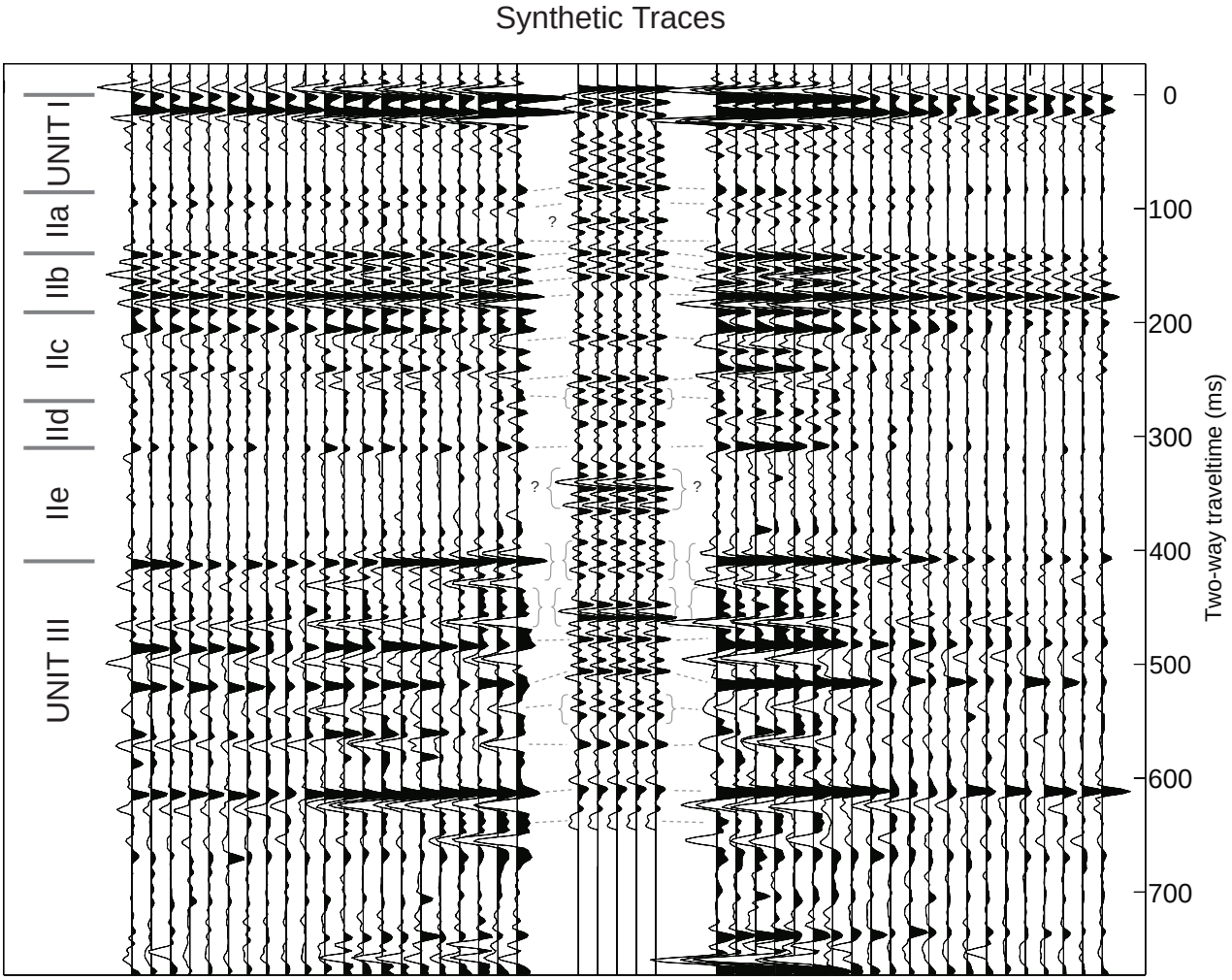

Figure F65. Comparison of the synthetic traces for Model A (seafloor source signal) and digital data of survey line I95-135A.

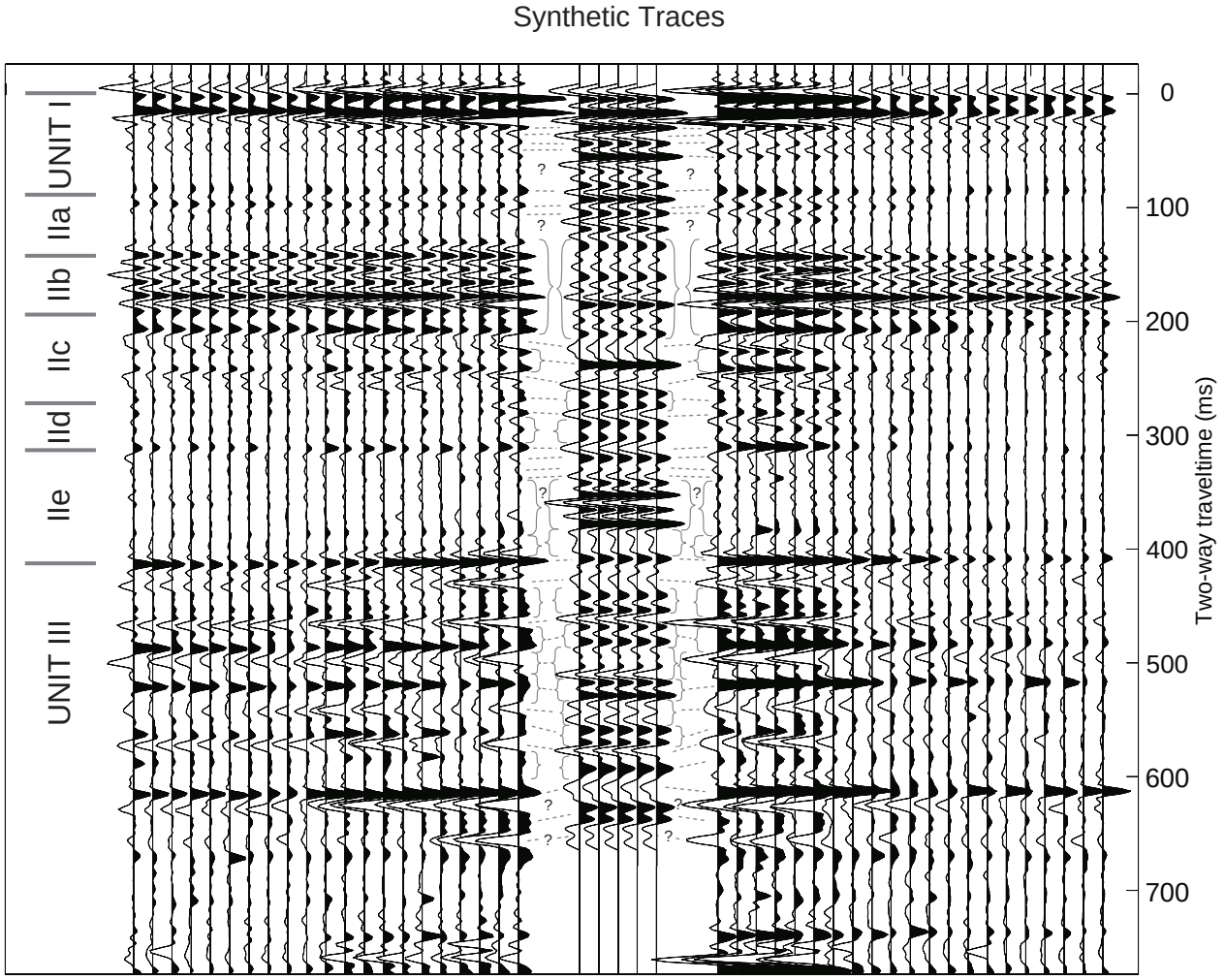

Figure F66. Comparison of the synthetic traces for Model B (far-field source signal) and digital data of survey line I95-135A.

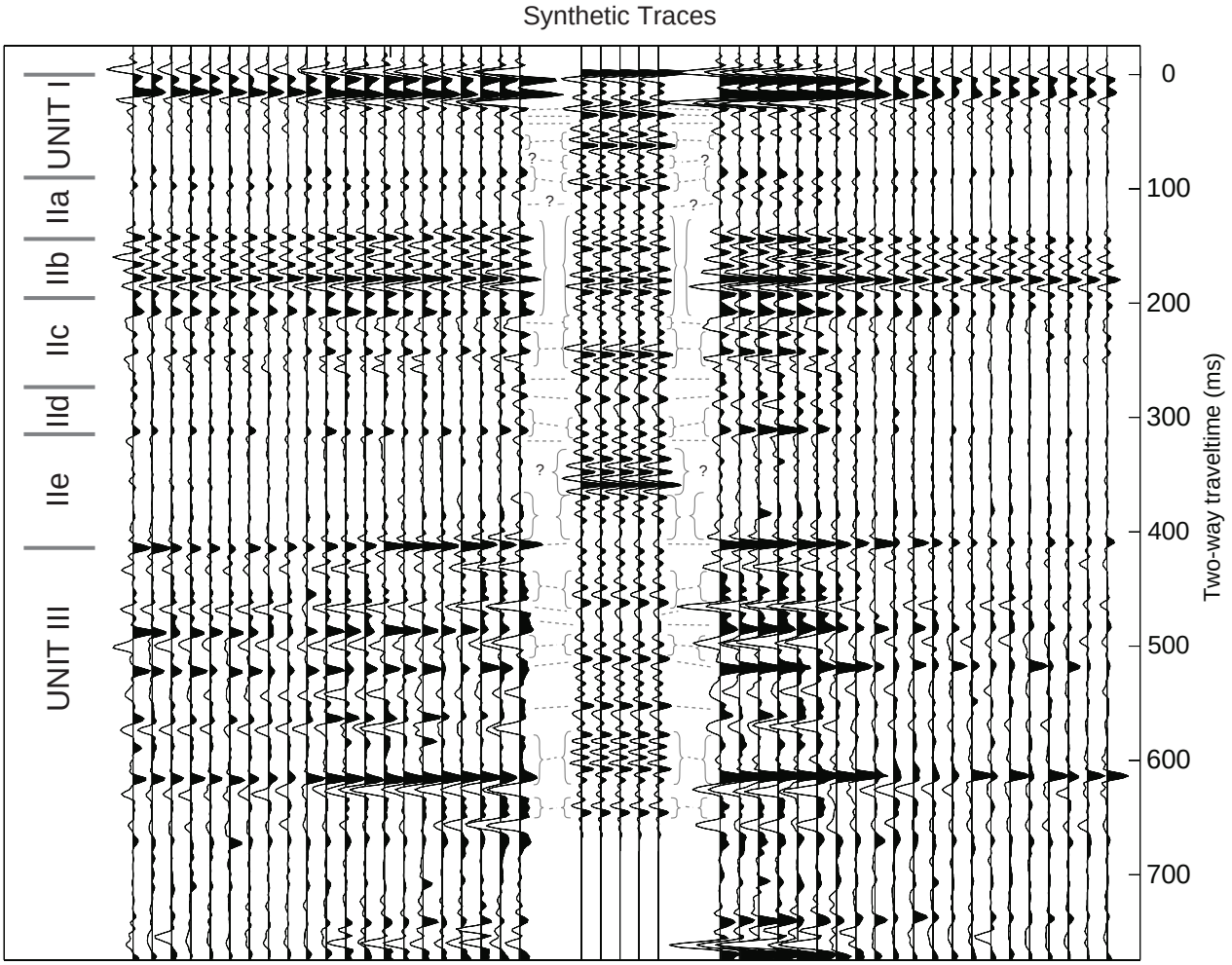

Figure F67. Comparison of the synthetic traces for Model B (seafloor source signal) and digital data of survey line I95-135A.

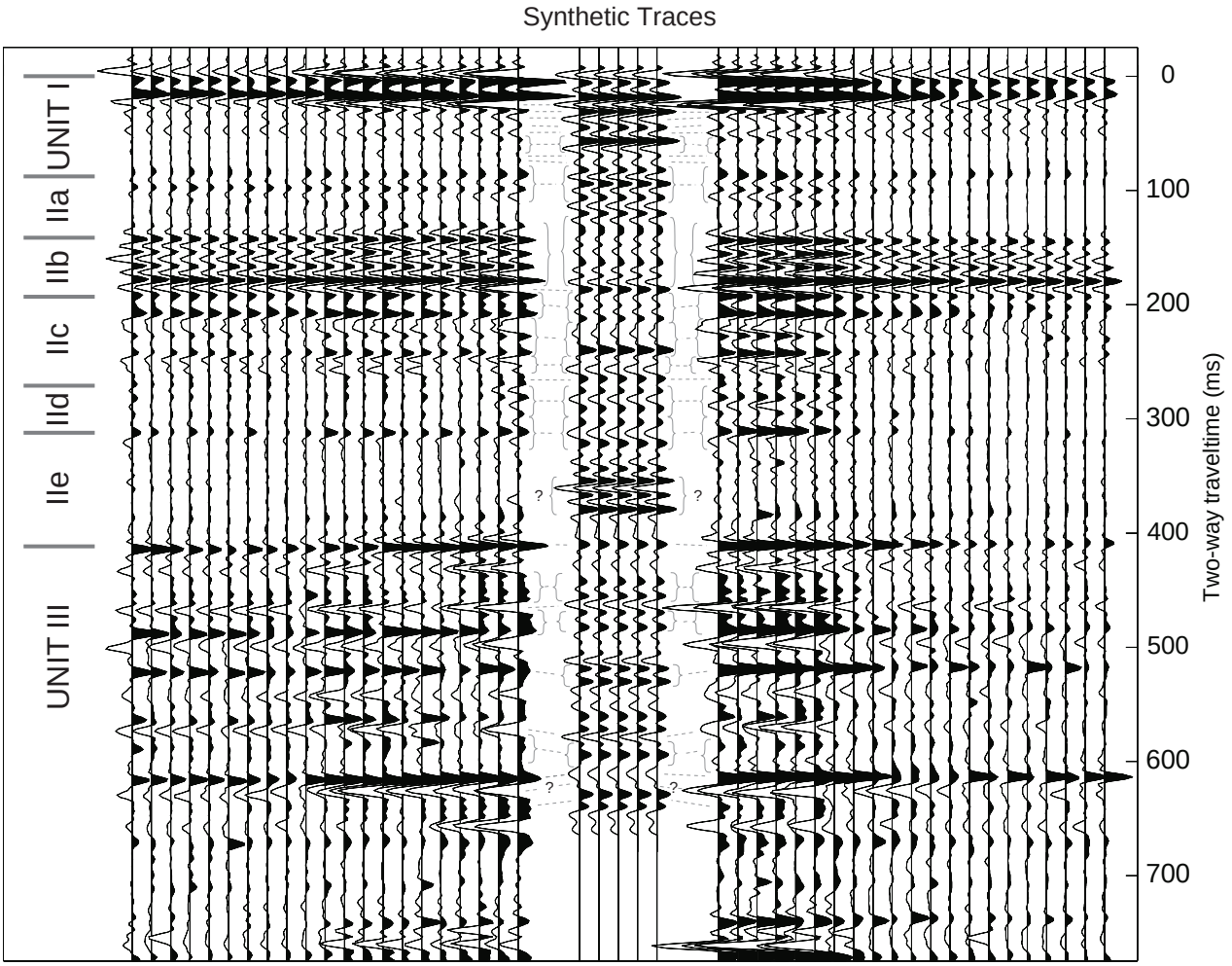

Figure F68. MCS profile across Site 1095 oriented parallel to the margin. Seismic stratigraphic units defined from drilling are also shown.

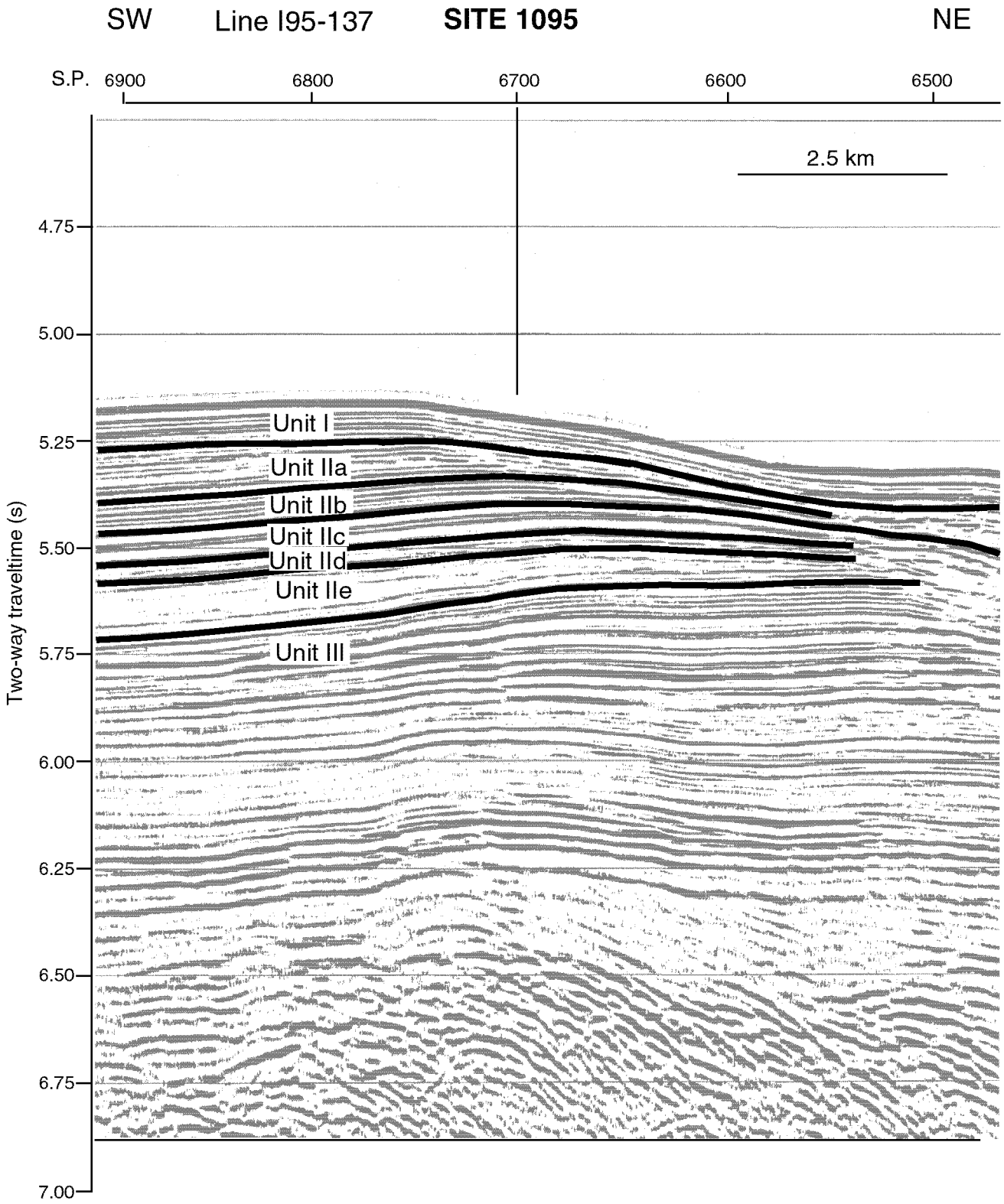

Figure F69. MCS profile across Site 1095 oriented perpendicular to the margin. Seismic stratigraphic units defined from drilling are also depicted.

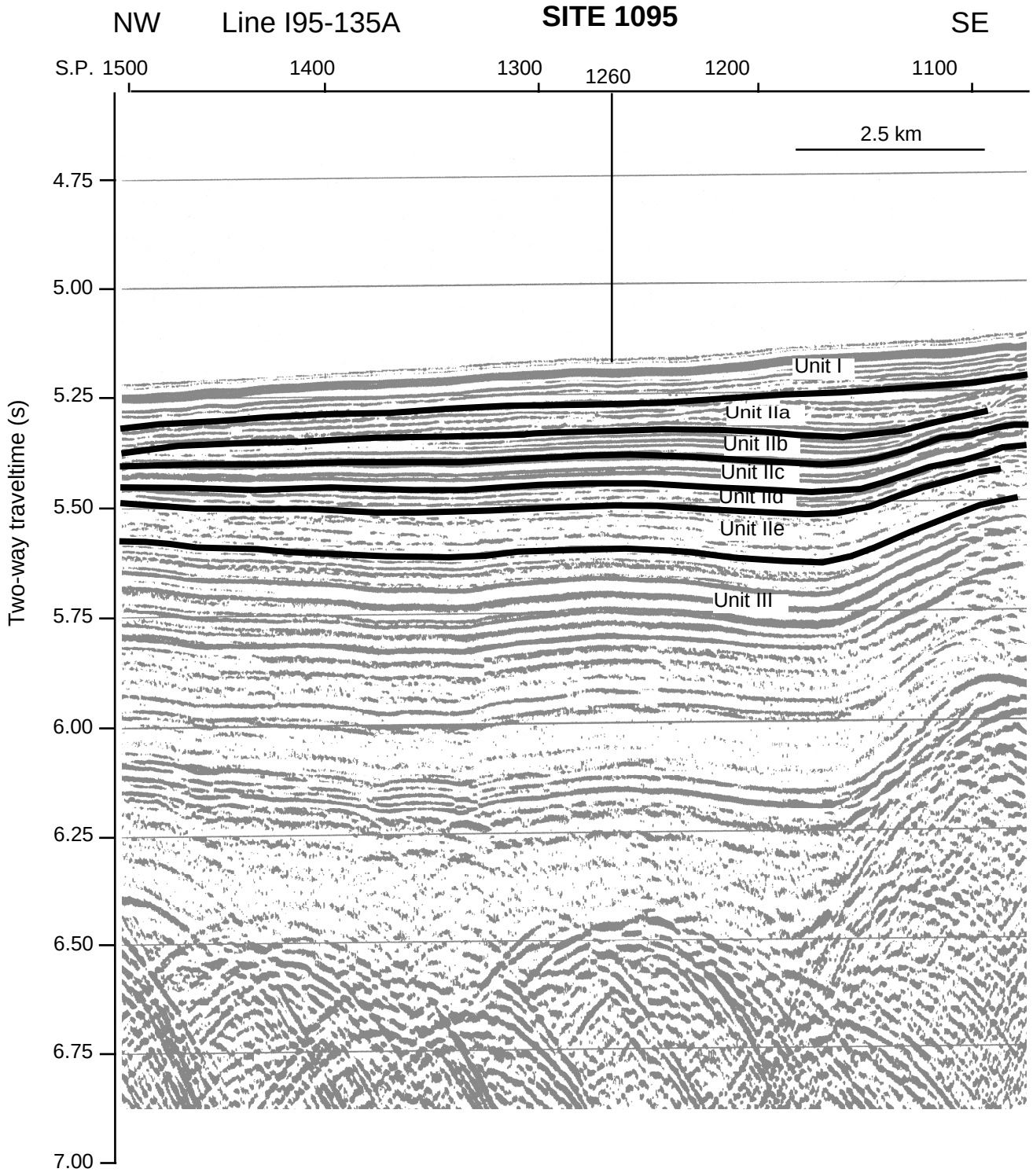

Figure F70. Seismic section over Site 1095 showing seismic units, depths to major lithologic units, and ages.

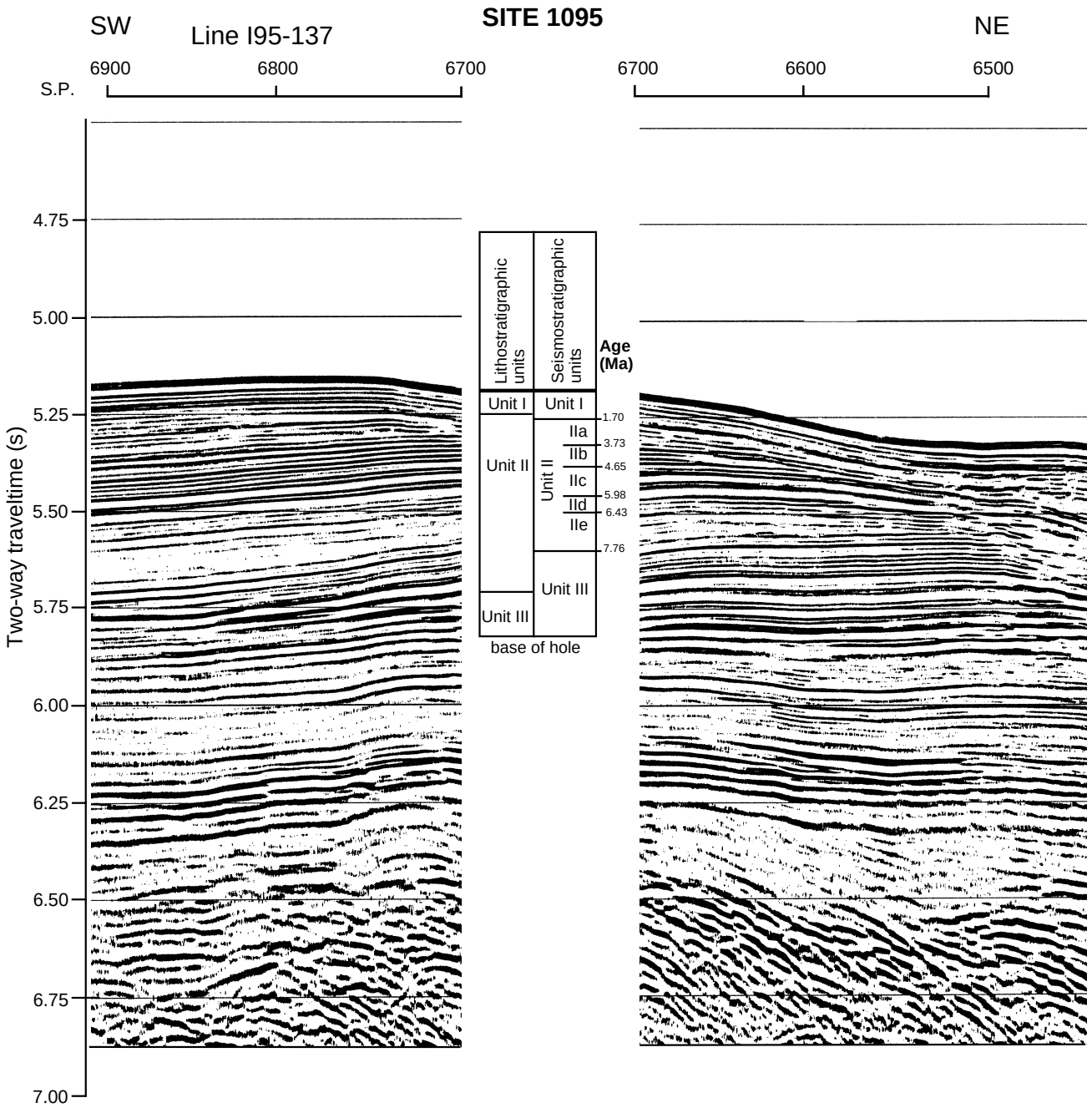

Table T1. Site 1095 coring summary. (See table note. Continued on next page.)

Core	Date (Feb 1998)	Time (UTC)	Depth (mbsf)	Length cored (m)	Length recovered (m)	Recovery (%)
178-1095A-						
1H	18	0900	0.0-5.9	5.9	5.88	99.7
2H	18	1020	5.9-11.3	5.4	6.80	125.9
3H	18	1120	11.3-20.8	9.5	8.71	91.7
4H	18	1220	20.8-30.3	9.5	8.00	84.2
5H	18	1520	30.3-39.8	9.5	8.19	86.2
6H	18	1700	39.8-49.3	9.5	8.97	94.4
7H	18	1800	49.3-58.8	9.5	9.97	104.9
8H	18	1910	58.8-68.3	9.5	10.15	106.8
9H	18	2010	68.3-77.8	9.5	9.82	103.4
10H	18	2110	77.8-87.3	9.5	9.99	105.2
Coring totals:				87.3	86.48	99.1
178-1095B-						
	******Drilled from 0.0 to 83.0 mbsf******					
1H	19	0355	83.0-92.5	9.5	9.83	103.5
2H	19	0500	92.5-102.0	9.5	8.33	87.7
3H	19	0550	102.0-111.5	9.5	10.12	106.5
4H	19	0655	111.5-121.0	9.5	9.88	104.0
5H	19	0750	121.0-130.5	9.5	9.78	102.9
6H	19	0850	130.5-140.0	9.5	9.54	100.4
7H	19	1020	140.0-149.5	9.5	9.89	104.1
8H	19	1125	149.5-159.0	9.5	9.38	98.7
9H	19	1220	159.0-168.5	9.5	9.97	104.9
10H	19	1345	168.5-178.0	9.5	9.49	99.9
11H	19	1420	178.0-187.5	9.5	9.68	101.9
12H	19	1610	187.5-197.0	9.5	9.56	100.6
13H	19	1830	197.0-205.0	8.0	6.68	83.5
14X	19	2025	205.0-214.7	9.7	6.11	63.0
15X	19	2145	214.7-224.3	9.6	3.80	39.6
16X	19	2315	224.3-233.9	9.6	4.51	47.0
17X	20	0030	233.9-243.5	9.6	9.77	101.8
18X	20	0145	243.5-253.1	9.6	9.64	100.4
19X	20	0250	253.1-262.7	9.6	0.02	0.2
20X	20	0355	262.7-272.4	9.7	9.71	100.1
21X	20	0500	272.4-282.1	9.7	9.76	100.6
22X	20	0605	282.1-291.7	9.6	6.25	65.1
23X	20	0705	291.7-301.3	9.6	9.56	99.6
24X	20	0820	301.3-310.9	9.6	9.78	101.9
25X	20	0925	310.9-320.6	9.7	9.60	99.0
26X	20	1030	320.6-330.2	9.6	9.80	102.1
27X	20	1145	330.2-339.8	9.6	9.61	100.1
28X	20	1255	339.8-349.5	9.7	9.74	100.4
29X	20	1400	349.5-359.2	9.7	9.67	99.7
30X	20	1530	359.2-368.8	9.6	9.64	100.4
31X	20	1645	368.8-378.4	9.6	9.79	102.0
32X	20	1800	378.4-387.7	9.3	9.77	105.1
33X	20	1915	387.7-397.3	9.6	9.75	101.6
34X	20	2025	397.3-406.6	9.3	9.64	103.7
35X	20	2215	406.6-416.2	9.6	8.53	88.9
36X	21	0015	416.2-425.8	9.6	9.61	100.1
37X	21	0210	425.8-435.5	9.7	5.54	57.1
38X	21	0355	435.5-445.1	9.6	9.68	100.8
39X	21	0550	445.1-454.8	9.7	9.77	100.7
40X	21	0805	454.8-464.5	9.7	9.61	99.1
41X	21	1005	464.5-474.1	9.6	9.68	100.8
42X	21	1200	474.1-483.8	9.7	9.69	99.9
43X	21	1355	483.8-493.4	9.6	2.22	23.1
44X	21	1615	493.4-498.0	4.6	0.27	5.9
45X	21	1840	498.0-503.0	5.0	2.18	43.6
46X	21	2055	503.0-512.7	9.7	2.23	23.0
47X	21	2320	512.7-522.4	9.7	1.06	10.9
48X	22	0200	522.4-532.1	9.7	1.35	13.9
49X	22	0425	532.1-541.7	9.6	1.46	15.2
50X	22	0715	541.7-551.4	9.7	2.64	27.2
51X	22	1020	551.4-560.8	9.4	1.20	12.8

Table T1 (continued).

Core	Date (Feb 1998)	Time (UTC)	Depth (mbsf)	Length cored (m)	Length recovered (m)	Recovery (%)
52X	22	1330	560.8-570.2	9.4	0.98	10.4
Coring totals:				487.2	385.75	79.2
Drilled:				83.0		
Total:				570.2		
178-1095C-						
1H	24	0515	0.0-2.9	2.9	2.87	99.0
Coring totals:				2.9	2.87	99.0
178-1095D-						
1H	24	0720	0.0-8.6	8.6	8.52	99.1
2H	24	0820	8.6-18.1	9.5	9.62	101.3
3H	24	0915	18.1-27.6	9.5	9.46	99.6
4H	24	1010	27.6-37.1	9.5	5.47	57.6
5H	24	1105	37.1-46.6	9.5	8.24	86.7
6H	24	1200	46.6-56.1	9.5	8.72	91.8
7H	24	1315	56.1-65.6	9.5	9.85	103.7
8H	24	1410	65.6-75.1	9.5	9.29	97.8
9H	24	1515	75.1-84.6	9.5	9.79	103.1
Coring totals:				84.6	78.96	93.3

Notes: UTC = Universal Time Coordinated. An expanded version of this coring summary table that includes lengths and depths of sections and comments on sampling is included in ASCII format in the **TABLES** directory.

Table T2. Summary of lithostratigraphic units identified at Site 1095.

Unit	Depth (mbsf)	Thickness (m)	Age	Lithology and characteristic features
I	0.0-49.3	49.3	Holocene to late Pliocene	Biogenic-rich, massive, intensely bioturbated, dominantly brown silty clays with ice-rafted debris (IRD). Interbedded with laminated silts, silty clays, and siliceous oozes. Separated from underlying Unit II by transition zone of parallel-laminated and cross-laminated silts, silty clays, and diamict beds.
II	49.3-435.5	386.2	late Pliocene to late Miocene	Dominantly repetitively bedded and diatom-bearing cross- and parallel-laminated sands, silts, and clays, gray-greenish. Frequency of sands and silts shows distinct cyclicity. These intervals are intensely bioturbated with enhanced IRD. As minor lithology, diatomaceous oozes are present.
III	435.5-570.2	134.7	late Miocene	Repetitively bedded, parallel-laminated claystone and siltstone with minor bioturbation and decrease of IRD content.

Table T3. Ice-rafted sand/granules and pebble contents at Site 1095.

Core	Core top (mbsf)	Sand and granules counts	Dropstone/pebble counts (0.5–5 cm)
178-1095A-			
1H	0.00	1	5
2H	5.90	1	0
3H	11.30	1	2
4H	20.80	1	0
5H	30.30	1	0
6H	39.80	1	5
7H	49.30	1	2
8H	58.80	1	3
9H	68.30	1	2
10H	77.80	0	0
178-1095B-			
1H	83.00	1	2
2H	92.50	1	0
3H	102.00	1	1
4H	111.50	1	0
5H	121.00	1	0
6H	130.50	1	1
7H	140.00	1	2
8H	149.50	1	2
9H	159.00	0	0
10H	168.50	1	1
11H	178.00	1	3
12H	187.50	1	4
13H	197.00	1	2
14X	205.00	1	1
15X	214.70	1	1
16X	224.30	0	0
17X	233.90	1	0
18X	243.50	1	1
19X	253.10	0	0
20X	262.70	1	0
21X	272.40	0	0
22X	282.10	1	1
23X	291.70	0	0
24X	301.30	1	1
25X	310.90	0	0
26X	320.60	1	1
27X	330.20	1	0
28X	339.80	1	1
29X	349.50	1	0
30X	359.20	1	0
31X	368.80	1	1
32X	378.40	0	0
33X	387.70	1	0
34X	397.30	1	0
35X	406.60	1	1
36X	416.20	1	0
37X	425.80	1	4
38X	435.50	0	0
39X	445.10	1	1
40X	454.80	1	1
41X	464.50	0	0
42X	474.10	0	3
43X	483.80	0	0
44X	493.40	0	2
45X	498.00	0	2
46X	503.00	0	0
47X	512.70	0	2
48X	522.40	1	0
49X	532.10	0	2
50X	541.70	0	4
51X	551.40	0	2
52X	560.80	0	0

Table T4. Biostratigraphically useful diatom datums for Site 1095. (Continued on next page.)

Diatom datums (published ages)	A BKSA95	B BKSA95	C	Chrons	Hole 1095A	Top depth (mbsf)	Bottom depth (mbsf)
TC *Hemidiscus karstenii*			**0.19**	C1n1			
BC *Hemidiscus karstenii*			0.42		—		
T *Actinocyclus ingens*	0.64	0.64	**0.65**	**C1n1**	1H-CC<, <2H-3, 90	5.67	9.80
T *Thalassiosira elliptipora*	0.68	0.7	1.04-1.11	C1n1	2H-3, 90<, <3H-6, 94	9.80	17.72
T *Thalassiosira fasciculata*	1.7	0.7		C1r.1r	—		
T *Fragilariopsis barronii*	1.39	1.4	**1.3**	C1r2	2H-3, 90<, <3H-6, 94	9.80	17.72
T *Thalassiosira torokina*	1.85	1.8		C2n1	—		
T *Thalassiosira kolbei*	1.85	2	**2**	C2n1			
T *Thalassiosira complicata*	3.4	2.5			—		
T *Thalassiosira inura*	1.85	2.5		C2n1	8H-CC<, <9H-3, 130	68.90	72.60
T *Thalassiosira vulnifica*	2.28	2.5	**2.3**	C2r3	—		
T *Fragilariopsis interfrigidaria*	2.67	2.63		C2An1	9H-CC<	77.80	
T *Thalassiosira insigna*	2.57	2.63	**2.6**	C2r3			
B *Thalassiosira vulnifica*	3.17	3.26		C2An2	Base of hole = 87.3 mbsf		
B *Fragilariopsis interfrigidaria*	3.8	3.8		C2Ar3			
B *Thalassiosira striata*	4.48			C3n2			
B *Fragilariopsis barronii*	4.48	4.44		C3n2			
B *Thalassiosira complicata*	4.62	4.44		C3n.2r			
B *Thalassiosira inura*	4.85	4.92		C3n.3r			
B *Fragilariopsis praeinterfrigidari*	4.85	5.3		C3n.3r			
B *Thalassiosira oestrupii*	5.62	5.56		C3r4			
T *Nitzschia donahuensis*	5.89			C3An1			
T *Actinocyclus ingens* var *ovalis*	6.27						
T *Hemidiscus ovalis*	6.32			C4An1			
B *Thalassiosira oliverana*	6.42	6.42		C3An2			
B *Actinocyclus ingens* var *ovalis*		8.68					
B *Hemidiscus ovalis*	8.68			C4An1			
B *Cosmiodiscus intersectus*	8.68						
B *Thalassiosira oliverana* var *sparsa*	8.68						
B *Thalassiosira torokina*	8.92	9.01					
T *Denticulopsis crassa*	9.23			C4Ar.1n			
B *Nitzschia donahuensis*	9.63			C4An3			
B *Asteromphalus kennettii*	10.23			C5n1			
B *Denticulopsis crassa*	10.29						

Notes: Species listed in bold print are used as zonal boundary markers. Three age columns are shown: (A) Harwood and Maruyama (1992); (B) Gersonde, Hodell, Blum, et al. (1999, Leg 177); and (C) Gersonde and Bárcena (1998). The chrons were assigned by Harwood and Maruyama (1992). Holes 1095A, 1095B, and 1095D are represented in the table with Hole 1095C missing, as its entire depth consisted of one core. Datums occur in the cores within the interval listed for each species. T = top/last occurrence datum, B = base/first occurrence datum, BC = base common/first common occurrence datum, TC = top common/last common occurrence datum. BKSA = Berggren et al. (1995). — = not observed; gray boxes = either an interval drilled but not cored, or an interval not drilled.

Table T4 (continued).

Diatom datums (published ages)	Hole 1095B	Top depth (mbsf)	Bottom depth (mbsf)	Hole 1095D	Top depth (mbsf)	Bottom depth (mbsf)
TC *Hemidiscus karstenii*				1H-2, 40<, <1H-4, 40	1.90	4.90
BC *Hemidiscus karstenii*				1H-4, 40<, <1H-CC	4.90	8.47
T *Actinocyclus ingens*				<2H-3, 32 cm		11.92
T *Thalassiosira elliptipora*	Drilled but not cored			1H-CC<?	8.47	
T *Thalassiosira fasciculata*				1H-CC<, <7H-CC	8.47	65.90
T *Fragilariopsis barronii*						
T *Thalassiosira torokina*				1H-CC<, <7H-4, 50	8.47	61.10
T *Thalassiosira kolbei*						
T *Thalassiosira complicata*				1H-CC<, <7H-CC	8.47	65.90
T *Thalassiosira inura*						
T *Thalassiosira vulnifica*	83.0 mbsf					
T *Fragilariopsis interfrigidaria*	<1H-1, 95		83.95			
T *Thalassiosira insigna*				6H-CC<, <7H-CC	55.30	65.90
B *Thalassiosira vulnifica*				Base of hole = 84.6 mbsf		
B *Fragilariopsis interfrigidaria*	3H-CC<, <4H-1, 104	111.5	112.50			
B *Thalassiosira striata*	5H-3, 33<, <5H-5, 44.5	124.3	127.50			
B *Fragilariopsis barronii*	5H-3, 33<, <5H-5, 44.6	124.3	127.50			
B *Thalassiosira complicata*	6H-CC<, 7H-3, 90	140.0	143.90			
B *Thalassiosira inura*	12H-4, 41<, 12H-6, 80	192.4	195.80			
B *Fragilariopsis praeinterfrigidari*	14X-4, 133<, <14X-CC	210.8	214.70			
B *Thalassiosira oestrupii*						
T *Nitzschia donahuensis*	14X-CC<, <15X-2, 126	214.7	217.50			
T *Actinocyclus ingens* var *ovalis*						
T *Hemidiscus ovalis*	21X-3, 128		276.70			
B *Thalassiosira oliverana*						
B *Actinocyclus ingens* var *ovalis*						
B *Hemidiscus ovalis*	28X-5, 104<, <28X-CC	346.8	349.50			
B *Cosmiodiscus intersectus*						
B *Thalassiosira oliverana* var *sparsa*	28X-5,104<, <28X-CC	346.8	349.50			
B *Thalassiosira torokina*	23X-CC<, <25X-CC	301.2	320.4			
T *Denticulopsis crassa*	32X-CC<, 36X-1, 100	388.1	417.2			
B *Nitzschia donahuensis*	43X-1, 81<, <45X-1, 32?	484.6	498.30			
B *Asteromphalus kennettii*						
B *Denticulopsis crassa*	46X-1, 16< Base of hole = 570.2 mbsf	503.2				

Table T5. Split-core paleomagnetic measurements for Hole 1095A before demagnetization (NRM results).

Leg	Site	Hole	Core	Type	Section	Interval (cm)	Depth (mbsf)	Inclination (°)	Declination (°)	Intensity (A/m)	Demagnetization step (mT)	Run #
178	1095	A	1	H	1	8	0.08	–44.7	1.36	9.56E-02	0	102
178	1095	A	1	H	1	12	0.12	–47.01	346.47	1.03E-01	0	102
178	1095	A	1	H	1	16	0.16	–42.78	334.33	1.02E-01	0	102
178	1095	A	1	H	1	20	0.2	–27.23	348.28	1.24E-01	0	102
178	1095	A	1	H	1	24	0.24	–14.11	353.04	1.49E-01	0	102
178	1095	A	1	H	1	28	0.28	–12.9	349.96	1.59E-01	0	102
178	1095	A	1	H	1	32	0.32	–15.46	349.27	1.52E-01	0	102
178	1095	A	1	H	1	36	0.36	–23.63	354.92	1.32E-01	0	102
178	1095	A	1	H	1	40	0.4	–27.49	1.52	1.30E-01	0	102
178	1095	A	1	H	1	44	0.44	–31.82	2.64	1.21E-01	0	102
178	1095	A	1	H	1	48	0.48	–35.32	0.57	1.19E-01	0	102
178	1095	A	1	H	1	52	0.52	–40.95	357.52	1.09E-01	0	102
178	1095	A	1	H	1	56	0.56	–41.99	354.5	1.12E-01	0	102
178	1095	A	1	H	1	60	0.6	–43.4	351.2	1.22E-01	0	102
178	1095	A	1	H	1	64	0.64	–48.51	347.14	1.26E-01	0	102
178	1095	A	1	H	1	68	0.68	–47.47	344.71	1.25E-01	0	102
178	1095	A	1	H	1	72	0.72	–44.74	347.45	1.15E-01	0	102
178	1095	A	1	H	1	76	0.76	–42.53	345.63	1.33E-01	0	102
178	1095	A	1	H	1	80	0.8	–28.54	346.86	1.89E-01	0	102
178	1095	A	1	H	1	84	0.84	–23.51	346.97	1.73E-01	0	102
178	1095	A	1	H	1	88	0.88	–32.2	341.23	1.20E-01	0	102
178	1095	A	1	H	1	92	0.92	–31.37	335.85	1.30E-01	0	102
178	1095	A	1	H	1	96	0.96	–29.05	336.58	1.57E-01	0	102
178	1095	A	1	H	1	100	1	–33.75	341.59	1.55E-01	0	102
178	1095	A	1	H	1	104	1.04	–40.36	346.09	1.55E-01	0	102
178	1095	A	1	H	1	108	1.08	–41.57	345.44	1.68E-01	0	102
178	1095	A	1	H	1	112	1.12	–43.53	338.75	1.68E-01	0	102
178	1095	A	1	H	1	116	1.16	–42.21	326.79	1.82E-01	0	102
178	1095	A	1	H	1	120	1.2	–39.66	324.8	1.86E-01	0	102
178	1095	A	1	H	1	124	1.24	–38.33	328.46	1.82E-01	0	102
178	1095	A	1	H	1	128	1.28	–32.69	329.83	1.91E-01	0	102
178	1095	A	1	H	1	132	1.32	–27.11	334.03	2.02E-01	0	102
178	1095	A	1	H	1	136	1.36	–23.6	345.12	1.94E-01	0	102
178	1095	A	1	H	2	8	1.54	–40.51	0.52	1.99E-01	0	106
178	1095	A	1	H	2	12	1.58	–39	358.38	2.03E-01	0	106
178	1095	A	1	H	2	16	1.62	–35.83	356.19	1.84E-01	0	106
178	1095	A	1	H	2	20	1.66	–33.34	356.83	1.62E-01	0	106
178	1095	A	1	H	2	24	1.7	–30.49	359.13	1.45E-01	0	106
178	1095	A	1	H	2	28	1.74	–30.78	357.03	1.28E-01	0	106
178	1095	A	1	H	2	32	1.78	–31.09	355	1.14E-01	0	106
178	1095	A	1	H	2	36	1.82	–28.98	351.39	9.30E-02	0	106
178	1095	A	1	H	2	40	1.86	–28.05	349.97	7.29E-02	0	106
178	1095	A	1	H	2	44	1.9	–27.93	353.59	7.11E-02	0	106
178	1095	A	1	H	2	48	1.94	–30.72	350.85	8.10E-02	0	106
178	1095	A	1	H	2	52	1.98	–32.03	351.56	9.73E-02	0	106
178	1095	A	1	H	2	56	2.02	–26.89	355.83	1.04E-01	0	106
178	1095	A	1	H	2	60	2.06	–24.81	355.95	8.96E-02	0	106
178	1095	A	1	H	2	64	2.1	–25.85	350.76	7.35E-02	0	106
178	1095	A	1	H	2	68	2.14	–26	347.79	6.38E-02	0	106
178	1095	A	1	H	2	72	2.18	–29.89	347.61	5.75E-02	0	106
178	1095	A	1	H	2	76	2.22	–36.56	341.89	6.38E-02	0	106
178	1095	A	1	H	2	80	2.26	–38.82	337.03	7.90E-02	0	106
178	1095	A	1	H	2	84	2.3	–38.36	336.71	8.80E-02	0	106
178	1095	A	1	H	2	88	2.34	–42.15	339.39	8.78E-02	0	106
178	1095	A	1	H	2	92	2.38	–48.91	343.74	9.47E-02	0	106
178	1095	A	1	H	2	96	2.42	–50.87	345.9	1.16E-01	0	106
178	1095	A	1	H	2	100	2.46	–47.84	346.21	1.40E-01	0	106
178	1095	A	1	H	2	104	2.5	–47.83	346.28	1.53E-01	0	106
178	1095	A	1	H	2	108	2.54	–52.08	345.02	1.48E-01	0	106
178	1095	A	1	H	2	112	2.58	–50.31	343.96	1.60E-01	0	106
178	1095	A	1	H	2	116	2.62	–42.08	344.62	1.81E-01	0	106
178	1095	A	1	H	2	120	2.66	–42.05	345.61	1.53E-01	0	106
178	1095	A	1	H	2	124	2.7	–57.34	340.85	1.21E-01	0	106
178	1095	A	1	H	2	128	2.74	–61.87	338.4	1.30E-01	0	106
178	1095	A	1	H	2	132	2.78	–57.51	346.24	1.39E-01	0	106

Note: Only a portion of this table appears here. The complete table is available in ASCII format in the **TABLES** directory.

Table T6. Split-core paleomagnetic measurements for Hole 1095A after 10-mT demagnetization.

Leg	Site	Hole	Core	Type	Section	Interval (cm)	Depth (mbsf)	Inclination (°)	Declination (°)	Intensity (A/m)	Demagnetization step (mT)	Run #
178	1095	A	1	H	1	8	0.08	–54.45	352.89	9.61E-02	10	103
178	1095	A	1	H	1	12	0.12	–53.69	341.38	9.99E-02	10	103
178	1095	A	1	H	1	16	0.16	–47.89	331.42	9.81E-02	10	103
178	1095	A	1	H	1	20	0.2	–32.32	345.55	1.13E-01	10	103
178	1095	A	1	H	1	24	0.24	–19.09	349.72	1.30E-01	10	103
178	1095	A	1	H	1	28	0.28	–19.74	344.84	1.29E-01	10	103
178	1095	A	1	H	1	32	0.32	–24.33	345.3	1.24E-01	10	103
178	1095	A	1	H	1	36	0.36	–31.26	354.01	1.16E-01	10	103
178	1095	A	1	H	1	40	0.4	–34.17	0.92	1.16E-01	10	103
178	1095	A	1	H	1	44	0.44	–39.9	0.79	1.05E-01	10	103
178	1095	A	1	H	1	48	0.48	–44.02	358.26	1.04E-01	10	103
178	1095	A	1	H	1	52	0.52	–48.55	355.54	9.91E-02	10	103
178	1095	A	1	H	1	56	0.56	–48.48	352.61	1.03E-01	10	103
178	1095	A	1	H	1	60	0.6	–49.57	348.25	1.13E-01	10	103
178	1095	A	1	H	1	64	0.64	–54.64	343.2	1.18E-01	10	103
178	1095	A	1	H	1	68	0.68	–54.07	340.53	1.17E-01	10	103
178	1095	A	1	H	1	72	0.72	–52.58	342.57	1.07E-01	10	103
178	1095	A	1	H	1	76	0.76	–49.2	341.14	1.23E-01	10	103
178	1095	A	1	H	1	80	0.8	–34.56	342.67	1.66E-01	10	103
178	1095	A	1	H	1	84	0.84	–29.64	342.75	1.52E-01	10	103
178	1095	A	1	H	1	88	0.88	–37.62	337.46	1.11E-01	10	103
178	1095	A	1	H	1	92	0.92	–36.88	330.93	1.19E-01	10	103
178	1095	A	1	H	1	96	0.96	–34.43	332.46	1.44E-01	10	103
178	1095	A	1	H	1	100	1	–38.31	338.61	1.46E-01	10	103
178	1095	A	1	H	1	104	1.04	–44.67	343.04	1.46E-01	10	103
178	1095	A	1	H	1	108	1.08	–46.1	342.24	1.58E-01	10	103
178	1095	A	1	H	1	112	1.12	–48.22	334.59	1.58E-01	10	103
178	1095	A	1	H	1	116	1.16	–46.15	321.79	1.74E-01	10	103
178	1095	A	1	H	1	120	1.2	–43.32	319.78	1.78E-01	10	103
178	1095	A	1	H	1	124	1.24	–42.59	323.6	1.72E-01	10	103
178	1095	A	1	H	1	128	1.28	–36.58	326	1.79E-01	10	103
178	1095	A	1	H	1	132	1.32	–30.83	330.6	1.88E-01	10	103
178	1095	A	1	H	1	136	1.36	–28.17	342.37	1.77E-01	10	103
178	1095	A	1	H	2	8	1.54	–46.05	358.69	1.85E-01	10	107
178	1095	A	1	H	2	12	1.58	–44.33	356.27	1.88E-01	10	107
178	1095	A	1	H	2	16	1.62	–41.25	353.49	1.69E-01	10	107
178	1095	A	1	H	2	20	1.66	–39.28	354.44	1.46E-01	10	107
178	1095	A	1	H	2	24	1.7	–36.48	357.59	1.27E-01	10	107
178	1095	A	1	H	2	28	1.74	–36.8	355.37	1.12E-01	10	107
178	1095	A	1	H	2	32	1.78	–36.92	353.27	9.95E-02	10	107
178	1095	A	1	H	2	36	1.82	–34.44	349.77	8.09E-02	10	107
178	1095	A	1	H	2	40	1.86	–33.95	349.08	6.26E-02	10	107
178	1095	A	1	H	2	44	1.9	–35.36	352.71	5.96E-02	10	107
178	1095	A	1	H	2	48	1.94	–40.13	347.15	6.75E-02	10	107
178	1095	A	1	H	2	52	1.98	–40.35	347.92	8.36E-02	10	107
178	1095	A	1	H	2	56	2.02	–34.08	352.95	9.03E-02	10	107
178	1095	A	1	H	2	60	2.06	–31.73	350.81	8.08E-02	10	107
178	1095	A	1	H	2	64	2.1	–33.03	347.04	6.62E-02	10	107
178	1095	A	1	H	2	68	2.14	–33.56	347.01	5.56E-02	10	107
178	1095	A	1	H	2	72	2.18	–38.01	345.96	5.04E-02	10	107
178	1095	A	1	H	2	76	2.22	–45.88	339.52	5.69E-02	10	107
178	1095	A	1	H	2	80	2.26	–48.2	332.85	7.22E-02	10	107
178	1095	A	1	H	2	84	2.3	–47.94	332.17	8.09E-02	10	107
178	1095	A	1	H	2	88	2.34	–51.36	335.95	8.17E-02	10	107
178	1095	A	1	H	2	92	2.38	–58.47	338.56	8.80E-02	10	107
178	1095	A	1	H	2	96	2.42	–59.98	339.58	1.08E-01	10	107
178	1095	A	1	H	2	100	2.46	–55.34	341.17	1.30E-01	10	107
178	1095	A	1	H	2	104	2.5	–55.17	342.29	1.42E-01	10	107
178	1095	A	1	H	2	108	2.54	–59.08	341.77	1.41E-01	10	107
178	1095	A	1	H	2	112	2.58	–56.31	340.78	1.54E-01	10	107
178	1095	A	1	H	2	116	2.62	–47.88	341.53	1.72E-01	10	107
178	1095	A	1	H	2	120	2.66	–47.2	343.33	1.49E-01	10	107
178	1095	A	1	H	2	124	2.7	–60.18	339.33	1.19E-01	10	107
178	1095	A	1	H	2	128	2.74	–65.47	335.47	1.23E-01	10	107
178	1095	A	1	H	2	132	2.78	–62.09	344.44	1.30E-01	10	107
178	1095	A	1	H	2	136	2.82	–57.48	345.56	1.22E-01	10	107

Note: Only a portion of this table appears here. The complete table is available in ASCII format in the **TABLES** directory.

Table T7. Split-core paleomagnetic measurements for Hole 1095A after 20-mT demagnetization.

Leg	Site	Hole	Core	Type	Section	Interval (cm)	Depth (mbsf)	Inclination (°)	Declination (°)	Intensity (A/m)	Demagnetization step (mT)	Run #
178	1095	A	1	H	1	8	0.08	–58.02	349.04	8.55E-02	20	104
178	1095	A	1	H	1	12	0.12	–55.8	339.5	9.03E-02	20	104
178	1095	A	1	H	1	16	0.16	–50.01	329.72	8.87E-02	20	104
178	1095	A	1	H	1	20	0.2	–35.74	342.98	9.92E-02	20	104
178	1095	A	1	H	1	24	0.24	–23.18	346.63	1.10E-01	20	104
178	1095	A	1	H	1	28	0.28	–24.85	341.78	1.08E-01	20	104
178	1095	A	1	H	1	32	0.32	–30.38	342.24	1.03E-01	20	104
178	1095	A	1	H	1	36	0.36	–36.4	352.62	1.02E-01	20	104
178	1095	A	1	H	1	40	0.4	–38.46	0.26	1.02E-01	20	104
178	1095	A	1	H	1	44	0.44	–44.39	0.7	9.22E-02	20	104
178	1095	A	1	H	1	48	0.48	–48.92	357.69	9.05E-02	20	104
178	1095	A	1	H	1	52	0.52	–52.8	353.91	8.76E-02	20	104
178	1095	A	1	H	1	56	0.56	–51.98	350.73	9.18E-02	20	104
178	1095	A	1	H	1	60	0.6	–53.03	346.04	1.01E-01	20	104
178	1095	A	1	H	1	64	0.64	–57.84	340.36	1.07E-01	20	104
178	1095	A	1	H	1	68	0.68	–57.15	337.62	1.06E-01	20	104
178	1095	A	1	H	1	72	0.72	–56.06	339.23	9.71E-02	20	104
178	1095	A	1	H	1	76	0.76	–52.34	337.26	1.11E-01	20	104
178	1095	A	1	H	1	80	0.8	–37.88	339.88	1.45E-01	20	104
178	1095	A	1	H	1	84	0.84	–33.18	340.62	1.32E-01	20	104
178	1095	A	1	H	1	88	0.88	–40.24	335.4	9.95E-02	20	104
178	1095	A	1	H	1	92	0.92	–39.74	327.93	1.06E-01	20	104
178	1095	A	1	H	1	96	0.96	–37.41	329.93	1.28E-01	20	104
178	1095	A	1	H	1	100	1	–40.72	337.16	1.32E-01	20	104
178	1095	A	1	H	1	104	1.04	–47.01	342.06	1.34E-01	20	104
178	1095	A	1	H	1	108	1.08	–48.73	340.7	1.43E-01	20	104
178	1095	A	1	H	1	112	1.12	–51.27	331.19	1.44E-01	20	104
178	1095	A	1	H	1	116	1.16	–48.54	318.15	1.60E-01	20	104
178	1095	A	1	H	1	120	1.2	–45.59	316.52	1.64E-01	20	104
178	1095	A	1	H	1	124	1.24	–45.47	319.9	1.56E-01	20	104
178	1095	A	1	H	1	128	1.28	–39.09	323.51	1.63E-01	20	104
178	1095	A	1	H	1	132	1.32	–33.08	329.03	1.70E-01	20	104
178	1095	A	1	H	1	136	1.36	–30.83	340.54	1.58E-01	20	104
178	1095	A	1	H	2	8	1.54	–48.25	357.9	1.69E-01	20	108
178	1095	A	1	H	2	12	1.58	–46.49	355.42	1.71E-01	20	108
178	1095	A	1	H	2	16	1.62	–43.54	351.88	1.51E-01	20	108
178	1095	A	1	H	2	20	1.66	–41.8	352.74	1.27E-01	20	108
178	1095	A	1	H	2	24	1.7	–39.1	356.78	1.09E-01	20	108
178	1095	A	1	H	2	28	1.74	–39.18	354.84	9.51E-02	20	108
178	1095	A	1	H	2	32	1.78	–38.93	352.66	8.40E-02	20	108
178	1095	A	1	H	2	36	1.82	–36.02	349.59	6.79E-02	20	108
178	1095	A	1	H	2	40	1.86	–35.19	349.33	5.21E-02	20	108
178	1095	A	1	H	2	44	1.9	–36.98	352.42	4.94E-02	20	108
178	1095	A	1	H	2	48	1.94	–42.24	346.05	5.64E-02	20	108
178	1095	A	1	H	2	52	1.98	–41.98	347.09	7.04E-02	20	108
178	1095	A	1	H	2	56	2.02	–35.31	352.38	7.54E-02	20	108
178	1095	A	1	H	2	60	2.06	–32.86	350.43	6.67E-02	20	108
178	1095	A	1	H	2	64	2.1	–33.01	347.75	5.54E-02	20	108
178	1095	A	1	H	2	68	2.14	–32.13	347.31	4.69E-02	20	108
178	1095	A	1	H	2	72	2.18	–36.49	345.52	4.26E-02	20	108
178	1095	A	1	H	2	76	2.22	–45.36	338.78	4.82E-02	20	108
178	1095	A	1	H	2	80	2.26	–47.93	331.92	6.19E-02	20	108
178	1095	A	1	H	2	84	2.3	–47.53	331.62	6.97E-02	20	108
178	1095	A	1	H	2	88	2.34	–51.44	335.71	7.00E-02	20	108
178	1095	A	1	H	2	92	2.38	–59.75	337.62	7.48E-02	20	108
178	1095	A	1	H	2	96	2.42	–61.82	337.67	9.26E-02	20	108
178	1095	A	1	H	2	100	2.46	–56.91	339.38	1.13E-01	20	108
178	1095	A	1	H	2	104	2.5	–56.59	340.83	1.25E-01	20	108
178	1095	A	1	H	2	108	2.54	–60.16	340.26	1.26E-01	20	108
178	1095	A	1	H	2	112	2.58	–57.19	339.35	1.37E-01	20	108
178	1095	A	1	H	2	116	2.62	–48.55	340.32	1.53E-01	20	108
178	1095	A	1	H	2	120	2.66	–47.59	342.81	1.31E-01	20	108
178	1095	A	1	H	2	124	2.7	–60.8	339.21	1.04E-01	20	108
178	1095	A	1	H	2	128	2.74	–66.58	334.32	1.09E-01	20	108
178	1095	A	1	H	2	132	2.78	–63.35	343.81	1.15E-01	20	108
178	1095	A	1	H	2	136	2.82	–58.82	344.87	1.07E-01	20	108

Note: Only a portion of this table appears here. The complete table is available in ASCII format in the **TABLES** directory.

Table T8. Split-core paleomagnetic measurements for Hole 1095A after 25-mT demagnetization. (See table note. Continued on next two pages.)

Leg	Site	Hole	Core	Type	Section	Interval (cm)	Depth (mbsf)	Inclination (°)	Declination (°)	Intensity (A/m)	Demagnetization step (mT)	Run #
178	1095	A	1	H	1	8	0.08	–59.39	347.54	7.89E-02	25	105
178	1095	A	1	H	1	12	0.12	–56.39	338.73	8.42E-02	25	105
178	1095	A	1	H	1	16	0.16	–50.59	328.49	8.26E-02	25	105
178	1095	A	1	H	1	20	0.2	–37.03	341.35	9.14E-02	25	105
178	1095	A	1	H	1	24	0.24	–24.5	344.94	1.01E-01	25	105
178	1095	A	1	H	1	28	0.28	–26.28	339.91	9.78E-02	25	105
178	1095	A	1	H	1	32	0.32	–32.31	341.1	9.31E-02	25	105
178	1095	A	1	H	1	36	0.36	–38.38	352.15	9.28E-02	25	105
178	1095	A	1	H	1	40	0.4	–39.91	0.07	9.37E-02	25	105
178	1095	A	1	H	1	44	0.44	–45.92	0.61	8.46E-02	25	105
178	1095	A	1	H	1	48	0.48	–50.65	357.35	8.26E-02	25	105
178	1095	A	1	H	1	52	0.52	–54.41	353.73	8.05E-02	25	105
178	1095	A	1	H	1	56	0.56	–53.31	350.35	8.49E-02	25	105
178	1095	A	1	H	1	60	0.6	–54.31	344.81	9.41E-02	25	105
178	1095	A	1	H	1	64	0.64	–59.07	338.71	1.01E-01	25	105
178	1095	A	1	H	1	68	0.68	–58.43	336.08	9.96E-02	25	105
178	1095	A	1	H	1	72	0.72	–57.52	337.6	9.06E-02	25	105
178	1095	A	1	H	1	76	0.76	–53.7	335.47	1.03E-01	25	105
178	1095	A	1	H	1	80	0.8	–39.15	338.28	1.34E-01	25	105
178	1095	A	1	H	1	84	0.84	–34.49	339.24	1.22E-01	25	105
178	1095	A	1	H	1	88	0.88	–41.23	334.09	9.28E-02	25	105
178	1095	A	1	H	1	92	0.92	–40.91	326.67	9.84E-02	25	105
178	1095	A	1	H	1	96	0.96	–38.7	328.82	1.19E-01	25	105
178	1095	A	1	H	1	100	1	–41.82	336.49	1.24E-01	25	105
178	1095	A	1	H	1	104	1.04	–48.13	341.55	1.26E-01	25	105
178	1095	A	1	H	1	108	1.08	–50.03	340.16	1.34E-01	25	105
178	1095	A	1	H	1	112	1.12	–52.7	329.81	1.35E-01	25	105
178	1095	A	1	H	1	116	1.16	–49.66	316.14	1.51E-01	25	105
178	1095	A	1	H	1	120	1.2	–46.6	314.76	1.55E-01	25	105
178	1095	A	1	H	1	124	1.24	–46.81	318.03	1.47E-01	25	105
178	1095	A	1	H	1	128	1.28	–40.42	321.96	1.53E-01	25	105
178	1095	A	1	H	1	132	1.32	–34.42	328.11	1.60E-01	25	105
178	1095	A	1	H	1	136	1.36	–32.42	339.37	1.48E-01	25	105
178	1095	A	1	H	2	8	1.54	–49.91	357.31	1.60E-01	25	109
178	1095	A	1	H	2	12	1.58	–48.13	354.86	1.60E-01	25	109
178	1095	A	1	H	2	16	1.62	–45.33	351.05	1.40E-01	25	109
178	1095	A	1	H	2	20	1.66	–43.74	351.73	1.17E-01	25	109
178	1095	A	1	H	2	24	1.7	–41.12	356.18	9.92E-02	25	109
178	1095	A	1	H	2	28	1.74	–41.12	354.78	8.56E-02	25	109
178	1095	A	1	H	2	32	1.78	–40.62	352.36	7.54E-02	25	109
178	1095	A	1	H	2	36	1.82	–37.31	349.3	6.05E-02	25	109
178	1095	A	1	H	2	40	1.86	–36.27	349.3	4.61E-02	25	109
178	1095	A	1	H	2	44	1.9	–38.24	352.24	4.37E-02	25	109
178	1095	A	1	H	2	48	1.94	–43.75	345.32	5.02E-02	25	109
178	1095	A	1	H	2	52	1.98	–43.24	346.58	6.29E-02	25	109
178	1095	A	1	H	2	56	2.02	–36.39	352.09	6.67E-02	25	109
178	1095	A	1	H	2	60	2.06	–33.65	350.39	5.85E-02	25	109
178	1095	A	1	H	2	64	2.1	–32.96	347.77	4.90E-02	25	109
178	1095	A	1	H	2	68	2.14	–31.25	347.19	4.20E-02	25	109
178	1095	A	1	H	2	72	2.18	–35.7	345.19	3.81E-02	25	109
178	1095	A	1	H	2	76	2.22	–45.05	338.57	4.32E-02	25	109
178	1095	A	1	H	2	80	2.26	–47.87	331.34	5.62E-02	25	109
178	1095	A	1	H	2	84	2.3	–47.26	331.05	6.35E-02	25	109
178	1095	A	1	H	2	88	2.34	–51.36	335.23	6.32E-02	25	109
178	1095	A	1	H	2	92	2.38	–60.63	336.75	6.74E-02	25	109
178	1095	A	1	H	2	96	2.42	–63.06	336.29	8.38E-02	25	109
178	1095	A	1	H	2	100	2.46	–58	338.14	1.03E-01	25	109
178	1095	A	1	H	2	104	2.5	–57.57	339.62	1.15E-01	25	109
178	1095	A	1	H	2	108	2.54	–60.94	339.3	1.17E-01	25	109
178	1095	A	1	H	2	112	2.58	–57.85	338.31	1.28E-01	25	109
178	1095	A	1	H	2	116	2.62	–49.06	339.44	1.41E-01	25	109
178	1095	A	1	H	2	120	2.66	–47.99	342.34	1.20E-01	25	109
178	1095	A	1	H	2	124	2.7	–61.38	339.13	9.55E-02	25	109
178	1095	A	1	H	2	128	2.74	–67.58	333.2	1.00E-01	25	109
178	1095	A	1	H	2	132	2.78	–64.47	343.21	1.06E-01	25	109
178	1095	A	1	H	2	136	2.82	–59.83	344.32	9.88E-02	25	109
178	1095	A	1	H	2	140	2.86	–49.5	337.72	1.07E-01	25	109
178	1095	A	1	H	3	8	3.01	–44.95	350.5	9.86E-02	25	113

Table T8 (continued).

Leg	Site	Hole	Core	Type	Section	Interval (cm)	Depth (mbsf)	Inclination (°)	Declination (°)	Intensity (A/m)	Demagnetization step (mT)	Run #
178	1095	A	1	H	3	12	3.05	–48.61	349.79	1.04E-01	25	113
178	1095	A	1	H	3	16	3.09	–54.67	341.62	1.15E-01	25	113
178	1095	A	1	H	3	20	3.13	–62.28	333.48	1.14E-01	25	113
178	1095	A	1	H	3	24	3.17	–66.26	325.01	1.07E-01	25	113
178	1095	A	1	H	3	28	3.21	–63.9	321.36	1.05E-01	25	113
178	1095	A	1	H	3	32	3.25	–60.82	336.29	1.05E-01	25	113
178	1095	A	1	H	3	36	3.29	–57.1	350.98	1.03E-01	25	113
178	1095	A	1	H	3	40	3.33	–58.07	351.63	1.06E-01	25	113
178	1095	A	1	H	3	44	3.37	–59.82	350.65	1.04E-01	25	113
178	1095	A	1	H	3	48	3.41	–58.63	347.2	1.01E-01	25	113
178	1095	A	1	H	3	52	3.45	–59.94	347.52	1.04E-01	25	113
178	1095	A	1	H	3	56	3.49	–56.35	343.63	1.08E-01	25	113
178	1095	A	1	H	3	60	3.53	–50.42	342.94	1.02E-01	25	113
178	1095	A	1	H	3	64	3.57	–51.43	347.25	8.16E-02	25	113
178	1095	A	1	H	3	68	3.61	–51.33	350.66	6.80E-02	25	113
178	1095	A	1	H	3	72	3.65	–48.3	342.51	6.85E-02	25	113
178	1095	A	1	H	3	76	3.69	–48.91	331.11	7.86E-02	25	113
178	1095	A	1	H	3	80	3.73	–52.21	329.6	8.65E-02	25	113
178	1095	A	1	H	3	84	3.77	–57.18	335.75	9.25E-02	25	113
178	1095	A	1	H	3	88	3.81	–57.66	342.19	9.77E-02	25	113
178	1095	A	1	H	3	92	3.85	–56.96	343.62	9.26E-02	25	113
178	1095	A	1	H	3	96	3.89	–56.97	343.62	8.65E-02	25	113
178	1095	A	1	H	3	100	3.93	–56.02	345.58	7.62E-02	25	113
178	1095	A	1	H	3	104	3.97	–56.99	351.91	6.45E-02	25	113
178	1095	A	1	H	3	108	4.01	–59.56	352.2	6.31E-02	25	113
178	1095	A	1	H	3	112	4.05	–61.22	348.34	7.00E-02	25	113
178	1095	A	1	H	3	116	4.09	–62.67	347.19	7.37E-02	25	113
178	1095	A	1	H	3	120	4.13	–64.85	344.34	7.36E-02	25	113
178	1095	A	1	H	3	124	4.17	–65.42	344.62	7.44E-02	25	113
178	1095	A	1	H	3	128	4.21	–62.57	348.77	7.19E-02	25	113
178	1095	A	1	H	3	132	4.25	–59.39	356.3	6.81E-02	25	113
178	1095	A	1	H	3	136	4.29	–53.86	4.54	6.31E-02	25	113
178	1095	A	1	H	3	140	4.33	–47.8	9.56	5.11E-02	25	113
178	1095	A	1	H	4	8	4.51	–52.16	338.71	4.73E-02	25	117
178	1095	A	1	H	4	12	4.55	–58.43	351.89	4.90E-02	25	117
178	1095	A	1	H	4	16	4.59	–63.03	358.81	5.25E-02	25	117
178	1095	A	1	H	4	20	4.63	–61.97	353.18	5.95E-02	25	117
178	1095	A	1	H	4	24	4.67	–61.03	352.44	6.48E-02	25	117
178	1095	A	1	H	4	28	4.71	–59.36	350.39	7.26E-02	25	117
178	1095	A	1	H	4	32	4.75	–58.26	345.65	7.36E-02	25	117
178	1095	A	1	H	4	36	4.79	–59.91	349.86	7.23E-02	25	117
178	1095	A	1	H	4	40	4.83	–58.16	352.34	6.89E-02	25	117
178	1095	A	1	H	4	44	4.87	–60.03	354.13	6.19E-02	25	117
178	1095	A	1	H	4	48	4.91	–57.16	355.44	6.26E-02	25	117
178	1095	A	1	H	4	52	4.95	–49.72	354.79	7.26E-02	25	117
178	1095	A	1	H	4	56	4.99	–53.66	354.85	8.07E-02	25	117
178	1095	A	1	H	4	60	5.03	–64.26	350.12	8.88E-02	25	117
178	1095	A	1	H	4	64	5.07	–68.24	343.62	9.83E-02	25	117
178	1095	A	1	H	4	68	5.11	–69.65	334.52	1.04E-01	25	117
178	1095	A	1	H	4	72	5.15	–72.43	323.41	1.03E-01	25	117
178	1095	A	1	H	4	76	5.19	–75.83	327.72	9.91E-02	25	117
178	1095	A	1	H	4	80	5.23	–74.42	342.44	9.68E-02	25	117
178	1095	A	1	H	4	84	5.27	–69	347.67	8.47E-02	25	117
178	1095	A	1	H	4	88	5.31	–62.23	351.89	5.58E-02	25	117
178	1095	A	1	H	4	92	5.35	–52.44	13.83	2.76E-02	25	117
178	1095	A	1	H	4	96	5.39	–57.45	62.92	2.08E-02	25	117
178	1095	A	1	H	4	100	5.43	–72.59	57.16	3.12E-02	25	117
178	1095	A	1	H	4	104	5.47	–42.95	340.43	5.24E-02	25	117
178	1095	A	1	H	4	108	5.51	–10.61	311.02	1.08E-01	25	117
178	1095	A	1	H	4	112	5.55	–16.34	294.77	1.03E-01	25	117
178	1095	A	2	H	1	8	5.98	18.07	34.72	4.34E-02	25	189
178	1095	A	2	H	1	12	6.02	19.05	41	4.43E-02	25	189
178	1095	A	2	H	1	16	6.06	18.51	44.09	5.03E-02	25	189
178	1095	A	2	H	1	20	6.1	23.34	38	4.11E-02	25	189
178	1095	A	2	H	1	24	6.14	14.47	40.14	3.85E-02	25	189
178	1095	A	2	H	1	28	6.18	7.88	39.41	4.83E-02	25	189
178	1095	A	2	H	1	32	6.22	4.95	60.9	6.11E-02	25	189
178	1095	A	2	H	1	36	6.26	–0.38	72.18	8.60E-02	25	189
178	1095	A	2	H	1	40	6.3	0.59	65.79	8.09E-02	25	189

Table T8 (continued).

Leg	Site	Hole	Core	Type	Section	Interval (cm)	Depth (mbsf)	Inclination (°)	Declination (°)	Intensity (A/m)	Demagnetization step (mT)	Run #
178	1095	A	2	H	1	44	6.34	4.11	64.01	7.76E-02	25	189
178	1095	A	2	H	1	48	6.38	6.96	68.37	8.09E-02	25	189
178	1095	A	2	H	1	52	6.42	5.99	67.28	8.12E-02	25	189
178	1095	A	2	H	1	56	6.46	6.43	66.96	9.16E-02	25	189
178	1095	A	2	H	1	60	6.5	9.32	61.53	8.54E-02	25	189
178	1095	A	2	H	1	64	6.54	9.38	70.78	8.25E-02	25	189
178	1095	A	2	H	1	68	6.58	8.95	92.18	7.44E-02	25	189
178	1095	A	2	H	1	72	6.62	2.68	91.07	4.69E-02	25	189
178	1095	A	2	H	1	76	6.66	–8.07	71.66	5.39E-02	25	189
178	1095	A	2	H	1	80	6.7	–18.08	56.05	4.88E-02	25	189
178	1095	A	2	H	1	84	6.74	–38.46	39.96	3.13E-02	25	189
178	1095	A	2	H	1	88	6.78	–70.73	36.69	3.71E-02	25	189
178	1095	A	2	H	1	92	6.82	–75.87	44.68	5.52E-02	25	189
178	1095	A	2	H	1	96	6.86	–71.73	39.44	7.70E-02	25	189
178	1095	A	2	H	1	100	6.9	–65.85	34.48	9.48E-02	25	189
178	1095	A	2	H	1	104	6.94	–62.51	39.44	1.06E-01	25	189
178	1095	A	2	H	1	108	6.98	–65.34	39.23	1.06E-01	25	189
178	1095	A	2	H	1	112	7.02	–71.2	33.07	1.12E-01	25	189
178	1095	A	2	H	1	116	7.06	–69.16	28.72	1.20E-01	25	189
178	1095	A	2	H	1	120	7.1	–65.97	26.51	1.15E-01	25	189
178	1095	A	2	H	1	124	7.14	–63.3	20.64	9.97E-02	25	189
178	1095	A	2	H	1	128	7.18	–60.59	16.24	7.20E-02	25	189
178	1095	A	2	H	1	132	7.22	–53.05	30.43	5.77E-02	25	189

Note: This table is also available in ASCII format in the **TABLES** directory.

Table T9. Split-core paleomagnetic measurements for Hole 1095A after 30-mT demagnetization.

Leg	Site	Hole	Core	Type	Section	Interval (cm)	Depth (mbsf)	Inclination (°)	Declination (°)	Intensity (A/m)	Demagnetization step (mT)	Run #
178	1095	A	2	H	1	8	5.98	19.07	35.35	3.74E-02	30	190
178	1095	A	2	H	1	12	6.02	19.51	40.73	3.82E-02	30	190
178	1095	A	2	H	1	16	6.06	18.6	43.68	4.39E-02	30	190
178	1095	A	2	H	1	20	6.1	23.93	37.48	3.53E-02	30	190
178	1095	A	2	H	1	24	6.14	14.86	40.04	3.24E-02	30	190
178	1095	A	2	H	1	28	6.18	8.14	38.52	4.11E-02	30	190
178	1095	A	2	H	1	32	6.22	5.38	60.74	5.26E-02	30	190
178	1095	A	2	H	1	36	6.26	–0.38	72.97	7.48E-02	30	190
178	1095	A	2	H	1	40	6.3	0.29	66.5	6.99E-02	30	190
178	1095	A	2	H	1	44	6.34	3.86	64.63	6.66E-02	30	190
178	1095	A	2	H	1	48	6.38	6.97	69.09	6.98E-02	30	190
178	1095	A	2	H	1	52	6.42	6.17	67.9	7.03E-02	30	190
178	1095	A	2	H	1	56	6.46	6.68	67.59	7.99E-02	30	190
178	1095	A	2	H	1	60	6.5	9.9	62.06	7.44E-02	30	190
178	1095	A	2	H	1	64	6.54	10.27	71.82	7.21E-02	30	190
178	1095	A	2	H	1	68	6.58	10.18	94.11	6.61E-02	30	190
178	1095	A	2	H	1	72	6.62	4.47	93.84	4.05E-02	30	190
178	1095	A	2	H	1	76	6.66	–7.73	72.09	4.58E-02	30	190
178	1095	A	2	H	1	80	6.7	–18.25	55.43	4.20E-02	30	190
178	1095	A	2	H	1	84	6.74	–39.04	37.55	2.70E-02	30	190
178	1095	A	2	H	1	88	6.78	–71.5	33.26	3.31E-02	30	190
178	1095	A	2	H	1	92	6.82	–77.14	43.55	5.01E-02	30	190
178	1095	A	2	H	1	96	6.86	–73.26	37.65	7.06E-02	30	190
178	1095	A	2	H	1	100	6.9	–67.1	33.29	8.73E-02	30	190
178	1095	A	2	H	1	104	6.94	–63.41	39.1	9.80E-02	30	190
178	1095	A	2	H	1	108	6.98	–65.85	38.77	9.93E-02	30	190
178	1095	A	2	H	1	112	7.02	–71.77	32.21	1.05E-01	30	190
178	1095	A	2	H	1	116	7.06	–69.94	28.2	1.12E-01	30	190
178	1095	A	2	H	1	120	7.1	–66.83	25.64	1.08E-01	30	190
178	1095	A	2	H	1	124	7.14	–64.32	19.08	9.28E-02	30	190
178	1095	A	2	H	1	128	7.18	–61.73	14.08	6.67E-02	30	190
178	1095	A	2	H	1	132	7.22	–54.53	28.33	5.26E-02	30	190
178	1095	A	2	H	2	8	7.48	–64.9	70.99	1.01E-01	30	194
178	1095	A	2	H	2	12	7.52	–62.64	65.7	1.23E-01	30	194
178	1095	A	2	H	2	16	7.56	–64.7	61.8	1.31E-01	30	194
178	1095	A	2	H	2	20	7.6	–65.3	52.37	1.37E-01	30	194
178	1095	A	2	H	2	24	7.64	–60.48	40.05	1.48E-01	30	194
178	1095	A	2	H	2	28	7.68	–59.68	38.09	1.31E-01	30	194
178	1095	A	2	H	2	32	7.72	–59.68	41.04	1.15E-01	30	194
178	1095	A	2	H	2	36	7.76	–54.98	39.27	8.77E-02	30	194
178	1095	A	2	H	2	40	7.8	–73.12	65.7	6.17E-02	30	194
178	1095	A	2	H	2	44	7.84	–73.63	69.35	8.15E-02	30	194
178	1095	A	2	H	2	48	7.88	–60.03	41.47	8.37E-02	30	194
178	1095	A	2	H	2	52	7.92	–60.2	32.85	7.22E-02	30	194
178	1095	A	2	H	2	56	7.96	–57.87	34.19	8.58E-02	30	194
178	1095	A	2	H	2	60	8	–48.61	35.1	9.93E-02	30	194
178	1095	A	2	H	2	64	8.04	–47.6	38.27	8.84E-02	30	194
178	1095	A	2	H	2	68	8.08	–52.44	44.16	7.70E-02	30	194
178	1095	A	2	H	2	72	8.12	–51.14	65.46	7.91E-02	30	194
178	1095	A	2	H	2	76	8.16	–56.33	76.95	8.15E-02	30	194
178	1095	A	2	H	2	80	8.2	–78.09	97.02	1.01E-01	30	194
178	1095	A	2	H	2	84	8.24	–78.02	76.32	1.58E-01	30	194
178	1095	A	2	H	2	88	8.28	–73.26	50.24	1.74E-01	30	194
178	1095	A	2	H	2	92	8.32	–71.52	32.48	1.67E-01	30	194
178	1095	A	2	H	2	96	8.36	–59.84	33.32	1.60E-01	30	194
178	1095	A	2	H	2	100	8.4	–53.33	41.67	1.42E-01	30	194
178	1095	A	2	H	2	104	8.44	–54.32	40.99	1.11E-01	30	194
178	1095	A	2	H	2	108	8.48	–61.54	35.1	7.50E-02	30	194
178	1095	A	2	H	2	112	8.52	–75.11	54.68	6.53E-02	30	194
178	1095	A	2	H	2	116	8.56	–67.18	73.41	8.96E-02	30	194
178	1095	A	2	H	2	120	8.6	–61.48	56.47	1.32E-01	30	194
178	1095	A	2	H	2	124	8.64	–55.69	41.11	1.63E-01	30	194
178	1095	A	2	H	2	128	8.68	–53.1	27.06	1.50E-01	30	194
178	1095	A	2	H	2	132	8.72	–71.17	36.78	1.31E-01	30	194
178	1095	A	2	H	2	136	8.76	–77.86	47.42	1.88E-01	30	194
178	1095	A	2	H	3	8	8.98	–62.48	68.19	6.43E-02	30	198

Note: Only a portion of this table appears here. The complete table is available in ASCII format in the **TABLES** directory.

Table T10. Split-core paleomagnetic measurements for Hole 1095A after processing the results from the 25- and 30- mT demagnetization steps.

Leg	Site	Hole	Core	Type	Section	Interval (cm)	Depth (mbsf)	Inclination (°)	Declination (°)	Intensity (A/m)	Demagnetization step (mT)	Run #
178	1095	A	1	H	3	56	3.49	–56.35	343.63	0.108	25	113
178	1095	A	1	H	3	60	3.53	–50.42	342.94	0.102	25	113
178	1095	A	1	H	3	64	3.57	–51.43	347.25	0.0816	25	113
178	1095	A	1	H	3	52	3.45	–59.94	347.52	0.104	25	113
178	1095	A	1	H	3	40	3.33	–58.07	351.63	0.106	25	113
178	1095	A	1	H	3	44	3.37	–59.82	350.65	0.104	25	113
178	1095	A	1	H	3	48	3.41	–58.63	347.2	0.101	25	113
178	1095	A	1	H	3	68	3.61	–51.33	350.66	0.068	25	113
178	1095	A	1	H	3	88	3.81	–57.66	342.19	0.0977	25	113
178	1095	A	1	H	3	92	3.85	–56.96	343.62	0.0926	25	113
178	1095	A	1	H	3	96	3.89	–56.97	343.62	0.0865	25	113
178	1095	A	1	H	3	84	3.77	–57.18	335.75	0.0925	25	113
178	1095	A	1	H	3	72	3.65	–48.3	342.51	0.0685	25	113
178	1095	A	1	H	3	76	3.69	–48.91	331.11	0.0786	25	113
178	1095	A	1	H	3	80	3.73	–52.21	329.6	0.0865	25	113
178	1095	A	1	H	2	132	2.78	–64.47	343.21	0.106	25	109
178	1095	A	1	H	2	136	2.82	–59.83	344.32	0.0988	25	109
178	1095	A	1	H	2	140	2.86	–49.5	337.72	0.107	25	109
178	1095	A	1	H	2	128	2.74	–67.58	333.2	0.1	25	109
178	1095	A	1	H	2	116	2.62	–49.06	339.44	0.141	25	109
178	1095	A	1	H	2	120	2.66	–47.99	342.34	0.12	25	109
178	1095	A	1	H	2	124	2.7	–61.38	339.13	0.0955	25	109
178	1095	A	1	H	3	8	3.01	–44.95	350.5	0.0986	25	113
178	1095	A	1	H	3	28	3.21	–63.9	321.36	0.105	25	113
178	1095	A	1	H	3	32	3.25	–60.82	336.29	0.105	25	113
178	1095	A	1	H	3	36	3.29	–57.1	350.98	0.103	25	113
178	1095	A	1	H	3	24	3.17	–66.26	325.01	0.107	25	113
178	1095	A	1	H	3	12	3.05	–48.61	349.79	0.104	25	113
178	1095	A	1	H	3	16	3.09	–54.67	341.62	0.115	25	113
178	1095	A	1	H	3	20	3.13	–62.28	333.48	0.114	25	113
178	1095	A	1	H	4	40	4.83	–58.16	352.34	0.0689	25	117
178	1095	A	1	H	4	44	4.87	–60.03	354.13	0.0619	25	117
178	1095	A	1	H	4	48	4.91	–57.16	355.44	0.0626	25	117
178	1095	A	1	H	4	36	4.79	–59.91	349.86	0.0723	25	117
178	1095	A	1	H	4	24	4.67	–61.03	352.44	0.0648	25	117
178	1095	A	1	H	4	28	4.71	–59.36	350.39	0.0726	25	117
178	1095	A	1	H	4	32	4.75	–58.26	345.65	0.0736	25	117
178	1095	A	1	H	4	52	4.95	–49.72	354.79	0.0726	25	117
178	1095	A	1	H	4	72	5.15	–72.43	323.41	0.103	25	117
178	1095	A	1	H	4	76	5.19	–75.83	327.72	0.0991	25	117
178	1095	A	1	H	4	80	5.23	–74.42	342.44	0.0968	25	117
178	1095	A	1	H	4	68	5.11	–69.65	334.52	0.104	25	117
178	1095	A	1	H	4	56	4.99	–53.66	354.85	0.0807	25	117
178	1095	A	1	H	4	60	5.03	–64.26	350.12	0.0888	25	117
178	1095	A	1	H	4	64	5.07	–68.24	343.62	0.0983	25	117
178	1095	A	1	H	3	116	4.09	–62.67	347.19	0.0737	25	113
178	1095	A	1	H	3	120	4.13	–64.85	344.34	0.0736	25	113
178	1095	A	1	H	3	124	4.17	–65.42	344.62	0.0744	25	113
178	1095	A	1	H	3	112	4.05	–61.22	348.34	0.07	25	113
178	1095	A	1	H	3	100	3.93	–56.02	345.58	0.0762	25	113
178	1095	A	1	H	3	104	3.97	–56.99	351.91	0.0645	25	113
178	1095	A	1	H	3	108	4.01	–59.56	352.2	0.0631	25	113
178	1095	A	1	H	3	128	4.21	–62.57	348.77	0.0719	25	113
178	1095	A	1	H	4	12	4.55	–58.43	351.89	0.049	25	117
178	1095	A	1	H	4	16	4.59	–63.03	358.81	0.0525	25	117
178	1095	A	1	H	4	20	4.63	–61.97	353.18	0.0595	25	117
178	1095	A	1	H	4	8	4.51	–52.16	338.71	0.0473	25	117
178	1095	A	1	H	3	132	4.25	–59.39	356.3	0.0681	25	113
178	1095	A	1	H	3	136	4.29	–53.86	4.54	0.0631	25	113
178	1095	A	1	H	3	140	4.33	–47.8	9.56	0.0511	25	113
178	1095	A	1	H	1	112	1.12	–52.7	329.81	0.135	25	105
178	1095	A	1	H	1	116	1.16	–49.66	316.14	0.151	25	105
178	1095	A	1	H	1	120	1.2	–46.6	314.76	0.155	25	105
178	1095	A	1	H	1	100	1	–41.82	336.49	0.124	25	105
178	1095	A	1	H	1	104	1.04	–48.13	341.55	0.126	25	105

Note: Only a portion of this table appears here. The complete table is available in ASCII format in the **TABLES** directory.

Table T11. Split-core paleomagnetic measurements for Hole 1095B before demagnetization (NRM results).

Leg	Site	Hole	Core	Type	Section	Interval (cm)	Depth (mbsf)	Inclination (°)	Declination (°)	Intensity (A/m)	Demagnetization step (mT)	Run #
178	1095	B	1	H	1	8	83.08	–2.74	178.67	3.87E-02	0	431
178	1095	B	1	H	1	12	83.12	–25.9	30.43	4.45E-01	0	431
178	1095	B	1	H	1	16	83.16	–18.04	334.44	9.09E-01	0	431
178	1095	B	1	H	1	20	83.2	–10.04	316.39	5.27E-01	0	431
178	1095	B	1	H	1	24	83.24	–19.67	16.97	3.99E-01	0	431
178	1095	B	1	H	1	28	83.28	–13.28	7.13	4.26E-01	0	431
178	1095	B	1	H	1	32	83.32	21.2	297.33	4.40E-02	0	431
178	1095	B	1	H	1	36	83.36	28.39	157.18	1.31E-01	0	431
178	1095	B	1	H	1	40	83.4	36.01	106.25	1.41E-01	0	431
178	1095	B	1	H	1	44	83.44	53.42	70.9	1.10E-01	0	431
178	1095	B	1	H	1	48	83.48	14.15	282.95	2.94E-01	0	431
178	1095	B	1	H	1	52	83.52	2.38	299.6	3.60E-01	0	431
178	1095	B	1	H	1	56	83.56	26.21	77.89	1.92E-01	0	431
178	1095	B	1	H	1	60	83.6	22.71	38.92	8.20E-01	0	431
178	1095	B	1	H	1	64	83.64	42.48	334.2	1.40E+00	0	431
178	1095	B	1	H	1	68	83.68	56.78	265.57	1.47E+00	0	431
178	1095	B	1	H	1	72	83.72	34.42	117.56	1.39E+00	0	431
178	1095	B	1	H	1	76	83.76	12.89	103.17	6.68E-01	0	431
178	1095	B	1	H	1	80	83.8	26.44	7.34	9.19E-02	0	431
178	1095	B	1	H	1	84	83.84	5.75	297.98	9.47E-02	0	431
178	1095	B	1	H	1	88	83.88	–10.71	303.64	3.29E-02	0	431
178	1095	B	1	H	1	92	83.92	–25.41	324.03	1.90E-02	0	431
178	1095	B	1	H	1	96	83.96	–19.39	353.63	1.84E-02	0	431
178	1095	B	1	H	1	100	84	–4.83	8.37	1.95E-02	0	431
178	1095	B	1	H	1	104	84.04	14.82	16.9	1.63E-02	0	431
178	1095	B	1	H	1	108	84.08	30.65	42.4	1.71E-02	0	431
178	1095	B	1	H	1	112	84.12	38.13	24.22	2.75E-02	0	431
178	1095	B	1	H	1	116	84.16	23.57	312.41	7.62E-02	0	431
178	1095	B	1	H	1	120	84.2	14.4	298.13	8.43E-02	0	431
178	1095	B	1	H	1	124	84.24	1.98	57.96	7.54E-02	0	431
178	1095	B	1	H	1	128	84.28	0.84	50.36	1.68E-01	0	431
178	1095	B	1	H	1	132	84.32	20.16	22.26	9.75E-02	0	431
178	1095	B	1	H	1	136	84.36	27.09	319.99	6.73E-02	0	431
178	1095	B	1	H	1	140	84.4	16.22	307.44	8.05E-02	0	431
178	1095	B	1	H	2	8	84.58	75.05	72.61	2.44E-01	0	435
178	1095	B	1	H	2	12	84.62	41.46	180.44	1.79E-01	0	435
178	1095	B	1	H	2	16	84.66	66.1	0.25	3.85E-02	0	435
178	1095	B	1	H	2	20	84.7	29.17	348.5	3.02E-02	0	435
178	1095	B	1	H	2	24	84.74	45.41	4.37	2.05E-02	0	435
178	1095	B	1	H	2	28	84.78	42.78	45.96	3.10E-02	0	435
178	1095	B	1	H	2	32	84.82	45.08	348.26	4.15E-02	0	435
178	1095	B	1	H	2	36	84.86	26.37	339.11	7.20E-02	0	435
178	1095	B	1	H	2	40	84.9	36.14	7.76	8.11E-02	0	435
178	1095	B	1	H	2	44	84.94	52.62	356.54	6.76E-02	0	435
178	1095	B	1	H	2	48	84.98	50.15	350.62	7.58E-02	0	435
178	1095	B	1	H	2	52	85.02	51.76	6.61	7.87E-02	0	435
178	1095	B	1	H	2	56	85.06	55.3	352.84	7.80E-02	0	435
178	1095	B	1	H	2	60	85.1	59.5	6.62	8.09E-02	0	435
178	1095	B	1	H	2	64	85.14	54.31	20.4	8.36E-02	0	435
178	1095	B	1	H	2	68	85.18	50.97	15.01	9.05E-02	0	435
178	1095	B	1	H	2	72	85.22	42.13	9.58	9.55E-02	0	435
178	1095	B	1	H	2	76	85.26	26.8	316.29	9.80E-02	0	435
178	1095	B	1	H	2	80	85.3	–14.57	224.07	1.33E-01	0	435
178	1095	B	1	H	2	84	85.34	–11.47	132.17	1.90E-01	0	435
178	1095	B	1	H	2	88	85.38	28.26	69.54	6.97E-02	0	435
178	1095	B	1	H	2	92	85.42	43.44	333.68	5.91E-02	0	435
178	1095	B	1	H	2	96	85.46	29.54	348.18	7.01E-02	0	435
178	1095	B	1	H	2	100	85.5	13.7	14.13	1.71E-01	0	435
178	1095	B	1	H	2	104	85.54	19.34	5.49	2.24E-01	0	435
178	1095	B	1	H	2	108	85.58	22.05	347.28	2.05E-01	0	435
178	1095	B	1	H	2	112	85.62	18.25	5.26	1.69E-01	0	435
178	1095	B	1	H	2	116	85.66	9.9	23.09	1.88E-01	0	435
178	1095	B	1	H	2	120	85.7	15.02	36.89	1.81E-01	0	435
178	1095	B	1	H	2	124	85.74	24.5	23.62	1.02E-01	0	435
178	1095	B	1	H	2	128	85.78	10.89	354.56	1.52E-01	0	435
178	1095	B	1	H	2	132	85.82	9.91	358.83	2.12E-01	0	435

Note: Only a portion of this table appears here. The complete table is available in ASCII format in the **TABLES** directory.

Table T12. Split-core paleomagnetic measurements for Hole 1095B after 10-mT demagnetization.

Leg	Site	Hole	Core	Type	Section	Interval (cm)	Depth (mbsf)	Inclination (°)	Declination (°)	Intensity (A/m)	Demagnetization step (mT)	Run #
178	1095	B	1	H	1	8	83.08	–25.7	209.88	3.65E-02	10	432
178	1095	B	1	H	1	12	83.12	–26.76	31.64	4.04E-01	10	432
178	1095	B	1	H	1	16	83.16	–19.81	334.23	7.77E-01	10	432
178	1095	B	1	H	1	20	83.2	–13.69	314.78	4.60E-01	10	432
178	1095	B	1	H	1	24	83.24	–23.23	17.05	3.85E-01	10	432
178	1095	B	1	H	1	28	83.28	–16.78	6.4	4.06E-01	10	432
178	1095	B	1	H	1	32	83.32	–5.62	291.05	5.28E-02	10	432
178	1095	B	1	H	1	36	83.36	20.28	165.32	1.09E-01	10	432
178	1095	B	1	H	1	40	83.4	30.97	123.57	9.90E-02	10	432
178	1095	B	1	H	1	44	83.44	70.33	143.66	4.82E-02	10	432
178	1095	B	1	H	1	48	83.48	–0.58	275.93	2.64E-01	10	432
178	1095	B	1	H	1	52	83.52	–16.22	299.89	2.78E-01	10	432
178	1095	B	1	H	1	56	83.56	7.8	83.5	1.85E-01	10	432
178	1095	B	1	H	1	60	83.6	20.73	38.33	7.11E-01	10	432
178	1095	B	1	H	1	64	83.64	43.33	331.63	1.22E+00	10	432
178	1095	B	1	H	1	68	83.68	56.44	266.37	1.30E+00	10	432
178	1095	B	1	H	1	72	83.72	31.92	116.39	1.29E+00	10	432
178	1095	B	1	H	1	76	83.76	8.34	105.09	6.12E-01	10	432
178	1095	B	1	H	1	80	83.8	–1.01	8.02	7.12E-02	10	432
178	1095	B	1	H	1	84	83.84	–14.3	299.34	9.03E-02	10	432
178	1095	B	1	H	1	88	83.88	–41.97	294.16	4.53E-02	10	432
178	1095	B	1	H	1	92	83.92	–67.06	296.63	3.45E-02	10	432
178	1095	B	1	H	1	96	83.96	–79.01	317.71	3.13E-02	10	432
178	1095	B	1	H	1	100	84	–81.92	333	2.91E-02	10	432
178	1095	B	1	H	1	104	84.04	–83.3	4.11	2.69E-02	10	432
178	1095	B	1	H	1	108	84.08	–81.35	60.08	2.52E-02	10	432
178	1095	B	1	H	1	112	84.12	–63.01	3.1	2.16E-02	10	432
178	1095	B	1	H	1	116	84.16	–8.11	305.51	6.71E-02	10	432
178	1095	B	1	H	1	120	84.2	–13.11	295.05	7.87E-02	10	432
178	1095	B	1	H	1	124	84.24	–27.03	79.67	7.00E-02	10	432
178	1095	B	1	H	1	128	84.28	–16.2	68.74	1.47E-01	10	432
178	1095	B	1	H	1	132	84.32	–16.14	33.95	5.92E-02	10	432
178	1095	B	1	H	1	136	84.36	–15.6	326.8	2.78E-02	10	432
178	1095	B	1	H	1	140	84.4	–35.02	295.61	2.14E-02	10	432
178	1095	B	1	H	2	8	84.58	51.6	124.54	2.34E-01	10	436
178	1095	B	1	H	2	12	84.62	22.27	165.48	1.80E-01	10	436
178	1095	B	1	H	2	16	84.66	29.57	345.74	2.74E-02	10	436
178	1095	B	1	H	2	20	84.7	6.48	345.79	3.38E-02	10	436
178	1095	B	1	H	2	24	84.74	10.21	354.92	1.31E-02	10	436
178	1095	B	1	H	2	28	84.78	5.92	21.01	6.73E-03	10	436
178	1095	B	1	H	2	32	84.82	–11.61	288.46	1.76E-02	10	436
178	1095	B	1	H	2	36	84.86	–27.83	320.38	3.41E-02	10	436
178	1095	B	1	H	2	40	84.9	–13.09	14	3.27E-02	10	436
178	1095	B	1	H	2	44	84.94	–4.2	355.99	1.40E-02	10	436
178	1095	B	1	H	2	48	84.98	0.86	352.59	1.63E-02	10	436
178	1095	B	1	H	2	52	85.02	4.6	7.48	1.93E-02	10	436
178	1095	B	1	H	2	56	85.06	5.39	0.8	1.84E-02	10	436
178	1095	B	1	H	2	60	85.1	5.75	3.02	1.79E-02	10	436
178	1095	B	1	H	2	64	85.14	4.19	7.47	1.87E-02	10	436
178	1095	B	1	H	2	68	85.18	2.52	19.64	2.48E-02	10	436
178	1095	B	1	H	2	72	85.22	–10.29	13.86	4.20E-02	10	436
178	1095	B	1	H	2	76	85.26	–22.32	298.53	7.21E-02	10	436
178	1095	B	1	H	2	80	85.3	–34.6	217.09	1.78E-01	10	436
178	1095	B	1	H	2	84	85.34	–26.8	138.21	2.17E-01	10	436
178	1095	B	1	H	2	88	85.38	–23.11	88.14	6.65E-02	10	436
178	1095	B	1	H	2	92	85.42	–25.49	337.26	3.15E-02	10	436
178	1095	B	1	H	2	96	85.46	–22.86	333.59	4.52E-02	10	436
178	1095	B	1	H	2	100	85.5	–18.97	12.65	8.39E-02	10	436
178	1095	B	1	H	2	104	85.54	–16.11	14.52	8.42E-02	10	436
178	1095	B	1	H	2	108	85.58	–27.53	352.64	6.83E-02	10	436
178	1095	B	1	H	2	112	85.62	–43.64	9.16	7.58E-02	10	436
178	1095	B	1	H	2	116	85.66	–46.8	26.56	9.89E-02	10	436
178	1095	B	1	H	2	120	85.7	–44.48	39.81	1.02E-01	10	436
178	1095	B	1	H	2	124	85.74	–56.04	38.93	8.36E-02	10	436
178	1095	B	1	H	2	128	85.78	–52.88	11.64	9.70E-02	10	436
178	1095	B	1	H	2	132	85.82	–43.4	9.31	1.11E-01	10	436

Note: Only a portion of this table appears here. The complete table is available in ASCII format in the **TABLES** directory.

Table T13. Split-core paleomagnetic measurements for Hole 1095B after 20-mT demagnetization.

Leg	Site	Hole	Core	Type	Section	Interval (cm)	Depth (mbsf)	Inclination (°)	Declination (°)	Intensity (A/m)	Demagnetization step (mT)	Run #
178	1095	B	1	H	1	8	83.08	-39.25	225.7	4.99E-02	20	433
178	1095	B	1	H	1	12	83.12	–29.91	31.66	3.23E-01	20	433
178	1095	B	1	H	1	16	83.16	–21.28	332.34	6.23E-01	20	433
178	1095	B	1	H	1	20	83.2	–16.98	313.63	3.80E-01	20	433
178	1095	B	1	H	1	24	83.24	–27.02	17.16	3.44E-01	20	433
178	1095	B	1	H	1	28	83.28	–20.7	5.33	3.61E-01	20	433
178	1095	B	1	H	1	32	83.32	–30.81	291.89	5.87E-02	20	433
178	1095	B	1	H	1	36	83.36	3.58	172.72	8.63E-02	20	433
178	1095	B	1	H	1	40	83.4	12.71	129.99	6.47E-02	20	433
178	1095	B	1	H	1	44	83.44	39.99	141.42	1.63E-02	20	433
178	1095	B	1	H	1	48	83.48	–6.38	275.13	1.65E-01	20	433
178	1095	B	1	H	1	52	83.52	–21.42	292.24	1.74E-01	20	433
178	1095	B	1	H	1	56	83.56	–0.3	93.04	1.27E-01	20	433
178	1095	B	1	H	1	60	83.6	18.21	37.36	5.81E-01	20	433
178	1095	B	1	H	1	64	83.64	46.85	334.79	9.80E-01	20	433
178	1095	B	1	H	1	68	83.68	55.18	262.69	1.03E+00	20	433
178	1095	B	1	H	1	72	83.72	34.7	121.03	9.08E-01	20	433
178	1095	B	1	H	1	76	83.76	12.64	106.57	4.28E-01	20	433
178	1095	B	1	H	1	80	83.8	27.31	14.02	6.02E-02	20	433
178	1095	B	1	H	1	84	83.84	11.98	304.18	6.05E-02	20	433
178	1095	B	1	H	1	88	83.88	15.14	298.14	2.45E-02	20	433
178	1095	B	1	H	1	92	83.92	25.43	298.67	1.06E-02	20	433
178	1095	B	1	H	1	96	83.96	42.6	315	5.71E-03	20	433
178	1095	B	1	H	1	100	84	53.45	322.38	4.69E-03	20	433
178	1095	B	1	H	1	104	84.04	63.5	358.83	4.24E-03	20	433
178	1095	B	1	H	1	108	84.08	52.35	73.33	4.61E-03	20	433
178	1095	B	1	H	1	112	84.12	40.35	0.14	9.62E-03	20	433
178	1095	B	1	H	1	116	84.16	11.61	307.48	5.61E-02	20	433
178	1095	B	1	H	1	120	84.2	3.09	298.63	6.09E-02	20	433
178	1095	B	1	H	1	124	84.24	–10.68	84.8	4.54E-02	20	433
178	1095	B	1	H	1	128	84.28	–10.48	70.65	1.03E-01	20	433
178	1095	B	1	H	1	132	84.32	–0.88	32.45	4.21E-02	20	433
178	1095	B	1	H	1	136	84.36	17.05	329.28	2.10E-02	20	433
178	1095	B	1	H	1	140	84.4	6.42	283.78	1.06E-02	20	433
178	1095	B	1	H	2	8	84.58	53.88	125.25	1.92E-01	20	437
178	1095	B	1	H	2	12	84.62	21.76	166.56	1.55E-01	20	437
178	1095	B	1	H	2	16	84.66	32.75	347.49	2.02E-02	20	437
178	1095	B	1	H	2	20	84.7	6.21	347.56	2.80E-02	20	437
178	1095	B	1	H	2	24	84.74	9.71	354.98	1.13E-02	20	437
178	1095	B	1	H	2	28	84.78	4.19	16.91	4.69E-03	20	437
178	1095	B	1	H	2	32	84.82	–14.28	279.01	1.49E-02	20	437
178	1095	B	1	H	2	36	84.86	–33.36	318.97	2.66E-02	20	437
178	1095	B	1	H	2	40	84.9	–17.47	17.04	2.53E-02	20	437
178	1095	B	1	H	2	44	84.94	–12.77	354.84	8.99E-03	20	437
178	1095	B	1	H	2	48	84.98	–5.77	351.1	1.01E-02	20	437
178	1095	B	1	H	2	52	85.02	–0.54	8.02	1.24E-02	20	437
178	1095	B	1	H	2	56	85.06	–0.68	2.46	1.19E-02	20	437
178	1095	B	1	H	2	60	85.1	–2.26	1.62	1.15E-02	20	437
178	1095	B	1	H	2	64	85.14	–2.69	2.44	1.23E-02	20	437
178	1095	B	1	H	2	68	85.18	–2.43	17.88	1.60E-02	20	437
178	1095	B	1	H	2	72	85.22	–14.57	14.07	2.88E-02	20	437
178	1095	B	1	H	2	76	85.26	–24.96	299.87	4.94E-02	20	437
178	1095	B	1	H	2	80	85.3	–35.02	216.54	1.24E-01	20	437
178	1095	B	1	H	2	84	85.34	–26.58	138.36	1.55E-01	20	437
178	1095	B	1	H	2	88	85.38	–23.76	90.46	4.73E-02	20	437
178	1095	B	1	H	2	92	85.42	–27.14	336.77	2.23E-02	20	437
178	1095	B	1	H	2	96	85.46	–22.3	331.51	3.26E-02	20	437
178	1095	B	1	H	2	100	85.5	–18.69	12.55	5.72E-02	20	437
178	1095	B	1	H	2	104	85.54	–16.01	17.89	5.26E-02	20	437
178	1095	B	1	H	2	108	85.58	–30	354.33	3.99E-02	20	437
178	1095	B	1	H	2	112	85.62	–46.56	9.5	4.73E-02	20	437
178	1095	B	1	H	2	116	85.66	–49.96	26.61	6.26E-02	20	437
178	1095	B	1	H	2	120	85.7	–48.02	39.85	6.59E-02	20	437
178	1095	B	1	H	2	124	85.74	–57.34	41.96	5.53E-02	20	437
178	1095	B	1	H	2	128	85.78	–55.82	18.62	6.13E-02	20	437
178	1095	B	1	H	2	132	85.82	–47.85	13.6	6.87E-02	20	437

Note: Only a portion of this table appears here. The complete table is available in ASCII format in the **TABLES** directory.

Table T14. Split-core paleomagnetic measurements for Hole 1095B after 30-mT demagnetization.

Leg	Site	Hole	Core	Type	Section	Interval (cm)	Depth (mbsf)	Inclination (°)	Declination (°)	Intensity (A/m)	Demagnetization step (mT)	Run #
178	1095	B	1	H	1	8	83.08	–39.24	220.4	4.58E-02	30	434
178	1095	B	1	H	1	12	83.12	–34.29	30.83	2.63E-01	30	434
178	1095	B	1	H	1	16	83.16	–23.29	330.41	5.30E-01	30	434
178	1095	B	1	H	1	20	83.2	–17.97	313.27	3.29E-01	30	434
178	1095	B	1	H	1	24	83.24	–28.15	16.55	2.85E-01	30	434
178	1095	B	1	H	1	28	83.28	–21.33	5.67	2.98E-01	30	434
178	1095	B	1	H	1	32	83.32	–31.03	289.58	4.77E-02	30	434
178	1095	B	1	H	1	36	83.36	3.8	176.68	7.38E-02	30	434
178	1095	B	1	H	1	40	83.4	13.88	136.38	5.23E-02	30	434
178	1095	B	1	H	1	44	83.44	38.69	147	1.66E-02	30	434
178	1095	B	1	H	1	48	83.48	–4.37	272.24	1.17E-01	30	434
178	1095	B	1	H	1	52	83.52	–19.84	285.53	1.21E-01	30	434
178	1095	B	1	H	1	56	83.56	3.94	96.6	9.96E-02	30	434
178	1095	B	1	H	1	60	83.6	19.33	36.48	4.80E-01	30	434
178	1095	B	1	H	1	64	83.64	47.98	334.09	7.88E-01	30	434
178	1095	B	1	H	1	68	83.68	53.83	259.74	8.19E-01	30	434
178	1095	B	1	H	1	72	83.72	35.99	123.98	6.93E-01	30	434
178	1095	B	1	H	1	76	83.76	14	107.64	3.27E-01	30	434
178	1095	B	1	H	1	80	83.8	31.79	9.47	4.54E-02	30	434
178	1095	B	1	H	1	84	83.84	13.63	305.85	4.62E-02	30	434
178	1095	B	1	H	1	88	83.88	18.98	301.63	1.83E-02	30	434
178	1095	B	1	H	1	92	83.92	31.81	301.12	8.11E-03	30	434
178	1095	B	1	H	1	96	83.96	51.11	312.33	4.79E-03	30	434
178	1095	B	1	H	1	100	84	63.45	311.3	4.08E-03	30	434
178	1095	B	1	H	1	104	84.04	78.05	1.37	3.72E-03	30	434
178	1095	B	1	H	1	108	84.08	55.26	97.1	4.27E-03	30	434
178	1095	B	1	H	1	112	84.12	44.93	2.46	7.76E-03	30	434
178	1095	B	1	H	1	116	84.16	11.51	309.02	4.63E-02	30	434
178	1095	B	1	H	1	120	84.2	2.92	299.96	4.96E-02	30	434
178	1095	B	1	H	1	124	84.24	–12.1	89.72	3.45E-02	30	434
178	1095	B	1	H	1	128	84.28	–12.1	71.51	7.87E-02	30	434
178	1095	B	1	H	1	132	84.32	–2.85	32.16	3.31E-02	30	434
178	1095	B	1	H	1	136	84.36	17.84	330.02	1.42E-02	30	434
178	1095	B	1	H	1	140	84.4	5.29	259.1	6.94E-03	30	434
178	1095	B	1	H	2	8	84.58	56.22	127.98	1.62E-01	30	438
178	1095	B	1	H	2	12	84.62	21.83	168.28	1.33E-01	30	438
178	1095	B	1	H	2	16	84.66	36.32	348.06	1.54E-02	30	438
178	1095	B	1	H	2	20	84.7	6.17	348.48	2.20E-02	30	438
178	1095	B	1	H	2	24	84.74	10.15	355.49	8.62E-03	30	438
178	1095	B	1	H	2	28	84.78	5.88	11.73	2.95E-03	30	438
178	1095	B	1	H	2	32	84.82	–14.39	272.19	1.28E-02	30	438
178	1095	B	1	H	2	36	84.86	–35.41	319.5	2.13E-02	30	438
178	1095	B	1	H	2	40	84.9	–17.13	19.57	1.98E-02	30	438
178	1095	B	1	H	2	44	84.94	–11.5	352.79	6.01E-03	30	438
178	1095	B	1	H	2	48	84.98	–1.99	348.39	6.53E-03	30	438
178	1095	B	1	H	2	52	85.02	3.19	8.57	8.04E-03	30	438
178	1095	B	1	H	2	56	85.06	3.24	1.22	7.70E-03	30	438
178	1095	B	1	H	2	60	85.1	1.33	359.55	7.42E-03	30	438
178	1095	B	1	H	2	64	85.14	0.85	1.1	8.33E-03	30	438
178	1095	B	1	H	2	68	85.18	0.36	20.03	1.13E-02	30	438
178	1095	B	1	H	2	72	85.22	–13.85	15.37	2.05E-02	30	438
178	1095	B	1	H	2	76	85.26	–23.92	294.92	3.85E-02	30	438
178	1095	B	1	H	2	80	85.3	–35.22	215.44	9.56E-02	30	438
178	1095	B	1	H	2	84	85.34	–25.9	136.8	1.18E-01	30	438
178	1095	B	1	H	2	88	85.38	–21.51	91.09	3.52E-02	30	438
178	1095	B	1	H	2	92	85.42	–22.3	334.79	1.58E-02	30	438
178	1095	B	1	H	2	96	85.46	–17.45	329.62	2.46E-02	30	438
178	1095	B	1	H	2	100	85.5	–15.16	10.68	3.97E-02	30	438
178	1095	B	1	H	2	104	85.54	–9.87	19.31	3.23E-02	30	438
178	1095	B	1	H	2	108	85.58	–22.82	353.83	2.10E-02	30	438
178	1095	B	1	H	2	112	85.62	–41.7	10.71	2.54E-02	30	438
178	1095	B	1	H	2	116	85.66	–45.91	27.54	3.48E-02	30	438
178	1095	B	1	H	2	120	85.7	–44.67	39.12	3.61E-02	30	438
178	1095	B	1	H	2	124	85.74	–54.15	38.27	2.91E-02	30	438
178	1095	B	1	H	2	128	85.78	–50.91	17.15	3.20E-02	30	438
178	1095	B	1	H	2	132	85.82	–43.18	14.85	3.63E-02	30	438

Note: Only a portion of this table appears here. The complete table is available in ASCII format in the **TABLES** directory.

Table T15. Split-core paleomagnetic measurements for Hole 1095B after processing the results from the 30-mT demagnetization step.

Leg	Site	Hole	Core	Type	Section	Interval (cm)	Depth (mbsf)	Inclination (°)	Declination (°)	Intensity (A/m)	Demagnetization step (mT)	Run #
178	1095	B	1	H	3	128	87.28	–28.78	56.68	0.0415	30	442
178	1095	B	1	H	3	132	87.32	–30.24	63.15	0.0404	30	442
178	1095	B	1	H	3	136	87.36	–24.65	69.45	0.0375	30	442
178	1095	B	1	H	3	140	87.4	–15.14	72.47	0.0323	30	442
178	1095	B	1	H	4	8	87.58	15.2	80.62	0.0264	30	446
178	1095	B	1	H	4	12	87.62	41.28	121.1	0.0202	30	446
178	1095	B	1	H	4	16	87.66	31.88	150.19	0.0227	30	446
178	1095	B	1	H	4	20	87.7	8.88	81.92	0.0227	30	446
178	1095	B	1	H	4	24	87.74	3.5	60.45	0.0326	30	446
178	1095	B	1	H	4	28	87.78	11.88	71.1	0.0182	30	446
178	1095	B	1	H	4	32	87.82	36.34	132.97	0.011	30	446
178	1095	B	1	H	4	36	87.86	46.27	100.8	0.0143	30	446
178	1095	B	1	H	4	40	87.9	52.91	78.38	0.0295	30	446
178	1095	B	1	H	4	44	87.94	56.58	100.19	0.0341	30	446
178	1095	B	1	H	4	48	87.98	57.58	124.82	0.0282	30	446
178	1095	B	1	H	4	52	88.02	26.97	57.76	0.0257	30	446
178	1095	B	1	H	4	56	88.06	16.57	32.91	0.0502	30	446
178	1095	B	1	H	4	60	88.1	29.42	23.18	0.0494	30	446
178	1095	B	1	H	4	64	88.14	42.47	21.88	0.0403	30	446
178	1095	B	1	H	4	68	88.18	27.85	43.15	0.0309	30	446
178	1095	B	1	H	4	72	88.22	12.98	49.95	0.0444	30	446
178	1095	B	1	H	4	76	88.26	35.35	52.93	0.0425	30	446
178	1095	B	1	H	4	80	88.3	55.99	67.47	0.0359	30	446
178	1095	B	1	H	4	84	88.34	56.35	24.72	0.033	30	446
178	1095	B	1	H	4	88	88.38	53.45	6.82	0.0324	30	446
178	1095	B	1	H	4	92	88.42	64.32	44.54	0.0257	30	446
178	1095	B	1	H	4	96	88.46	59.52	72.06	0.0325	30	446
178	1095	B	1	H	4	100	88.5	57.31	74.82	0.0413	30	446
178	1095	B	1	H	4	104	88.54	64.72	91.66	0.0493	30	446
178	1095	B	1	H	4	108	88.58	64.71	132.82	0.0504	30	446
178	1095	B	1	H	4	112	88.62	62.52	155.24	0.0259	30	446
178	1095	B	1	H	4	116	88.66	77.81	231.92	0.0048	30	446
178	1095	B	1	H	4	120	88.7	–66.42	301.84	0.00384	30	446
178	1095	B	1	H	4	124	88.74	–84.05	314.83	0.0106	30	446
178	1095	B	1	H	4	128	88.78	–80.45	18.35	0.0155	30	446
178	1095	B	1	H	4	132	88.82	–78.47	357.09	0.0165	30	446
178	1095	B	1	H	4	136	88.86	–80.05	348.41	0.0166	30	446
178	1095	B	1	H	4	140	88.9	–81.33	22.97	0.0165	30	446
178	1095	B	1	H	5	8	89.08	–79.98	19.38	0.0158	30	450
178	1095	B	1	H	5	12	89.12	–80.3	41.19	0.0146	30	450
178	1095	B	1	H	5	16	89.16	–78.46	6.4	0.0142	30	450
178	1095	B	1	H	5	20	89.2	–74.48	2.46	0.0159	30	450
178	1095	B	1	H	5	24	89.24	–73.09	1.07	0.0186	30	450
178	1095	B	1	H	5	28	89.28	–78.48	318.54	0.0209	30	450
178	1095	B	1	H	5	32	89.32	–76.47	271.19	0.0256	30	450
178	1095	B	1	H	5	36	89.36	–72.84	217.12	0.0277	30	450
178	1095	B	1	H	5	40	89.4	–75.34	227.12	0.0347	30	450
178	1095	B	1	H	5	44	89.44	–80.37	298.55	0.0411	30	450
178	1095	B	1	H	5	48	89.48	–77.4	334.29	0.0503	30	450
178	1095	B	1	H	5	52	89.52	–72.18	344.62	0.0598	30	450
178	1095	B	1	H	5	56	89.56	–70.72	349.59	0.062	30	450
178	1095	B	1	H	5	60	89.6	–67.32	6.96	0.0549	30	450
178	1095	B	1	H	5	64	89.64	–68.41	20.06	0.0375	30	450
178	1095	B	1	H	5	68	89.68	–76.88	40.39	0.0215	30	450
178	1095	B	1	H	5	72	89.72	–79.37	49.67	0.00952	30	450
178	1095	B	1	H	5	76	89.76	–86.45	328.39	0.00581	30	450
178	1095	B	1	H	5	80	89.8	–74.41	341.21	0.00455	30	450
178	1095	B	1	H	5	84	89.84	–79.72	36.59	0.00379	30	450
178	1095	B	1	H	5	88	89.88	–82.74	212.16	0.00718	30	450
178	1095	B	1	H	5	92	89.92	–73.34	277.41	0.0126	30	450
178	1095	B	1	H	5	96	89.96	–66.78	286.61	0.0178	30	450
178	1095	B	1	H	5	100	90	–77.25	245.73	0.024	30	450
178	1095	B	1	H	5	104	90.04	–72.28	203.42	0.0444	30	450
178	1095	B	1	H	5	108	90.08	–73.52	233.48	0.0662	30	450
178	1095	B	1	H	5	112	90.12	–75.13	234.23	0.0719	30	450

Note: Only a portion of this table appears here. The complete table is available in ASCII format in the **TABLES** directory.

Table T16. Split-core paleomagnetic measurements for Hole 1095C before demagnetization (NRM results).

Leg	Site	Hole	Core	Type	Section	Interval (cm)	Depth (mbsf)	Inclination (°)	Declination (°)	Intensity (A/m)	Demagnetization step (mT)	Run #
178	1095	C	1	H	2	8	1.58	–37.2	359.65	2.31E-01	0	4539
178	1095	C	1	H	2	12	1.62	–39.08	355.38	2.34E-01	0	4539
178	1095	C	1	H	2	16	1.66	–37.09	358.3	2.25E-01	0	4539
178	1095	C	1	H	2	20	1.7	–36.34	359.69	2.06E-01	0	4539
178	1095	C	1	H	2	24	1.74	–36.5	357.48	1.82E-01	0	4539
178	1095	C	1	H	2	28	1.78	–36.63	354.89	1.61E-01	0	4539
178	1095	C	1	H	2	32	1.82	–34.16	355.86	1.55E-01	0	4539
178	1095	C	1	H	2	36	1.86	–26.44	358.87	1.54E-01	0	4539
178	1095	C	1	H	2	40	1.9	–11.58	356.42	1.42E-01	0	4539
178	1095	C	1	H	2	44	1.94	–2.49	351.34	9.56E-02	0	4539
178	1095	C	1	H	2	48	1.98	–12.59	354.88	7.49E-02	0	4539
178	1095	C	1	H	2	52	2.02	–20.73	358.31	8.64E-02	0	4539
178	1095	C	1	H	2	56	2.06	–19.8	355.73	9.17E-02	0	4539
178	1095	C	1	H	2	60	2.1	–12.48	356.84	8.78E-02	0	4539
178	1095	C	1	H	2	64	2.14	–7.59	357.08	9.20E-02	0	4539
178	1095	C	1	H	2	68	2.18	0.04	356.84	7.98E-02	0	4539
178	1095	C	1	H	2	72	2.22	8.41	351.76	5.63E-02	0	4539
178	1095	C	1	H	2	76	2.26	14	3.29	6.38E-02	0	4539
178	1095	C	1	H	2	80	2.3	20.05	14.84	8.75E-02	0	4539
178	1095	C	1	H	2	84	2.34	21.98	355.95	8.26E-02	0	4539
178	1095	C	1	H	2	88	2.38	2.54	347.89	6.56E-02	0	4539
178	1095	C	1	H	2	92	2.42	–18.6	359.79	7.51E-02	0	4539
178	1095	C	1	H	2	96	2.46	–23.58	7.63	1.05E-01	0	4539
178	1095	C	1	H	2	100	2.5	–7.52	16.21	1.36E-01	0	4539
178	1095	C	1	H	2	104	2.54	25.4	18.51	1.79E-01	0	4539
178	1095	C	1	H	2	108	2.58	61.89	14.63	1.96E-01	0	4539
178	1095	C	1	H	2	112	2.62	76.35	10.87	1.55E-01	0	4539
178	1095	C	1	H	2	116	2.66	81.68	57.28	7.27E-02	0	4539

Note: This table is also available in ASCII format in the **TABLES** directory.

Table T17. Split-core paleomagnetic measurements for Hole 1095C after 20-mT demagnetization.

Leg	Site	Hole	Core	Type	Section	Interval (cm)	Depth (mbsf)	Inclination (°)	Declination (°)	Intensity (A/m)	Demagnetization step (mT)	Run #
178	1095	C	1	H	2	8	1.58	–51.68	356.87	2.05E-01	20	4540
178	1095	C	1	H	2	12	1.62	–52.83	351.79	2.13E-01	20	4540
178	1095	C	1	H	2	16	1.66	–51.56	356.24	2.01E-01	20	4540
178	1095	C	1	H	2	20	1.7	–51.95	359.22	1.80E-01	20	4540
178	1095	C	1	H	2	24	1.74	–52.78	356.44	1.59E-01	20	4540
178	1095	C	1	H	2	28	1.78	–53.25	353.19	1.42E-01	20	4540
178	1095	C	1	H	2	32	1.82	–49.96	353	1.36E-01	20	4540
178	1095	C	1	H	2	36	1.86	–41.33	356.89	1.30E-01	20	4540
178	1095	C	1	H	2	40	1.9	–27.56	356.65	1.09E-01	20	4540
178	1095	C	1	H	2	44	1.94	–25.58	347.8	7.10E-02	20	4540
178	1095	C	1	H	2	48	1.98	–42	347.35	6.42E-02	20	4540
178	1095	C	1	H	2	52	2.02	–50.95	357.21	7.43E-02	20	4540
178	1095	C	1	H	2	56	2.06	–53.95	354.03	8.05E-02	20	4540
178	1095	C	1	H	2	60	2.1	–49.75	348.4	8.13E-02	20	4540
178	1095	C	1	H	2	64	2.14	–41.73	348.8	8.06E-02	20	4540
178	1095	C	1	H	2	68	2.18	–35.4	352.49	6.41E-02	20	4540
178	1095	C	1	H	2	72	2.22	–42.79	347.72	4.23E-02	20	4540
178	1095	C	1	H	2	76	2.26	–43.82	355.96	4.06E-02	20	4540
178	1095	C	1	H	2	80	2.3	–43.89	7.59	4.38E-02	20	4540
178	1095	C	1	H	2	84	2.34	–49.29	357.07	5.37E-02	20	4540
178	1095	C	1	H	2	88	2.38	–55.91	346.74	6.53E-02	20	4540
178	1095	C	1	H	2	92	2.42	–62.05	357.01	8.19E-02	20	4540
178	1095	C	1	H	2	96	2.46	–59.8	10.24	1.05E-01	20	4540
178	1095	C	1	H	2	100	2.5	–46.87	20.48	1.12E-01	20	4540
178	1095	C	1	H	2	104	2.54	–21.11	24.04	1.02E-01	20	4540
178	1095	C	1	H	2	108	2.58	18.2	14.83	7.77E-02	20	4540
178	1095	C	1	H	2	112	2.62	48.57	6.33	5.58E-02	20	4540
178	1095	C	1	H	2	116	2.66	78.54	180.95	9.40E-03	20	4540

Note: This table is also available in ASCII format in the **TABLES** directory.

Table T18. Split-core paleomagnetic measurements for Hole 1095C after 30-mT demagnetization.

Leg	Site	Hole	Core	Type	Section	Interval (cm)	Depth (mbsf)	Inclination (°)	Declination (°)	Intensity (A/m)	Demagnetization step (mT)	Run #
178	1095	C	1	H	2	8	1.58	–55.58	355.75	1.82E-01	30	4541
178	1095	C	1	H	2	12	1.62	–55.95	350.51	1.90E-01	30	4541
178	1095	C	1	H	2	16	1.66	–54.52	355.59	1.77E-01	30	4541
178	1095	C	1	H	2	20	1.7	–54.85	359.05	1.57E-01	30	4541
178	1095	C	1	H	2	24	1.74	–55.57	355.96	1.37E-01	30	4541
178	1095	C	1	H	2	28	1.78	–55.84	352.02	1.22E-01	30	4541
178	1095	C	1	H	2	32	1.82	–51.89	351.21	1.16E-01	30	4541
178	1095	C	1	H	2	36	1.86	–42.66	354.93	1.10E-01	30	4541
178	1095	C	1	H	2	40	1.9	–28.46	354.39	9.20E-02	30	4541
178	1095	C	1	H	2	44	1.94	–26.79	344.65	6.03E-02	30	4541
178	1095	C	1	H	2	48	1.98	–43.4	344.21	5.53E-02	30	4541
178	1095	C	1	H	2	52	2.02	–52.9	355.16	6.34E-02	30	4541
178	1095	C	1	H	2	56	2.06	–56.02	351.62	6.84E-02	30	4541
178	1095	C	1	H	2	60	2.1	–51.02	345.5	6.90E-02	30	4541
178	1095	C	1	H	2	64	2.14	–42.25	345.58	6.78E-02	30	4541
178	1095	C	1	H	2	68	2.18	–35.32	348.72	5.33E-02	30	4541
178	1095	C	1	H	2	72	2.22	–42.93	342.32	3.48E-02	30	4541
178	1095	C	1	H	2	76	2.26	–44.6	351.46	3.34E-02	30	4541
178	1095	C	1	H	2	80	2.3	–45.99	3.44	3.59E-02	30	4541
178	1095	C	1	H	2	84	2.34	–52.04	352.35	4.52E-02	30	4541
178	1095	C	1	H	2	88	2.38	–57.93	342.2	5.66E-02	30	4541
178	1095	C	1	H	2	92	2.42	–64.37	354.01	7.19E-02	30	4541
178	1095	C	1	H	2	96	2.46	–62.75	9.08	9.21E-02	30	4541
178	1095	C	1	H	2	100	2.5	–50.42	20.28	9.84E-02	30	4541
178	1095	C	1	H	2	104	2.54	–25.75	24.35	8.68E-02	30	4541
178	1095	C	1	H	2	108	2.58	11.48	14.22	6.21E-02	30	4541
178	1095	C	1	H	2	112	2.62	42.76	4.35	4.15E-02	30	4541
178	1095	C	1	H	2	116	2.66	36.49	205.48	3.87E-03	30	4541

Note: This table is also available in ASCII format in the **TABLES** directory.

Table T19. Split-core paleomagnetic measurements for Hole 1095D before demagnetization (NRM results).

Leg	Site	Hole	Core	Type	Section	Interval (cm)	Depth (mbsf)	Inclination (°)	Declination (°)	Intensity (A/m)	Demagnetization step (mT)	Run #
178	1095	D	1	H	2	8	1.58	–46.32	333.07	1.86E-01	0	4542
178	1095	D	1	H	2	12	1.62	–50.51	323.12	1.82E-01	0	4542
178	1095	D	1	H	2	16	1.66	–49.69	321.55	1.71E-01	0	4542
178	1095	D	1	H	2	20	1.7	–47.09	322.02	1.55E-01	0	4542
178	1095	D	1	H	2	24	1.74	–46.03	314.43	1.26E-01	0	4542
178	1095	D	1	H	2	28	1.78	–45.85	308.07	1.06E-01	0	4542
178	1095	D	1	H	2	32	1.82	–46.5	320.34	9.36E-02	0	4542
178	1095	D	1	H	2	36	1.86	–45.27	325.08	8.16E-02	0	4542
178	1095	D	1	H	2	40	1.9	–43.64	317.75	6.80E-02	0	4542
178	1095	D	1	H	2	44	1.94	–46.8	312.6	6.07E-02	0	4542
178	1095	D	1	H	2	48	1.98	–50.33	310.1	6.94E-02	0	4542
178	1095	D	1	H	2	52	2.02	–47.66	307.11	8.61E-02	0	4542
178	1095	D	1	H	2	56	2.06	–44.58	311	9.12E-02	0	4542
178	1095	D	1	H	2	60	2.1	–39.55	316.36	8.42E-02	0	4542
178	1095	D	1	H	2	64	2.14	–31.13	312.35	7.13E-02	0	4542
178	1095	D	1	H	2	68	2.18	–24.52	308.94	5.44E-02	0	4542
178	1095	D	1	H	2	72	2.22	–24.13	309.72	4.49E-02	0	4542
178	1095	D	1	H	2	76	2.26	–27.34	307.61	4.82E-02	0	4542
178	1095	D	1	H	2	80	2.3	–27.48	303.09	5.16E-02	0	4542
178	1095	D	1	H	2	84	2.34	–28.29	299.6	5.60E-02	0	4542
178	1095	D	1	H	2	88	2.38	–37.65	291.27	6.11E-02	0	4542
178	1095	D	1	H	2	92	2.42	–45.28	289.05	7.92E-02	0	4542
178	1095	D	1	H	2	96	2.46	–44.26	298.58	1.02E-01	0	4542
178	1095	D	1	H	2	100	2.5	–45.36	311.97	1.12E-01	0	4542
178	1095	D	1	H	2	104	2.54	–44.07	320.18	1.10E-01	0	4542
178	1095	D	1	H	2	108	2.58	–45.16	318.33	1.02E-01	0	4542
178	1095	D	1	H	2	112	2.62	–40.72	332.67	1.01E-01	0	4542
178	1095	D	1	H	2	116	2.66	–26.32	343.2	1.01E-01	0	4542
178	1095	D	1	H	2	120	2.7	–30.7	332.12	7.85E-02	0	4542
178	1095	D	1	H	2	124	2.74	–43.13	330.77	7.79E-02	0	4542
178	1095	D	1	H	2	128	2.78	–38.94	351.05	8.93E-02	0	4542
178	1095	D	1	H	2	132	2.82	–33.88	5.29	8.49E-02	0	4542
178	1095	D	1	H	2	136	2.86	–26.04	2.3	8.28E-02	0	4542
178	1095	D	1	H	2	140	2.9	–13.68	355.2	1.12E-01	0	4542
178	1095	D	1	H	3	8	3.08	–15.04	35.46	1.22E-01	0	4545
178	1095	D	1	H	3	12	3.12	–21.34	10.72	1.01E-01	0	4545
178	1095	D	1	H	3	16	3.16	–31.39	340.98	9.66E-02	0	4545
178	1095	D	1	H	3	20	3.2	–33.87	326.82	1.02E-01	0	4545
178	1095	D	1	H	3	24	3.24	–31.95	318.87	1.05E-01	0	4545
178	1095	D	1	H	3	28	3.28	–24.55	309.84	1.29E-01	0	4545
178	1095	D	1	H	3	32	3.32	–20.93	307.47	1.37E-01	0	4545
178	1095	D	1	H	3	36	3.36	–27.13	307.44	1.08E-01	0	4545
178	1095	D	1	H	3	40	3.4	–39.61	309.04	9.87E-02	0	4545
178	1095	D	1	H	3	44	3.44	–44.41	318.02	9.54E-02	0	4545
178	1095	D	1	H	3	48	3.48	–54.61	326.7	9.18E-02	0	4545
178	1095	D	1	H	3	52	3.52	–65.66	320.21	1.08E-01	0	4545
178	1095	D	1	H	3	56	3.56	–63	307.65	1.48E-01	0	4545
178	1095	D	1	H	3	60	3.6	–59.15	309.84	1.62E-01	0	4545
178	1095	D	1	H	3	64	3.64	–61.21	317.9	1.50E-01	0	4545
178	1095	D	1	H	3	68	3.68	–55.53	323.91	1.37E-01	0	4545
178	1095	D	1	H	3	72	3.72	–49.93	315.5	1.24E-01	0	4545
178	1095	D	1	H	3	76	3.76	–46.07	315.01	1.12E-01	0	4545
178	1095	D	1	H	3	80	3.8	–49.49	320.03	1.05E-01	0	4545
178	1095	D	1	H	3	84	3.84	–57.91	318.55	1.28E-01	0	4545
178	1095	D	1	H	3	88	3.88	–57.58	313.59	1.49E-01	0	4545
178	1095	D	1	H	3	92	3.92	–55.59	305.45	1.49E-01	0	4545
178	1095	D	1	H	3	96	3.96	–53.19	302.49	1.50E-01	0	4545
178	1095	D	1	H	3	100	4	–51.94	304.25	1.59E-01	0	4545
178	1095	D	1	H	3	104	4.04	–50.96	306.19	1.46E-01	0	4545
178	1095	D	1	H	3	108	4.08	–53.83	306.86	1.18E-01	0	4545
178	1095	D	1	H	3	112	4.12	–48.71	310.35	1.00E-01	0	4545
178	1095	D	1	H	3	116	4.16	–38	311.09	9.83E-02	0	4545
178	1095	D	1	H	3	120	4.2	–32.05	304.54	9.36E-02	0	4545
178	1095	D	1	H	3	124	4.24	–29.97	300.91	8.83E-02	0	4545
178	1095	D	1	H	3	128	4.28	–25.4	302.58	8.91E-02	0	4545

Note: Only a portion of this table appears here. The complete table is available in ASCII format in the **TABLES** directory.

Table T20. Split-core paleomagnetic measurements for Hole 1095D after 10-mT demagnetization.

Leg	Site	Hole	Core	Type	Section	Interval (cm)	Depth (mbsf)	Inclination (°)	Declination (°)	Intensity (A/m)	Demagnetization step (mT)	Run #
178	1095	D	1	H	4	8	4.58	6.86	332.52	6.06E-02	10	4549
178	1095	D	1	H	4	12	4.62	2.19	291.9	4.98E-02	10	4549
178	1095	D	1	H	4	16	4.66	–9.12	277.71	5.71E-02	10	4549
178	1095	D	1	H	4	20	4.7	–15.99	293.78	5.42E-02	10	4549
178	1095	D	1	H	4	24	4.74	–15.53	313.1	5.84E-02	10	4549
178	1095	D	1	H	4	28	4.78	–14.7	308.41	7.17E-02	10	4549
178	1095	D	1	H	4	32	4.82	–16.93	294.73	8.19E-02	10	4549
178	1095	D	1	H	4	36	4.86	–17.78	286.44	8.77E-02	10	4549
178	1095	D	1	H	4	40	4.9	–17.2	291	1.04E-01	10	4549
178	1095	D	1	H	4	44	4.94	–20.96	290.06	1.24E-01	10	4549
178	1095	D	1	H	4	48	4.98	–26.39	296.6	1.21E-01	10	4549
178	1095	D	1	H	4	52	5.02	–27.43	331.76	9.70E-02	10	4549
178	1095	D	1	H	4	56	5.06	–29.07	344.75	8.49E-02	10	4549
178	1095	D	1	H	4	60	5.1	–39.85	303.56	9.85E-02	10	4549
178	1095	D	1	H	4	64	5.14	–41.11	283.32	1.19E-01	10	4549
178	1095	D	1	H	4	68	5.18	–43.41	275.41	1.30E-01	10	4549
178	1095	D	1	H	4	72	5.22	–46.32	274.56	1.41E-01	10	4549
178	1095	D	1	H	4	76	5.26	–49.07	276.84	1.43E-01	10	4549
178	1095	D	1	H	4	80	5.3	–49.81	283.3	1.41E-01	10	4549
178	1095	D	1	H	4	84	5.34	–48.97	286.48	1.48E-01	10	4549
178	1095	D	1	H	4	88	5.38	–51.16	286.8	1.53E-01	10	4549
178	1095	D	1	H	4	92	5.42	–54.99	287.67	1.51E-01	10	4549
178	1095	D	1	H	4	96	5.46	–53.67	289.03	1.51E-01	10	4549
178	1095	D	1	H	4	100	5.5	–50.95	289.71	1.47E-01	10	4549
178	1095	D	1	H	4	104	5.54	–53.62	285.91	1.33E-01	10	4549
178	1095	D	1	H	4	108	5.58	–55.75	280.25	1.23E-01	10	4549
178	1095	D	1	H	4	112	5.62	–54.56	282.11	1.12E-01	10	4549
178	1095	D	1	H	4	116	5.66	–51.68	284.66	9.30E-02	10	4549
178	1095	D	1	H	4	120	5.7	–49.59	289.27	8.10E-02	10	4549
178	1095	D	1	H	4	124	5.74	–47.19	295.11	7.41E-02	10	4549
178	1095	D	1	H	4	128	5.78	–45.61	291.21	7.03E-02	10	4549
178	1095	D	1	H	4	132	5.82	–46.76	287.12	6.66E-02	10	4549
178	1095	D	1	H	4	136	5.86	–47.42	289.24	6.22E-02	10	4549
178	1095	D	1	H	4	140	5.9	–42.42	285.1	5.79E-02	10	4549
178	1095	D	1	H	5	8	6.08	–36.78	318.48	3.47E-02	10	4552
178	1095	D	1	H	5	12	6.12	–26.85	287.31	6.85E-02	10	4552
178	1095	D	1	H	5	16	6.16	–21.09	284.89	9.34E-02	10	4552
178	1095	D	1	H	5	20	6.2	–15.85	289.25	9.90E-02	10	4552
178	1095	D	1	H	5	24	6.24	–9.81	291.64	9.58E-02	10	4552
178	1095	D	1	H	5	28	6.28	–4.62	286.93	9.76E-02	10	4552
178	1095	D	1	H	5	32	6.32	–1.93	282.03	9.64E-02	10	4552
178	1095	D	1	H	5	36	6.36	0.4	280.48	9.39E-02	10	4552
178	1095	D	1	H	5	40	6.4	1.8	277.51	8.94E-02	10	4552
178	1095	D	1	H	5	44	6.44	1.85	273.72	8.74E-02	10	4552
178	1095	D	1	H	5	48	6.48	3.15	271.27	9.39E-02	10	4552
178	1095	D	1	H	5	52	6.52	3.59	268.83	1.02E-01	10	4552
178	1095	D	1	H	5	56	6.56	0.36	266.27	1.00E-01	10	4552
178	1095	D	1	H	5	60	6.6	–8.23	267.89	1.06E-01	10	4552
178	1095	D	1	H	5	64	6.64	–17.06	276.32	1.12E-01	10	4552
178	1095	D	1	H	5	68	6.68	–20.61	283.55	1.08E-01	10	4552
178	1095	D	1	H	5	72	6.72	–21.8	283.08	1.05E-01	10	4552
178	1095	D	1	H	5	76	6.76	–23.4	286.53	9.83E-02	10	4552
178	1095	D	1	H	5	80	6.8	–21.76	283.9	9.69E-02	10	4552
178	1095	D	1	H	5	84	6.84	–25.22	275.25	1.05E-01	10	4552
178	1095	D	1	H	5	88	6.88	–32.74	267.48	1.19E-01	10	4552
178	1095	D	1	H	5	92	6.92	–40.34	263.66	1.38E-01	10	4552
178	1095	D	1	H	5	96	6.96	–44.15	268.39	1.58E-01	10	4552
178	1095	D	1	H	5	100	7	–48.73	271.73	1.59E-01	10	4552
178	1095	D	1	H	5	104	7.04	–53.49	267.28	1.52E-01	10	4552
178	1095	D	1	H	5	108	7.08	–55.8	259.34	1.49E-01	10	4552
178	1095	D	1	H	5	112	7.12	–54.79	258.15	1.56E-01	10	4552
178	1095	D	1	H	5	116	7.16	–52.69	266.81	1.71E-01	10	4552
178	1095	D	1	H	5	120	7.2	–53.03	271.12	1.76E-01	10	4552
178	1095	D	1	H	5	124	7.24	–55.05	265.47	1.68E-01	10	4552
178	1095	D	1	H	5	128	7.28	–55.48	265.02	1.65E-01	10	4552
178	1095	D	1	H	5	132	7.32	–54.59	271.24	1.65E-01	10	4552

Note: Only a portion of this table appears here. The complete table is available in ASCII format in the **TABLES** directory.

Table T21. Split-core paleomagnetic measurements for Hole 1095D after 20-mT demagnetization.

Leg	Site	Hole	Core	Type	Section	Interval (cm)	Depth (mbsf)	Inclination (°)	Declination (°)	Intensity (A/m)	Demagnetization step (mT)	Run #
178	1095	D	1	H	2	8	1.58	–62.13	314.59	1.82E-01	20	4543
178	1095	D	1	H	2	12	1.62	–63.1	303.39	1.86E-01	20	4543
178	1095	D	1	H	2	16	1.66	–62.23	301.55	1.69E-01	20	4543
178	1095	D	1	H	2	20	1.7	–62.17	302.37	1.48E-01	20	4543
178	1095	D	1	H	2	24	1.74	–61.47	294.81	1.25E-01	20	4543
178	1095	D	1	H	2	28	1.78	–60.06	285.45	1.08E-01	20	4543
178	1095	D	1	H	2	32	1.82	–64.66	294	9.21E-02	20	4543
178	1095	D	1	H	2	36	1.86	–65.56	305.77	7.85E-02	20	4543
178	1095	D	1	H	2	40	1.9	–62.71	299.84	6.67E-02	20	4543
178	1095	D	1	H	2	44	1.94	–65.83	287.39	6.35E-02	20	4543
178	1095	D	1	H	2	48	1.98	–66.59	282.42	7.48E-02	20	4543
178	1095	D	1	H	2	52	2.02	–63.19	284.23	8.95E-02	20	4543
178	1095	D	1	H	2	56	2.06	–61.8	290.07	9.38E-02	20	4543
178	1095	D	1	H	2	60	2.1	–62.4	293.15	8.67E-02	20	4543
178	1095	D	1	H	2	64	2.14	–61.18	292.5	7.69E-02	20	4543
178	1095	D	1	H	2	68	2.18	–58.69	293.51	6.77E-02	20	4543
178	1095	D	1	H	2	72	2.22	–59.02	291.85	6.40E-02	20	4543
178	1095	D	1	H	2	76	2.26	–61.06	280.82	6.58E-02	20	4543
178	1095	D	1	H	2	80	2.3	–61.34	274.37	7.25E-02	20	4543
178	1095	D	1	H	2	84	2.34	–62.79	273.58	7.83E-02	20	4543
178	1095	D	1	H	2	88	2.38	–64.18	266.1	8.90E-02	20	4543
178	1095	D	1	H	2	92	2.42	–63.77	264.44	1.06E-01	20	4543
178	1095	D	1	H	2	96	2.46	–62.85	273.66	1.24E-01	20	4543
178	1095	D	1	H	2	100	2.5	–64.78	285.91	1.33E-01	20	4543
178	1095	D	1	H	2	104	2.54	–66.41	293.64	1.28E-01	20	4543
178	1095	D	1	H	2	108	2.58	–66.76	289.31	1.27E-01	20	4543
178	1095	D	1	H	2	112	2.62	–67.9	300.63	1.23E-01	20	4543
178	1095	D	1	H	2	116	2.66	–63.36	321.89	1.10E-01	20	4543
178	1095	D	1	H	2	120	2.7	–62.57	316.56	9.53E-02	20	4543
178	1095	D	1	H	2	124	2.74	–65.21	313.38	9.19E-02	20	4543
178	1095	D	1	H	2	128	2.78	–66.12	329.87	9.22E-02	20	4543
178	1095	D	1	H	2	132	2.82	–66.94	352.86	8.34E-02	20	4543
178	1095	D	1	H	2	136	2.86	–61.51	349.17	7.64E-02	20	4543
178	1095	D	1	H	2	140	2.9	–45.07	343.1	8.51E-02	20	4543
178	1095	D	1	H	3	8	3.08	–37.68	39.54	9.51E-02	20	4546
178	1095	D	1	H	3	12	3.12	–53.23	5.26	8.87E-02	20	4546
178	1095	D	1	H	3	16	3.16	–56.67	327.49	1.00E-01	20	4546
178	1095	D	1	H	3	20	3.2	–54.37	312.63	1.09E-01	20	4546
178	1095	D	1	H	3	24	3.24	–51.4	305.59	1.14E-01	20	4546
178	1095	D	1	H	3	28	3.28	–44.52	296.66	1.33E-01	20	4546
178	1095	D	1	H	3	32	3.32	–43.78	293.04	1.40E-01	20	4546
178	1095	D	1	H	3	36	3.36	–51.55	292.11	1.21E-01	20	4546
178	1095	D	1	H	3	40	3.4	–59.31	292.62	1.15E-01	20	4546
178	1095	D	1	H	3	44	3.44	–62.96	302.61	1.09E-01	20	4546
178	1095	D	1	H	3	48	3.48	–71.27	310.04	1.08E-01	20	4546
178	1095	D	1	H	3	52	3.52	–76.68	295.1	1.26E-01	20	4546
178	1095	D	1	H	3	56	3.56	–71.45	285.46	1.61E-01	20	4546
178	1095	D	1	H	3	60	3.6	–68.28	292.52	1.74E-01	20	4546
178	1095	D	1	H	3	64	3.64	–68.93	297.61	1.65E-01	20	4546
178	1095	D	1	H	3	68	3.68	–67.97	299.67	1.49E-01	20	4546
178	1095	D	1	H	3	72	3.72	–66.21	300.7	1.30E-01	20	4546
178	1095	D	1	H	3	76	3.76	–60.97	302.87	1.22E-01	20	4546
178	1095	D	1	H	3	80	3.8	–63.87	300.88	1.19E-01	20	4546
178	1095	D	1	H	3	84	3.84	–69.36	296.08	1.43E-01	20	4546
178	1095	D	1	H	3	88	3.88	–68.33	296.21	1.65E-01	20	4546
178	1095	D	1	H	3	92	3.92	–66.59	287.03	1.67E-01	20	4546
178	1095	D	1	H	3	96	3.96	–64.44	283.92	1.69E-01	20	4546
178	1095	D	1	H	3	100	4	–63.05	287.05	1.72E-01	20	4546
178	1095	D	1	H	3	104	4.04	–63.39	287.95	1.55E-01	20	4546
178	1095	D	1	H	3	108	4.08	–66.15	286.85	1.29E-01	20	4546
178	1095	D	1	H	3	112	4.12	–64.15	291.64	1.10E-01	20	4546
178	1095	D	1	H	3	116	4.16	–57.28	294.97	1.03E-01	20	4546
178	1095	D	1	H	3	120	4.2	–53.19	286.01	9.86E-02	20	4546
178	1095	D	1	H	3	124	4.24	–52.15	281.7	9.59E-02	20	4546
178	1095	D	1	H	3	128	4.28	–49.36	285.61	9.23E-02	20	4546
178	1095	D	1	H	3	132	4.32	–44.59	289.58	9.15E-02	20	4546

Note: Only a portion of this table appears here. The complete table is available in ASCII format in the **TABLES** directory.

Table T22. Split-core paleomagnetic measurements for Hole 1095D after 30-mT demagnetization.

Leg	Site	Hole	Core	Type	Section	Interval (cm)	Depth (mbsf)	Inclination (°)	Declination (°)	Intensity (A/m)	Demagnetization step (mT)	Run #
178	1095	D	1	H	2	8	1.58	–63.9	308.82	1.64E-01	30	4544
178	1095	D	1	H	2	12	1.62	–64.48	298.94	1.67E-01	30	4544
178	1095	D	1	H	2	16	1.66	–63.48	297.55	1.49E-01	30	4544
178	1095	D	1	H	2	20	1.7	–63.61	299.01	1.29E-01	30	4544
178	1095	D	1	H	2	24	1.74	–63.11	292.58	1.07E-01	30	4544
178	1095	D	1	H	2	28	1.78	–61.47	282.87	9.17E-02	30	4544
178	1095	D	1	H	2	32	1.82	–66.06	289.68	7.75E-02	30	4544
178	1095	D	1	H	2	36	1.86	–67.48	301.35	6.52E-02	30	4544
178	1095	D	1	H	2	40	1.9	–64.3	295.8	5.43E-02	30	4544
178	1095	D	1	H	2	44	1.94	–66.73	282.17	5.23E-02	30	4544
178	1095	D	1	H	2	48	1.98	–67.06	277.37	6.23E-02	30	4544
178	1095	D	1	H	2	52	2.02	–63.8	280.39	7.45E-02	30	4544
178	1095	D	1	H	2	56	2.06	–62.41	287.06	7.72E-02	30	4544
178	1095	D	1	H	2	60	2.1	–63.02	290.45	6.98E-02	30	4544
178	1095	D	1	H	2	64	2.14	–62.05	290.06	6.03E-02	30	4544
178	1095	D	1	H	2	68	2.18	–59.33	291.32	5.31E-02	30	4544
178	1095	D	1	H	2	72	2.22	–59.43	289.32	5.08E-02	30	4544
178	1095	D	1	H	2	76	2.26	–61.64	277.61	5.27E-02	30	4544
178	1095	D	1	H	2	80	2.3	–61.86	271.32	5.89E-02	30	4544
178	1095	D	1	H	2	84	2.34	–63.04	271.37	6.46E-02	30	4544
178	1095	D	1	H	2	88	2.38	–64.07	263.55	7.43E-02	30	4544
178	1095	D	1	H	2	92	2.42	–63.34	261.25	8.98E-02	30	4544
178	1095	D	1	H	2	96	2.46	–62.57	269.32	1.05E-01	30	4544
178	1095	D	1	H	2	100	2.5	–65.07	278.93	1.13E-01	30	4544
178	1095	D	1	H	2	104	2.54	–67.2	285.62	1.09E-01	30	4544
178	1095	D	1	H	2	108	2.58	–67.41	281.4	1.08E-01	30	4544
178	1095	D	1	H	2	112	2.62	–68.91	290.89	1.05E-01	30	4544
178	1095	D	1	H	2	116	2.66	–65.38	314.39	9.24E-02	30	4544
178	1095	D	1	H	2	120	2.7	–63.99	310.11	7.89E-02	30	4544
178	1095	D	1	H	2	124	2.74	–66.08	305.18	7.65E-02	30	4544
178	1095	D	1	H	2	128	2.78	–68.68	317.6	7.69E-02	30	4544
178	1095	D	1	H	2	132	2.82	–72.06	342.01	6.93E-02	30	4544
178	1095	D	1	H	2	136	2.86	–66.76	338.41	6.36E-02	30	4544
178	1095	D	1	H	2	140	2.9	–50.07	334.96	6.99E-02	30	4544
178	1095	D	1	H	3	8	3.08	–41.03	37.66	7.75E-02	30	4547
178	1095	D	1	H	3	12	3.12	–56.68	0.66	7.37E-02	30	4547
178	1095	D	1	H	3	16	3.16	–58.42	319.57	8.64E-02	30	4547
178	1095	D	1	H	3	20	3.2	–55.36	306.26	9.57E-02	30	4547
178	1095	D	1	H	3	24	3.24	–52	301.22	9.97E-02	30	4547
178	1095	D	1	H	3	28	3.28	–45.17	293.84	1.15E-01	30	4547
178	1095	D	1	H	3	32	3.32	–44.88	290.63	1.20E-01	30	4547
178	1095	D	1	H	3	36	3.36	–52.8	289.58	1.03E-01	30	4547
178	1095	D	1	H	3	40	3.4	–60.08	289.64	9.81E-02	30	4547
178	1095	D	1	H	3	44	3.44	–63.5	299.47	9.21E-02	30	4547
178	1095	D	1	H	3	48	3.48	–71.77	307.14	9.08E-02	30	4547
178	1095	D	1	H	3	52	3.52	–76.99	290.8	1.06E-01	30	4547
178	1095	D	1	H	3	56	3.56	–71.34	282.16	1.36E-01	30	4547
178	1095	D	1	H	3	60	3.6	–68.22	289.45	1.46E-01	30	4547
178	1095	D	1	H	3	64	3.64	–69.1	295.16	1.37E-01	30	4547
178	1095	D	1	H	3	68	3.68	–68.29	298.04	1.23E-01	30	4547
178	1095	D	1	H	3	72	3.72	–66.51	298.5	1.07E-01	30	4547
178	1095	D	1	H	3	76	3.76	–60.98	299.82	1.01E-01	30	4547
178	1095	D	1	H	3	80	3.8	–63.42	296.15	1.01E-01	30	4547
178	1095	D	1	H	3	84	3.84	–68.69	291.1	1.22E-01	30	4547
178	1095	D	1	H	3	88	3.88	–68.08	292.45	1.40E-01	30	4547
178	1095	D	1	H	3	92	3.92	–66.4	283.86	1.42E-01	30	4547
178	1095	D	1	H	3	96	3.96	–64.27	280.97	1.44E-01	30	4547
178	1095	D	1	H	3	100	4	–63.06	284.06	1.47E-01	30	4547
178	1095	D	1	H	3	104	4.04	–63.46	284.56	1.31E-01	30	4547
178	1095	D	1	H	3	108	4.08	–66.36	282.7	1.08E-01	30	4547
178	1095	D	1	H	3	112	4.12	–64.59	287.57	9.13E-02	30	4547
178	1095	D	1	H	3	116	4.16	–57.72	292.04	8.43E-02	30	4547
178	1095	D	1	H	3	120	4.2	–53.57	283.04	8.06E-02	30	4547
178	1095	D	1	H	3	124	4.24	–52.46	278.52	7.85E-02	30	4547
178	1095	D	1	H	3	128	4.28	–49.52	282.64	7.58E-02	30	4547
178	1095	D	1	H	3	132	4.32	–44.73	286.82	7.50E-02	30	4547
178	1095	D	1	H	3	136	4.36	–40.6	288.43	7.04E-02	30	4547
178	1095	D	1	H	3	140	4.4	–37.66	284.76	6.03E-02	30	4547

Note: This table is also available in ASCII format in the **TABLES** directory.

Table T23. Split-core paleomagnetic measurements for Hole 1095D after processing the results from the 30-mT demagnetization step.

Leg	Site	Hole	Core	Type	Section	Interval (cm)	Depth (mbsf)	Inclination (°)	Declination (°)	Intensity (A/m)	Demagnetization step (mT)	Run #
178	1095	D	1	H	4	140	5.9	–43.75	282.73	0.0491	20	4550
178	1095	D	1	H	4	136	5.86	–48.53	287.09	0.0528	20	4550
178	1095	D	1	H	5	16	6.16	–21.9	282.84	0.08	20	4553
178	1095	D	1	H	5	12	6.12	–27.59	284.21	0.0595	20	4553
178	1095	D	1	H	4	132	5.82	–47.4	284.98	0.0567	20	4550
178	1095	D	1	H	4	120	5.7	–49.74	287.64	0.0681	20	4550
178	1095	D	1	H	4	116	5.66	–52.15	282.69	0.0787	20	4550
178	1095	D	1	H	4	128	5.78	–45.94	289.14	0.0595	20	4550
178	1095	D	1	H	4	124	5.74	–47.43	293.38	0.0623	20	4550
178	1095	D	1	H	5	44	6.44	0.19	271.32	0.0759	20	4553
178	1095	D	1	H	5	40	6.4	0.17	275.05	0.0772	20	4553
178	1095	D	1	H	5	52	6.52	2.01	266.86	0.0893	20	4553
178	1095	D	1	H	5	48	6.48	1.4	269.04	0.0819	20	4553
178	1095	D	1	H	5	36	6.36	–1.11	278.16	0.0809	20	4553
178	1095	D	1	H	5	24	6.24	–10.92	289.26	0.0817	20	4553
178	1095	D	1	H	5	20	6.2	–16.7	287.23	0.0844	20	4553
178	1095	D	1	H	5	32	6.32	–3.3	279.71	0.0828	20	4553
178	1095	D	1	H	5	28	6.28	–5.83	284.43	0.0835	20	4553
178	1095	D	1	H	4	112	5.62	–55.2	279.81	0.0946	20	4550
178	1095	D	1	H	4	64	5.14	–41.12	281.83	0.103	20	4550
178	1095	D	1	H	4	60	5.1	–40.59	301.28	0.0843	20	4550
178	1095	D	1	H	4	72	5.22	–46.57	272.97	0.124	20	4550
178	1095	D	1	H	4	68	5.18	–43.36	273.99	0.114	20	4550
178	1095	D	1	H	4	48	4.98	–27.65	293.99	0.105	20	4550
178	1095	D	1	H	4	36	4.86	–18.3	284.43	0.0743	20	4550
178	1095	D	1	H	4	32	4.82	–17.71	294.57	0.0706	20	4550
178	1095	D	1	H	4	44	4.94	–23.18	283.64	0.105	20	4550
178	1095	D	1	H	4	40	4.9	–18.49	282.54	0.0869	20	4550
178	1095	D	1	H	4	100	5.5	–51.9	287.61	0.127	20	4550
178	1095	D	1	H	4	96	5.46	–54.7	286.73	0.131	20	4550
178	1095	D	1	H	4	108	5.58	–56.5	278.15	0.106	20	4550
178	1095	D	1	H	4	104	5.54	–54.53	283.87	0.115	20	4550
178	1095	D	1	H	4	92	5.42	–56.09	285.63	0.132	20	4550
178	1095	D	1	H	4	80	5.3	–50.49	281.07	0.124	20	4550
178	1095	D	1	H	4	76	5.26	–49.56	274.57	0.126	20	4550
178	1095	D	1	H	4	88	5.38	–52.17	285.03	0.134	20	4550
178	1095	D	1	H	4	84	5.34	–49.81	284.71	0.13	20	4550
178	1095	D	1	H	6	20	7.7	–56.13	80.45	0.0824	20	4556
178	1095	D	1	H	6	16	7.66	–61.25	80.61	0.0821	20	4556
178	1095	D	1	H	6	28	7.78	–45.72	90.37	0.0727	20	4556
178	1095	D	1	H	6	24	7.74	–45.89	80.88	0.0837	20	4556
178	1095	D	1	H	6	12	7.62	–56.66	79.02	0.0929	20	4556
178	1095	D	1	H	5	136	7.36	–50.86	269.56	0.14	20	4553
178	1095	D	1	H	5	132	7.32	–54.66	269.01	0.141	20	4553
178	1095	D	1	H	6	8	7.58	–48.29	83.48	0.116	20	4556
178	1095	D	1	H	5	140	7.4	–44.21	268.88	0.147	20	4553
178	1095	D	1	H	6	56	8.06	–33.98	37.85	0.0631	20	4556
178	1095	D	1	H	6	52	8.02	–69.4	76.68	0.0858	20	4556
178	1095	D	1	H	6	64	8.14	14.95	110.31	0.0746	20	4556
178	1095	D	1	H	6	60	8.1	12.04	85.12	0.0511	20	4556
178	1095	D	1	H	6	48	7.98	–69	108.36	0.0887	20	4556
178	1095	D	1	H	6	36	7.86	–52.76	67.25	0.063	20	4556
178	1095	D	1	H	6	32	7.82	–52.49	76.65	0.0704	20	4556
178	1095	D	1	H	6	44	7.94	–70.02	84.81	0.0807	20	4556
178	1095	D	1	H	6	40	7.9	–68.38	82.89	0.0696	20	4556
178	1095	D	1	H	5	128	7.28	–55.47	262.86	0.141	20	4553
178	1095	D	1	H	5	80	6.8	–22.81	280.97	0.0843	20	4553
178	1095	D	1	H	5	76	6.76	–24.41	283.18	0.0852	20	4553
178	1095	D	1	H	5	88	6.88	–32.78	265.22	0.104	20	4553
178	1095	D	1	H	5	84	6.84	–25.63	273.07	0.0917	20	4553
178	1095	D	1	H	5	72	6.72	–22.59	279.95	0.091	20	4553
178	1095	D	1	H	5	60	6.6	–9.28	265.73	0.0935	20	4553
178	1095	D	1	H	5	56	6.56	–1.1	264.3	0.0879	20	4553
178	1095	D	1	H	5	68	6.68	–21.29	280.44	0.094	20	4553
178	1095	D	1	H	5	64	6.64	–17.79	273.76	0.0977	20	4553

Note: Only a portion of this table appears here. The complete table is available in ASCII format in the **TABLES** directory.

Table T24. Discrete sample NRM and AF demagnetization results for Hole 1095A.

Leg	Site	Hole	Core	Type	Section	Interval (cm)	Depth (mbsf)	Inclination (°)	Declination (°)	Intensity (A/m)	Mx (A·m)	My (A·m)	Mz (A·m)	Demagnetization step (mT)
178	1095	A	1	H	1	68	0.68	–51.28	11.58	3.06E-01	1.50E-06	3.08E-07	–1.91E-06	0
178	1095	A	1	H	1	68	0.68	–53.8	14.35	2.71E-01	1.24E-06	3.17E-07	–1.75E-06	10
178	1095	A	1	H	1	68	0.68	–54.84	15.13	2.45E-01	1.09E-06	2.95E-07	–1.61E-06	20
178	1095	A	1	H	1	68	0.68	–55.9	15.25	2.16E-01	9.36E-07	2.55E-07	–1.43E-06	30
178	1095	A	1	H	1	68	0.68	–56.96	15.14	1.91E-01	8.03E-07	2.17E-07	–1.28E-06	40
178	1095	A	1	H	1	68	0.68	–57.8	15.04	1.63E-01	6.72E-07	1.81E-07	–1.10E-06	50
178	1095	A	1	H	1	68	0.68	–58.01	14.7	1.34E-01	5.50E-07	1.44E-07	–9.10E-07	60
178	1095	A	1	H	1	68	0.68	–60.8	15.39	1.16E-01	4.38E-07	1.21E-07	–8.13E-07	70
178	1095	A	1	H	1	68	0.68	–56.27	18.1	8.54E-02	3.61E-07	1.18E-07	–5.68E-07	80
178	1095	A	1	H	1	141	1.41	–34.6	22.44	3.79E-01	2.31E-06	9.52E-07	–1.72E-06	0
178	1095	A	1	H	1	141	1.41	–35.61	23.28	3.35E-01	2.00E-06	8.62E-07	–1.56E-06	10
178	1095	A	1	H	1	141	1.41	–36.58	23.3	3.07E-01	1.81E-06	7.80E-07	–1.46E-06	20
178	1095	A	1	H	1	141	1.41	–37.57	22.89	2.74E-01	1.60E-06	6.76E-07	–1.34E-06	30
178	1095	A	1	H	1	141	1.41	–38.83	22.67	2.47E-01	1.42E-06	5.93E-07	–1.24E-06	40
178	1095	A	1	H	1	141	1.41	–40.89	22.84	2.12E-01	1.18E-06	4.97E-07	–1.11E-06	50
178	1095	A	1	H	1	141	1.41	–40.39	23.24	1.82E-01	1.02E-06	4.37E-07	–9.43E-07	60
178	1095	A	1	H	1	141	1.41	–44.19	22	1.56E-01	8.28E-07	3.34E-07	–8.68E-07	70
178	1095	A	1	H	1	141	1.41	–40.79	23.23	1.21E-01	6.74E-07	2.89E-07	–6.33E-07	80
178	1095	A	1	H	2	61	2.07	–13.26	17.49	1.39E-01	1.03E-06	3.24E-07	–2.54E-07	0
178	1095	A	1	H	2	61	2.07	–18.31	20.46	9.79E-02	6.96E-07	2.60E-07	–2.46E-07	10
178	1095	A	1	H	2	61	2.07	–21.4	20.73	7.96E-02	5.54E-07	2.10E-07	–2.32E-07	20
178	1095	A	1	H	2	61	2.07	–24	20.73	6.24E-02	4.26E-07	1.61E-07	–2.03E-07	30
178	1095	A	1	H	2	61	2.07	–27.15	20.4	5.04E-02	3.36E-07	1.25E-07	–1.84E-07	40
178	1095	A	1	H	2	61	2.07	–29.9	21.36	3.85E-02	2.49E-07	9.73E-08	–1.54E-07	50
178	1095	A	1	H	2	61	2.07	–28.21	21.25	3.03E-02	1.99E-07	7.75E-08	–1.15E-07	60
178	1095	A	1	H	2	61	2.07	–38.79	22.34	2.73E-02	1.57E-07	6.46E-08	–1.37E-07	70
178	1095	A	1	H	2	61	2.07	–12.33	22.38	1.77E-02	1.28E-07	5.27E-08	–3.03E-08	80
178	1095	A	1	H	2	144	2.9	–24.18	22.62	2.79E-01	1.88E-06	7.84E-07	–9.15E-07	0
178	1095	A	1	H	2	144	2.9	–28.04	21.07	2.59E-01	1.71E-06	6.57E-07	–9.74E-07	10
178	1095	A	1	H	2	144	2.9	–29	20.65	2.37E-01	1.55E-06	5.86E-07	–9.21E-07	20
178	1095	A	1	H	2	144	2.9	–29.91	21.01	2.06E-01	1.34E-06	5.13E-07	–8.23E-07	30
178	1095	A	1	H	2	144	2.9	–31.22	20.66	1.79E-01	1.15E-06	4.33E-07	–7.44E-07	40
178	1095	A	1	H	2	144	2.9	–31.7	21.07	1.53E-01	9.69E-07	3.73E-07	–6.41E-07	50
178	1095	A	1	H	2	144	2.9	–30.82	21.47	1.31E-01	8.39E-07	3.30E-07	–5.38E-07	60
178	1095	A	1	H	2	144	2.9	–34.89	21.24	1.10E-01	6.71E-07	2.61E-07	–5.02E-07	70
178	1095	A	1	H	2	144	2.9	–28.96	23.11	8.84E-02	5.69E-07	2.43E-07	–3.42E-07	80
178	1095	A	1	H	3	71	3.64	–74.38	330.91	1.28E-01	2.42E-07	–1.34E-07	–9.90E-07	0
178	1095	A	1	H	3	71	3.64	–78.31	341.2	9.66E-02	1.48E-07	–5.05E-08	–7.57E-07	10
178	1095	A	1	H	3	71	3.64	–78.75	339.65	8.15E-02	1.19E-07	–4.42E-08	–6.40E-07	20
178	1095	A	1	H	3	71	3.64	–80.25	335.96	6.84E-02	8.47E-08	–3.78E-08	–5.39E-07	30
178	1095	A	1	H	3	71	3.64	–81.4	337.51	5.77E-02	6.38E-08	–2.64E-08	–4.56E-07	40
178	1095	A	1	H	3	71	3.64	–81.84	342.48	4.76E-02	5.16E-08	–1.63E-08	–3.77E-07	50
178	1095	A	1	H	3	71	3.64	–82.53	330.15	3.81E-02	3.44E-08	–1.97E-08	–3.02E-07	60
178	1095	A	1	H	3	71	3.64	–83.02	355.02	3.55E-02	3.44E-08	–2.99E-09	–2.82E-07	70
178	1095	A	1	H	3	71	3.64	–79.99	15.11	2.02E-02	2.71E-08	7.31E-09	–1.59E-07	80
178	1095	A	1	H	3	135	4.28	–71.4	91.54	6.41E-02	–4.39E-09	1.64E-07	–4.86E-07	0
178	1095	A	1	H	3	135	4.28	–71.95	79.22	5.29E-02	2.45E-08	1.29E-07	–4.02E-07	10
178	1095	A	1	H	3	135	4.28	–72.88	79.06	4.44E-02	1.99E-08	1.03E-07	–3.40E-07	20
178	1095	A	1	H	3	135	4.28	–74.39	82.36	3.72E-02	1.07E-08	7.94E-08	–2.87E-07	30
178	1095	A	1	H	3	135	4.28	–73.09	109.48	3.03E-02	–2.35E-08	6.65E-08	–2.32E-07	40
178	1095	A	1	H	3	135	4.28	–71.89	49.71	2.98E-02	4.79E-08	5.65E-08	–2.26E-07	50
178	1095	A	1	H	3	135	4.28	–70.59	70.28	1.94E-02	1.74E-08	4.87E-08	–1.47E-07	60
178	1095	A	1	H	3	135	4.28	–77.96	75.94	1.90E-02	7.69E-09	3.07E-08	–1.48E-07	70
178	1095	A	1	H	3	135	4.28	–44.18	123.22	5.43E-03	–1.71E-08	2.61E-08	–3.03E-08	80
178	1095	A	1	H	4	74	5.17	–31.02	235.83	2.24E-01	–8.63E-07	–1.27E-06	–9.24E-07	0
178	1095	A	1	H	4	74	5.17	–36.03	237.01	1.46E-01	–5.15E-07	–7.93E-07	–6.87E-07	10
178	1095	A	1	H	4	74	5.17	–38.8	236.27	1.15E-01	–3.99E-07	–5.97E-07	–5.77E-07	20
178	1095	A	1	H	4	74	5.17	–41.08	234.71	9.26E-02	–3.23E-07	–4.56E-07	–4.87E-07	30
178	1095	A	1	H	4	74	5.17	–43.43	234.44	7.63E-02	–2.58E-07	–3.61E-07	–4.20E-07	40
178	1095	A	1	H	4	74	5.17	–47.36	234.66	6.25E-02	–1.96E-07	–2.76E-07	–3.68E-07	50
178	1095	A	1	H	4	74	5.17	–43.68	231.31	5.04E-02	–1.82E-07	–2.27E-07	–2.78E-07	60
178	1095	A	1	H	4	74	5.17	–49	228.08	4.39E-02	–1.54E-07	–1.71E-07	–2.65E-07	70
178	1095	A	1	H	4	74	5.17	–38.04	224.71	2.52E-02	–1.13E-07	–1.12E-07	–1.24E-07	80
178	1095	A	1	H	4	117	5.6	–43.46	60.68	6.40E-02	1.82E-07	3.24E-07	–3.52E-07	0
178	1095	A	1	H	4	117	5.6	–44.3	61.27	6.43E-02	1.77E-07	3.23E-07	–3.59E-07	0
178	1095	A	1	H	4	117	5.6	–51.44	56.61	5.18E-02	1.42E-07	2.16E-07	–3.24E-07	10

Note: Only a portion of this table appears here. The complete table is available in ASCII format in the **TABLES** directory.

Table T25. Discrete sample NRM and AF demagnetization results for Hole 1095B.

Leg	Site	Hole	Core	Type	Section	Interval (cm)	Depth (mbsf)	Inclination (°)	Declination (°)	Intensity (A/m)	Mx (A·m)	My (A·m)	Mz (A·m)	Demagnetization step (mT)
178	1095	B	1	H	1	120	84.2	12.16	282.97	5.35E-03	9.38E-09	–4.08E-08	9.01E-09	0
178	1095	B	1	H	1	120	84.2	18.96	255.15	1.17E-03	–2.27E-09	–8.57E-09	3.05E-09	10
178	1095	B	1	H	1	120	84.2	15.03	236.41	5.66E-04	–2.42E-09	–3.64E-09	1.17E-09	20
178	1095	B	1	H	1	120	84.2	–0.36	273.3	4.05E-04	1.86E-10	–3.24E-09	–2.05E-11	30
178	1095	B	1	H	1	120	84.2	–9.13	249.58	3.91E-04	–1.08E-09	–2.90E-09	–4.97E-10	40
178	1095	B	1	H	1	120	84.2	–43	161.78	2.90E-04	–1.61E-09	5.31E-10	–1.58E-09	50
178	1095	B	1	H	1	120	84.2	–7.35	185.29	2.96E-04	–2.34E-09	–2.17E-10	–3.03E-10	60
178	1095	B	1	H	1	120	84.2	–28.53	322.16	1.55E-04	8.61E-10	–6.69E-10	–5.93E-10	70
178	1095	B	1	H	1	120	84.2	–39.96	24.34	3.78E-04	2.11E-09	9.55E-10	–1.94E-09	80
178	1095	B	1	H	1	140	84.4	–16.87	176.53	5.08E-02	–3.89E-07	2.35E-08	–1.18E-07	0
178	1095	B	1	H	1	140	84.4	–49.24	165.59	6.87E-02	–3.48E-07	8.93E-08	–4.16E-07	10
178	1095	B	1	H	1	140	84.4	–51.48	164.66	5.51E-02	–2.65E-07	7.26E-08	–3.45E-07	20
178	1095	B	1	H	1	140	84.4	–53.49	164.42	3.90E-02	–1.79E-07	4.99E-08	–2.51E-07	30
178	1095	B	1	H	1	140	84.4	–55.13	162.87	2.79E-02	–1.22E-07	3.77E-08	–1.83E-07	40
178	1095	B	1	H	1	140	84.4	–59.97	161.06	1.88E-02	–7.12E-08	2.44E-08	–1.30E-07	50
178	1095	B	1	H	1	140	84.4	–54.15	143.1	1.31E-02	–4.90E-08	3.68E-08	–8.49E-08	60
178	1095	B	1	H	1	140	84.4	–60.7	163.76	8.15E-03	–3.06E-08	8.93E-09	–5.69E-08	70
178	1095	B	1	H	1	140	84.4	–53.3	171.42	5.29E-03	–2.50E-08	3.78E-09	–3.40E-08	80
178	1095	B	1	H	2	70	85.2	53.46	127.12	6.81E-02	–1.96E-07	2.59E-07	4.37E-07	0
178	1095	B	1	H	2	70	85.2	20.64	120.46	8.14E-03	–3.09E-08	5.25E-08	2.30E-08	10
178	1095	B	1	H	2	70	85.2	–9.23	112.73	3.19E-03	–9.75E-09	2.33E-08	–4.10E-09	20
178	1095	B	1	H	2	70	85.2	–17.86	120.19	2.06E-03	–7.91E-09	1.36E-08	–5.07E-09	30
178	1095	B	1	H	2	70	85.2	–23.36	88.32	1.15E-03	2.48E-10	8.45E-09	–3.65E-09	40
178	1095	B	1	H	2	70	85.2	–3.76	69.17	7.28E-04	2.07E-09	5.43E-09	–3.82E-10	50
178	1095	B	1	H	2	70	85.2	–35.7	39.57	5.96E-04	2.99E-09	2.47E-09	–2.78E-09	60
178	1095	B	1	H	2	70	85.2	–48.14	30.56	4.08E-04	1.87E-09	1.11E-09	–2.43E-09	70
178	1095	B	1	H	2	70	85.2	–65.93	71.65	1.11E-03	1.14E-09	3.45E-09	–8.13E-09	80
178	1095	B	1	H	2	71	85.21	–79.86	207.77	1.62E-01	–2.02E-07	–1.06E-07	–1.28E-06	0
178	1095	B	1	H	2	71	85.21	–76.54	162.76	2.96E-01	–5.27E-07	1.64E-07	–2.31E-06	10
178	1095	B	1	H	2	71	85.21	–76.4	161.11	2.56E-01	–4.55E-07	1.56E-07	–1.99E-06	20
178	1095	B	1	H	2	71	85.21	–76.24	161.42	1.92E-01	–3.46E-07	1.16E-07	–1.49E-06	30
178	1095	B	1	H	2	71	85.21	–76.43	160.78	1.43E-01	–2.53E-07	8.81E-08	–1.11E-06	40
178	1095	B	1	H	2	71	85.21	–76.99	160.94	1.01E-01	–1.72E-07	5.94E-08	–7.88E-07	50
178	1095	B	1	H	2	71	85.21	–75.01	146.42	6.94E-02	–1.20E-07	7.94E-08	–5.36E-07	60
178	1095	B	1	H	2	71	85.21	–79.56	147.75	4.51E-02	–5.54E-08	3.49E-08	–3.55E-07	70
178	1095	B	1	H	2	71	85.21	–77.4	156.77	2.72E-02	–4.36E-08	1.87E-08	–2.12E-07	80
178	1095	B	1	H	2	145	85.95	36.98	107.65	4.97E-02	–9.63E-08	3.03E-07	2.39E-07	0
178	1095	B	1	H	2	145	85.95	–30.91	119.7	2.55E-02	–8.68E-08	1.52E-07	–1.05E-07	10
178	1095	B	1	H	2	145	85.95	–38.92	115.01	1.96E-02	–5.17E-08	1.11E-07	–9.87E-08	20
178	1095	B	1	H	2	145	85.95	–42.07	101.18	1.28E-02	–1.47E-08	7.44E-08	–6.85E-08	30
178	1095	B	1	H	2	145	85.95	–39.88	102.88	8.02E-03	–1.10E-08	4.80E-08	–4.12E-08	40
178	1095	B	1	H	2	145	85.95	–35.42	90.97	5.48E-03	–6.08E-10	3.57E-08	–2.54E-08	50
178	1095	B	1	H	2	145	85.95	–27.35	40.69	4.43E-03	2.38E-08	2.05E-08	–1.63E-08	60
178	1095	B	1	H	2	145	85.95	–41.35	85.9	3.15E-03	1.35E-09	1.88E-08	–1.66E-08	70
178	1095	B	1	H	2	145	85.95	–50.85	55.08	2.30E-03	6.66E-09	9.54E-09	–1.43E-08	80
178	1095	B	1	H	3	71	86.71	–36.58	219.72	6.99E-02	–3.45E-07	–2.87E-07	–3.33E-07	0
178	1095	B	1	H	3	71	86.71	–69.55	200.11	6.83E-02	–1.79E-07	–6.56E-08	–5.12E-07	10
178	1095	B	1	H	3	71	86.71	–71.06	193.39	5.23E-02	–1.32E-07	–3.15E-08	–3.96E-07	20
178	1095	B	1	H	3	71	86.71	–71.19	193.35	3.40E-02	–8.54E-08	–2.03E-08	–2.58E-07	30
178	1095	B	1	H	3	71	86.71	–70.73	196.89	2.15E-02	–5.44E-08	–1.65E-08	–1.63E-07	40
178	1095	B	1	H	3	71	86.71	–69.87	205.33	1.15E-02	–2.85E-08	–1.35E-08	–8.61E-08	50
178	1095	B	1	H	3	71	86.71	–69.82	208.85	6.66E-03	–1.61E-08	–8.87E-09	–5.00E-08	60
178	1095	B	1	H	3	71	86.71	–59.47	183.54	3.65E-03	–1.48E-08	–9.14E-10	–2.51E-08	70
178	1095	B	1	H	3	71	86.71	–69.34	225.18	3.70E-03	–7.37E-09	–7.41E-09	–2.77E-08	80
178	1095	B	1	H	3	141	87.41	–18.36	165.32	9.30E-02	–6.83E-07	1.79E-07	–2.34E-07	0
178	1095	B	1	H	3	141	87.41	–30.98	163.58	7.58E-02	–4.99E-07	1.47E-07	–3.12E-07	10
178	1095	B	1	H	3	141	87.41	–31.36	163.81	5.87E-02	–3.85E-07	1.12E-07	–2.44E-07	20
178	1095	B	1	H	3	141	87.41	–30.51	163.32	4.02E-02	–2.65E-07	7.95E-08	–1.63E-07	30
178	1095	B	1	H	3	141	87.41	–27.57	165.63	2.72E-02	–1.87E-07	4.78E-08	–1.01E-07	40
178	1095	B	1	H	3	141	87.41	–28.71	154.2	1.71E-02	–1.08E-07	5.22E-08	–6.57E-08	50
178	1095	B	1	H	3	141	87.41	–20.06	164.41	1.00E-02	–7.26E-08	2.02E-08	–2.75E-08	60
178	1095	B	1	H	3	141	87.41	–16.17	181.49	8.40E-03	–6.46E-08	–1.68E-09	–1.87E-08	70
178	1095	B	1	H	3	141	87.41	–44.64	180.98	4.99E-03	–2.84E-08	–4.86E-10	–2.81E-08	80
178	1095	B	1	H	4	76	88.26	43.28	293.66	4.17E-02	9.75E-08	–2.23E-07	2.29E-07	0
178	1095	B	1	H	4	76	88.26	34.8	289.84	2.64E-02	5.89E-08	–1.63E-07	1.21E-07	10
178	1095	B	1	H	4	76	88.26	39.89	289.37	2.12E-02	4.32E-08	–1.23E-07	1.09E-07	20

Note: Only a portion of this table appears here. The complete table is available in ASCII format in the **TABLES** directory.

Table T26. Discrete sample NRM and thermal demagnetization results for samples from Hole 1095B. (See table note. Continued on next two pages.)

Leg	Site	Hole	Core	Type	Section	Interval (cm)	Depth (mbsf)	Inclination (°)	Declination (°)	Intensity (A/m)	Mx (A·m)	My (A·m)	Mz (A·m)	Demagnetization step (°C)
178	1095	B	34	X	2	33	399.13	65.29	44.05	4.09E-03	9.83E-09	9.51E-09	2.97E-08	0
178	1095	B	34	X	2	33	399.13	65.5	41.76	4.08E-03	1.01E-08	9.01E-09	2.97E-08	0
178	1095	B	34	X	2	33	399.13	67.31	47.73	3.35E-03	6.94E-09	7.64E-09	2.47E-08	100
178	1095	B	34	X	2	33	399.13	68.41	44.84	3.31E-03	6.91E-09	6.87E-09	2.46E-08	100
178	1095	B	34	X	2	33	399.13	66.42	46.91	2.33E-03	5.10E-09	5.46E-09	1.71E-08	125
178	1095	B	34	X	2	33	399.13	66.68	47.72	2.34E-03	4.99E-09	5.49E-09	1.72E-08	125
178	1095	B	34	X	2	33	399.13	73.37	168.26	7.52E-02	–1.69E-07	3.50E-08	5.76E-07	150
178	1095	B	34	X	2	33	399.13	73.47	169.13	7.51E-02	–1.68E-07	3.22E-08	5.76E-07	150
178	1095	B	34	X	2	33	399.13	73.72	168.84	7.13E-02	–1.57E-07	3.09E-08	5.47E-07	175
178	1095	B	34	X	2	33	399.13	73.88	168	7.14E-02	–1.55E-07	3.30E-08	5.49E-07	175
178	1095	B	34	X	2	33	399.13	74.9	172.2	6.76E-02	–1.40E-07	1.91E-08	5.22E-07	200
178	1095	B	34	X	2	33	399.13	75.84	172.71	6.48E-02	–1.26E-07	1.61E-08	5.03E-07	225
178	1095	B	34	X	2	33	399.13	75.06	175.73	6.02E-02	–1.24E-07	9.23E-09	4.65E-07	250
178	1095	B	34	X	2	33	399.13	75.95	173.96	5.26E-02	–1.02E-07	1.07E-08	4.08E-07	275
178	1095	B	34	X	2	33	399.13	78.07	176.55	3.70E-02	–6.11E-08	3.68E-09	2.90E-07	300
178	1095	B	34	X	2	33	399.13	76.92	175.08	2.47E-02	–4.46E-08	3.83E-09	1.92E-07	325
178	1095	B	34	X	2	33	399.13	79.35	182.37	1.63E-02	–2.41E-08	–9.95E-10	1.28E-07	350
178	1095	B	34	X	2	33	399.13	75.75	147.32	1.09E-02	–1.80E-08	1.16E-08	8.44E-08	375
178	1095	B	34	X	2	33	399.13	82.91	200.98	9.38E-03	–8.65E-09	–3.32E-09	7.45E-08	400
178	1095	B	34	X	2	33	399.13	86.85	182.78	7.81E-03	–3.43E-09	–1.67E-10	6.24E-08	425
178	1095	B	34	X	2	33	399.13	87.83	172.47	7.62E-03	–2.29E-09	3.02E-10	6.10E-08	425
178	1095	B	34	X	2	33	399.13	83.11	147.59	7.19E-03	–5.82E-09	3.70E-09	5.71E-08	450
178	1095	B	34	X	2	33	399.13	83.28	146.52	7.10E-03	–5.54E-09	3.67E-09	5.64E-08	450
178	1095	B	34	X	2	33	399.13	83.77	169.73	6.82E-03	–5.83E-09	1.06E-09	5.42E-08	475
178	1095	B	34	X	2	33	399.13	84.96	159.35	6.66E-03	–4.38E-09	1.65E-09	5.31E-08	475
178	1095	B	34	X	2	33	399.13	80.29	185.27	6.76E-03	–9.08E-09	–8.37E-10	5.33E-08	500
178	1095	B	34	X	2	33	399.13	82.73	181.67	6.50E-03	–6.57E-09	–1.91E-10	5.16E-08	500
178	1095	B	34	X	2	33	399.13	89.16	53.7	6.26E-03	4.36E-10	5.94E-10	5.01E-08	525
178	1095	B	34	X	2	33	399.13	89.3	308.02	6.40E-03	3.83E-10	–4.90E-10	5.12E-08	525
178	1095	B	34	X	2	33	399.13	79.16	180.62	6.46E-03	–9.72E-09	–1.05E-10	5.08E-08	550
178	1095	B	34	X	2	33	399.13	79.25	178.78	6.43E-03	–9.60E-09	2.05E-10	5.06E-08	550
178	1095	B	34	X	2	33	399.13	77.7	192.9	5.60E-03	–9.30E-09	–2.13E-09	4.38E-08	575
178	1095	B	34	X	2	33	399.13	78.32	193.53	5.58E-03	–8.78E-09	–2.11E-09	4.37E-08	575
178	1095	B	34	X	2	33	399.13	86.53	243.66	3.77E-03	–8.10E-10	–1.64E-09	3.01E-08	600
178	1095	B	34	X	2	33	399.13	87.25	262.59	3.77E-03	–1.87E-10	–1.43E-09	3.01E-08	600
178	1095	B	34	X	2	33	399.13	73.55	309.77	1.87E-03	2.71E-09	–3.25E-09	1.43E-08	625
178	1095	B	34	X	2	33	399.13	80.7	287.06	1.76E-03	6.67E-10	–2.17E-09	1.39E-08	625
178	1095	B	34	X	2	33	399.13	–47.01	276.93	1.44E-03	9.45E-10	–7.77E-09	–8.40E-09	650
178	1095	B	34	X	2	33	399.13	–47.08	277.83	1.46E-03	1.08E-09	–7.89E-09	–8.56E-09	650
178	1095	B	34	X	2	33	399.13	15.56	309.52	5.23E-04	2.57E-09	–3.11E-09	1.12E-09	675
178	1095	B	34	X	2	33	399.13	17.45	315.08	5.43E-04	2.93E-09	–2.93E-09	1.30E-09	675
178	1095	B	34	X	2	33	399.13	56.59	122.77	1.25E-03	–2.98E-09	4.63E-09	8.36E-09	700
178	1095	B	34	X	2	33	399.13	56.85	124.01	1.28E-03	–3.14E-09	4.65E-09	8.59E-09	700
178	1095	B	34	X	2	96	399.76	71.47	167.67	1.04E-01	–2.58E-07	5.63E-08	7.87E-07	0
178	1095	B	34	X	2	96	399.76	71.52	167.5	1.04E-01	–2.57E-07	5.69E-08	7.87E-07	0
178	1095	B	34	X	2	96	399.76	71.77	169.33	9.56E-02	–2.35E-07	4.43E-08	7.26E-07	100
178	1095	B	34	X	2	96	399.76	71.88	169.3	9.56E-02	–2.34E-07	4.41E-08	7.27E-07	100
178	1095	B	34	X	2	96	399.76	72.46	168.37	7.91E-02	–1.87E-07	3.84E-08	6.03E-07	125
178	1095	B	34	X	2	96	399.76	72.58	168.48	7.91E-02	–1.86E-07	3.78E-08	6.03E-07	125
178	1095	B	34	X	2	96	399.76	68.16	53.46	2.08E-03	3.68E-09	4.97E-09	1.54E-08	150
178	1095	B	34	X	2	96	399.76	68.5	53.54	2.07E-03	3.61E-09	4.88E-09	1.54E-08	150
178	1095	B	34	X	2	96	399.76	67.11	47.36	1.87E-03	3.95E-09	4.28E-09	1.38E-08	175
178	1095	B	34	X	2	96	399.76	67.88	47.38	1.87E-03	3.82E-09	4.15E-09	1.39E-08	175
178	1095	B	34	X	2	96	399.76	66.36	94	2.76E-03	–6.19E-10	8.84E-09	2.03E-08	200
178	1095	B	34	X	2	96	399.76	76.98	291.6	1.87E-03	1.24E-09	–3.14E-09	1.46E-08	225
178	1095	B	34	X	2	96	399.76	56.42	35.59	1.44E-03	5.17E-09	3.70E-09	9.58E-09	250
178	1095	B	34	X	2	96	399.76	18.94	95.42	1.50E-03	–1.07E-09	1.13E-08	3.90E-09	275
178	1095	B	34	X	2	96	399.76	–22.54	272	2.50E-04	6.45E-11	–1.84E-09	–7.66E-10	300
178	1095	B	34	X	2	96	399.76	61.14	109.81	1.87E-03	–2.45E-09	6.80E-09	1.31E-08	325
178	1095	B	34	X	2	96	399.76	55.22	115.93	1.51E-03	–3.02E-09	6.20E-09	9.94E-09	350
178	1095	B	34	X	2	96	399.76	23.87	20.5	2.92E-04	2.00E-09	7.49E-10	9.46E-10	375
178	1095	B	34	X	2	96	399.76	6.41	29.62	2.91E-04	2.01E-09	1.14E-09	2.60E-10	400
178	1095	B	34	X	2	96	399.76	0.68	21.96	2.06E-04	1.53E-09	6.17E-10	1.95E-11	425
178	1095	B	34	X	2	96	399.76	2.67	18	2.14E-04	1.63E-09	5.29E-10	7.97E-11	425
178	1095	B	34	X	2	96	399.76	–7.31	23.23	3.05E-04	2.23E-09	9.55E-10	–3.11E-10	450
178	1095	B	34	X	2	96	399.76	–7.84	24.6	3.09E-04	2.22E-09	1.02E-09	–3.37E-10	450
178	1095	B	34	X	2	96	399.76	–12.99	28.53	2.32E-04	1.59E-09	8.64E-10	–4.17E-10	475
178	1095	B	34	X	2	96	399.76	–18.18	27.29	2.51E-04	1.70E-09	8.75E-10	–6.27E-10	475

Table T26 (continued).

Leg	Site	Hole	Core	Type	Section	Interval (cm)	Depth (mbsf)	Inclination (°)	Declination (°)	Intensity (A/m)	Mx (A·m)	My (A·m)	Mz (A·m)	Demagnetization step (°C)
178	1095	B	34	X	2	96	399.76	–5.09	75.59	1.05E-04	2.09E-10	8.14E-10	–7.48E-11	500
178	1095	B	34	X	2	96	399.76	25.33	118.78	1.14E-04	–3.97E-10	7.24E-10	3.91E-10	500
178	1095	B	34	X	2	96	399.76	–11.33	12.6	2.06E-04	1.57E-09	3.52E-10	–3.23E-10	525
178	1095	B	34	X	2	96	399.76	–26.43	24.72	2.04E-04	1.33E-09	6.11E-10	–7.27E-10	525
178	1095	B	34	X	2	96	399.76	66.09	289.52	7.74E-05	8.38E-11	–2.36E-10	5.66E-10	550
178	1095	B	34	X	2	96	399.76	69.42	295.29	1.11E-04	1.34E-10	–2.83E-10	8.33E-10	550
178	1095	B	34	X	2	96	399.76	–1.96	304.97	1.23E-04	5.63E-10	–8.05E-10	–3.36E-11	575
178	1095	B	34	X	2	96	399.76	30.65	288.83	1.27E-04	2.82E-10	–8.27E-10	5.18E-10	575
178	1095	B	34	X	2	96	399.76	–27.85	115.06	1.13E-03	–3.38E-09	7.23E-09	–4.21E-09	600
178	1095	B	34	X	2	96	399.76	–28.57	116.48	1.12E-03	–3.51E-09	7.04E-09	–4.29E-09	600
178	1095	B	34	X	2	96	399.76	–25.47	116.34	1.09E-03	–3.48E-09	7.03E-09	–3.74E-09	625
178	1095	B	34	X	2	96	399.76	–26.47	119.24	1.15E-03	–4.02E-09	7.17E-09	–4.09E-09	625
178	1095	B	34	X	2	96	399.76	–3.15	311.53	1.00E-04	5.31E-10	–5.99E-10	–4.41E-11	650
178	1095	B	34	X	2	96	399.76	–11.06	307.41	8.63E-05	4.11E-10	–5.38E-10	–1.32E-10	650
178	1095	B	34	X	2	96	399.76	–52.41	246.78	1.17E-03	–2.26E-09	–5.26E-09	–7.44E-09	675
178	1095	B	34	X	2	96	399.76	–53.12	248.07	1.23E-03	–2.20E-09	–5.47E-09	–7.85E-09	675
178	1095	B	34	X	2	96	399.76	15.95	331.28	9.59E-05	6.47E-10	–3.54E-10	2.11E-10	700
178	1095	B	34	X	2	96	399.76	–31.01	335.29	5.59E-05	3.48E-10	–1.60E-10	–2.30E-10	700
178	1095	B	34	X	4	79	402.59	–68.22	289.38	5.68E-02	5.60E-08	–1.59E-07	–4.22E-07	0
178	1095	B	34	X	4	79	402.59	–68.46	288.72	5.69E-02	5.36E-08	–1.58E-07	–4.23E-07	0
178	1095	B	34	X	4	79	402.59	–60.52	329.46	6.86E-02	2.33E-07	–1.37E-07	–4.78E-07	100
178	1095	B	34	X	4	79	402.59	–60.8	330.74	6.87E-02	2.34E-07	–1.31E-07	–4.80E-07	100
178	1095	B	34	X	4	79	402.59	–66.8	309.71	6.57E-02	1.32E-07	–1.59E-07	–4.83E-07	125
178	1095	B	34	X	4	79	402.59	–67.45	310.08	6.59E-02	1.30E-07	–1.55E-07	–4.87E-07	125
178	1095	B	34	X	4	79	402.59	–68.17	291.18	6.45E-02	6.93E-08	–1.79E-07	–4.79E-07	150
178	1095	B	34	X	4	79	402.59	–69.78	294.52	6.48E-02	7.44E-08	–1.63E-07	–4.87E-07	150
178	1095	B	34	X	4	79	402.59	–71.31	290.95	6.54E-02	6.00E-08	–1.57E-07	–4.96E-07	175
178	1095	B	34	X	4	79	402.59	–71.5	290.97	6.52E-02	5.92E-08	–1.55E-07	–4.95E-07	175
178	1095	B	34	X	4	79	402.59	–69.55	289.53	6.56E-02	6.13E-08	–1.73E-07	–4.92E-07	200
178	1095	B	34	X	4	79	402.59	–71.99	291.22	6.62E-02	5.92E-08	–1.53E-07	–5.04E-07	225
178	1095	B	34	X	4	79	402.59	–73.16	287.68	6.52E-02	4.59E-08	–1.44E-07	–5.00E-07	250
178	1095	B	34	X	4	79	402.59	–72.82	283.22	6.48E-02	3.50E-08	–1.49E-07	–4.95E-07	275
178	1095	B	34	X	4	79	402.59	–73.85	284.63	5.96E-02	3.35E-08	–1.28E-07	–4.58E-07	300
178	1095	B	34	X	4	79	402.59	–74.59	280.19	4.55E-02	1.71E-08	–9.52E-08	–3.51E-07	325
178	1095	B	34	X	4	79	402.59	–73.55	282.37	3.43E-02	1.67E-08	–7.60E-08	–2.63E-07	350
178	1095	B	34	X	4	79	402.59	–76.04	288.07	2.15E-02	1.29E-08	–3.95E-08	–1.67E-07	375
178	1095	B	34	X	4	79	402.59	–72.11	291.6	1.41E-02	1.28E-08	–3.23E-08	–1.08E-07	400
178	1095	B	34	X	4	79	402.59	–66.59	292.62	1.15E-02	1.41E-08	–3.38E-08	–8.46E-08	425
178	1095	B	34	X	4	79	402.59	–68.03	293.08	1.14E-02	1.34E-08	–3.15E-08	–8.49E-08	425
178	1095	B	34	X	4	79	402.59	–72.91	301.25	1.03E-02	1.25E-08	–2.06E-08	–7.85E-08	450
178	1095	B	34	X	4	79	402.59	–73.03	302.33	1.03E-02	1.29E-08	–2.04E-08	–7.89E-08	450
178	1095	B	34	X	4	79	402.59	–71.5	282.36	9.18E-03	4.98E-09	–2.27E-08	–6.96E-08	475
178	1095	B	34	X	4	79	402.59	–71.55	286.62	9.30E-03	6.74E-09	–2.26E-08	–7.06E-08	475
178	1095	B	34	X	4	79	402.59	–72.2	298.86	8.36E-03	9.87E-09	–1.79E-08	–6.37E-08	500
178	1095	B	34	X	4	79	402.59	–72.52	295.77	8.28E-03	8.65E-09	–1.79E-08	–6.32E-08	500
178	1095	B	34	X	4	79	402.59	–67.61	289.27	8.26E-03	8.30E-09	–2.38E-08	–6.11E-08	525
178	1095	B	34	X	4	79	402.59	–68.02	290.77	8.30E-03	8.81E-09	–2.32E-08	–6.16E-08	525
178	1095	B	34	X	4	79	402.59	–68.63	288.83	7.13E-03	6.71E-09	–1.97E-08	–5.31E-08	550
178	1095	B	34	X	4	79	402.59	–69.28	284.83	7.05E-03	5.11E-09	–1.93E-08	–5.28E-08	550
178	1095	B	34	X	4	79	402.59	–68.04	280.89	5.12E-03	2.90E-09	–1.51E-08	–3.80E-08	575
178	1095	B	34	X	4	79	402.59	–68.31	283.9	5.06E-03	3.59E-09	–1.45E-08	–3.76E-08	575
178	1095	B	34	X	4	79	402.59	–63.05	304.28	3.33E-03	6.81E-09	–9.99E-09	–2.38E-08	600
178	1095	B	34	X	4	79	402.59	–63.38	302.79	3.36E-03	6.53E-09	–1.01E-08	–2.41E-08	600
178	1095	B	34	X	4	79	402.59	–24.94	329.29	9.01E-04	5.62E-09	–3.34E-09	–3.04E-09	625
178	1095	B	34	X	4	79	402.59	–38.19	311.49	6.34E-04	2.64E-09	–2.99E-09	–3.14E-09	625
178	1095	B	34	X	4	79	402.59	–10.69	314.92	3.28E-04	1.82E-09	–1.83E-09	–4.87E-10	650
178	1095	B	34	X	4	79	402.59	–27	316.62	3.21E-04	1.66E-09	–1.57E-09	–1.16E-09	650
178	1095	B	34	X	4	79	402.59	63.73	324.32	3.03E-04	8.70E-10	–6.25E-10	2.17E-09	675
178	1095	B	34	X	4	79	402.59	68.06	317.16	2.55E-04	5.58E-10	–5.18E-10	1.89E-09	675
178	1095	B	34	X	4	79	402.59	47.17	335.9	3.37E-04	1.67E-09	–7.48E-10	1.98E-09	700
178	1095	B	34	X	4	79	402.59	47.96	341.12	3.09E-04	1.57E-09	–5.36E-10	1.84E-09	700
178	1095	B	34	X	5	147	404.77	30.12	338.55	2.60E-02	1.67E-07	–6.58E-08	1.04E-07	0
178	1095	B	34	X	5	147	404.77	30.43	336.86	2.59E-02	1.64E-07	–7.02E-08	1.05E-07	0
178	1095	B	34	X	5	147	404.77	20.09	337.74	1.93E-02	1.34E-07	–5.50E-08	5.31E-08	100
178	1095	B	34	X	5	147	404.77	20.37	338.15	1.93E-02	1.35E-07	–5.40E-08	5.39E-08	100
178	1095	B	34	X	5	147	404.77	–23.55	343.93	1.63E-02	1.15E-07	–3.32E-08	–5.22E-08	125
178	1095	B	34	X	5	147	404.77	–23.68	343.45	1.61E-02	1.13E-07	–3.37E-08	–5.18E-08	125
178	1095	B	34	X	5	147	404.77	–57.74	354.1	1.84E-02	7.81E-08	–8.06E-09	–1.24E-07	5
178	1095	B	34	X	5	147	404.77	–71.8	4.62	2.25E-02	5.61E-08	4.53E-09	–1.71E-07	10

Table T26 (continued).

Leg	Site	Hole	Core	Type	Section	Interval (cm)	Depth (mbsf)	Inclination (°)	Declination (°)	Intensity (A/m)	Mx (A·m)	My (A·m)	Mz (A·m)	Demagnetization step (°C)
178	1095	B	34	X	5	147	404.77	–74.89	9.27	2.18E-02	4.48E-08	7.30E-09	–1.68E-07	15
178	1095	B	34	X	5	147	404.77	–76.22	11.89	1.93E-02	3.59E-08	7.56E-09	–1.50E-07	20
178	1095	B	34	X	5	147	404.77	–77.01	10.88	1.60E-02	2.82E-08	5.42E-09	–1.24E-07	25
178	1095	B	34	X	5	147	404.77	–76.8	9.28	1.26E-02	2.27E-08	3.72E-09	–9.82E-08	30
178	1095	B	34	X	5	147	404.77	–76.36	4.13	9.89E-03	1.86E-08	1.34E-09	–7.69E-08	35
178	1095	B	34	X	5	147	404.77	–77.08	6.3	8.20E-03	1.46E-08	1.61E-09	–6.39E-08	40
178	1095	B	34	X	5	147	404.77	–76.82	5.77	4.93E-03	8.94E-09	9.03E-10	–3.84E-08	50
178	1095	B	34	X	5	147	404.77	–73.71	25.14	3.20E-03	6.49E-09	3.05E-09	–2.45E-08	60
178	1095	B	34	X	5	147	404.77	–84.03	269.95	2.04E-03	–1.56E-12	–1.69E-09	–1.62E-08	70
178	1095	B	34	X	5	147	404.77	–43.34	357.96	8.82E-04	5.13E-09	–1.83E-10	–4.84E-09	80

Note: This table is also available in ASCII format in the **TABLES** directory.

Table T27. Results from the principal component analysis of discrete paleomagnetic samples. (See table note. Continued on next four pages.)

Leg	Site	Core	Section	Interval (cm)	Depth (mbsf)	Inclination (°)	Declination (°)	MAD	Length	Devang	Steps	Low	High	Option
178	1095A	1H	1	141	1.41	–37.7	22.1	3.22	1.26E+00	2.47	4	40	80	FRE
178	1095A	1H	1	68	0.68	–57.7	12.7	2.35	1.05E+00	1.54	4	40	80	FRE
178	1095A	1H	2	144	2.9	–33.7	18.2	1.57	9.13E-01	3.9	4	40	80	FRE
178	1095A	1H	2	61	2.07	–35.3	19.3	7.83	3.36E-01	9.21	4	40	80	FRE
178	1095A	1H	3	135	4.28	–70.3	25.3	6.59	2.61E-01	14.33	4	50	80	FRE
178	1095A	1H	3	71	3.64	–80.3	317.8	1.77	3.77E-01	4.83	4	40	80	FRE
178	1095A	1H	4	117	5.6	–46.6	52	2.29	2.35E-01	7.99	4	20	70	FRE
178	1095A	1H	4	74	5.17	–51.9	242.7	8.19	3.82E-01	10.17	4	50	80	FRE
178	1095A	2H	1	140	7.3	–82.6	349.7	2.14	6.46E-01	1.75	4	40	80	FRE
178	1095A	2H	2	138	8.78	–34.6	1	1.42	8.77E+00	9.35	4	50	80	FRE
178	1095A	2H	2	72	8.12	–63.2	315.6	2.33	3.51E-01	2.58	4	10	80	FRE
178	1095A	2H	3	146	10.36	–87.9	9.2	4.16	2.19E-01	10.5	4	10	70	FRE
178	1095A	2H	3	79	9.69	–82.2	296.6	2.42	3.97E-01	10.03	4	10	80	FRE
178	1095A	2H	4	131	11.71	–87	194.5	0.4	9.29E-01	1.35	4	30	70	FRE
178	1095A	2H	4	71	11.11	–81.7	148.4	1.49	4.22E-01	6.3	4	40	80	FRE
178	1095A	2H	5	35	12.25	–56.7	293.6	2.11	9.76E-01	3.4	4	20	70	FRE
178	1095A	3H	1	18	11.48	–5.7	356.9	0.74	7.67E-01	9.95	4	20	70	FRE
178	1095A	3H	2	35	12.25	17.3	53.5	0.95	1.89E+00	5.73	4	20	80	FRE
178	1095A	3H	2	80	12.7	10.8	346.8	0.81	1.35E+00	1.34	4	20	80	FRE
178	1095A	3H	4	146	16.36	–4.7	355.8	2.07	1.11E+00	17.33	4	30	70	FRE
178	1095A	3H	4	70	15.6	–76.9	56.6	5.72	1.57E-01	5.38	4	30	80	FRE
178	1095A	3H	6	71	17.49	71.8	28.1	21.25	1.64E-01	10.83	4	50	80	FRE
178	1095A	3H	7	71	18.76	67.8	286.3	4.1	3.96E-01	8.66	4	30	80	FRE
178	1095A	3H	8	70	19.69	30.3	359.5	0.51	2.12E+00	1.62	4	20	60	FRE
178	1095A	4H	1	64	21.44	–32.9	44.2	1.64	1.25E+00	4.83	4	20	80	FRE
178	1095A	4H	2	146	23.76	24.8	345.6	10.03	1.78E-01	32.61	4	20	80	FRE
178	1095A	4H	2	71	23.01	12.4	21.9	2.06	9.85E-01	8.84	4	30	80	FRE
178	1095A	4H	3	137	25.17	25.2	220.2	30.04	9.13E-02	86.93	4	50	80	FRE
178	1095A	4H	3	71	24.51	1.5	34.2	2.83	1.26E+00	3.67	4	20	80	FRE
178	1095A	4H	4	145	26.75	–23.7	54.3	1.1	3.91E-01	11.59	4	20	70	FRE
178	1095A	4H	4	71	26.01	–57.8	117.2	24.56	1.17E-01	153.6	4	50	80	FRE
178	1095A	4H	5	71	27.51	–3.4	72.2	7.46	1.40E-01	41.09	4	20	80	FRE
178	1095A	4H	6	71	28.51	–54.8	357	5.29	5.12E-01	5.73	4	20	80	FRE
178	1095A	5H	1	143	31.73	58.2	282	5.88	3.04E-01	17.24	4	40	80	FRE
178	1095A	5H	1	71	31.01	73	308.7	0.78	5.75E-01	2.43	4	20	80	FRE
178	1095A	5H	2	143	33.23	86	266.2	7.66	1.40E-01	12.18	4	30	60	FRE
178	1095A	5H	2	71	32.51	–2.4	144.9	12.51	3.02E-01	41.17	4	20	60	FRE
178	1095A	5H	3	144	34.74	73.2	185.8	11.36	1.00E-01	1.6	4	30	60	FRE
178	1095A	5H	3	71	34.01	29.6	231.9	6.92	1.84E-01	39.98	4	20	60	FRE
178	1095A	5H	4	144	36.24	79.1	290.4	9.08	2.97E-01	6.97	4	20	60	FRE
178	1095A	5H	4	71	35.51	75.7	23.9	12.21	8.40E-02	18.96	4	30	60	FRE
178	1095A	5H	5	144	37.74	60.5	239.9	10.22	2.08E-01	28.43	4	20	60	FRE
178	1095A	5H	5	71	37.01	74	125.8	2.29	7.83E-01	3.64	4	30	60	FRE
178	1095A	6H	1	145	41.25	–82.9	169.4	6.36	2.65E-01	8.2	4	20	60	FRE
178	1095A	6H	1	64	40.44	68.1	39.5	2.54	2.20E-01	1.05	4	20	60	FRE
178	1095A	6H	2	142	42.72	45.3	284.7	12.94	1.53E-01	16.51	4	20	60	FRE
178	1095A	6H	2	71	42.01	64.7	264.4	15.91	1.27E-01	25.28	4	20	60	FRE
178	1095A	6H	3	145	44.25	44.7	282	20.16	1.30E-01	44.8	4	30	60	FRE
178	1095A	6H	3	75	43.55	44.8	268.6	19.34	1.98E-01	23.96	4	30	60	FRE
178	1095A	6H	4	147	45.77	15.8	203.7	9.28	3.42E-01	14.03	4	30	60	FRE
178	1095A	6H	4	70	45	36.1	330.6	6.84	3.91E-01	8.19	4	20	60	FRE
178	1095A	6H	5	145	47.25	–2.9	341.9	11.31	1.27E-01	43.27	4	30	60	FRE
178	1095A	6H	5	69	46.49	43.8	270.6	0.65	9.84E-01	10.13	4	20	60	FRE
178	1095A	6H	6	140	48.7	14.4	6.8	27.99	5.87E-02	76.4	4	30	60	FRE
178	1095A	6H	6	69	47.99	31.2	340.2	5.01	2.66E-01	14.88	4	20	60	FRE
178	1095A	7H	1	145	50.75	79.4	238.8	2.58	3.93E-01	5.2	4	20	60	FRE
178	1095A	7H	1	74	50.04	70.6	250.1	0.45	4.70E-01	1.41	4	20	60	FRE
178	1095A	7H	2	146	52.26	75.3	225	0.95	3.67E-01	1.68	4	30	60	FRE
178	1095A	7H	2	71	51.51	73.9	29.9	0.47	7.77E-01	0.47	4	20	60	FRE
178	1095A	7H	3	141	53.71	75.3	226.2	0.61	1.04E+00	0.41	4	20	60	FRE
178	1095A	7H	3	71	53.01	74.2	55.8	1.64	2.98E-01	3.89	4	20	60	FRE
178	1095A	7H	4	146	55.26	69.9	188.8	1.45	6.51E-01	2.61	4	20	60	FRE
178	1095A	7H	4	71	54.51	58.1	247.6	0.77	3.31E-01	3.64	4	30	60	FRE
178	1095A	7H	5	145	56.75	80.2	240.9	1.44	6.84E-01	2.48	4	30	80	FRE
178	1095A	7H	5	71	56.01	70.4	279.1	1.62	1.90E+00	4.49	4	20	70	FRE
178	1095A	7H	6	146	58.26	69.3	50.1	2.85	1.63E-01	1.88	4	20	80	FRE
178	1095A	7H	6	71	57.51	26.1	16.9	2.37	7.74E-02	18.11	4	30	80	FRE
178	1095A	7H	7	65	58.95	85.5	128.2	8.78	6.32E-02	45.82	4	40	80	FRE

Table T27 (continued).

Leg	Site	Core	Section	Interval (cm)	Depth (mbsf)	Inclination (°)	Declination (°)	MAD	Length	Devang	Steps	Low	High	Option
178	1095A	8H	1	77	58.57	29.7	9.5	3.49	3.75E-01	6.87	4	20	80	FRE
178	1095A	8H	2	90	61.2	–65.3	60.4	3.72	3.85E-01	11.36	4	30	80	FRE
178	1095A	8H	3	144	63.24	–13	91	2.72	2.25E-01	0.74	4	20	80	FRE
178	1095A	8H	3	71	62.51	–84.6	326	2	3.70E-02	7.58	4	20	80	FRE
178	1095A	8H	4	145	64.75	–69.5	83	1.32	7.33E-02	4.9	4	20	60	FRE
178	1095A	8H	4	71	64.01	–57.5	295.9	0.79	3.14E-01	2.27	4	20	80	FRE
178	1095A	8H	5	147	66.27	–77.1	4.9	0.91	6.10E-01	2.31	4	30	80	FRE
178	1095A	8H	5	75	65.55	–85.1	2.1	9.75	6.02E-02	17.77	4	20	70	FRE
178	1095A	8H	6	147	67.77	–80	300.2	1.17	1.23E-01	3.36	4	20	80	FRE
178	1095A	8H	6	69	66.99	–52.4	308.4	3.05	1.46E-01	1.67	4	20	80	FRE
178	1095A	8H	7	62	68.42	–85.7	230.3	2.35	2.27E-02	14.47	4	40	80	FRE
178	1095A	9H	1	146	69.76	–68.6	222.8	8.7	2.57E-02	18.56	4	20	80	FRE
178	1095A	9H	2	146	71.26	–70.1	281	9.32	5.62E-02	4.6	4	20	80	FRE
178	1095A	9H	2	69	70.49	–85.6	330.8	0.69	8.15E-02	3.8	4	30	70	FRE
178	1095A	9H	3	146	72.76	–80	82.4	0.41	7.41E-01	1.82	4	30	80	FRE
178	1095A	9H	3	66	71.96	–79.5	122.3	0.64	7.69E-01	0.41	4	20	80	FRE
178	1095A	9H	4	146	74.26	–61.5	120	2.17	5.91E-01	4.7	4	40	80	FRE
178	1095A	9H	4	71	73.51	–71	96.1	0.75	5.12E-01	0.39	4	30	80	FRE
178	1095A	9H	5	145	75.75	–62.5	25.7	1.06	6.48E-01	1.32	4	40	80	FRE
178	1095A	9H	5	71	75.01	–84.6	158.2	2.48	3.36E-01	0.58	4	40	80	FRE
178	1095A	9H	6	145	77.25	–0.6	149.3	5.85	5.53E-01	19.36	4	20	80	FRE
178	1095A	9H	6	75	76.55	–56.2	109.7	1.67	2.04E-01	0.7	4	40	80	FRE
178	1095A	10H	1	141	79.21	66.3	319.4	20.16	8.14E-02	118.45	4	50	80	FRE
178	1095A	10H	2	145	80.75	–77.1	237.4	2.68	1.33E-01	7.42	4	30	70	FRE
178	1095A	10H	2	68	79.98	–72.5	187.4	1.3	3.96E-01	2.02	4	20	80	FRE
178	1095A	10H	3	141	82.21	13.3	38.5	0.77	6.83E-01	3.42	4	20	80	FRE
178	1095A	10H	3	70	81.5	–70	129.4	8.84	4.50E-02	29.36	4	40	80	FRE
178	1095A	10H	4	143	83.73	35.4	263.7	4.32	1.41E-01	4.02	4	20	80	FRE
178	1095A	10H	4	71	83.01	54.5	252.7	17.38	1.40E-02	51.18	4	30	80	FRE
178	1095A	10H	5	68	84.48	64.9	2.4	1.43	6.99E-01	8.49	4	20	80	FRE
178	1095A	10H	5	71	84.51	0.2	5.7	1.48	5.06E-01	3.67	4	20	80	FRE
178	1095A	10H	6	145	86.75	80.2	308.1	1.96	1.44E-01	13.49	4	30	80	FRE
178	1095A	10H	7	70	87.5	–81.1	152.8	1.92	1.61E-01	4.14	4	20	70	FRE
178	1095B	1H	1	120	84.2	12.4	187.4	24.04	4.71E-03	90.88	4	50	80	FRE
178	1095B	1H	1	140	84.4	–53	163.4	2.1	3.37E-01	1.83	4	30	80	FRE
178	1095B	1H	2	70	85.2	–8.9	130.2	11.61	2.01E-02	37.38	4	30	70	FRE
178	1095B	1H	2	71	85.21	–76.2	161.5	0.24	2.29E+00	0.39	4	20	80	FRE
178	1095B	1H	2	145	85.95	–36.7	120	2.43	1.80E-01	11.59	4	20	80	FRE
178	1095B	1H	3	71	86.71	–71	191	0.21	4.87E-01	1.97	4	20	80	FRE
178	1095B	1H	3	141	87.41	–31.4	162.8	3.12	5.40E-01	1.48	4	20	80	FRE
178	1095B	1H	4	76	88.26	61.5	281.3	10.9	7.81E-02	8.49	4	50	80	FRE
178	1095B	1H	4	141	88.91	–84.7	132.6	1.11	1.23E-01	4.43	4	20	80	FRE
178	1095B	1H	5	71	89.71	–1.8	91	5.66	7.52E-03	26.24	4	50	80	FRE
178	1095B	1H	5	143	90.43	–68.8	109	2.85	5.95E-01	2.98	4	40	80	FRE
178	1095B	1H	6	69	91.19	–78.8	97.9	1.17	7.77E-01	3.12	4	40	80	FRE
178	1095B	1H	6	129	91.79	–71.6	135.1	0.33	5.73E-01	1.36	4	30	80	FRE
178	1095B	1H	7	50	92.5	74.4	153.8	1.44	6.33E-01	4.91	4	30	80	FRE
178	1095B	2H	2	146	95.46	–72	112.8	1.37	1.50E-01	0.96	4	20	80	FRE
178	1095B	2H	3	71	96.21	–83.3	161.5	3.63	3.15E-02	2.46	4	20	80	FRE
178	1095B	2H	3	146	96.96	–4.1	179.7	25.63	2.36E-02	23.9	4	50	80	FRE
178	1095B	2H	4	71	97.71	–12.2	252.3	9.89	4.47E-03	30.63	4	30	70	FRE
178	1095B	2H	4	146	98.46	–7	27.4	0.22	4.30E-01	1.53	4	20	70	FRE
178	1095B	2H	5	71	99.21	–43.9	35.6	0.21	1.67E-01	6.77	4	20	60	FRE
178	1095B	2H	5	146	99.96	–47	125.6	8.81	3.30E-02	9.78	4	20	80	FRE
178	1095B	3H	1	76	102.76	51.3	355.5	3.37	1.35E-01	2.96	4	30	80	FRE
178	1095B	3H	1	146	103.46	21.8	318	7.73	2.98E-02	11.61	4	30	80	FRE
178	1095B	3H	2	141	104.91	21.7	281.4	1.38	2.08E-01	2.14	4	40	80	FRE
178	1095B	3H	3	78	105.78	52.5	359.2	0.58	4.42E-01	0.31	4	30	80	FRE
178	1095B	3H	3	141	106.41	69.8	346.2	0.58	4.45E-01	1.16	4	30	80	FRE
178	1095B	3H	4	73	107.23	57.7	332.1	2.48	7.46E-01	1.19	4	20	80	FRE
178	1095B	3H	4	146	107.96	81.5	166.4	1.53	8.90E-01	4.89	4	40	80	FRE
178	1095B	3H	5	71	108.71	77.8	291.9	1.06	1.46E-01	1.44	4	20	70	FRE
178	1095B	3H	5	146	109.46	73.5	346.6	4.15	1.44E-01	15.58	4	20	80	FRE
178	1095B	3H	6	71	110.21	60.9	271.3	10.93	4.85E-03	86.36	4	50	80	FRE
178	1095B	3H	6	144	110.94	27.1	11.5	2.88	5.06E-02	8.75	4	20	80	FRE
178	1095B	3H	7	71	111.71	57.6	79.5	3.48	2.57E-01	1.43	4	40	80	FRE
178	1095B	4H	1	139	112.89	73.7	247.1	2.17	3.40E-01	4.48	4	30	80	FRE
178	1095B	4H	2	59	113.59	31.7	265.8	5.39	6.09E-02	6.9	4	50	80	FRE
178	1095B	4H	2	141	114.41	30.3	291.6	3.39	2.12E-01	5.97	4	30	70	FRE

Table T27 (continued).

Leg	Site	Core	Section	Interval (cm)	Depth (mbsf)	Inclination (°)	Declination (°)	MAD	Length	Devang	Steps	Low	High	Option
178	1095B	4H	3	74	115.24	–66.4	304.4	3.1	1.04E-01	29.86	4	30	60	FRE
178	1095B	4H	3	146	115.96	48.1	306.5	8.46	1.97E-01	5.48	4	50	80	FRE
178	1095B	4H	4	71	116.71	–51.6	337.1	8.63	7.97E-02	41.23	4	20	80	FRE
178	1095B	4H	5	45	117.95	77.4	137.1	2.79	3.04E-01	5.07	4	20	80	FRE
178	1095B	4H	6	72	119.72	64.6	308.5	0.68	1.98E-01	3.57	4	20	70	FRE
178	1095B	4H	6	146	120.46	77.6	316.7	4.02	1.64E-01	5.41	4	20	80	FRE
178	1095B	4H	CC	9	121.11	33.1	199.9	3.12	5.51E-02	4.6	4	20	80	FRE
178	1095B	5H	1	71	121.71	–73.3	300.8	1.46	2.11E-01	16.26	4	20	80	FRE
178	1095B	5H	1	146	122.46	57.7	302.8	3.54	7.24E-02	7.65	4	50	80	FRE
178	1095B	5H	2	71	123.21	19.9	72.6	1.38	3.26E-01	6.77	4	40	70	FRE
178	1095B	5H	2	146	123.96	72.1	59.1	4.05	1.87E-01	33.94	4	40	70	FRE
178	1095B	5H	3	71	124.71	54.3	217.4	2.68	1.03E-01	3.64	4	20	80	FRE
178	1095B	5H	3	146	125.46	71	308.7	9.81	5.97E-02	64.13	4	40	80	FRE
178	1095B	5H	4	71	126.21	55.8	199.4	12.35	5.48E-03	142.18	4	50	80	FRE
178	1095B	5H	4	146	126.96	–71.2	25.9	4.56	5.10E-03	13.26	4	30	80	FRE
178	1095B	5H	5	71	127.71	–59	82.2	4.32	2.11E-02	7.32	4	20	80	FRE
178	1095B	5H	5	145	128.45	–66.9	56.2	0.63	3.03E-01	1.3	4	40	80	FRE
178	1095B	5H	6	71	129.21	–67.6	353.7	2.86	5.39E-01	7.4	4	30	70	FRE
178	1095B	5H	6	141	129.91	–61.8	78.7	1.32	7.97E-01	7.11	4	30	80	FRE
178	1095B	6H	1	147	131.97	–34.7	227.5	1.52	1.70E-01	9.94	4	40	70	FRE
178	1095B	6H	2	63	132.63	–51.7	243.1	1.4	4.45E-01	8.09	4	20	80	FRE
178	1095B	6H	2	145	133.45	–40	312.5	2.99	2.71E-01	11.39	4	30	80	FRE
178	1095B	6H	3	72	134.22	–53.8	313	6.96	1.39E-01	19.24	4	20	80	FRE
178	1095B	6H	3	138	134.88	–75.1	235.8	14.33	2.95E-03	5.47	4	20	80	FRE
178	1095B	6H	4	73	135.73	78.7	96	4.92	2.34E-02	3.48	4	20	80	FRE
178	1095B	6H	4	147	136.47	17	115.7	24.67	1.80E-03	105.86	4	50	80	FRE
178	1095B	6H	5	61	137.11	75.7	144.9	0.52	1.68E-01	3.24	4	20	80	FRE
178	1095B	6H	5	136	137.86	79.9	153.7	2.09	2.03E-01	1.4	4	20	60	FRE
178	1095B	6H	6	53	138.53	85	101.8	0.89	5.95E-02	3.59	4	20	60	FRE
178	1095B	6H	7	47	139.47	78.1	14.2	5.91	3.85E-01	8.49	4	20	60	FRE
178	1095B	7H	3	71	143.68	–76.1	352.3	1.72	4.41E-01	1.36	4	20	60	FRE
178	1095B	7H	3	147	144.44	–29.2	7.8	13.15	5.42E-03	63.61	4	30	60	FRE
178	1095B	7H	4	71	145.18	–60.1	276.4	2.65	1.32E-01	1.43	4	30	60	FRE
178	1095B	7H	4	146	145.93	–64	13.1	1.09	6.55E-01	1.13	4	20	60	FRE
178	1095B	7H	5	61	146.58	–69.3	19.6	1.16	7.24E-01	0.71	4	20	60	FRE
178	1095B	7H	5	141	147.38	–73.6	357.5	0.43	8.11E-01	0.55	4	30	60	FRE
178	1095B	7H	6	62	148.09	–84.1	224.4	0.64	1.86E-01	0.49	4	20	60	FRE
178	1095B	7H	6	147	148.94	77.8	51	0.52	5.10E-01	0.44	4	20	60	FRE
178	1095B	7H	7	26	149.23	48.2	175.6	15.32	2.02E-03	86.19	4	20	60	FRE
178	1095B	8H	1	131	150.81	20.4	28.7	24.81	3.56E-03	110.18	4	30	60	FRE
178	1095B	8H	2	61	151.61	–79.4	8.1	1.78	1.66E-01	2.57	4	20	60	FRE
178	1095B	8H	2	146	152.46	61.7	201.7	1.81	1.89E-01	1.39	4	20	60	FRE
178	1095B	8H	3	63	153.13	24	103.4	15.62	5.46E-02	5.88	4	20	60	FRE
178	1095B	8H	3	146	153.96	76.7	284.1	1.69	2.48E-01	3.55	4	20	60	FRE
178	1095B	8H	4	73	154.73	56.8	232.2	0.8	4.79E-01	0.59	4	20	60	FRE
178	1095B	8H	4	145	155.45	86.5	346.6	0.77	5.32E-01	1.17	4	20	60	FRE
178	1095B	8H	5	55	156.05	79.4	320.8	0.5	6.29E-01	0.76	4	20	60	FRE
178	1095B	8H	5	145	156.95	66.7	214.6	0.33	9.67E-01	0.75	4	20	60	FRE
178	1095B	8H	6	71	157.71	76.4	204.3	0.15	1.25E+00	0.83	4	20	60	FRE
178	1095B	8H	6	145	158.45	71.9	146.2	0.26	1.14E+00	0.62	4	20	60	FRE
178	1095B	9H	1	143	160.43	51	119.8	6.85	6.58E-02	9.82	4	20	60	FRE
178	1095B	9H	2	71	161.21	76.7	18.2	7.07	5.10E-02	5.74	4	20	60	FRE
178	1095B	9H	2	131	161.81	6	96.6	7.37	3.72E-02	6.97	4	30	60	FRE
178	1095B	9H	3	71	162.71	46.5	157.8	9.36	4.31E-02	19.09	4	20	60	FRE
178	1095B	9H	3	131	163.31	–25.5	182.2	2.98	2.31E-02	9.09	4	20	60	FRE
178	1095B	9H	4	131	164.81	34.1	242.7	40.26	2.90E-03	63.62	4	30	60	FRE
178	1095B	9H	5	76	165.76	–72.8	352.3	18.19	1.49E-03	28.62	4	30	60	FRE
178	1095B	9H	5	141	166.41	15.5	334.9	39.76	2.95E-03	106.61	4	30	60	FRE
178	1095B	9H	6	76	167.26	–60.6	310.8	16.35	1.18E-03	19.49	4	30	60	FRE
178	1095B	9H	6	141	167.91	–76.9	170	11.03	2.70E-03	16.09	4	30	60	FRE
178	1095B	9H	7	38	168.38	–11.1	177.9	33.09	1.59E-03	74.21	4	30	60	FRE
178	1095B	10H	1	146	169.96	–48.8	137.9	18.15	1.42E-03	42.2	4	30	60	FRE
178	1095B	10H	2	74	170.74	–46.7	350.7	35.01	9.92E-04	60.3	4	30	60	FRE
178	1095B	10H	2	144	171.44	–84.1	304.9	5.87	3.04E-03	13.96	4	20	60	FRE
178	1095B	10H	3	73	172.23	–47.1	91.4	1.53	5.23E-02	6.3	4	30	60	FRE
178	1095B	10H	3	145	172.95	–67.8	135.5	9.17	1.35E-02	3.81	4	30	60	FRE
178	1095B	10H	4	75	173.75	–69.3	243.5	4.78	2.98E-02	6.3	4	20	60	FRE
178	1095B	10H	4	146	174.46	–48.3	158	25.94	1.32E-03	27.83	4	30	60	FRE
178	1095B	10H	5	75	175.25	–66.7	126.7	9.04	3.30E-03	2.69	4	30	60	FRE

Table T27 (continued).

Leg	Site	Core	Section	Interval (cm)	Depth (mbsf)	Inclination (°)	Declination (°)	MAD	Length	Devang	Steps	Low	High	Option
178	1095B	10H	5	145	175.95	–39.6	159.7	5.49	1.36E-02	10.46	4	20	60	FRE
178	1095B	10H	6	73	176.73	–37.5	310.3	3.59	4.57E-02	5.48	4	30	60	FRE
178	1095B	10H	6	131	177.31	–48	40.2	5.13	3.84E-02	13.47	4	30	60	FRE
178	1095B	11H	1	71	178.71	60.4	316.2	8.52	3.28E-03	33.66	4	20	60	FRE
178	1095B	11H	1	146	179.46	65	27.2	19.72	2.99E-03	21.69	4	30	60	FRE
178	1095B	11H	2	71	180.21	75.6	130.4	7.26	2.23E-01	4.05	4	20	60	FRE
178	1095B	11H	2	146	180.96	80.5	287.4	5.45	4.15E-02	12.52	4	20	60	FRE
178	1095B	11H	3	71	181.71	65.8	154.2	5.09	3.07E-02	3.87	4	20	60	FRE
178	1095B	11H	3	146	182.46	87.7	12	3.87	1.33E-02	9.97	4	20	60	FRE
178	1095B	11H	4	71	183.21	81.6	158.9	1.18	1.86E-01	5.87	4	30	60	FRE
178	1095B	11H	4	146	183.96	85.5	13.1	9.41	4.32E-03	44.6	4	20	60	FRE
178	1095B	11H	5	75	184.75	39.5	140.1	5.74	2.42E-01	1.32	4	20	60	FRE
178	1095B	11H	5	146	185.46	75	120	1.42	5.95E-01	2.93	4	20	60	FRE
178	1095B	11H	6	71	186.21	40.8	145.8	0.85	5.17E-01	2.4	4	20	60	FRE
178	1095B	11H	6	146	186.96	52.3	143.2	2.28	4.89E-01	2.24	4	20	60	FRE
178	1095B	12H	1	71	188.21	–83.8	89	37.22	2.38E-03	140.9	4	30	60	FRE
178	1095B	12H	1	146	188.96	48	331.8	1.41	2.26E-01	0.46	4	20	60	FRE
178	1095B	12H	2	74	189.74	83.9	32.8	1.55	1.40E-01	3.2	4	20	60	FRE
178	1095B	12H	2	146	190.46	79.7	304.9	2.01	2.99E-01	0.76	4	20	60	FRE
178	1095B	12H	3	76	191.26	80.8	358.5	0.43	6.94E-01	0.13	4	20	60	FRE
178	1095B	12H	3	142	191.92	71.1	357.2	0.2	1.17E+00	0.28	4	20	60	FRE
178	1095B	12H	4	51	192.51	79.8	299.7	1.78	1.32E-01	6.27	4	30	60	FRE
178	1095B	12H	4	146	193.46	65.1	3.8	10.07	1.55E-02	36.69	4	20	60	FRE
178	1095B	12H	5	79	194.29	28.9	13	1.95	5.38E-02	6.07	4	20	60	FRE
178	1095B	12H	5	146	194.96	35.9	62.4	2.52	2.23E-01	5.04	4	20	60	FRE
178	1095B	12H	6	73	195.73	–46.6	341.3	3.34	1.51E-01	9.7	4	20	60	FRE
178	1095B	12H	6	149	196.49	–38	346.3	5.93	1.19E-01	11.31	4	20	60	FRE
178	1095B	13H	2	81	198.23	40.6	41.2	0.71	1.84E-01	0.3	4	20	60	FRE
178	1095B	13H	3	70	199.62	62.7	74.8	1.08	1.45E-01	0.55	4	20	60	FRE
178	1095B	13H	4	62	201.04	65.2	89.2	0.74	1.57E-01	1.29	4	20	60	FRE
178	1095B	13H	4	145	201.87	82.4	221.4	1.61	2.18E-01	1.17	4	20	60	FRE
178	1095B	13H	5	71	202.63	80.7	26.9	7.08	3.97E-03	30.72	4	20	60	FRE
178	1095B	14X	1	71	205.71	3.1	139.1	9.55	6.12E-03	49.32	4	20	60	FRE
178	1095B	14X	2	140	207.85	42.8	336.6	3.19	1.00E-01	10.62	4	20	60	FRE
178	1095B	14X	3	120	209.15	74.3	137.5	5.79	6.01E-02	10.01	4	20	60	FRE
178	1095B	14X	4	71	210.16	–65.4	177.3	20.55	2.47E-02	33.77	4	20	60	FRE
178	1095B	14X	4	135	210.8	–64.9	262.9	4.28	2.32E-01	9.41	4	20	60	FRE
178	1095B	15X	1	61	215.31	–74	311.6	1.81	6.14E-02	0.84	4	20	60	FRE
178	1095B	15X	1	137	216.07	–78.5	246.6	0.4	1.58E-01	0.5	4	30	60	FRE
178	1095B	15X	2	135	217.55	–74.4	263.2	1.15	7.78E-02	2.77	4	20	60	FRE
178	1095B	16X	1	72	225.02	49.4	132.8	1.57	1.19E-01	2.18	4	20	60	FRE
178	1095B	16X	2	71	226.51	19.2	340.3	5.84	1.28E-01	10.58	4	30	60	FRE
178	1095B	16X	2	138	227.18	43.9	250.1	1.62	1.23E-01	3.12	4	20	60	FRE
178	1095B	16X	3	65	227.95	16.1	183.2	2.25	3.24E-01	3.23	4	20	60	FRE
178	1095B	17X	1	95	234.85	37.9	11.9	2.66	5.79E-02	3.91	4	30	60	FRE
178	1095B	17X	2	71	236.11	51.3	236.2	1.03	1.46E-01	1.37	4	30	60	FRE
178	1095B	17X	2	143	236.83	72.9	137.1	0.96	1.79E-01	1.02	4	20	60	FRE
178	1095B	17X	3	74	237.64	41.6	236.1	3.49	6.04E-02	9.67	4	20	60	FRE
178	1095B	17X	3	137	238.27	52.4	244.8	1.67	2.19E-01	10.22	4	20	60	FRE
178	1095B	17X	4	78	239.18	43.8	176.8	1.48	2.66E-01	1.02	4	20	60	FRE
178	1095B	17X	6	66	242.06	–58.4	337.3	1.06	1.28E-01	2.48	4	30	60	FRE
178	1095B	17X	7	28	243.18	–48.7	108.5	18.56	2.48E-03	15.66	4	20	60	FRE
178	1095B	18X	1	73	244.25	–71.1	314.1	18.21	2.00E-02	8.15	4	30	60	FRE
178	1095B	18X	1	146	244.96	–14.4	327.6	12	2.89E-02	35.99	4	20	50	FRE
178	1095B	18X	2	71	245.71	1.7	304.9	1.61	3.09E-01	19.58	4	20	60	FRE
178	1095B	18X	2	146	246.46	–13.5	1.8	4.22	2.18E-01	15.69	4	30	60	FRE
178	1095B	18X	3	69	247.19	–47.1	143.3	3.78	7.49E-02	7.83	4	20	60	FRE
178	1095B	18X	4	74	248.74	–64.5	325.8	0.77	5.14E-01	0.93	4	20	60	FRE
178	1095B	18X	4	125	249.25	–72.8	340.7	1.69	1.21E-01	1.77	4	20	60	FRE
178	1095B	18X	5	73	250.2	–1.3	62.8	6.07	2.75E-02	16.45	4	20	60	FRE
178	1095B	18X	5	143	250.93	–1.5	271.3	3.59	3.41E-02	24.62	4	20	60	FRE
178	1095B	18X	6	71	251.71	–50.5	203.7	11.34	4.86E-02	7.66	4	30	60	FRE
178	1095B	18X	7	31	252.81	–82.2	219.6	1.24	2.07E-01	0.17	4	20	60	FRE
178	1095B	20X	1	56	263.26	77.4	237.2	3.11	3.65E-01	1.96	4	20	60	FRE
178	1095B	20X	1	135	264.05	59.8	222.6	4.84	3.70E-02	0.24	4	20	60	FRE
178	1095B	20X	2	61	264.81	73.5	355.9	3.04	2.68E-02	5.77	4	20	60	FRE
178	1095B	20X	3	140	267.1	64.6	104.1	1.28	1.77E-01	0.43	4	30	60	FRE
178	1095B	20X	4	72	267.92	63.6	263.2	0.95	3.25E-01	0.96	4	20	60	FRE
178	1095B	20X	4	141	268.61	63	224	1.25	1.88E-01	1.42	4	20	60	FRE

Table T27 (continued).

Leg	Site	Core	Section	Interval (cm)	Depth (mbsf)	Inclination (°)	Declination (°)	MAD	Length	Devang	Steps	Low	High	Option
178	1095B	20X	5	59	269.29	79.4	322.3	2.67	8.46E-02	4.54	4	20	60	FRE
178	1095B	20X	6	34	270.54	64.2	339	1.61	1.19E-01	1.85	4	30	60	FRE
178	1095B	21X	1	8	272.48	68.1	172.6	1.62	2.28E-01	1.22	4	30	60	FRE
178	1095B	21X	2	64	274.54	44.2	273.2	1.93	1.31E-01	1.63	4	30	60	FRE
178	1095B	21X	3	28	275.68	30	240.9	1.08	2.47E-01	1.06	4	20	60	FRE
178	1095B	21X	3	146	276.86	51.9	308	6.89	1.17E-02	15.6	4	30	60	FRE
178	1095B	21X	4	91	277.81	–0.3	270.3	16.74	2.52E-02	13.83	4	30	60	FRE
178	1095B	21X	5	57	278.97	75.5	240.2	1.53	7.82E-02	3.68	4	30	60	FRE
178	1095B	21X	6	54	280.44	–20.7	48.9	2.9	9.89E-02	3.19	4	20	60	FRE
178	1095B	21X	7	19	281.59	64.8	78.2	1.51	2.69E-01	1.23	4	20	60	FRE
178	1095B	22X	2	122	284.82	56.1	214.8	0.78	1.88E-01	0.33	4	20	60	FRE
178	1095B	22X	3	79	285.89	–2.7	271.8	0.59	3.25E-01	0.79	4	20	60	FRE
178	1095B	22X	4	107	287.67	59.4	142.6	4.01	8.41E-02	12.75	4	20	60	FRE
178	1095B	23X	3	14	294.84	–62.3	322.1	1.55	1.16E-01	1.67	4	30	60	FRE
178	1095B	24X	3	143	305.73	–17.2	32.1	5.28	6.68E-02	1.65	4	20	60	FRE
178	1095B	25X	4	143	316.83	65.4	136.2	0.21	4.67E-01	0.76	4	20	60	FRE
178	1095B	26X	4	112	326.22	78	15.6	0.84	2.06E-01	1.34	4	20	60	FRE
178	1095B	30X	3	55	362.75	68.1	284.8	2.32	2.39E-01	0.79	4	30	60	FRE
178	1095B	31X	1	65	369.45	54	81.8	6.18	2.28E-02	5.28	4	20	60	FRE
178	1095B	31X	5	81	375.61	23.2	325.8	3.82	7.22E-02	10.16	4	20	60	FRE
178	1095B	32X	3	68	382.08	79.7	161.6	0.46	3.60E-01	1.44	4	20	60	FRE
178	1095B	32X	6	79	386.69	70.3	163.4	2.78	1.38E-01	2.85	4	20	60	FRE
178	1095B	33X	3	61	391.31	61.3	72.6	0.53	1.83E-01	1.62	4	20	60	FRE
178	1095B	34X	1	27	397.57	80	89.3	0.38	7.52E-01	0.83	4	20	80	FRE
178	1095B	34X	1	51	397.81	67.5	129.1	0.55	4.10E-01	1.57	4	20	80	FRE
178	1095B	34X	1	77	398.07	66.4	145.8	0.55	4.03E-01	2.23	4	20	80	FRE
178	1095B	34X	1	108	398.38	63.6	134	0.9	5.74E-01	2.85	4	20	80	FRE
178	1095B	34X	1	134	398.64	62.7	157.3	0.27	2.15E-01	1.09	4	30	70	FRE
178	1095B	34X	1	135	398.65	64.8	157	1.45	5.91E-01	3.01	4	20	80	FRE
178	1095B	34X	1	139	398.69	68.6	17.4	0.36	8.34E-01	1.29	4	20	70	FRE
178	1095B	34X	2	4	398.84	85.4	154.5	0.84	3.93E-01	1.65	4	30	80	FRE
178	1095B	34X	2	46	399.26	–66.4	129.5	12.51	1.15E-02	142.11	4	40	80	FRE
178	1095B	34X	2	51	399.31	65.1	240.6	7.77	3.89E-02	5.12	4	30	80	FRE
178	1095B	34X	2	64	399.44	72	167.6	1.74	2.32E-01	2.64	4	20	60	FRE
178	1095B	34X	2	96	399.76	–51.1	109.1	4.66	4.70E-03	40.03	4	25	60	FRE
178	1095B	34X	2	107	399.87	–18	358.9	4.14	1.28E-02	173.6	4	30	80	FRE
178	1095B	34X	2	109	399.89	–3.3	271.7	5.67	6.89E-02	18.12	4	20	80	FRE
178	1095B	34X	2	112	399.92	–20.7	180	5.17	9.12E-03	85.58	4	20	80	FRE
178	1095B	34X	2	118	399.98	–79.6	339.4	0.78	3.41E-01	5.98	4	30	80	FRE
178	1095B	34X	2	120	400	–80.7	293.2	0.49	4.86E-01	1.9	4	15	80	FRE
178	1095B	34X	2	130	400.1	–74.2	58.4	1.45	3.81E-01	1.03	4	30	80	FRE
178	1095B	34X	2	149	400.29	–9.2	270.5	3.87	7.98E-02	15.7	4	20	80	FRE
178	1095B	34X	3	47	400.77	–41.6	326.3	1.96	1.13E-01	9.12	4	15	80	FRE
178	1095B	34X	3	74	401.04	–66.3	301.5	0.48	1.90E-01	0.92	4	20	50	FRE
178	1095B	34X	3	104	401.34	–75.8	179.3	0.37	5.95E-01	0.27	4	15	80	FRE
178	1095B	34X	4	35	402.15	–65.9	241.2	1	3.57E-01	0.49	7	20	80	FRE
178	1095B	34X	4	77	402.57	–81.9	303	1.21	3.93E-01	0.35	9	15	80	FRE
178	1095B	34X	4	93	402.73	–75.8	102.3	1.05	3.02E-01	3.82	4	20	70	FRE
178	1095B	34X	4	125	403.05	–58.8	24.2	0.51	3.52E-01	2.6	4	20	60	FRE
178	1095B	34X	5	55	403.85	–80.6	27.9	0.56	3.42E-01	3.54	4	20	60	FRE
178	1095B	34X	5	109	404.39	–79.6	107.8	0.2	5.27E-01	6.06	4	15	80	FRE
178	1095B	34X	5	125	404.55	–61.2	103.2	2.57	5.31E-02	12.67	4	20	80	FRE
178	1095B	34X	5	136	404.66	–85.6	251.2	1.32	1.94E-01	2.71	4	25	80	FRE
178	1095B	34X	5	147	404.77	–75.2	31.4	2.66	2.14E-01	3.76	7	15	80	FRE
178	1095B	34X	6	1	404.81	–62.9	339.3	4.91	1.56E-01	18.16	4	15	80	FRE
178	1095B	34X	6	31	405.11	74.2	33.3	0.64	3.19E-01	2.83	4	15	70	FRE
178	1095B	34X	6	107	405.87	85.6	223.5	0.43	1.58E-01	1.54	4	25	80	FRE
178	1095B	34X	6	132	406.12	67.6	345.2	0.82	1.96E-01	8.86	4	20	80	FRE
178	1095B	35X	4	59	411.69	–58.7	16.1	23.25	3.35E-02	25.83	4	30	60	FRE
178	1095B	36X	3	39	419.59	–80.2	233.1	1.26	6.74E-01	1.06	4	20	60	FRE

Note: This table is also available in ASCII format in the **TABLES** directory.

Table T28. Depths of geomagnetic reversals in Holes 1095A, 1095B, and 1095D.

Chron	Depth interval (mbsf)				Age (Ma)
	Hole 1095A	Hole 1095B	Hole 1095D	Hole 1095B (logging)	
C1n(o)	17.10-17.14		17.96-18.18		0.78
C1r.1n(t)	23.18-23.22				0.99
C1r.1n(o)	28.52-30.98				1.07
C2n(t)	58.82-61.96		58.84-58.88		1.77
C2n(o)	—				1.95
C2r.1n(t)	—				2.14
C2r.1n(o)	—				2.15
C2An.1n(t)	—				2.581
C2An.1n(o)	81.36-85.45				3.04
C2An.2n(t)					3.11
C2An.2n(o)					3.22
C2An.3n(t)					3.33
C2An.3n(o)		96.90-105.08			3.58
C3n.1n(t)		126.18-126.22		126.04-126.19	4.18
C3n.1n(o)		134.86-135.08		137.17-137.32	4.29
C3n.2n(t)		139.60-142.43		139.76-139.91	4.48
C3n.2n(o)		148.47-148.51		147.38-147.68	4.62
C3n.3n(t)		—		150.27-150.43	4.80
C3n.3n(o)		—		153.63-153.78	4.89
C3n.4n(t)		163.66-165.32		159.42-160.57	4.98
C3n.4n(o)		177.32-178.40		177.70-177.86	5.23
C3An.1n(t)		209.30-210.17		203.92-206.36	5.894
C3An.1n(o)		217.60-224.38		222.21-222.36	6.137
C3An.2n(t)		239.44-239.48		236.68-237.14	6.269
C3An.2n(o)		252.82-262.78		259.85-260.46	6.567
C3Bn(t)		292.02-292.06		293.83-293.99	6.935
C3Bn(o)		303.60-304.46		302.67-302.83	7.091
C3Br.1n(t)		—		304.96-305.11	7.135
C3Br.1n(o)		—		306.18-306.33	7.17
C3Br.2n(t)		—		—	7.341
C3Br.2n(o)		—		—	7.375
C4n.1n(t)		321.84-322.62		323.25-323.40	7.432
C4n.1n(o)		325.78-325.82		325.23-325.38	7.562
C4n.2n(t)		331.04-332.18		332.07-332.24	7.65
C4n.2n(o)		355.28-356.06		355.71-357.84	8.072
C4r.1n(t)		—		—	8.225
C4r.1n(o)		—		—	8.257
C4r.2r-1(t)		399.84-399.88		402.95-403.1	8.635
C4r.2r-1(o)		404.70-404.88		406.00-406.15	8.651
C4An(t)		411.70-411.74		413.77-413.90	8.699
C4An(o)		445.98-446.02		447.61-447.76	9.025
C4Ar.1n(t)		460.07-461.04		460.86-461.02	9.23
C4Ar.1n(o)				486.92-487.08	9.308
C4Ar.2n(t)				518.0	9.580
C4Ar.2n(o)				520.0	9.642
C5n.1n(t)				523.0	9.740
C5n.1n(o)				546.0	9.880
C5n.2n(t)				548.0	9.920

Notes: The depths of the geomagnetic reversals from the logging results have been shifted upward by 5 m to align them with the core depth scale. Ages after Cande and Kent (1995). (t) = termination, (o) = onset. — = chrons not interpreted in this interval.

Table T29. Results of headspace monitoring of hydrocarbon gases at Site 1095.

Core, section, interval (cm)	Depth (mbsf)	Methane C_1 (ppm)	Ethane C_2 (ppm)	C_1/C_2
178-1095A-				
1H-2, 0-5	1.46	125	0	
2H-2, 0-5	7.40	4	0	
4H-4, 0-5	25.30	3	0	
5H-3, 0-5	33.30	4	0	
6H-4, 0-5	44.30	2	0	
7H-4, 0-5	53.80	6	0	
8H-4, 0-5	63.30	4	0	
9H-4, 0-5	72.80	5	0	
10H-4, 0-5	82.30	4	0	
178-1095B-				
1H-4, 0-5	87.50	3	0	
2H-4, 0-5	97.00	4	0	
3H-4, 0-5	106.50	5	0	
4H-4, 0-5	116.00	6	0	
5H-4, 0-5	125.50	5	0	
6H-4, 0-5	135.00	4	0	
7H-4, 0-5	144.47	3	0	
8H-3, 0-5	152.50	3	0	
9H-4, 0-5	163.50	5	0	
10H-4, 0-5	173.00	1,010	1.3	777
11H-4, 0-5	182.50	2,050	3.3	620
12H-4, 0-5	192.00	2,580	3.2	806
13H-3, 0-5	198.92	1,730	2.1	823
14X-2, 0-5	206.45	3,070	4.0	769
15X-2, 100-105	217.20	3,340	3.3	1,011
16X-1, 89-94	225.19	5,980	7.2	830
17X-4, 0-5	238.40	12,280	12.4	990
18X-4, 0-5	248.00	12,220	17.6	694
20X-4, 0-5	267.20	5,230	6.0	871
21X-4, 0-5	276.90	9,960	9.0	1,107
22X-3, 0-5	285.10	15,370	15.7	979
23X-4, 0-5	296.20	12,200	10.8	1,130
24X-4, 0-5	305.80	11,660	10.3	1,132
25X-4, 0-5	315.40	8,570	7.6	1,128
26X-4, 0-5	325.10	5,280	6.4	824
27X-4, 0-5	334.70	6,380	7.8	818
28X-4, 0-5	344.30	6,300	7.3	863
29X-3, 0-5	352.50	9,690	11.4	850
30X-4, 0-5	363.70	11,840	13.3	890
31X-4, 0-5	373.30	9,020	9.9	912
32X-2, 0-5	379.90	11,750	12.4	947
33X-3, 0-5	390.70	7,950	10.4	764
34X-4, 0-5	401.80	8,760	10.4	842
35X-4, 0-5	411.10	10,850	12.2	889
36X-4, 0-5	420.70	7,290	9.0	810
37X-3, 0-5	428.80	17,020	22.2	766
38X-4, 0-5	440.00	10,660	15.5	688
39X-4, 0-5	449.60	22,010	35.9	613
40X-4, 0-5	459.30	12,490	13.3	939
41X-3, 0-5	467.50	8,370	15.9	527
42X-4, 0-5	478.60	9,470	14.2	667
43X-2, 0-5	484.80	13,040	19.3	676
44X-CC, 0-5	493.40	8,950	20.7	432
45X-1, 0-5	498.00	8,770	13.2	664
46X-1, 98-100	503.98	15,610	31.1	502
47X-1, 64-65	513.34	8,690	20.0	435
48X-1, 0-2	522.40	702	2.5	281
49X-1, 108-109	533.18	6,060	13.6	445
50X-2, 0-2	543.20	6,500	16.3	399
51X-1, 0-5	551.40	4,250	13.3	319
52X-1, 0-5	560.80	6,000	16.1	373

Table T30. Results of total and inorganic carbon analyses for Site 1095. (Continued on next two pages.)

Core, section, interval (cm)	Depth (mbsf)	IC (wt%)	$CaCO_3$ (wt%)	TC (wt%)	TOC (wt%)
178-1095A-					
1H-1, 76-77	0.76	0.02	0.15		
1H-3, 77-78	3.70	0.04	0.30	0.10	0.06
2H-1, 109-110	6.99	0.04	0.31		
2H-3, 111-112	10.01	0.02	0.17	0.04	0.02
2H-5, 16-17	12.06	0.03	0.26		
3H-4, 76-77	15.66	0.11	0.88	0.32	0.21
4H-1, 140-141	22.20	0.08	0.63	0.29	0.21
4H-3, 114-115	24.94	0.03	0.23	0.17	0.14
4H-5, 73-76	27.53	0.15	1.24		
5H-1, 128-129	31.58	0.03	0.24		
5H-3, 26-27	33.56	0.02	0.19	0.07	0.05
5H-3, 100-101	34.30	0.03	0.22		
5H-5, 110-111	37.40	0.07	0.61		
6H-1, 76-78	40.56	0.03	0.26		
6H-2, 74-76	42.04	0.02	0.20		
6H-3, 79-81	43.59	0.01	0.12	0.12	0.11
6H-5, 88-89	46.68	0.08	0.66		
6H-6, 82-83	48.12	0.01	0.05		
7H-1, 100-102	50.30	0.03	0.27		
7H-3, 76-77	53.06	0.03	0.23	0.17	0.14
7H-5, 45-46	55.75	0.05	0.41		
8H-1, 81-82	59.61	0.03	0.26		
8H-2, 96-97	61.26	0.02	0.13		
8H-3, 108-109	62.88	0.04	0.30	0.16	0.13
8H-4, 50-51	63.80	0.05	0.43		
8H-5, 123-124	66.03	0.04	0.29		
8H-6, 74-75	67.04	0.03	0.29		
8H-7, 43-44	68.23	0.03	0.22		
9H-1, 116-117	69.46	0.04	0.30		
9H-2, 92-93	70.72	0.05	0.41		
9H-3, 43-44	71.73	0.04	0.32	0.20	0.17
9H-4, 59-60	73.39	0.05	0.43		
9H-5, 62-63	74.92	0.03	0.26		
9H-6, 26-27	76.06	0.04	0.31		
9H-7, 15-16	77.45	0.05	0.45		
10H-1, 108-109	78.88	0.06	0.47		
10H-3, 75-76	81.55	0.04	0.32	0.13	0.09
10H-4, 73-74	83.03	0.02	0.15		
10H-5, 68-69	84.48	0.05	0.42		
10H-6, 52-53	85.82	0.04	0.33		
178-1095B-					
1H-1, 96-97	83.96	0.03	0.22		
1H-3, 96-97	86.96	0.04	0.35	0.36	0.32
1H-5, 44-45	89.44	0.02	0.14		
2H-1, 100-101	93.50	0.03	0.29		
2H-3, 36-37	95.86	0.06	0.54	0.36	0.29
2H-5, 35-36	98.85	0.03	0.27		
4H-6, 139-140	120.39	0.03	0.26	0.19	0.16
5H-1, 49-50	121.49	0.05	0.40		
5H-3, 109-110	125.09	0.04	0.32	0.11	0.07
5H-5, 85-86	127.85	0.06	0.46		
6H-1, 93-94	131.43	0.07	0.61		
6H-3, 78-79	134.28	0.04	0.34	0.22	0.18
6H-4, 43-44	135.43	0.06	0.46		
6H-5, 70-71	137.20	0.05	0.42		
6H-7, 26-27	139.26	0.03	0.26		
7H-2, 125-126	142.72	0.03	0.24		
7H-4, 108-109	145.55	0.04	0.30	0.53	0.49
7H-5, 106-107	147.03	0.05	0.44		
7H-6, 105-106	148.52	0.04	0.36		
8H-1, 85-86	150.35	0.04	0.35		
8H-3, 87-88	153.37	0.04	0.37	0.23	0.19
8H-5, 67-68	156.17	0.05	0.40		
9H-1, 42-43	159.42	0.04	0.35		
9H-2, 41-42	160.91	0.05	0.41		

Table T30 (continued).

Core, section, interval (cm)	Depth (mbsf)	IC (wt%)	$CaCO_3$ (wt%)	TC (wt%)	TOC (wt%)
9H-3, 87-88	162.87	0.07	0.60	0.32	0.25
9H-4, 79-80	164.29	0.04	0.37		
9H-5, 63-64	165.63	0.05	0.39		
9H-6, 62-63	167.12	0.11	0.89		
9H-7, 42-43	168.42	0.04	0.37		
10H-1, 66-67	169.16	0.04	0.35		
10H-3, 66-67	172.16	0.12	0.98	0.48	0.36
10H-5, 66-67	175.16	0.04	0.36		
11H-1, 87-88	178.87	0.04	0.32		
11H-3, 86-87	181.86	0.03	0.27	0.24	0.21
11H-5, 86-87	184.86	0.16	1.36		
12H-1, 66-67	188.16	0.04	0.31		
12H-3, 71-72	191.21	0.03	0.28	0.28	0.25
12H-5, 64-65	194.14	0.04	0.30		
13H-2, 83-84	198.25	0.05	0.46		
13H-4, 77-78	201.19	0.06	0.51	0.32	0.26
14X-1, 43-44	205.43	0.04	0.34		
14X-4, 60-61	210.05	0.04	0.37	0.13	0.09
15X-1, 86-87	215.56	0.06	0.53		
18X-1, 19-20	243.69	0.05	0.43		
18X-3, 35-36	246.85	0.05	0.45		
18X-5, 120-121	250.70	0.05	0.40		
21X-1, 138-139	273.78	0.06	0.46		
21X-2, 81-82	274.71	0.06	0.50		
21X-4, 121-122	278.11	0.05	0.40		
21X-5, 71-72	279.11	0.08	0.71		
21X-6, 25-26	280.15	0.07	0.58		
21X-7, 25-26	281.65	0.05	0.39		
22X-1, 133-134	283.43	0.05	0.42		
22X-2, 127-128	284.87	0.06	0.52		
22X-3, 40-41	285.50	0.05	0.46		
22X-4, 59-60	287.19	0.05	0.40		
23X-1, 70-71	292.40	0.05	0.45		
23X-3, 59-60	295.29	0.09	0.71		
23X-5, 35-36	298.05	0.66	5.47		
24X-1, 39-40	301.69	0.16	1.32		
24X-3, 39-40	304.69	0.06	0.50		
24X-5, 34-35	307.64	0.04	0.36		
24X-6, 62-63	309.42	0.05	0.39		
25X-1, 37-38	311.27	0.03	0.26		
25X-3, 77-78	314.67	0.06	0.46		
25X-5, 48-49	317.38	0.06	0.47		
25X-7, 39-40	320.29	0.05	0.42		
26X-1, 70-71	321.30	0.05	0.41		
26X-3, 20-21	323.80	0.03	0.28		
26X-5, 46-47	327.06	0.04	0.30		
26X-7, 19-20	329.79	0.09	0.73		
27X-1, 28-29	330.48	0.05	0.38		
27X-3, 24-25	333.44	0.05	0.44		
27X-5, 31-32	336.51	0.05	0.46		
29X-1, 7-8	349.57	0.10	0.86		
29X-2, 51-53	351.51	0.04	0.33		
29X-3, 79-80	353.29	0.05	0.40		
29X-4, 97-98	354.97	0.06	0.51		
29X-5, 130-131	356.80	0.06	0.50		
29X-6, 100-101	358.00	0.03	0.29		
30X-1, 96-97	360.16	0.05	0.43		
30X-3, 88-89	363.08	0.04	0.37		
30X-5, 52-53	365.72	0.03	0.27		
33X-1, 60-61	388.30	0.05	0.38		
33X-4, 14-15	392.34	0.05	0.40		
33X-6, 54-55	395.74	0.04	0.32		
34X-2, 35-36	399.15	0.04	0.33		
34X-3, 30-31	400.60	0.11	0.94		
34X-5, 87-88	404.17	0.05	0.41		
35X-1, 123-124	407.83	0.11	0.94		
35X-3, 78-79	410.38	0.06	0.54		
35X-5, 40-41	413.00	0.05	0.42		
36X-2, 47-48	418.17	0.05	0.39		

Table T30 (continued).

Core, section, interval (cm)	Depth (mbsf)	IC (wt%)	$CaCO_3$ (wt%)	TC (wt%)	TOC (wt%)
36X-6, 94-95	424.64	0.05	0.43		
37X-1, 128-129	427.08	0.04	0.33		
37X-3, 96-97	429.76	0.12	0.99		
38X-1, 36-37	435.86	0.05	0.41		
38X-3, 75-76	439.25	0.05	0.40		
38X-5, 103-104	442.53	0.05	0.45		
39X-1, 124-125	446.34	0.04	0.30		
39X-3, 98-99	449.08	0.07	0.58		
39X-5, 136-137	452.46	0.04	0.30		
40X-1, 59-60	455.39	0.09	0.78		
40X-3, 27-28	458.07	0.04	0.41		
40X-5, 8-10	460.88	0.03	0.29		
41X-1, 113-114	465.63	0.08	0.64		
41X-4, 99-100	469.99	0.04	0.33		
41X-6, 43-44	472.43	0.05	0.45		
42X-1, 18-19	474.28	0.08	0.64		
42X-3, 12-13	477.22	0.04	0.36		
42X-5, 30-31	480.40	0.06	0.52		
43X-1, 33-34	484.13	0.06	0.51		
45X-1, 81-82	498.81	0.04	0.31		
46X-1, 46-47	503.46	0.13	1.04		
47X-1, 60-60	513.30	0.08	0.67		
48X-1, 69-70	523.09	0.02	0.17		
49X-1, 51-52	532.61	0.05	0.41		
52X-1, 34-35	561.14	0.06	0.50		

Note: IC = inorganic carbon, $CaCO_3$ = calcium carbonate, TC = total carbon, TOC = total organic carbon.

Table T31. Results of interstitial water analyses for Holes 1095A and 1095B.

Core, section, interval (cm)	Depth (mbsf)	pH	Salinity	Cl^- (mM)	Alkalinity (mM)	NH_4^+ (mM)	$Si(OH)_4$ (mM)	SO_4^{2-} (mM)	Mn^{2+} (μM)	PO_4^{3-} (μM)	F^- (μM)	Ca^{2+} (mM)	Mg^{2+} (mM)	K^+ (mM)	Sr^{2+} (μM)
178-1095A-															
1H-1, 145-150	1.45	7.4	35	559	2.80	0.00	0.38	30.6	3	6.8	71.1	10.5	54.3	11.6	87
1H-4, 123-128	5.66	7.7	35	559	3.00	0.02	0.44	30.6	32	7.7	67.0	9.4	51.2	10.7	87
2H-1, 145-150	7.35	7.3	35	557	3.17	0.06	0.43	30.2	40	9.2	61.2	10.8	51.0	10.2	88
2H-2, 145-150	8.85	7.7	35	559	3.32	0.06	0.50	27.6	54	8.4	60.3	9.6	46.9	10.8	88
4H-3, 145-150	25.25	7.6	35	559	4.11	0.17	0.53	24.8	120	8.3	38.9	10.8	44.6	9.5	88
7H-3, 145-150	53.75	7.6	34	556	5.77	0.38	0.87	17.9	86	3.8	25.5	12.6	40.1	9.6	90
10H-3, 145-150	82.25	8.2	33	556	7.03	0.53	0.88	8.0	60	6.0	16.0	12.2	36.0	9.1	104
178-1095B-															
3H-3, 145-150	106.45	7.9	32	556	7.27	0.64	0.96	5.4	58	5.0	10.3	12.0	31.0	6.9	104
6H-3, 145-150	134.95	7.8	32	552	7.14	0.92	1.05	2.2	28	4.0	9.4	11.6	29.2	7.6	112
9H-3, 145-150	163.45	7.8	32	551	7.07	1.00	1.08	0.0	10	4.9	8.5	11.7	26.4	5.5	120
12H-3, 145-150	191.95	8.0	32	552	6.35	1.13	0.96	0.0	12	2.9	9.3	12.9	27.6	6.9	119
16X-1, 84-89	225.14	7.9	32	548	6.12	1.26	0.92	0.6	13	2.8	10.5	15.0	27.3	6.5	125
20X-3, 145-150	267.15	7.9	32	548	5.33	1.08	0.86	1.6	14	3.3	10.0	18.4	24.5	5.2	138
23X-3, 145-150	296.15	7.7	31	549	4.79	1.30	1.02	0.0	13	3.3	10.3	23.8	25.3	5.3	145
26X-3, 145-150	325.05	8.0	31	545	4.28	1.29	0.78	1.8	13	3.2	14.4	25.7	23.6	5.6	141
29X-2, 145-150	352.45	7.7	31	549	3.94	1.26	1.09	0.0	23	3.2	10.8	30.5	20.6	4.7	147
32X-1, 145-150	379.85	7.7	31	544	3.36	1.26	1.03	1.5	25	—	11.3	32.0	21.3	4.7	138
35X-3, 145-150	411.05	7.8	32	546	3.42	1.28	0.94	0.1	27	3.0	15.1	36.6	15.5	3.9	144
38X-3, 145-150	439.95	7.8	32	544	2.95	1.21	0.84	0.5	30	3.0	8.3	48.7	16.6	3.4	140
41X-2, 140-150	467.40	7.9	32	544	2.92	1.12	0.86	1.7	39	2.7	10.6	56.9	17.4	3.7	129
46X-1, 90-98	503.90	7.9	32	544	1.51	1.08	0.70	1.4	30	3.1	10.5	67.0	14.5	2.6	116
50X-1, 140-150	543.10	8.3	32	549	1.18	0.86	0.37	1.7	22	—	9.1	87.1	13.7	1.1	—

Note: — = no analysis.

Table T32. Relative intensities of selected X-ray diffraction peaks from bulk mineral samples of Site 1095 sediments.

Core, section interval (cm)	Depth (mbsf)	Chlorite (7 Å)	Quartz (3.34 Å)	Plagioclase (3.19 Å)
178-1095A-				
1H-3, 59-61	3.52	12	100	30
1H-4, 87-89	5.30	9	100	36
3H-6, 99-101	17.77	6	100	32
3H-8, 13-15	19.12	18	100	34
4H-2, 83-85	23.13	20	100	39
4H-5, 85-88	27.65	10	100	21
7H-1, 58-61	49.88	8	100	39
7H-2, 51-54	51.31	18	100	35
178-1095B-				
1H-5, 20-22	89.20	5	100	32
5H-5, 128-130	128.30	13	100	39
9H-3, 18-19	162.20	10	100	37
9H-5, 39-41	165.40	4	100	23
13H-3, 64-66	199.60	13	100	34
18X-3, 128-130	247.80	15	100	41
21X-2, 124-126	275.10	12	100	45
23X-3, 34-36	295.00	12	100	42
25X-2, 35-37	312.80	12	100	51
29X-4, 25-26	354.30	11	100	38
33X-3, 71-73	391.40	15	100	41
37X-2, 45-48	427.80	7	100	43
41X-3, 101-104	468.50	15	100	46
45X-1, 90-92	498.90	13	100	41

Note: Highest selected peak intensity is normalized to 100.

Table T33. Relative intensities of selected X-ray diffraction peaks from clay mineral samples of Site 1095 sediments.

Core, section, interval (cm)	Depth (mbsf)	Glacial/ Interglacial	Chlorite (7 Å)	Illite (5 Å)	Mixed layer (~12 Å)
178-1095A-					
1H-3, 59-61	3.52	G	100	19	19
1H-4, 87-89	5.30	I	100	31	68
3H-6, 99-101	17.77	I	100	33	38
3H-8, 13-15	19.12	G	100	28	20
4H-2, 83-85	23.13	G	100	18	14
4H-5, 85-88	27.65	I	100	27	44
7H-1, 58-61	49.88	?	55	37	100
7H-2, 51-54	51.31	G	100	21	30
178-1095B-					
1H-5, 20-22	89.20	G	75	28	100
5H-5, 128-130	128.30	I	100	16	33
9H-3, 18-19	162.20	G	100	13	33
9H-5, 39-41	165.40	G	61	42	100
13H-3, 64-66	199.60	G	100	14	36
18X-3, 128-130	247.80	G	100	13	17
21X-2, 124-126	275.10	G	100	13	21
23X-3, 34-36	295.00	G	100	15	30
25X-2, 35-37	312.80	G	100	13	21
29X-4, 25-26	354.30	G	100	13	24
33X-3, 71-73	391.40	G	100	20	13
37X-2, 45-48	427.80	G	100	34	100
41X-3, 101-104	468.50	G	100	13	25
45X-1, 90-92	498.90	G	100	19	37

Note: Highest selected peak intensity is normalized to 100.

Table T34. Trace-element chemistry of bulk sediment, Holes 1095A and 1095B.

Hole, section, interval (cm)	Depth (mbsf)	Glacial/ Interglacial	Nb (ppm)	Zr (ppm)	Y (ppm)	Sr (ppm)	Rb (ppm)	Zn (ppm)	Cu (ppm)	Ni (ppm)	Cr (ppm)	V (ppm)	Ce (ppm)	Ba (ppm)
178-1095A-														
1H-3, 59-61	3.52	G	12	165	36	257	107	113	29	34	47	140	61	639
1H-4, 87-89	5.30	I	15	150	30	275	86	101	66	44	40	145	51	1398
3H-6, 99-101	17.77	I	13	190	32	277	101	107	49	32	40	138	53	971
3H-8, 13-15	19.12	G	13	180	35	261	108	112	20	29	43	141	47	583
4H-2, 83-85	23.13	G	12	163	37	246	108	122	19	32	39	143	60	546
4H-5, 85-88	27.65	I	13	163	34	267	100	127	104	42	45	143	63	880
7H-1, 58-61	49.88	?	12	157	34	277	99	108	37	26	32	137	55	412
7H-2, 51-54	51.31	G	13	166	34	250	108	108	22	28	44	159	48	487
178-1095B-														
1H-5, 20-22	89.20	G	11	173	26	258	82	74	27	17	21	112	49	644
5H-5, 128-130	128.30	I	8	127	25	217	77	90	26	21	29	128	45	436
9H-3, 18-19	162.20	G	10	130	24	232	76	86	26	18	27	126	38	577
9H-5, 39-41	165.40	G	11	118	27	172	108	81	29	19	29	103	41	366
13H-3, 64-66	199.60	G	11	149	28	253	83	96	28	24	32	140	52	474
18X-3, 128-130	247.80	G	11	141	29	232	86	105	34	26	35	157	41	457
21X-2, 124-126	275.10	G	10	138	28	247	87	98	28	21	28	151	39	450
23X-3, 34-36	295.00	G	9	134	24	263	75	89	28	20	25	141	35	412
25X-2, 35-37	312.80	G	9	138	27	263	80	97	30	22	28	149	37	408
29X-4, 25-26	354.30	G	10	141	24	262	70	84	26	19	25	134	35	410
33X-3, 71-73	391.40	G	10	140	28	238	87	86	28	22	29	150	37	411
37X-2, 45-48	427.80	G	10	174	29	250	85	101	29	20	28	132	50	412
41X-3, 101-104	468.50	G	10	143	30	246	81	100	30	22	35	166	37	406
45X-1, 90-92	498.90	G	10	150	29	254	81	86	26	21	27	162	34	410

Note: ? = uncertain interpretation.

Table T35. Summary of logging operations at Site 1095.

Task	Start time
Hole preparation	10:30, 22 February 1998
Triple combination	16:00, 22 February 1998
GHMT	04:15, 23 February 1998
WST	13:45, 23 February 1998
End of logging operations	00:30, 24 February 1998

Note: GHMT = geological high-sensitivity magnetic tool, WST = well seismic tool.

Table T36. Depth offsets of the Site 1095 mcd scale relative to mbsf depth. (Continued on next page.)

Core	Depth (mbsf)	Depth (mcd)	Offset (m)
178-1095A-			
1H	5.62	5.62	0
2H	12.49	14.19	1.7
4H	28.57	30.27	1.7
5H	38.25	41.03	2.78
6H	48.69	51.47	2.78
7H	58.93	62.17	3.24
8H	68.57	73.19	4.62
9H	77.85	82.47	4.62
10H	87.45	92.07	4.62
178-1095B-			
1H	92.51	93.05	0.54
2H	100.67	101.21	0.54
3H	111.51	112.05	0.54
4H	120.97	121.51	0.54
5H	130.51	131.05	0.54
6H	139.95	140.49	0.54
7H	149.52	150.06	0.54
8H	158.47	159.01	0.54
9H	168.51	169.05	0.54
10H	177.35	177.89	0.54
11H	187.51	188.05	0.54
12H	196.87	197.41	0.54
13H	203.05	203.59	0.54
14X	210.82	211.36	0.54
15X	218.19	218.73	0.54
16X	228.51	229.05	0.54
17X	243.33	243.87	0.54
18X	252.89	253.43	0.54
20X	272.09	272.63	0.54
21X	281.79	282.33	0.54
22X	288.05	288.59	0.54
23X	300.65	301.19	0.54
24X	310.75	311.29	0.54
25X	320.29	320.83	0.54
26X	330.03	330.57	0.54
27X	339.53	340.07	0.54
28X	349.17	349.71	0.54
29X	358.85	359.39	0.54
30X	368.57	369.11	0.54
31X	378.23	378.77	0.54
32X	387.71	388.25	0.54
33X	397.15	397.69	0.54
34X	406.61	407.15	0.54
35X	414.99	415.53	0.54
36X	425.63	426.17	0.54
37X	431.19	431.73	0.54
38X	444.95	445.49	0.54
39X	454.59	455.13	0.54
40X	464.25	464.79	0.54
41X	473.95	474.49	0.54
42X	483.55	484.09	0.54
43X	485.53	486.07	0.54
45X	499.75	500.29	0.54
46X	504.81	505.35	0.54
47X	513.35	513.89	0.54
48X	523.57	524.11	0.54
49X	533.15	533.69	0.54
50X	543.95	544.49	0.54
51X	552.29	552.83	0.54
52X	561.37	561.91	0.54
178-1095D-			
1H	8.31	8.31	0
2H	18.03	18.03	0
3H	27.35	27.35	0
4H	32.99	34.11	1.12
5H	45.17	46.29	1.12

Table T36 (continued).

Core	Depth (mbsf)	Depth (mcd)	Offset (m)
6H	51.56	53.46	1.9
7H	65.67	67.57	1.9
8H	71.57	73.47	1.9

Note: To shift from one scale to another, add (or subtract) the offset values to the mbsf depths. The depths are from the bottom of each section.

Table T37. Spliced cores for Holes 1095A, 1095B, and 1095D.

Hole, core, section, interval (cm)	Depth (mbsf)	Depth (mcd)		Hole, core, section, interval (cm)	Depth (mbsf)	Depth (mcd)
1095A-1H-4, 113	5.56	5.56	Tie	1095D-1H-4, 105.5	5.56	5.56
1095D-2H-6, 73	8.23	8.23	Tie	1095A-2H-1, 63	6.53	8.23
1095A-2H-5, 57	12.47	14.17	Tie	1095D-2H-4, 107	14.17	14.17
1095D-2H-7, 43	18.03	18.03	Append	1095D-3H-1, 0	18.1	18.1
1095D-3H-7, 21	27.31	27.31	Tie	1095A-4H-4, 31	25.61	27.31
1095A-4H-6, 27	28.07	29.77	Tie	1095D-4H-1, 105	28.65	29.77
1095D-4H-4, 53	32.63	33.75	Tie	1095A-5H-1, 67	30.97	33.75
1095A-5H-6, 39	38.19	40.97	Tie	1095D-5H-2, 125	39.85	40.97
1095D-5H-6, 33	44.93	46.05	Tie	1095A-6H-3, 47	43.27	46.05
1095A-6H-6, 133	48.63	51.41	Tie	1095D-6H-4, 26	49.51	51.41
1095D-6H-5, 81	51.56	53.46	Tie	1095A-7H-1, 91.5	50.22	53.46
1095A-7H-7, 51	58.81	62.05	Tie	1095D-7H-3, 105	60.15	62.05
1095D-7H-7, 51	65.61	67.51	Tie	1095A-8H-3, 109	62.89	67.51
1095A-8H-7, 77	68.57	73.19	Append	1095A-9H-1, 0	68.3	72.92
1095A-9H-7, 55	77.85	82.47	Tie	1095A-10H-1, 5	77.85	82.47
1095A-10H-7, 61	87.41	92.03	Tie	1095B-1H-6, 99	91.49	92.03
1095B-1H-7, 51	92.51	93.05	Append	1095B-2H-1, 0	92.5	93.04
1095B-2H-6, 67	100.7	101.2	Append	1095B-3H-1, 0	102	102.5
1095B-3H-7, 51	111.5	112.1	Append	1095B-4H-1, 0	111.5	112
1095B-4H-7, 47	121	121.5	Append	1095B-5H-1, 0	121	121.5
1095B-5H-7, 51	130.5	131.1	Append	1095B-6H-1, 0	130.5	131
1095B-6H-7, 95	140	140.5	Append	1095B-7H-1, 0	140	140.5
1095B-7H-7, 55	149.5	150.1	Append	1095B-8H-1, 0	149.5	150
1095B-8H-6, 147	158.5	159	Append	1095B-9H-1, 0	159	159.5
1095B-9H-7, 51	168.5	169	Append	1095B-10H-1, 0	168.5	169
1095B-10H-6, 135	177.3	177.9	Append	1095B-11H-1, 0	178	178.5
1095B-11H-7, 51	187.5	188	Append	1095B-12H-1, 0	187.5	188
1095B-12H-7, 37	196.9	197.4	Append	1095B-13H-1, 0	195.9	196.5
1095B-13H-5, 113	203	203.6	Append	1095B-14X-1, 0	205	205.5
1095B-14X-4, 137	210.8	211.4	Append	1095B-15X-1, 0	214.7	215.2
1095B-15X-3, 49	218.2	218.7	Append	1095B-16X-1, 0	224.3	224.8
1095B-16X-3, 121	228.5	229.1	Append	1095B-17X-1, 0	233.9	234.4
1095B-17X-7, 43	243.3	243.9	Append	1095B-18X-1, 0	243.5	244
1095B-18X-7, 39	252.9	253.4	Append	1095B-20X-1, 0	262.7	263.2
1095B-20X-7, 39	272.1	272.6	Append	1095B-21X-1, 0	272.4	272.9
1095B-21X-7, 39	281.8	282.3	Append	1095B-22X-1, 0	282.1	282.6
1095B-22X-4, 145	288.1	288.6	Append	1095B-23X-1, 0	291.7	292.2
1095B-23X-6, 145	300.7	301.2	Append	1095B-24X-1, 0	301.3	301.8
1095B-24X-7, 45	310.8	311.3	Append	1095B-25X-1, 0	310.9	311.4
1095B-25X-7, 39	320.3	320.8	Append	1095B-26X-1, 0	320.6	321.1
1095B-26X-7, 43	330	330.6	Append	1095B-27X-1, 0	330.2	330.7
1095B-27X-7, 33	339.5	340.1	Append	1095B-28X-1, 0	339.8	340.3
1095B-28X-7, 37	349.2	349.7	Append	1095B-29X-1, 0	349.5	350
1095B-29X-7, 35	358.9	359.4	Append	1095B-30X-1, 0	359.2	359.7
1095B-30X-7, 37	368.6	369.1	Append	1095B-31X-1, 0	368.8	369.3
1095B-31X-7, 43	378.2	378.8	Append	1095B-32X-1, 0	378.4	378.9
1095B-32X-7, 31	387.7	388.3	Append	1095B-33X-1, 0	387.7	388.2
1095B-33X-7, 45	397.2	397.7	Append	1095B-34X-1, 0	397.3	397.8
1095B-34X-7, 31	406.6	407.2	Append	1095B-35X-1, 0	406.6	407.1
1095B-35X-6, 89	415	415.5	Append	1095B-36X-1, 0	416.2	416.7
1095B-36X-7, 43	425.6	426.2	Append	1095B-37X-1, 0	425.8	426.3
1095B-37X-4, 89	431.2	431.7	Append	1095B-38X-1, 0	435.5	436
1095B-38X-7, 45	445	445.5	Append	1095B-39X-1, 0	445.1	445.6
1095B-39X-7, 49	454.6	455.1	Append	1095B-40X-1, 0	454.8	455.3
1095B-40X-7, 45	464.2	464.8	Append	1095B-41X-1, 0	464.5	465
1095B-41X-7, 45	474	474.5	Append	1095B-42X-1, 0	474.1	474.6
1095B-42X-7, 45	483.6	484.1	Append	1095B-43X-1, 0	483.8	484.3
1095B-43X-2, 73	485.5	486.1	Append	1095B-45X-1, 0	498	498.5
1095B-45X-2, 75	499.8	500.3	Append	1095B-46X-1, 0	503	503.5
1095B-46X-2, 83	504.8	505.4	Append	1095B-47X-1, 0	512.7	513.2
1095B-47X-1, 55	513.4	513.9	Append	1095B-48X-1, 0	522.4	522.9
1095B-48X-1, 117	523.6	524.1	Append	1095B-49X-1, 0	532.1	532.6
1095B-49X-1, 105	533.2	533.7	Append	1095B-50X-1, 0	541.7	542.2
1095B-50X-2, 75	544	544.5	Append	1095B-51X-1, 0	551.4	551.9
1095B-51X-1, 89	552.3	552.8	Append	1095B-52X-1, 0	560.8	561.3
1095B-52X-1, 57	561.4	561.9				

Table T38. Sedimentation rates calculated from geomagnetic polarity transition data. (Continued on next page.)

Depth (mbsf)	Age (Ma)	Chron	SR (cm/k.y.)
0.00	0		
			2.2
17.12	0.78	C1n(o)	
			2.9
23.20	0.99	C1r.1n(t)	
			8.2
29.75	1.07	C1r.1n(o)	
			4.4
60.39	1.77	C2n(t)	
			1.8
83.40	3.04	C2An.1n(o)	
			3.2
100.99	3.58	C2An.3n(o)	
			4.2
126.20	4.18	C3n.1n(t)	
			8.0
134.97	4.29	C3n.1n(o)	
			3.2
141.01	4.48	C3n.2n(t)	
			5.3
148.49	4.62	C3n.2n(o)	
			10.3
150.35*	4.8	C3n.3n(t)	
			3.7
153.71*	4.89	C3n.3n(o)	
			12.0
164.49	4.98	C3n.4n(t)	
			5.3
177.86	5.23	C3n.4n(o)	
			4.8
209.74	5.894	C3An.1n(t)	
			4.6
220.99	6.137	C3An.1n(o)	
			14.0
239.46	6.269	C3An.2n(t)	
			6.2
257.80	6.567	C3An.2n(o)	
			9.3
292.04	6.935	C3Bn(t)	
			7.7
304.03	7.091	C3Bn(o)	
			2.3
305.03*	7.135	C3Br.1n(t)	
			3.5
306.26*	7.17	C3Br.1n(o)	
			6.1
322.23	7.432	C4n.1n(t)	
			2.7
325.80	7.562	C4n.1n(o)	
			6.6
331.60	7.65	C4n.2n(o)	
			5.7
355.67	8.072	C4n.2n(t)	
			7.8
399.86	8.635	C4r.2r-1(t)	
			30.8
404.79	8.651	C4r.2r-1(o)	
			14.4
411.72	8.699	C4An(t)	
			10.7
446.00	9.025	C4An(o)	
			7.2
460.87	9.230	C4Ar.1n(t)	
			33.5
487.00*	9.308	C4Ar.1n(o)	
			8.3

Table T38 (continued).

Depth (mbsf)	Age (Ma)	Chron	SR (cm/k.y.)
523.00*	9.740	C5n.1n(o)	
			14.0
548.00*	9.920	C5n.2n(t)	

Notes: The depths of the geomagnetic reversals from the logging results have been shifted upward by 5 m to align them with the core depth scale. Depths of reversals are from split-core analysis, except where an asterisk indicates GHMT data. SR = sedimentation rate.

Table T39. Sedimentation rates calculated from radiolarian datums.

Depth (mbsf)	SR (cm/k.y.)	Age (Ma)	Comments
0		0	Top of hole
	2.8		
68.3		2.4	T *Desmospyris spongiosa*
	3.3		
111.5		3.7	T *Lampromitra coronata*
	5.3		
159		4.6	B *Helotholus vema*
	18.7		
233.9		5	TC *Lychnocanium grande*
	4.5		
359.2		7.8	T *Siphonosphaera vesuvius*
	10.3		
493.4		9.1	T *Cycladophora spongothorax*

Note: SR = sedimentation rate, T = top/last occurrence, B = base/first occurrence, TC = top common occurrence (see **"Biostratigraphy,"** p. 13).

Table T40. Sedimentation rates calculated from diatom datums.

Depth (mbsf)	SR (cm/k.y.)	Age (Ma)	Comments
0.0		0.00	Top of hole
	1.1		
7.2		0.64	T *Actinocyclus ingens* (Leg 120)
	5.2		
70.8		1.85	T *Thalassiosira kolbei* (Leg 120)
	1.2		
80.9		2.67	T *Fragilariopsis interfrigidaria* (Leg 120)
	2.8		
112.0		3.80	B *Fragilariopsis interfrigidaria* (Leg 120)
	2.0		
125.9		4.48	B *Thalassiosira striata* and *Fragilariopsis barronii* (Leg 120)
	11.5		
142.0		4.62	B *Thalassiosira complicata* (Leg 120)
	17.4		
194.1		4.92	B *Thalassiosira inura* (Leg 177)
	4.9		
212.8		5.30	B *Fragilariopsis praeinterfrigidaria* (Leg 177)
	10.8		
276.7		5.89	B *Actinocyclus ingens* v. ovalis (Ac.sp.A; Leg 120)
	2.6		
349.5		8.68	B *Actinocyclus ingens* v. ovalis

Notes: SR = sedimentation rate, T = top/last occurrence, B = base/first occurrence. The number in the comment column denotes the ODP leg in which the absolute age for a marker species datum was determined (see "Biostratigraphy," p. 9, in the "Explanatory Notes" chapter).

Table T41. TWT and depth to base of seismic units at Site 1095.

Seismic Unit	TWT (ms)	Depth (mbsf)	Age (Ma)
Unit I	84	64	1.7 (hiatus?)
Subunit IIa	138	107	3.73
Subunit IIb	190	149	4.65
Subunit IIc	267	214	5.98
Subunit IId	309	250	6.43
Subunit IIe	409	338	7.76
Base of hole	654	570.2	

Note: Ages according to magnetic reversal identifications (Table **T38,** p. 169).